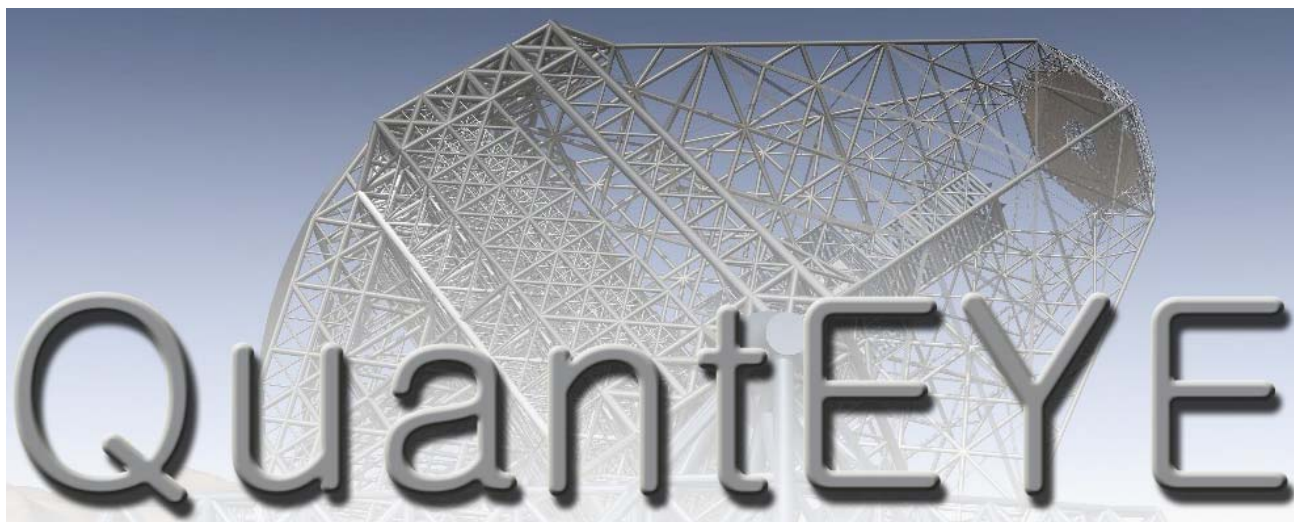


## OWL Instrument Concept Study



### QUANTUM OPTICS INSTRUMENTATION FOR ASTRONOMY

**D. Dravins<sup>1</sup>, C. Barbieri<sup>2</sup>,**

**V. Da Deppo<sup>3</sup>, D. Faria<sup>1</sup>, S. Fornasier<sup>2</sup>,**

**R. A. E. Fosbury<sup>4</sup>, L. Lindegren<sup>1</sup>, G. Naletto<sup>3</sup>, R. Nilsson<sup>1</sup>,**

**T. Occhipinti<sup>3</sup>, F. Tamburini<sup>2</sup>, H. Uthas<sup>1</sup>, L. Zampieri<sup>5</sup>**

(1) Lund Observatory, Box 43, SE-22100 Lund, Sweden

(2) Department of Astronomy, University of Padova, Vicolo dell'Osservatorio 2, IT-35122 Padova, Italy

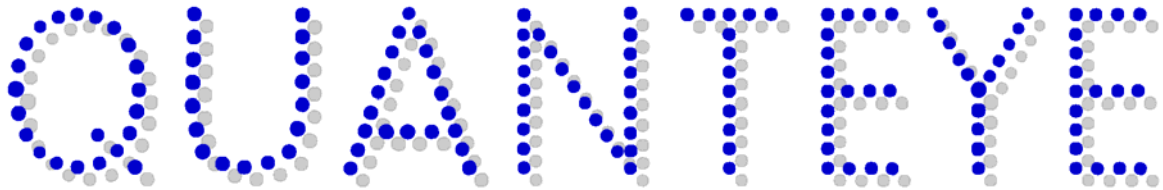
(3) Dept. of Information Engineering, University of Padova, Via Gradenigo, 6/B, IT-35131 Padova, Italy

(4) Space Telescope-European Coordinating Facility & European Southern Observatory,  
Karl-Schwarzschild-Straße 2, DE-85748 Garching bei München, Germany

(5) INAF – Astronomical Observatory of Padova, Vicolo dell'Osservatorio 5, IT-35122 Padova, Italy







QUANTEYE

**Quantum Optics Instrumentation for Astronomy**

**D. Dravins, C. Barbieri**

**V. Da Deppo, D. Faria, S. Fornasier**

**R. A. E. Fosbury, L. Lindegren, G. Naletto, R. Nilsson**

**T. Occhipinti, F. Tamburini, H. Uthas, L. Zampieri**

OWL Instrument Concept Study, OWL-CSR-ESO-00000-0162

Version 1.0 — October 2005



<b>TABLE OF CONTENTS</b> .....	<b>3</b>
<b>Scope, Participants, and Schedule</b> .....	<b>7</b>
<b>Executive Summary</b> .....	<b>9</b>
<b>1. The Road to Quantum Astronomy</b> .....	<b>13</b>
1.1. Introduction	
1.2. Aims of the Study	
1.3. High Time-Resolution Astrophysics	
1.4. Which Timescales are Observationally Accessible?	
1.5. Astrophysics on Subsecond Scales	
1.6. Nanoseconds and Quantum Optics	
1.7. Beyond Imaging, Photometry, and Spectroscopy	
1.8. One-Photon Experiments	
1.9. Two- and Multi-Photon Properties of Light	
1.10. The Intensity Interferometer	
1.10.1. The Narrabri interferometer	
1.10.2. Intensity fluctuations when photon counting	
1.10.3. The situation with a resolved star	
1.10.4. Resolution vs. stellar surface temperature	
1.10.5. The effect of atmospheric scintillation	
1.10.6. The effect of polarization	
1.11. Possible Modern Realizations of Intensity Interferometry	
1.11.1. Very long baseline optical intensity interferometry?	
1.11.2. Combining intensity interferometry with optical heterodyne	
1.12. Intensity-Correlation Spectroscopy	
1.13. Intensity Interferometry of Non-Photons	
<b>2. Quantum Phenomena in Astronomy</b> .....	<b>43</b>
2.1. Physics of Emission Processes	
2.2. Cosmic Laser/Maser Sources	
2.2.1. Non-equilibrium radiation in astrophysics	
2.2.2. Mechanisms producing astrophysical lasers	
2.2.3. A case study: Astrophysical lasers in Eta Carinae	
2.2.4. Lasers in Wolf-Rayet and symbiotic stars	
2.2.5. Hydrogen lasers/masers in the emission-line star MWC349A	

- 2.2.6. First masers in the Universe
- 2.2.7. CO<sub>2</sub> lasers in planetary atmospheres
- 2.2.8. Lasers without population inversion?
- 2.2.9. Nanosecond pulses in pulsars
- 2.2.10. How short (and bright) pulses exist in nature?
- 2.2.11. Emission in magnetic fields of magnetars
- 2.2.12. Maser mechanism for optical pulsations in X-ray pulsars?
- 2.3. Photon Statistics as a Diagnostic Tool
  - 2.3.1. Identifying laser effects in astronomical sources
  - 2.3.2. Modeling photon statistics
- 2.4. Photon Orbital Angular Momentum
- 2.5. Quantum Gravity Effects?

**3. Observational High-Speed Astrophysics ..... 77**

- 3.1. Examples of High-Speed Phenomena
  - 3.1.1. Time domain and reprocessing: High-frequency phenomena in optical and infrared
  - 3.1.2. Galactic X-ray binaries
  - 3.1.3. Finding exoplanets through dark speckles
  - 3.1.4. Occultations by the Moon, asteroids, and Kuiper-belt objects
- 3.2 Advantages of the Optical
- 3.3. Advantages of Great Light-Collecting Power
- 3.4. Advantages of Large Telescope Area
- 3.5. Using Optical Flux Collectors
  - 3.5.1. *MAGIC* on La Palma
  - 3.5.2. The H.E.S.S. observatory in Namibia
  - 3.5.3. The Pierre Auger observatory in Argentina
  - 3.5.4. Solar flux collectors

**4. Instrumental Requirements ..... 103**

- 4.1. Optical and Near-IR Detectors for Nanosecond Astrophysics
  - 4.1.1. Photomultipliers
  - 4.1.2. Avalanche photodiodes
  - 4.1.3. Futuristic detectors
- 4.2. Time Tagging and Time Distribution

**5. *QuantEYE* Conceptual Instrument Design ..... 127**

- 5.1. *QuantEYE* Requirements and Identified Solutions
  - 5.1.1. Time tagging accuracy and duration of operation
  - 5.1.2 Spectral range and choice of detectors
  - 5.1.3 Optical design requirements
  - 5.1.4 Filters and polarizers
  - 5.1.5 Electronic acquisition and data storage

- 5.2. Requirements set by *QuantEYE* on OWL
- 5.3. Optical Design
  - 5.3.1. Baseline: A non-imaging solution
    - 5.4.1.1. Variants of the non-imaging solution
    - 5.3.1.2. Further advantages of the non-imaging solution
  - 5.3.2. An imaging solution
  - 5.3.3. The second optical head
- 5.4. Photon Budget and Limiting Magnitude
  - 5.4.1. Linear regime
  - 5.4.2. Limiting magnitude
  - 5.4.3. Integration times
- 5.5. Data Acquisition
  - 5.5.1. Time-to-digital converter (TDC)
  - 5.5.2. Clock reference and time precision
- 5.6. Electronics
  - 5.6.1. Scenario (1): *Ad hoc* electronics
  - 5.6.2. Scenario (2): Commercial solutions
- 5.7. Mechanical and Electrical Characteristics
- 5.8. Cost Estimates
- 5.9. Technical Issues in Current Design
- 5.10. Future Design Challenges
- 5.11. Instrumentation Physics
- 5.12. Quantum Information and Quantum Computing
- 5.13. A Possible Precursor for VLT

**6. Observing with *QuantEYE* ..... 169**

- 6.1. Astronomical Targets
- 6.2. Connection to Other Astronomy Projects

**7. Conclusions ..... 177**

**Appendices**

**A1. Coherence Properties of Light ..... 179**

- A1.1. Deviation from the Average, and Correlation Functions
- A1.2. Correlation Functions
- A1.3. Temporal Coherence and the Coherence Time
- A1.4. Spatial Coherence and the Coherence Area

- A1.5. Coherence Volume and the Degeneracy Parameter
- A1.6. Bose-Einstein Statistics
- A1.7. Photon Antibunching and Sub-Poissonian Statistics
- A1.8. Photons from a Black Body
- A1.9. Fluctuations of Black-Body and Thermal Radiation
- A1.10. Statistical Analysis when Photon Counting
- A1.11. Experimental Evidence of Correlated Photon Fluctuations from Thermal Sources

**A2. Intensity Interferometry ..... 197**

- A2.1. The Original Interferometer at Narrabri
- A2.2. Examples of Intensity Fluctuations When Photon Counting
- A2.3. Resolution vs. Stellar Surface Temperature

**A3. High-Speed Instrumentation Worldwide ..... 205**

- A3.1. HSP on Hubble Space Telescope
- A3.2. HIPO on the SOFIA Airborne Telescope
- A3.3. ULTRACAM
- A3.4. STJ & TES: Superconducting Energy-Resolving Detectors
- A3.5. OPTIMA
- A3.6. MANIA
- A3.7. Optical SETI
- A3.8. Lunar- & Satellite Laser Ranging
- A3.9. QVANTOS
- A3.10. TRIFFID, MEKASPEK & MCCP, SUBARU, SALT, ESO-VLT, Opticon, and Other

**Acknowledgements ..... 245**

**References and bibliography ..... 247**



## Scope, Participants, and Schedule

**Scope:** This is the report of a conceptual design study of an instrument for optical astrophysics with the very highest time resolution feasible, adequate to identify and study also quantum-optical phenomena in the light from astronomical sources.

It is *not*, however, any complete nor really comprehensive study of such an instrument, nor of all the science to be carried out with it. The limit of its scope should be understood from the fact that this document is the result of part-time work by a limited number of persons during a quite limited period of time, and thus parts of this report may more resemble “lecture notes” rather than an exhaustive monograph. Nevertheless, the combined documentation of various relevant issues, building upon previous varied experiences in observations, instrumentation, data analysis, and astrophysical theory, should give an adequate base upon which to build both a more detailed design study and the construction of a prototype instrument, to eventually evolve into a quantum eye for the future OWL telescope.

**Participants:** The following persons took part in this study and in the preparation of this document:

*Cesare Barbieri*, Department of Astronomy, University of Padova, Italy  
*Vania Da Deppo*, Department of Information Engineering, University of Padova  
*Dainis Dravins*, Lund Observatory, Lund University, Sweden  
*Daniel Faria*, Lund Observatory, Lund University, Sweden  
*Sonia Fornasier*, Department of Astronomy, University of Padova, Italy  
*Bob Fosbury*, ST-ECF, European Southern Observatory, Garching, Germany  
*Lennart Lindgren*, Lund Observatory, Lund University, Sweden  
*Giampiero Naletto*, Department of Information Engineering, University of Padova  
*Ricky Nilsson*, Lund Observatory, Lund University, Sweden  
*Tommaso Occhipinti*, Department of Information Engineering, University of Padova  
*Fabrizio Tamburini*, Department of Astronomy, University of Padova  
*Helena Uthas*, Lund Observatory, Lund University, Sweden  
*Luca Zampieri*, INAF, Astronomical Observatory of Padova, Italy

**Coordinator for this study at ESO:** *Bob Fosbury*

**Coordinator for the OWL instrumentation studies at ESO:** *Sandro D'Odorico*

**The working group held meetings:**

11 November 2004, at ESO Garching  
22-23 March 2005, at University of Padova  
7-9 June 2005, at Lund Observatory  
26-28 September 2005, at ESO Garching

**This document was finalized in October, 2005**

**Correspondence regarding this report should be directed to:**

*Dainis Dravins*, e-mail: [dainis@astro.lu.se](mailto:dainis@astro.lu.se)  
*Cesare Barbieri*, e-mail: [cesare.barbieri@unipd.it](mailto:cesare.barbieri@unipd.it)



## Executive Summary

### *QuantEYE*

*QuantEYE* is conceived to be the highest time-resolution instrument in optical astronomy. It is designed to explore astrophysical variability on microsecond and nanosecond scales, reaching down to the quantum-optical limit. Expected observable phenomena include instabilities of photon-gas bubbles in accretion flows, oscillations in neutron stars and quantum-optical photon bunching in time. The precise timescales of such phenomena are variable and unknown, and studies must be of photon-stream statistics, e.g., power spectra or autocorrelations. Such functions increase with the *square* of the *intensity*, implying an enormously increased sensitivity at the largest telescopes. *QuantEYE* covers the optical spectrum and its design utilizes an array of photon-counting avalanche diode detectors, each viewing one segment of the OWL entrance pupil. *QuantEYE* can begin operation while the OWL pupil is only partially filled, will not require [full] adaptive optics, and will be mainly used on relatively bright sources (visual magnitudes typically 15 – 20) during bright-Moon periods.

The concept study commences with a review of quantum optical phenomena in general and then focuses on those of potential interest in astrophysics. After examining the current state of high-speed astrophysics, it examines the instrumental requirements for extension to higher time resolution and then presents a conceptual design for an instrument that exploits the huge advantage offered by the OWL aperture.

### High-Speed Astrophysics and Quantum Optics

Numerous discoveries have been made with resolutions of milliseconds and slower: optical and X-ray pulsars; planetary-ring occultations; rotation of cometary nuclei; cataclysmic variable stars; pulsating white dwarfs; flickering high-luminosity stars; oscillations in X-ray binaries; gamma-ray burst afterglows, and many others. A limit to such optical studies has been that CCD-like detectors do not readily permit frame-rates faster than 1–10 ms, while photon-counting detectors either have low efficiency or else photon-count rates limited to no more than some hundreds of kHz. Such instrumental limitations have been compounded by the lack of adequate telescope light-collecting power. For reasonable sensitivity, the required photon flux must match the time resolution: microseconds require megahertz count rates.

*QuantEYE* on OWL is designed for sub-nanosecond resolutions with GHz photon count-rates to match. This will enable detailed searches for phenomena such as: millisecond pulsars; variability close to black holes; surface convection on white dwarfs; acoustic spectra of non-radial oscillations in neutron stars; fine structure across neutron-star surfaces; photon-gas bubbles in accretion flows; and possible free-electron lasers in the magnetic fields around magnetars. Nanosecond-resolution photon-correlation spectroscopy will enable spectral resolutions exceeding  $R = 100$  million (as is probably required to resolve narrow laser-line emission around sources such as Eta Carinae), and *QuantEYE* will have the power to examine quantum statistics of photon arrival times.

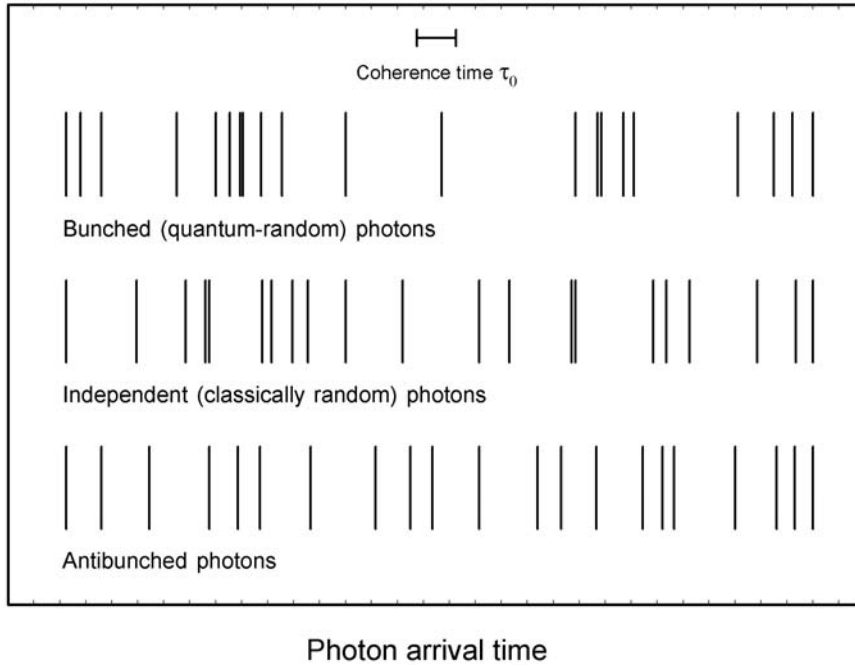


**Fig.1.** Statistics of photon arrival times in light beams with different entropies. Light may carry more information than that revealed by imaging and spectroscopy: Photons from given directions with given wavelengths give the same astronomical images and spectra, though the light may differ in statistics of photon arrival times. These can be “random”, as in maximum-entropy black-body radiation (Bose-Einstein distribution with a certain “bunching” in time), or may be quite different if the radiation deviates from thermodynamic equilibrium. (Loudon 2000)

## QuantEYE Conceptual Design

With *QuantEYE* aiming at timescales down to nanoseconds, there is the corresponding need to count photons at sustained rates up to some GHz. The requirement of a high quantum efficiency leads to single-photon counting avalanche diodes (SPAD) as the detectors of choice, although — at least at present — there appears not to exist any *single* detector that can handle such count rates. This leads us towards the concept of a multi-element — although not necessarily contiguous — detector array over which the light from the source is distributed. A further technical limit is set, at least at present, by the small physical size (of order 100  $\mu\text{m}$ ) of the detector elements which complicates the optical interface to large telescopes. Existing silicon-based SPAD cover the optical from 400–1000 nm, while for the near infrared (1–1.8  $\mu\text{m}$ ), SPAD based on germanium and similar materials are being developed in industry. Although such infrared SPAD already exist, their dark-count rates are still too high for our applications.

For the first conceptual design, a “conservative” approach has been taken, shaping the system within existing detector technologies. Besides demonstrating the feasibility of concept, this means that a prototype instrument could be constructed along these lines and using commercially available components.

The optical design is for point source observations and uses pupil-slicing by optically subdividing the OWL 100 m entrance pupil into one hundred 10m segments. Light from these 100 pupil segments is then focused onto an array of 100 fast ( $f/1$ ) lenslets to feed an array of 100 SPAD through optical-fibers. Each detector can sustain photon-count rates of up to some 10 MHz, enabling a combined output of 1 GHz. Although, after photon detection, each detector has a deadtime of around 50 ns, the timing of each photon can be recorded with

subnanosecond precision, as can the correlation between photon arrivals in different detectors. An exact differential timetag is assigned by a hydrogen maser clock (or future optical clock), and a GPS (or future *Galileo*) satellite receiver system provides an absolute time reference, thus enabling coordinated observations with other instruments on the ground or in space. A second detector unit, independently positionable over a 3 arcminute field of view, will allow calibration and reference measurements on a second source. Besides enabling GHz count rates, the segmented-pupil design has advantages in that (a) The detector redundancy enables the confirmation of possibly doubtful signals through their expected simultaneous occurrence in different channels; (b) Some events imply an illumination sweeping across the entrance pupil (e.g. occultations by Kuiper-belt asteroids), which can be both spatially and temporally resolved; and (c) By suitable cross-correlations of the detected signal, a digital intensity interferometer of the Hanbury-Brown & Twiss type can be realized between a large number of different sub-apertures. Raw data rates of 100–1000 Mb/s will be highly compressed in real time by on-line digital signal processors outputting only the appropriate statistical functions. Thanks to the pupil-slicing concept, *QuantEYE* will be able to work already with a partially filled OWL pupil, and (assuming the source is kept within the 1 arcsec aperture) will function well also without [full] adaptive optics. The present optical solution is outlined in Figure 2.

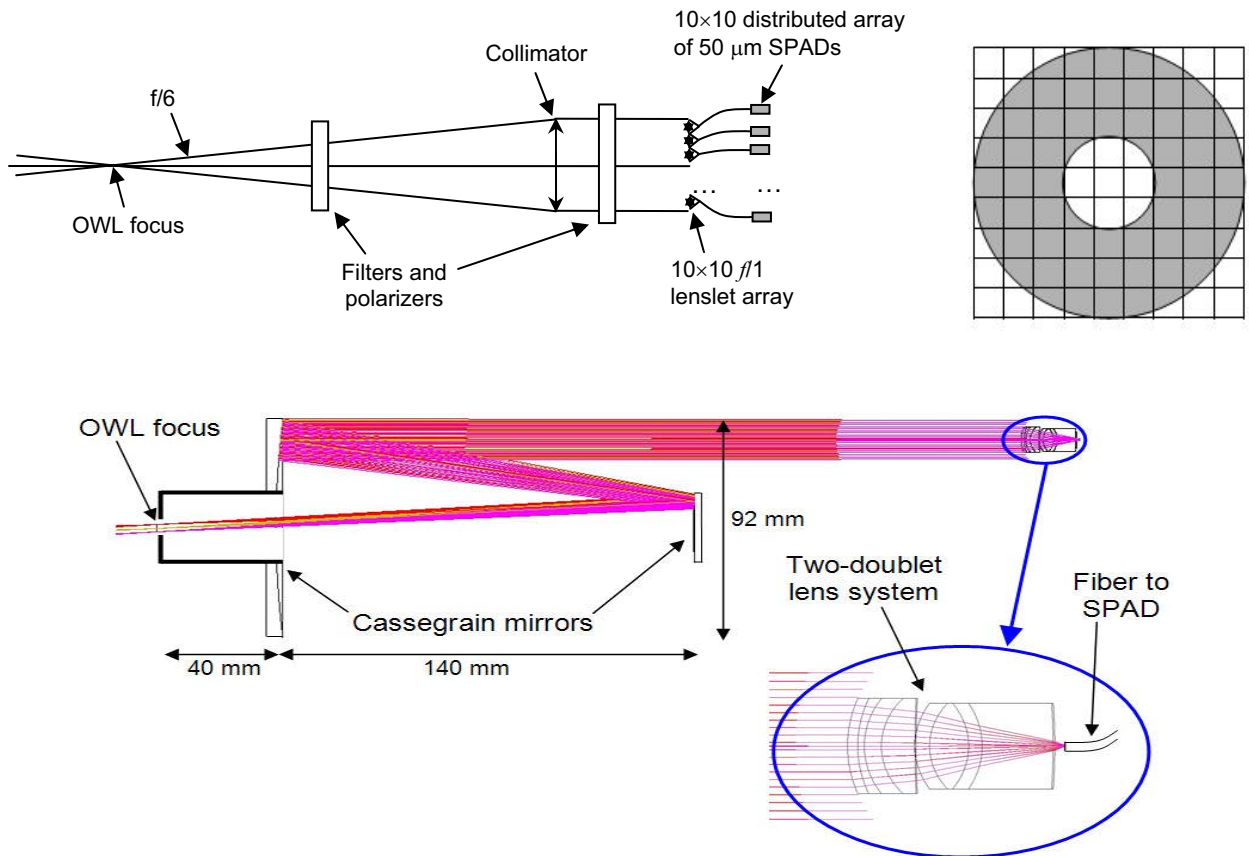






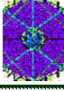
**Fig.2.** Current optical concept for *QuantEYE*: A distributed detector array and a segmented aperture. The collimator-lens system magnifies 1/60 times (collimator focal length = 600 mm, lens focal length = 10 mm), giving a nominal spot size of 50  $\mu$ m for a 1 arcsec source. At the focus of each lenslet there is an optical fiber leading to a single-photon counting avalanche diode detector. Some lenses are used to monitor the “dark” statistics

This present design has limitations, in particular only permitting observations of one point source per detector head at a time (field-of-view is one arcsecond). Developments in avalanche-diode array technology are in progress in industry and, when their performance reaches satisfactory levels, these should enable a fully *imaging* system with nanosecond

resolution. For example, such an imaging device could observe a globular cluster containing an active X-ray source of unknown location, and then search for an optically rapidly variable object over a field of perhaps a megapixel.

### The need for extremely large telescopes

The largest optical telescopes offer *enormously* increased sensitivity for studying astrophysical variability on timescales of milli-, micro-, and nanoseconds. Since the astrophysical phenomena are normally not periodic, and their exact timescales are both unknown and variable, studies must be of photon-stream statistics, e.g., power spectra or autocorrelations. Such functions increase with the *square* of the collected light intensity: doubling the telescope diameter increases the area four times but the signal by a factor of 16! Higher-order correlations increase even more steeply with telescope size.

Telescope diameter	Intensity $\langle I \rangle$	Second-order correlation $\langle I^2 \rangle$	Fourth-order photon statistics $\langle I^4 \rangle$
 3.6 m	1	1	1
 8.2 m	5	27	720
 4 × 8.2 m	21	430	185,000
 50 m	193	37,000	1,385,000,000
 100 m	770	595,000	355,000,000,000

**Table 1.** Light-curves become useless for time resolutions below microseconds where the time interval between successive photons may be longer than the time resolution. Instead studies have to be of the statistics of the arriving photon stream, such as its correlations or power-spectra. All such statistical functions depend on [at least] the second power of the source intensity. The table compares the observed signal ( $I$ ), its square and fourth powers, for telescopes of different size. The signal for classical quantities increases with the intensity  $I$ ; the signal in power-spectra as  $I^2$ ; and that of four-photon correlations as  $I^4$ . This very steep dependence makes the largest telescopes enormously more sensitive for high-speed astrophysics and quantum optics.



# 1. The Road to Quantum Astronomy

## 1.1. Introduction

Astronomy has always played a fundamental role in the advance of science, from chemistry to physics and now also to biology. This primary role has been both in discovering natural phenomena not known in the terrestrial laboratory and in promoting new technologies to overcome the measuring limitations of the time. As a consequence, astronomy has also been an *active promoter* and a *privileged user* of advanced technologies, for example of optics, detectors, computers, information technology. This multifaceted role will certainly be played also in the future, specifically for the theoretical advancement and practical utilization of quantum optics, quantum information and quantum computing, leading to a novel ‘quantum astronomy’, or probably better to an *astronomy to the quantum limit*.

Quantum mechanics has changed our understanding of the fundamental principles of nature. Its predictions are often intriguing and counterintuitive in their philosophical consequences. All physical systems can be described as complex vectors, thereby spanning the so-called Hilbert space, and all their possible representations are also members of this vector space, as are sums (*superpositions*) and products of state vectors. For example, a photon with horizontal polarization is represented by the state vector  $|H\rangle$ . The dynamic evolution of the state vectors is generally described by the Schrödinger equation. A projective measurement on a system is described as a linear operator acting on the state vector and thus projects the state of the system into one of the *eigenstates* of the measurement operator, which is the final state of the system after the projective measurement. This basic notion of vector calculus allows understanding the most fundamental principles of quantum mechanics: superposition and entanglement (see Zeilinger 1998).

The superposition principle contains the description of a physical system as a superposition of alternatives. This so-called “superposition of states” not only provides all predictions for the outcome of a physical measurement, but has also drastic consequences for the nature of the state which we ascribe to a system, because of the indistinguishability of states: if there exists more than one physical state for the system, the quantum mechanical state is in a coherent superposition (the term “coherent” indicates that those state vectors have a certain fixed angular relation, a so-called phase-relation) of indistinguishable alternative states. Then the question about the actual state of the system has no ontological meaning. As an example we might consider a typical double-slit experiment, which, according to Richard Feynman, “has in it the heart of quantum mechanics”: single particles are sent through a double slit configuration (with both slits A and B open) and their position is measured on a screen far behind the slit. Interference fringes can be observed on the screen after a sufficient number of particles has arrived, as was shown in experiments with photons, electrons, neutrons, atoms and molecules (in 1999, two slit interference of a single  $C_{60}$  molecule has been realized by A. Zeilinger and coworkers, see Arnd et al. 1999). The fringes cannot be explained by assuming that the particle passes through either one of the slits. Since one and only one particle passed the apparatus for one detection event, one could raise the question, which of the two slits the particle has actually come through. In quantum physics, without performing the actual measurement at the position of the two slits, this question has no meaning. If both slits A and B are open, the quantum mechanical state of the particle is in the coherent superposition  $|\Psi\rangle = \frac{1}{\sqrt{2}}(|\Psi_A\rangle + |\Psi_B\rangle)$ , where  $\Psi_A$  and  $\Psi_B$  describe the quantum state with only slit A or slit B open, i.e. the two possible indistinguishable alternatives of the double-slit system. Instead, if a measurement is performed to obtain the information about which of the ways A or B the

particle took through the double-slit (e.g. by closing one of the slits), no interference fringes can be observed. By obtaining information out of a coherently superposed system, we reduce its intrinsic quantum properties, i.e. its capability to show quantum interference: we introduce decoherence. Only when there is no way of knowing, not even in principle, through which slit the particle passes, we do observe interference. Paul Dirac (1958) stated: "The new theory which connects the wave function with probabilities for one photon, gets over the difficulty by making each photon go partly into each of the two components. Each photon then interferes only with itself." This is one of the most intriguing features of quantum physics.

The boldest consequence of the double slit experiment of interest to astronomy is the so called Wheeler's delayed choice experiment (Wheeler 1978), which shows in an impressive way how physical realism, namely that particles have definite paths (position and momentum are equally well defined), leads to contradictions with either quantum physics or locality. Delayed choice experiments are generally based on the fact, that, depending on the experimental setup, a quantum system can either exist in a superposition of two orthogonal states or is "localized" in one of the two states. However, the decision on the actual setup can be delayed way beyond the time when the system enters the apparatus, contradicting the realist notion that the properties of a physical system are predetermined during the whole time of the experiment. Taking this argument to the extreme, John Wheeler proposed a scaling up to cosmic proportions of Young's double slit experiment. In this *Gedanken* experiment, gravitational lenses (e.g. a galaxy or a black hole) are used as giant slits to create two paths for photons from a quasar or distant galaxy. All these photons have to pass the gravitational lens in a way that the possible paths cross in the vicinity of Earth. One may now ask, how the photons will behave depending on the experimenter placing a beamsplitter at the intersection or not. Quantum physics predicts that the presence or absence of interference only depends on the actual positioning of the beamsplitter as decided by the experimenter, although in a pure realist's particle-picture the particle had to choose its way millions of years ago. In other words, the realist seems to be "deciding what the photon shall have done after it has already done it!"

The superposition principle also leads to the concept of quantum bit, or *qubit*. In classical information and computation science, information is encoded in the most fundamental entity, the bit. Its two possible values "0" and "1" are physically realized in many ways, all of them having in common that one state mutually excludes the simultaneous presence of the other, the switch is either "on" or "off". Modern techniques make it possible to encode information on individual quantum systems. These so-called *qubits* also utilize a two-state system with separate states  $|0\rangle$  and  $|1\rangle$ . However, in contrast to its classical counterpart, the qubit entails the possibility of coherent superposition, i.e. the qubit is represented by the general state  $|Q\rangle = \alpha|0\rangle + \beta|1\rangle$ .

Quantum entanglement, a term originally coined by Erwin Schrödinger, is the essence of quantum physics. Two entangled particles (including photons) can only be described by their joint behavior. This has the intriguing consequence that measurements on the individual particles will always lead to random results on the single particle, although perfectly correlated between the two entangled particles, no matter how far apart the two particles are. For two imaginary "entangled dice" this would mean that although each throw of one dice has a random result (between 1 and 6), the throw on the second dice would always copy this result, independent of the separation between the dices. Albert Einstein called this astonishing behavior "spooky action at a distance". In theory, these correlations should be maintained over arbitrary distances. The principle of superposition holds for states containing several qubits, and therefore allows for multi-qubit systems which can only be described by a joint wavefunction, i.e. by a coherent superposition of orthogonal states. These states are called "entangled", describing the fact that none of the particles involved can be described by a wavefunction of its own. Entangled states have the astonishing property, that all of their



information content is completely entailed in the correlations of the two qubits. None of the qubits does carry any information on its own: by performing measurements on only one of the qubits of an entangled state it is impossible to obtain information stored in the entangled system (the outcome will be perfectly random), although it is clear, that, as it consists out of two qubits, it carries 2 bits of classical information. The information can only be obtained, when the outcomes of the measurements on the two separate subsystems are compared (correlated) via classical communication or if both qubits are measured together in the entangled basis, in which the state was initially prepared in. Moreover, a measurement of one of the qubits of an entangled state instantaneously projects the other qubit in the corresponding perfectly correlated state, thereby destroying this entanglement. In total, there are four independent possibilities for two qubits to store information in their correlations only. Those maximally entangled two-qubit states are called Bell-states. The intriguing feature about Bell-states is that any system consisting of two qubits can be completely described in terms of a superposition of Bell-states. This is of specific interest for cases, in which more than two particles are involved. For example, the projection of two independent qubits on a Bell-state can establish correlations between particles that never interacted, as is used in quantum communication schemes such as *quantum state teleportation*.

Therefore, entanglement is probably the most important concept of quantum mechanics and at the same time its most counterintuitive feature. The perfect correlations between two qubits of an entangled system are in conflict with the concepts of classical physics, above all the concepts of locality (i.e. events in spacelike separated regions cannot interact, specifically, a measurement at A cannot influence the outcome of a measurement at a spacelike separated place B) and realism (i.e. the notion that each physical quantity that can, in an undisturbed system, be predicted with certainty corresponds to an ontological entity, a so-called “element of reality”). This has led to various philosophical debates about whether quantum mechanics can serve as a complete description of reality (Einstein-Podolsky-Rosen debate, Einstein et al. 1935, Bohr 1935) until John Bell (1964) put forward an experimental scheme to show, that the predictions of quantum mechanics are in contradiction to predictions of a physical theory based on local realism. The latter one has to obey certain bounds, given by Bell’s Inequalities, which are clearly violated by predictions of quantum theory. Experiments have been performed which can not only be described by quantum theory, but are also in clear conflict with Bell’s Inequalities, even under strict space-like separation of two distant observers (Weihs et al. 1998). On the astrophysical side, a possible link between EPR-type quantum phenomena and astrophysical objects like black holes has been suggested, under a new general definition of entanglement bringing to a definition of the system black hole - worm hole - white hole as an entangled system (Basini et al. 2003).

In conclusion, many of the controversial predictions of quantum mechanics have been verified extensively, leading to the development of new concepts and new instruments. Quantum technologies in optics, information, communication and computing are emerging, their practical implementations have proved successful and industrial applications are currently being developed in laboratories all over the world. Starting years ago with the development of the laser, current frontline work includes physical measurements of the highest accuracy such as the development of optical clocks or the use of squeezed light for gravitational wave detection. The information-carrying capacities of photons are utilized for quantum computing and in quantum teleportation. Indeed, there is a tendency to rename the whole science of optics to photonics in reflecting the increasingly dominant role of photon physics.

The European Community and the European Space Agency are very active in this field of quantum technologies, a further indication that quantum research has indeed taken the step from laboratories investigating the foundations of physics into the world of industry and of space applications. The focus on ambitious long-term research and development goals intends to secure Europe a position at the forefront of novel technologies and their markets.

It is therefore highly realistic to take these emerging technologies and facilities as available also to the European astronomy, both on ground and on orbit. In particular, the development of extremely large telescopes such as OWL dictates a novel appraisal of the information content carried by photons of cosmic origin and of the means to detect, store and analyze them. The present document proposes to start this exploration in the context of OWL's instrumentation complement.

## 1.2. Aims of the Study

When discussing the scientific use of future telescopes, one may easily tend to extrapolate current observing programs to qualitatively similar ones, merely with the quantitative difference of going to fainter sources. However, extremely large telescopes – just like other major instrumental advances – might well bring in fundamentally novel and qualitatively different fields which have so far not been accessible by the smaller telescopes of the past. Here we will discuss one such potential new information channel for optical astronomy.

To understand, on a fundamental level, what really is being observed by astronomical telescopes and instruments, we first try to identify the basic foundations of observational astronomy. Almost all of astronomy depends on the interpretation of properties of electromagnetic radiation (“light”) from celestial sources. The exceptions are neutrino detections; gravitational-wave searches; analyses of cosmic rays, meteorites, and other extraterrestrial materials; and in-situ studies of planetary-system bodies. All our other understanding of the Universe rests upon observing and interpreting more or less subtle properties in the light reaching us from celestial bodies.

What exactly, then, is being observed in electromagnetic radiation? Figure 1.1 attempts to summarize all of astrophysics (save the exceptions noted), by subdividing electromagnetic radiation in parameter domains with respect to timescale of study, and wavelength.

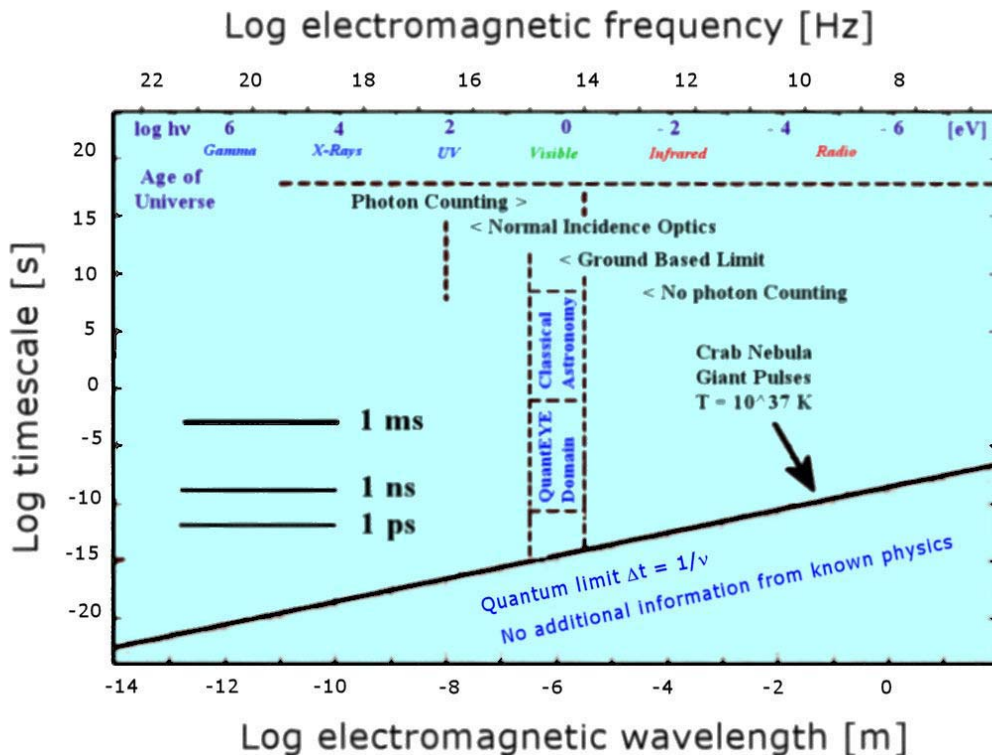


**Fig.1.1.** All of astronomy on the log(timescale)-log(frequency) diagram (adapted from Dravins 1994)

Astronomical telescopes are equipped with myriads of auxiliary instruments which, on first sight, may give an impression of being vastly different. However, a closer examination of the physical principles behind reveals that they all are measuring either the spatial or temporal coherence of light (or perhaps some combination of these). All imaging devices (cameras, interferometers) are studying aspects of the spatial coherence (in various directions, and for different angular extents on the sky). All spectrally analyzing devices measure aspects of the temporal coherence (with different temporal/spectral resolution, and in the different polarizations). Although a gamma-ray satellite may superficially look different from a long-baseline radio interferometer, the basic physical property they are measuring is the same.

These spatial and temporal coherences can be traced back to be properties of the electromagnetic field amplitude and can be ascribed to individual photons, or to groups of individual photons. Thus all existing astronomical instruments are limited to studies of such one-photon properties. However, light can carry information also beyond this [first-order] coherence, e.g. encoded in the temporal distribution of photon arrival times. Photons that arrive from the given directions with the same energy (wavelength) will generate the same astronomical images and spectra, although the light might differ in its statistics of photon arrival times. These statistics can be "random", as in chaotic, maximum-entropy thermal radiation (then following the Bose-Einstein statistics for photons, predicting a certain "bunching" in time, as appropriate for any group of bosons with integer quantum spin); however the statistics might also be quite different if the radiation is not in a maximum-entropy state (perhaps originating in stimulated laser-type emission or having undergone scattering on the way to the observer).

Different physical processes in the generation of light may thus cause quantum-statistical differences (different degrees of photon bunching in time) between light with otherwise identical spectrum, polarization, intensity, etc., and studies of such non-classical properties of light are actively pursued in laboratory optics.

Classical physics merges all radiation of a certain wavelength into the quantity "intensity". When treating radiation as a three-dimensional photon gas, other effects also become significant, e.g. higher-order coherence and the temporal correlation between photons. The best-known non-classical property of light is the bunching of photons, first measured by Hanbury Brown and Twiss in those experiments that led to the astronomical intensity interferometer.

Such properties may be revealed by studying second-, and higher-order degrees of coherence, which reflect correlated properties of two or more photons in the light from the source. For example, in stimulated emission there is a causal coupling between a first photon that is stimulating the emission of the next photon; stimulated emission thus is a property that can not be ascribed to a single photon; there must always be at least two. An idealized laser emits light whose photons are evenly distributed in time: in contrast to thermal emission there is no "bunching". The observation of such effects exemplifies non-linear optical instrumentation: measuring the second- (or higher-) order coherence involves finding the probability that two (or more) photons arrive within the same time interval. The second-order signal is thus proportional to the conditional probability that a second photon is detected immediately after the first; since the signal thus is proportional to the intensity for the first photon multiplied by the intensity for the second one, it thus increases as the *square* of the observed light intensity or the fourth power of telescope diameter. Higher-order coherences increase even more rapidly with telescope size. While such effects of non-linear optics are familiar in the laboratory, they are not [yet] familiar to astronomers. The so far only astronomical instrument to exploit the second-order coherence of light was the stellar intensity interferometer, developed already long ago by Hanbury Brown & Twiss; today that would be seen as a quantum-optical

instrument (however, usable for maximum-entropy, chaotic light only), and its legacy actually is quite valuable when discussing future astronomical observations.

There exist other effects of quantum optics which might be exploited in astronomy, but where the [known] advantages offered by Extremely Large Telescopes are less specific. Not long ago, it has been realized that individual photons may carry also photon orbital angular momentum, POAM (besides the “classically” known angular momentum associated with photon spin and polarization), a property earlier known for classical light beams, but one which now can be measured also for individual photons. This POAM in the direction of propagation is characterized by an integer  $\ell$  in units of  $\hbar$  so that an absorber placed in the path of such a beam will, for each photon absorbed, acquire an angular momentum  $\ell \hbar$ . The integer  $\ell$  gives the POAM states of the photon and determines – in a quantum information context – how many bits of information that can be encoded in a single photon. Since, in the laboratory, photons can now be prepared with  $\ell$  up to the order of 300, it implies that single photons may carry [at least] 8 bits of information, of considerable interest for quantum computing, and a main reason for the current interest in these phenomena. Of course, in an astronomical context, the question arises whether, and in which astronomical sources photons with such properties might be produced?

That a single photon, of any given wavelength and polarization, and coming from any given direction, still can have hundreds of different states regarding its orbital angular momentum has come as a surprise to many, who believed that photon properties were already well understood. Perhaps the main conclusion to be drawn from these quantum studies is that light, and its photons can be much more complex, and carry much more information than was commonly believed in the past.

For astronomy, this poses an opportunity and a challenge: since our understanding of the Universe is based upon the delicate decoding of information carried by light from celestial sources, we should exploit every opportunity to extract additional information, even if one moving into uncharted and unknown territory, and can not know beforehand what type of information will be conveyed. Quantum optics offers such an opportunity, and this study is about the conceptual design of instrumentation for OWL with a capacity to measure also quantum-optical effects in the distribution of photons arriving from astronomical sources.

This ideal “quantum-optical spectrometer” instrument would be a spatially and spectrally resolving, POAM-resolving, and photon-counting instrument, which for each spatial and spectral position can time-tag each detected photon with picosecond accuracy. The present day technology (in particular, the available detectors) permits a partial realization of this ideal quantum instrument, which we shall call *QuantEYE*. While the instrumental capabilities are set to permit the detection of quantum-optical phenomena, *QuantEYE* will also be unparalleled for general high-time-resolution observations, for any application where photon counting is essential or where the readout times of other detectors are too slow, thus assuring a broader user base besides the physically more challenging quantum-optical issues.

### **1.3. High Time-Resolution Astrophysics**

With high time-resolution detectors, high-speed astrophysical phenomena have become accessible and astrophysical phenomena on successively shorter timescales have been discovered. Historically, perhaps the most notable discovery was that of pulsars, enabled by the development of high-time-resolution techniques in radio astronomy (originally aiming at studying interstellar scintillation). More recent findings include the structure of gamma-ray bursts and quasi-periodic oscillations on millisecond scales in compact accretion sources.

Generally, the environments of compact objects are likely places for very rapid phenomena to occur: the geometrical extent is small, the energy density high, the magnetic fields enormous, and a series of phenomena, ranging from magneto-hydrodynamic turbulence to stimulated synchrotron radiation may take place. Some processes may extend over scales of less than kilometers, and there is no immediate hope for their spatial imaging. Insights can instead be gained through studies of their small-scale instabilities, such as hydrodynamic oscillations or magneto-hydrodynamic flares. Such phenomena may be studied in high-time-resolution astrophysics, on timescales of seconds, milli-, or even microseconds.

#### **1.4. Which Timescales are Observationally Accessible?**

Not all timescales can be practically observed in all sources: many astronomical sources are too faint (or, rather, the telescopes observing them are too small). For example, the finite sizes of current X-ray telescopes implies that the number of X-ray photons detected from typical sources do not exceed perhaps some thousand per second, in practice precluding studies of variability on scales much shorter than milliseconds (and in particular not allowing observations on the very short timescales that would be required to search for quantum effects in radiation). In other wavelength regions – e.g., in radio, the number of detectable photons in principle may be very great (permitting studies also on very short timescales) but, since there are as yet no practical means of photon-counting in radio, searches for quantum effects in radiation are limited to such that can be represented by continuous radio waves (e.g., the effect corresponding to the Hanbury Brown-Twiss effect of bunching of photons in visible light, in radio is seen as ‘wave noise’).

#### **1.5. Astrophysics on Subsecond Scales**



*Fig.1.2.. Artist's vision of accretion from a red giant star onto a black hole and its surrounding disk. Artwork by Catrina Liljegren (Dravins 1994)*

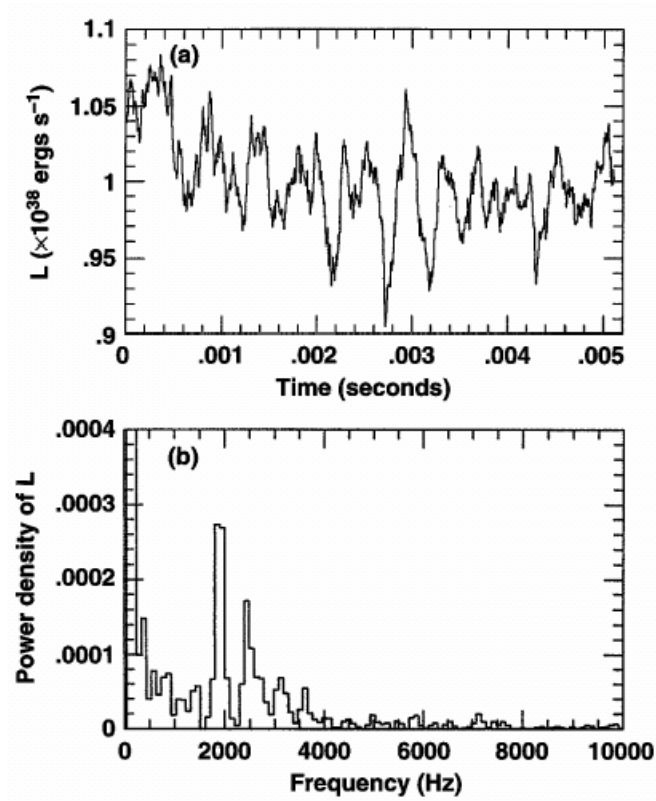


Fig.1.3. Theoretically predicted photon-bubble oscillations in accretion (Klein et al. 1996)

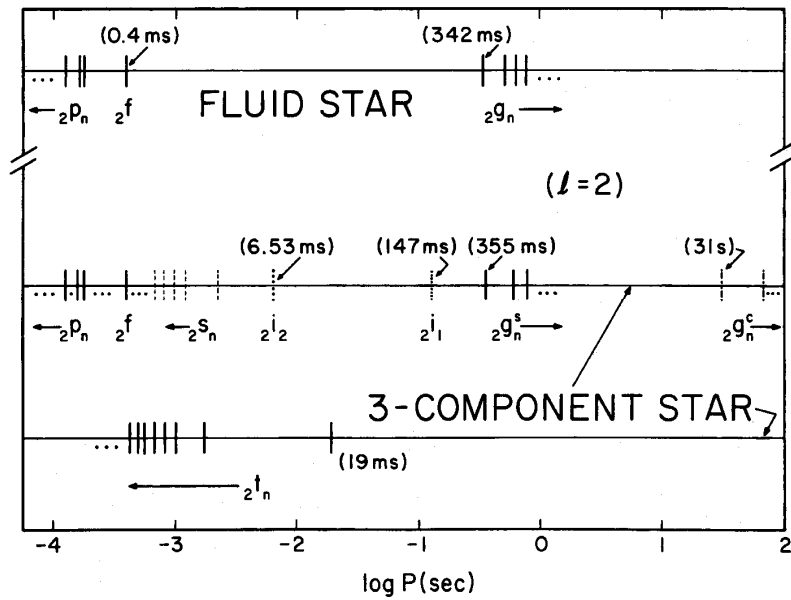
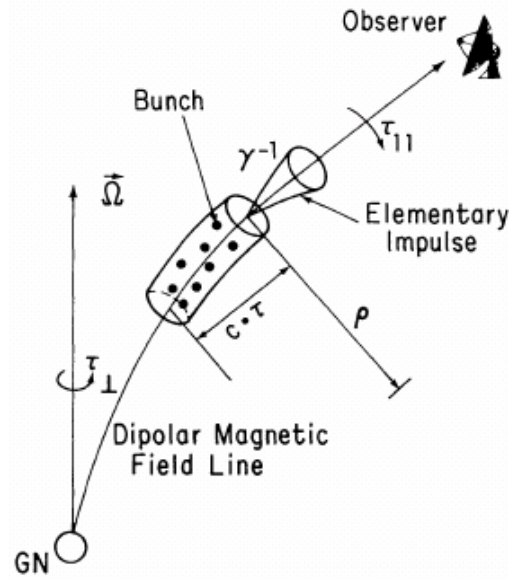
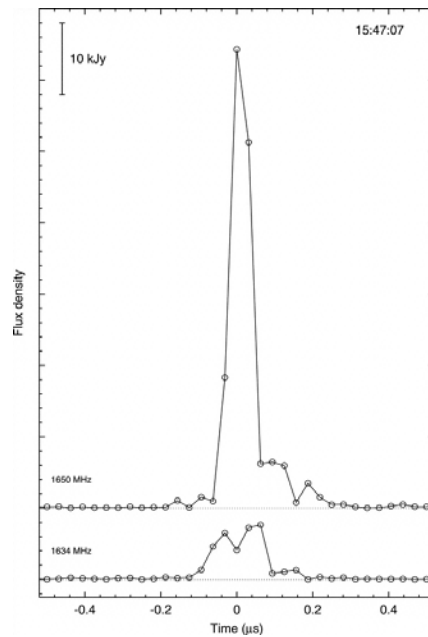


Fig.1.4. Predicted non-radial oscillations in neutron stars (McDermott et al. 1988)



**Fig.1.5.** *Fluctuations of pulsar emission with sub-microsecond timescales (Gil 1985)*



**Fig.1.6.** *Giant radio pulse from the millisecond pulsar B1937+21. These pulses have been observed as strong as 65,000 Jy with widths  $\leq 15$  ns, corresponding to a brightness temperature of  $T_b \geq 5 \times 10^{39}$  K, the highest observed in the Universe. The pulse is shown with the original sampling time of 31 ns for each sideband (Soglasnov et al. 2004)*

These nanosecond phenomena recently discovered (with large radio telescopes) represent the currently most rapid fluctuations found in astronomical sources. If – as in classical textbooks – one would assume that the source size corresponds to the light-travel-time during the source variability, the structures responsible for the nanopulses from the Crab pulsar must be less than one meter in extent (the speed of light is 30 cm/ns). Such observations also show how astronomical phenomena can be found on shorter and shorter timescales, making the time

domain the perhaps principal frontier in the expansion of the parameter domains accessible to observational astronomy (until the recent past, the main expansion was in accessing new wavelength regions). What is then the “ultimate” time resolution, how rapid a variability can be detected, and what might one find out there?

### 1.6. Nanoseconds and Quantum Optics

Time resolutions of nanoseconds and below lead into the microscopic realm of quantum optics, and the quantum-mechanical statistics of photon counts. To understand what phenomena exist at such timescales, and what information they carry, we have to examine the physical properties of light.

Classical physics merges all radiation of a certain wavelength into the quantity "intensity". When instead treating radiation as a three-dimensional photon gas, other effects also become significant, e.g. higher-order coherence and the temporal correlation between photons. The best-known non-classical property of light is the bunching of photons, first measured by Hanbury Brown and Twiss in those experiments that led to the astronomical intensity interferometer (Hanbury Brown 1974).

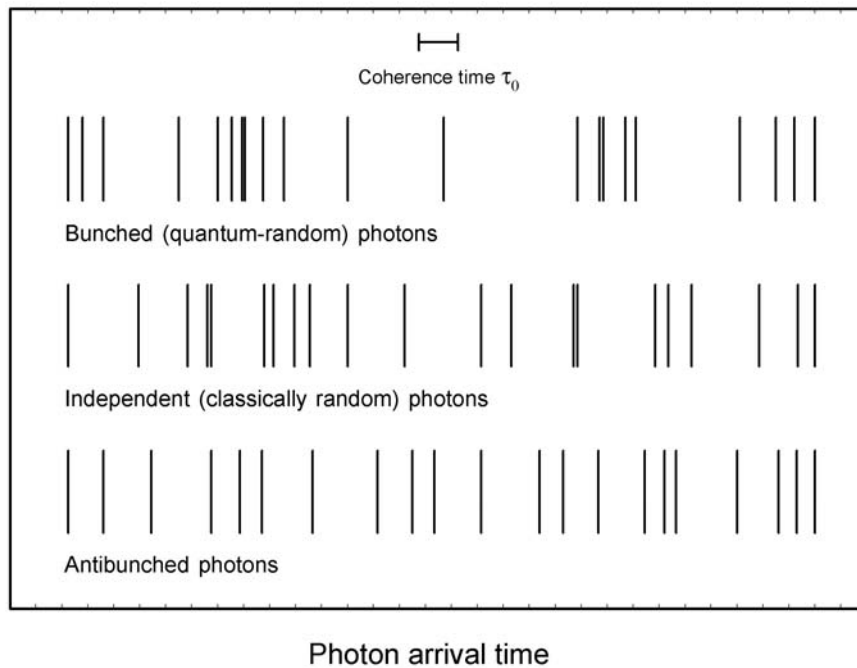


**Fig.1.7.** Statistics of photon arrival times in light beams with different entropies (different degrees of ‘ordering’). Light may carry more information than that revealed by imaging and spectroscopy: Photons from given directions with given wavelengths give the same astronomical images and spectra, though the light may differ in statistics of photon arrival times. These can be “random”, as in maximum-entropy black-body radiation (Bose-Einstein distribution with a certain “bunching” in time), or may be quite different if the radiation deviates from thermodynamic equilibrium. (Loudon 2000)

Although its function was perhaps not fully appreciated at the time it was developed, it is now realized that such an instrument works correctly only for sources whose emitted light is in maximum entropy, thermodynamic equilibrium state. Different physical processes in the generation of light may cause quantum-statistical differences (different degrees of photon bunching in time) between light with otherwise identical spectrum, polarization, intensity,



etc., and studies of such non-classical properties of light are actively pursued in laboratory optics. Although its observability in celestial sources is not yet established, quantum optics could ultimately offer a fundamentally novel information channel also for astronomy.

These quantum correlation effects are fully developed over timescales equal to the inverse bandwidth of light. For example, the use of a 1 nm bandpass optical filter gives a frequency bandwidth of  $10^{12}$  Hz, and the effects are then fully developed on timescales of  $10^{-12}$  seconds. Instrumentation with continuous data processing facilities with such resolutions is not yet available, but it is possible to detect the effects, albeit with a decreased amplitude, also at the more manageable nanosecond timescales.

### 1.7. Beyond Imaging, Photometry, and Spectroscopy

What information is contained in light? What is currently being observed, and what is not? Conventional optical instruments, like photometers, spectrometers, polarimeters or interferometers, are capable of measuring properties of light such as its intensity, spectrum, polarization or coherence. However, such properties are generally insufficient to determine the physical conditions under which light has been created.

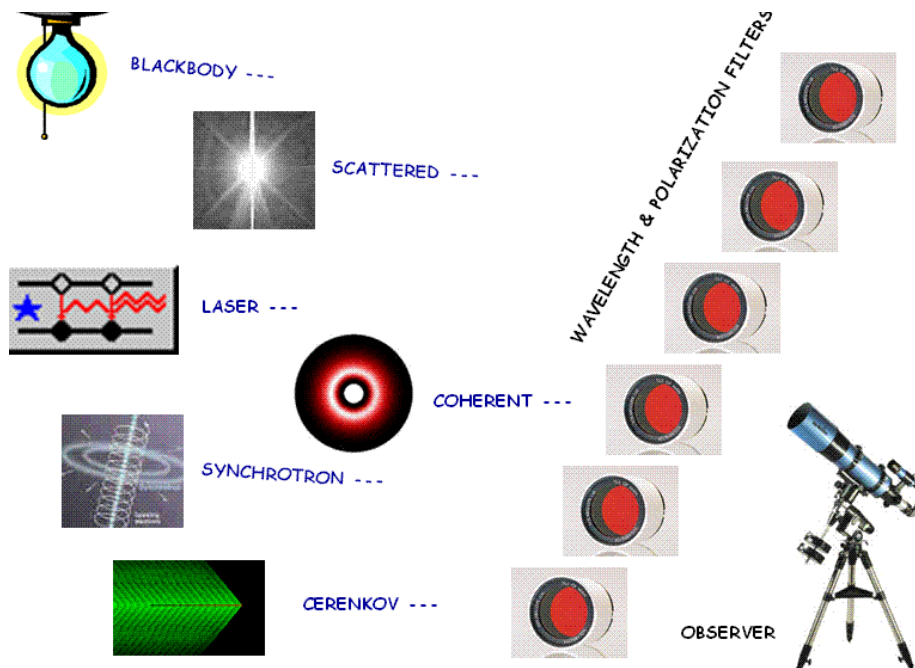


**Fig.1.8.** Schematic illustration of different light sources (left), where the photon stream (photon gas) leaving the source has been produced through different physical mechanisms. These sources are observed at a distance with a telescope who is viewing all sources through identical spatial and spectral filters, adjusted so that the images and spectra of all sources are identical. Thus, the first-order spatial and spectral coherence of all sources are identical, and no classical optical instrument is able to distinguish the sources from one another. The only astronomical instrument capable of distinguishing some of them is the intensity interferometer (although it would not be able to identify the causes for the differences); QuantEYE aims at studying those quantum statistical properties of light that may reveal the physical processes of light emission.

Thus it is not possible, not even in principle, to distinguish between e.g. spontaneously emitted light reaching the observer directly from the source; similar light that has undergone scattering on its way to the observer; or light predominantly created through stimulated emission, provided these types of light have the same intensity, polarization and coherence as function of wavelength. The deduction of the processes of light emission is therefore made indirectly via theoretical models (see Figure 1.8). Yet, such types of light may have quantum-statistical differences regarding collective multi-photon properties in the photon gas. Such properties are known for light from laboratory sources and, might ultimately become experimentally measurable also for astronomical objects.

To understand the "parameter domains" in "knowledge space" that are accessed by e.g. photometers or spectrometers, we need to understand their working principles on a very fundamental level, i.e. not superficial specifications such as field-of-view or spectral resolution, but rather their workings concerning the fundamental physical observables measured.

### 1.8. One-Photon Experiments

We describe light as an electromagnetic wave of one linear polarization component whose electric field  $E$  contains terms of the type  $e^{-i\omega t}$  for angular frequencies  $\omega$ . All classical optical instruments measure properties of light that can be deduced from the first-order correlation function of light,  $G^{(1)}$ , for two coordinates in space  $r$  and time  $t$  (Glauber, 1970). The different classes are collected in Figure 1.9, where  $\langle \rangle$  denotes time average, and  $*$  complex conjugate.

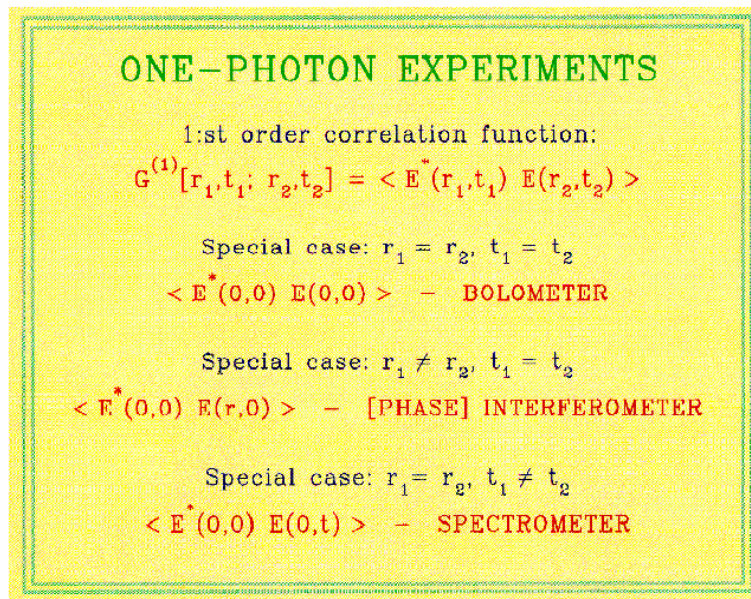


**Fig.1.9.** Fundamental quantities measured in one-photon experiments. All such measurements can be ascribed to quantities of type  $E^*E$ , corresponding to intensity  $I$ , which in the quantum limit means observations of individual photons or of statistical one-photon properties. To this category belong all direct and interferometric imagers, spectrometers, and photometers, i.e. all ordinary instruments used in astronomy. Time average is denoted by  $\langle \rangle$  while  $*$  marks complex conjugate.

For example, a bolometer measures  $\langle E^*(0,0) E(0,0) \rangle$ , yielding the classical field intensity irrespective of the spectrum or geometry of the source. For the case  $r_1 = r_2$  but  $t_1 \neq t_2$ ,  $G^{(1)}$  becomes the autocorrelation function with respect to time,  $\langle E^*(0,0) E(0,t) \rangle$ , whose Fourier

transform yields the power density as function of electromagnetic frequency. That is the spectrum of light which is measured by spectrometers. The function is explicitly sampled by Fourier transfer spectrometers while e.g. gratings "perform" the transform to the spectrum through diffractive interference. For the case  $r_1 \neq r_2$  but  $t_1 = t_2$  we have the spatial autocorrelation function  $\langle E^*(0,0) E(r,0) \rangle$ , which is measured by interferometers and yields the angular distribution of the source power density. The need for accurate timekeeping at both sites  $r_1$  and  $r_2$  originates from the requirement  $t_1 = t_2$ . In the absence of absolute flux calibrations,  $G^{(1)}$  is usually normalized to the first-order coherence  $g^{(1)}$ .

### 1.9. Two- and Multi-Photon Properties of Light

Thus, classical measurements do not distinguish light sources with identical  $G^{(1)}$ . All such measurements can be ascribed to quantities of type  $E^*E$ , corresponding to intensity  $I$ , which in the quantum limit means observations of individual photons or of statistical one-photon properties. Thus possible multi-photon phenomena in the photon stream reaching the observer are not identified, not even in principle.

The description of collective multi-photon phenomena in a photon gas, in general requires a quantum-mechanical treatment since photons have integer spin ( $S = 1$ ), and therefore constitute a boson fluid with properties different from a fluid of classical distinguishable particles. The first treatment of the quantum theory of coherence in a photon gas was by Glauber (1963a, 1963b), although some properties were inferred earlier from classical treatments, notably the bunching of photons in chaotic (thermal) light, first observed by Hanbury Brown and Twiss. Glauber showed that an arbitrary state of light can be specified with a series of coherence functions essentially describing one-, two-, three-, etc. -photon-correlations. A simplified expression for the second-order correlation function is given in Figure 1.10. It describes the correlation of intensity between two coordinates in space and time.

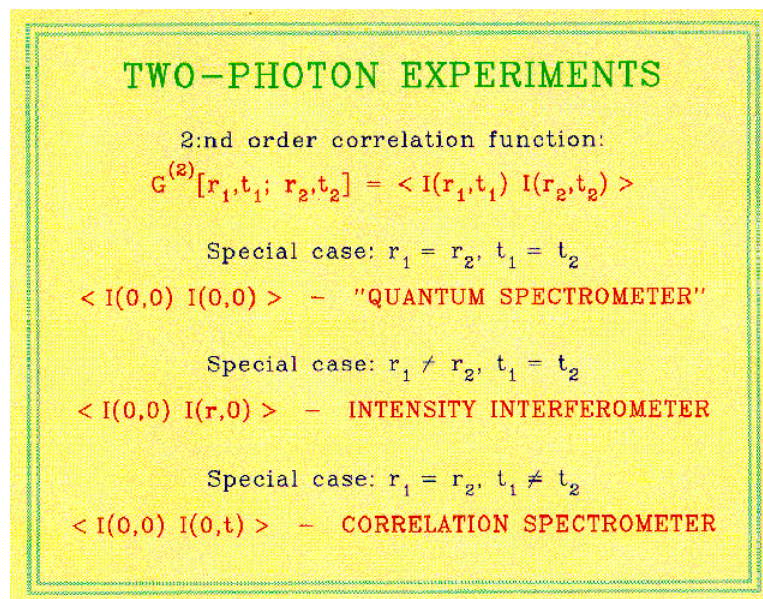


**Fig.1.10.** Fundamental quantities measured in two-photon experiments. All such measurements can be ascribed to quantities of type  $I^*I$ , i.e. intensity multiplied by itself, which in the quantum limit means observations of pairs of photons or of statistical two-photon properties. The intensity interferometer was the first astronomical instrument in this category.

Since a detection of a photon (measurement of  $I$ ) enters twice,  $G^{(2)}$  describes two-photon properties of light.  $G^{(2)}$  is often normalized to the second-order coherence of light,  $g^{(2)}$ . Although its strict definition involves quantum-mechanical operators, a simplified expression can be given in terms of intensities:  $g^{(2)} = \langle I(r_1, t_1) I(r_2, t_2) \rangle / \langle I(r_1, t_1) \rangle \langle I(r_2, t_2) \rangle$ . If the distribution of photons is chaotic, i.e. the photon gas is in a maximum entropy state, the second-order coherence  $g^{(2)}$  can be deduced as  $g^{(2)} = [g^{(1)}]^2 + 1$  (e.g. Loudon, 2000). This property can be used to determine  $|g^{(1)}|$  from measurements of  $g^{(2)}$ . In the intensity interferometer this is measured for  $r_1 \neq r_2$  but  $t_1 = t_2$ :  $\langle I(0,0) I(r,0) \rangle$ , thus deducing angular sizes of stars, reminiscent of a classical interferometer. For  $r_1 = r_2$  but  $t_1 \neq t_2$  we instead have an intensity-correlation spectrometer, which measures  $\langle I(0,0) I(0,t) \rangle$ , determining the spectral width of e.g. scattered laser light.

In thermodynamic equilibrium, the chaotic distribution of photons corresponds to the value  $g^{(2)} = 2$  for first-order coherent [ $g^{(1)} = 1$ ] light. Such photons follow a Bose-Einstein distribution, analogous to a Maxwellian one for classical particles. However, away from equilibrium, photons may deviate from Bose-Einstein distributions (just as classical particles can be non-Maxwellian).

For example, light created by stimulated emission in the limiting case of a stable wave without any intensity fluctuations has  $g^{(2)} = 1$ , corresponding to analogous states in other boson fluids, e.g. superfluidity in liquid helium. Chaotic light scattered against a Gaussian frequency-redistributing medium has  $g^{(2)} = 4$ . In the laboratory, one can observe how the physical nature of the photon gas gradually changes from chaotic [ $g^{(2)} = 2$ ] to ordered [ $g^{(2)} = 1$ ] when a laser is "turned on" and the emission gradually changes from spontaneous to stimulated. Measuring  $g^{(2)}$  and knowing the laser parameters involved, it is possible to deduce the atomic energy level populations, which is an example of an astrophysically important parameter (non-LTE departure coefficient) which cannot be directly observed with classical measurements of one-photon properties. Just as it is not possible to determine whether one individual helium atom is superfluid or not, it is not possible to determine whether one individual photon is due to spontaneous or stimulated emission: both cases require studies of statistical properties of the respective boson fluid.

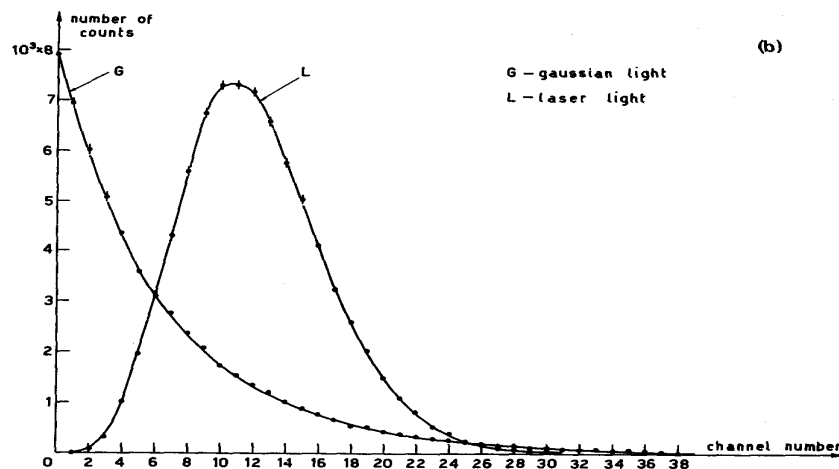
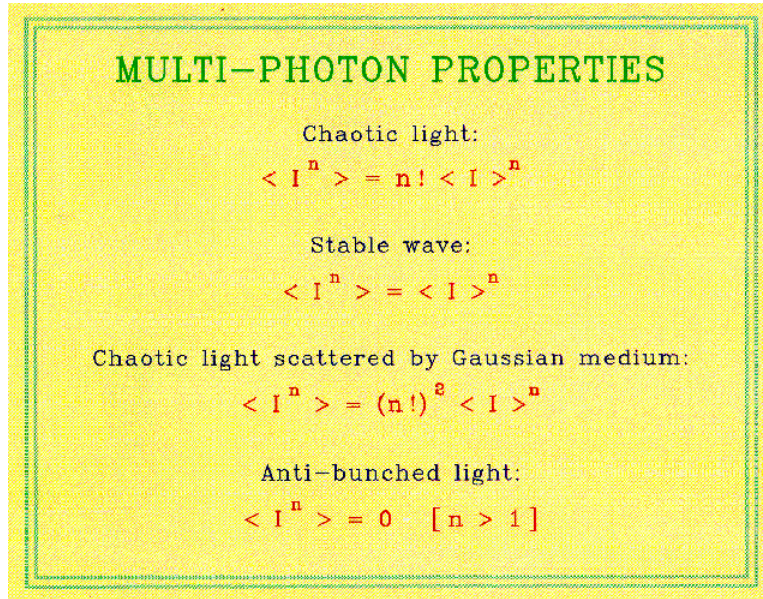
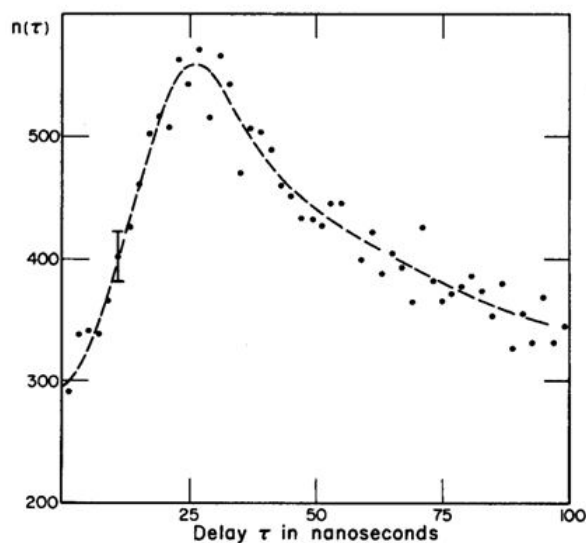


Fig.1.11. Photon statistics in Gaussian and laser sources (Arecchi 1965)



**Fig.1.12.** Properties of light, measurable in multi-photon experiments. Such measurements can be ascribed to quantities of type  $I^n$ , i.e. intensity multiplied  $n$  times by itself, which in the quantum limit means observations of groups of  $n$  photons or of statistical  $n$ -photon properties. The information contained in such higher-order photon correlations may include thermodynamic information of how the light was created or how it has been redistributed (scattered) since its creation. Although such problems are studied in theoretical astrophysics, they are not yet accessible to direct observational tests.

For a source with  $g^{(2)} \neq 2$ , neither an intensity interferometer nor an intensity-correlation spectrometer will yield correct results. E.g., a monochromatic point source emitting a monochromatic stable wave whose  $g^{(2)} = 1$  everywhere, would appear to be spatially resolved by an intensity interferometer at any spatial baseline and spectrally resolved by an intensity-correlation spectrometer at any temporal baseline and hence give the false impression of an arbitrarily large source emitting white light. This example merely indicates that additional measurements are required to fully extract the information content of light (see Figure 1.12).



**Fig.1.13.** Photon antibunching observed in resonance fluorescence. The recorded pulse pairs are shown as function of time delay; for short delays there is a clear avoidance of pulse pairs, indicating that photons “avoid one another”. (Kimble et al. 1977)

Many different quantum states of optical fields exist, not only those mentioned above (which can be given classical analogs) but also e.g. photon antibunching which with  $g^{(2)} = 0$  is a purely quantum-mechanical state. This implies that neighboring photons "avoid" one another in space and time. While such properties are normal for fermions (e.g. electrons), which obey the Pauli exclusion principle, ensembles of bosons (e.g. photons) show such properties only in special situations. An antibunching tendency implies that the detection of a photon at a given time is followed by a decreased probability to detect another immediately afterward.

Experimentally, this is seen through sub-Poissonian statistics, i.e. narrower distributions of recorded photon counts than would be expected in a "random" situation. For an introduction to the theory of such quantum optical phenomena, see e.g. Loudon (1980; 2000), Meystre & Sargent (1990), or Mandel & Wolf (1995). Experimental procedures for studying photon statistics are in Saleh (1978).

### 1.10. The Intensity Interferometer

Experiments bearing on large photon fluctuations from a thermal source were reported by Hanbury Brown and Twiss in 1956. They found positive correlations between photons in two coherent beams of light originating from a *thermal* source: when a photon is registered in one channel, the probability of detecting a photon in the second channel in the same time interval is higher than if the events were uncorrelated.

The correlation depends on the *square of the number of quanta* per unit time in the beam.

According to Bose-Einstein statistics, this correlation can be explained by *bunching of photons* in the same phase-space cell (see Appendix 1). For very short intervals, the probability of finding a second photon is twice than for two independent particles. If the two detectors are effectively in the same cell of the phase space, for example they are separated parallel to the incoming wavefront, then the arrival of photons will appear to be correlated in time; they will tend to arrive in pairs.

Purcell (1956) explained the phenomenon in terms of wave packets, each about  $c/\Delta\nu$  long, in a random sequence. Each packet contains one photon. There is a certain probability that two such wave trains accidentally overlap. When the packet overlap they interfere, and the result is a packet with something in between 0 and 4 photons. *Thus the photon density fluctuations are large* (with electrons instead of photons we would find a fluctuations *suppression*, not an enhancement, because of the Pauli exclusion principle).

We can express the same concept in a semi-classical way: the two currents fluctuate, and the fluctuations are partially correlated. The principal component of the fluctuations is the uncorrelated shot noise in the electronics. In addition, there is a smaller component called *wave noise* which corresponds to the fluctuations in intensity of the light wave. Those two wave noises are at least partially correlated, provided there is some degree of coherence between the light at the two detectors.

It is well known that the fringe visibility in the Michelson interferometer is given by:

$$V_d = \frac{I_{\max} - I_{\min}}{I_{\max} + I_{\min}}$$

In the *intensity interferometer*, the correlation of the wave noise component is proportional to the square of the degree of coherence of light at the two detectors, and thus to the square of the of the fringe visibility that would be observed in a Michelson interferometer under the same conditions:

$$c(d) = c_0(d) \langle \Delta i_1 \Delta i_2 \rangle / (\langle i_1 \rangle \langle i_2 \rangle) = |\gamma_d|^2 = V_d^2, \quad V_d = |\gamma_d|$$

The degree of coherence  $\gamma_d$  of the light at the two apertures depends upon the angular diameter  $\theta$  of the star, the wavelength  $\lambda$  of the light and the separation  $d$  of the two mirrors. For a uniform disc of size  $\theta$ , the first zero of the visibility function is reached at  $d = 1.22\lambda / \theta$ .

### 1.10.1. The Narrabri interferometer

The Hanbury Brown – Twiss interferometer at Narrabri (New South Wales, Australia; Hanbury Brown 1974) is shown in Figure 1.14. See Appendix 2 for further details.

The mirrors were paraboloidal so that all light incident on the reflector reached the focus at the same time. Each reflector was formed by a mosaic of 252 hexagonal mirrors 38cm from side to side, of 11m focal lengths ( $\pm 15$  cm). The optical quality of the telescope was very poor, with a sky of radius 6 arcmin. The sky brightness was equivalent to a 4<sup>th</sup> mag star per sq degree.

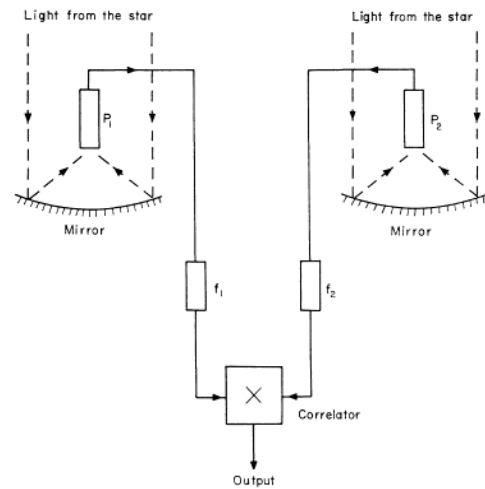


**Fig.1.14.** The original Narrabri stellar intensity interferometer circa 1970.

The two 6.5 m mirrors could be separated from a minimum value  $d = 10$  m to a maximum value  $d = 188$  m. The fluctuations in the anode current were carried by high-frequency coaxial cables to the central station, where they were amplified by wide-band amplifiers (10-110 MHz) and combined in the linear multiplier (correlator).

The main observing program was started in 1965, and led to the measurement of the diameters of 32 *hot* stars.

As already said, in the HBT interferometer there *is no interference of light*. The interference is between the electric currents from the two photomultipliers, as measured by a linear correlator in a frequency range  $\Delta f$  from  $10^7$  to  $10^8$  Hz. Because the instrument measures the

square of the modulus of the complex degree of coherence  $c(d)$ , the phase of this complex function is lost. *One cannot reconstruct unambiguously the angular distribution across an asymmetric source.*

Notice that the phase difference between the two correlated components is *not* the phase difference of the light waves at the two detectors, but it is the difference of the relative phases of the two Fourier components at the detectors. *The correlation therefore does not depend on the path difference between the two apertures.* We might delay the light reaching one detector by several thousands wavelengths without affecting the correlation, *provided this delay is small compared with the period of the highest beat-frequency (say  $10^8$  Hz) we pass through the multiplier.*

*Intensity interferometry can thus be carried out very effectively also in the blue and visible.*

Measuring  $c(d)$  as function of the separation we can find the distribution of intensity across the light source, and hence its angular size, subject to two restrictions:

1. The phase information is lost
2. The finer details (e.g. the limb darkening) are contained in the *wings* of the Fourier transform, in particular in the relative amplitude of the second maximum (high S/N ratio required to measure e.g. the stellar limb darkening).

### 1.10.2. Intensity fluctuations when photon counting

The original HBT interferometer was entirely analog. Here we discuss the situation when photon counting. Consider a stream of photons through a very narrow spectral bandwidth  $B = \Delta\nu = 1/\tau_0$ , incident upon two identical photodetectors of quantum efficiency  $q_e$ . We are looking for coincidences between the emission times of these two detectors by means of a coincidence counter which registers a count when and only when the difference between these emission times is less than  $\tau_c$  (the resolution time). If there were a zero correlation between the arrival times of photons, we should observe  $N_r(T_0)$  random coincidences in an interval  $T_0$  given by:

$$N_r(T_0) = 2q_e^2 N_0^2 \tau_c T_0$$

where  $q_e N_0$  is the average number of electrons emitted in the unit time by either detector. However, if the arrival times of photons are correlated, we must observe an *additional number* of coincidences given by:

$$N_c(T_0) = \frac{1}{2} q_e^2 N_0^2 \tau_0 T_0$$

where  $\tau_0 \approx 1/B = 1/\Delta\nu$  is the *coherence time* of the radiation from the light source. This expression is rigorously valid if  $\tau_c/\tau_0 \ll 1$ ,  $\tau_c \ll 1/\Delta\nu$  (in other words, the optical bandwidth must be much wider of the electrical bandwidth), which is certainly realized in our case. Therefore, in the simplest analysis we expect a total number of counts given by:

$$\begin{aligned} N_{tot}(T_0) &= N_r(T_0) + N_c(T_0) = N_r(T_0) \left[ 1 + \frac{q_e^2 N_0^2 \tau_0 T_0}{4q_e^2 N_0^2 \tau_c T_0} \right] = N_r(T_0) \left[ 1 + \frac{\tau_0}{4\tau_c} \right] = \\ &= N_r(T_0) \left[ 1 + \frac{1}{4(\Delta\nu/\nu_0)\nu_0\tau_c} \right] \end{aligned}$$



In order to maximize the second term, one must keep both  $\Delta v/v$  ( $= \Delta\lambda/\lambda$ ) and  $\tau_c$  as small as possible.

What is  $\tau_c$  in the photon counting regime? One has to distinguish carefully between the dead time of a detector and its time tagging capability. In the linear regime where each photon is counted,  $\tau_c$  can be approximately identified with the *time tagging accuracy*. Both for PMTs and SPADs we can assume  $\tau_c \approx 10^{-10}\text{s} = 100\text{ ps}$ , analogous to an electrical bandwidth  $\Delta f \approx 10^{10}\text{ Hz}$  (approximately 100 times better than in the original HBT experiment).

The r.m.s. fluctuation in the number of random coincidences is:

$$f_r(T_0) = \sqrt{\langle (N_r(T_0) - \bar{N}_r(T_0))^2 \rangle} = q_e N_0 \sqrt{2\tau_c T_0}$$

(assuming that these coincidences obey a Poisson distribution).

The Signal to Noise ratio S/N (namely, the excess counts over the fluctuations of the random coincidences) is:

$$\frac{S}{N} = \frac{N_c(T_0)}{f_r(T_0)} = \frac{1}{2} q_e N_0 \tau_0 \sqrt{\frac{T_0}{2\tau_c}} = \frac{1}{2} q_e \frac{N_0}{\Delta v} \sqrt{\frac{T_0}{2\tau_c}} = \frac{1}{2} q_e A n_0 \sqrt{\frac{T_0}{2\tau_c}}$$

which increases proportionally to  $q_e$ , to the area  $A$  of each telescope (assumed of the same diameter  $D$ ) and to  $n_0$  (the photon flux per unit area per unit time per *unit bandwidth*). This latter property insures that the *S/N is independent of the optical bandwidth*.

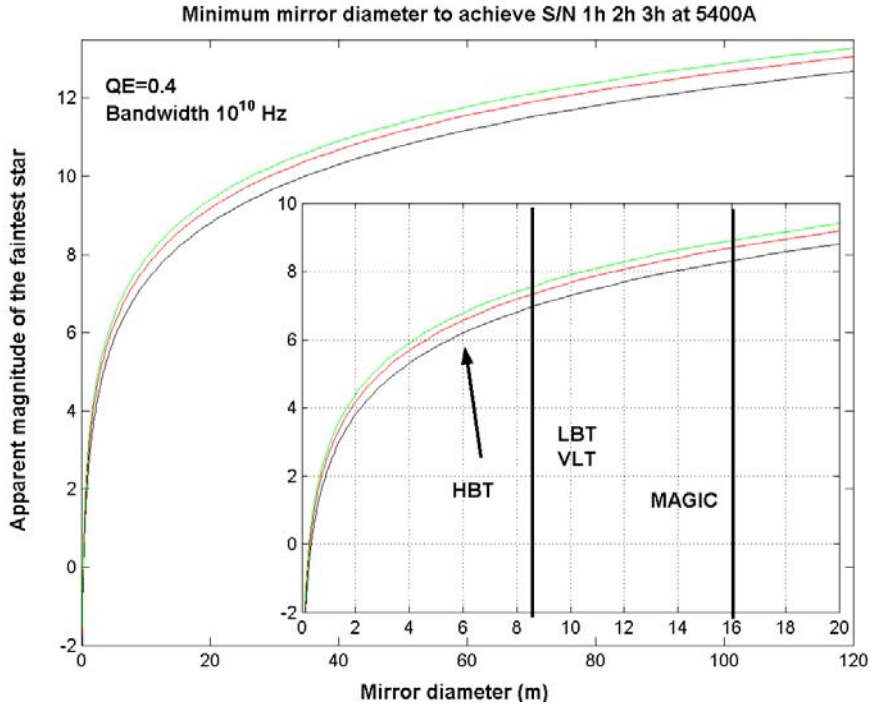


**Fig.1.15.** The minimum mirror diameter needed to achieve  $S/N = 3$  in  $1^h$ ,  $2^h$ ,  $3^h$  at a given  $V$  magnitude, assuming a QE of 0.4 and an electrical bandwidth of  $10^{10}\text{ Hz}$ . The inset expands the curve to show the capabilities of VLT and LBT, and of MAGIC. The arrow HBT indicates the limiting magnitude achieved by the original Narrabri interferometer, often with week-long integrations.

In order to examine the influence of the several parameters, the S/N ratio from an unresolved star can be rewritten in the following way:

$$\frac{S}{N} = K_{instr} \cdot q_e \cdot A \cdot n_0(m) \cdot \sqrt{T \cdot ElectricalBandwidth} \cdot g(sky)$$

The quantum efficiency  $q_e$ , the area  $A$  and the photon flux per unit frequency bandwidth  $n_0$  enter with the first power, the exposure time and the electric bandwidth with the  $\frac{1}{2}$  power. Therefore we can use a better detector and a wider electric bandwidth ( $\tau_c$  as short as possible), in conjunction with a larger telescope of excellent optical quality and a dark site to minimize the influence of the sky background.

As an example of this relation, Figure 1.15 gives the minimum mirror diameter needed to achieve  $S/N = 3$  in 1<sup>h</sup>, 2<sup>h</sup>, 3<sup>h</sup> at a given  $V$  magnitude, assuming a QE of 0.4 for the detector, the OWL reflectivity, an optical quality and seeing consistent with 1", a sky of 21<sup>st</sup> mag per (arcsec)<sup>2</sup> and an electrical bandwidth of 10<sup>10</sup> Hz. The inset expands the curve to show the capabilities of VLT and LBT, and of MAGIC under the same conditions. The arrow HBT indicates the limiting magnitude achieved by the original Narrabri interferometer, often with *week-long* integrations.

Additional examples are provided in Appendix 2.

### 1.10.3 The situation with a resolved star

To complete the analysis, one must take into account the possibility that the star is resolved by the interferometer, or even by the single mirror. In such case, the S/N ratio becomes:

$$\frac{S}{N} = \frac{N_c(T_0)}{f_r(T_0)} = \frac{1}{2} q_e N_0 \tau_0 \sqrt{\frac{T_0}{2\tau_c}} \Delta(D, \nu_0) \Gamma^2(d, \nu_0) \gamma_1 \gamma_2$$

which can be interpreted in the following way:

- 1) The factor  $\Delta(D, \nu_0)$  is proportional to the average number of photons emitted in the unit angle in unit frequency interval from unit area of the source, so that the sensitivity of the experiment is affected by the *surface brightness* of the source. *If the size of the reflector ( $D$ ) is so large to resolve the star, the light fluctuations are not fully correlated over the aperture.*
- 2) The factor  $\Gamma^2(d, \nu_0)$  is a function of the angular size of the star and of the separation  $d$  between the two detectors. In the simple case of aperture small with respect to the distance  $d$ ,  $\Gamma^2(d, \nu_0)$  is proportional to *the square of the fringe visibility in the Michelson interferometer*. If the star is a uniformly illuminated circular disc:

$$\Gamma^2(d, \lambda) = \left| 2 \frac{J_1(\pi \theta_{UD} d / \lambda_0)}{\pi \theta_{UD} d / \lambda_0} \right|^2$$

where  $J_1$  is Bessel function,  $\theta_{UD}$  is the angular diameter of the star (considered as uniform disc) and  $\lambda_0$  is the central wavelength.

The behavior of the two functions  $\Delta$  and  $\Gamma^2$  are given in Figure 1.16:

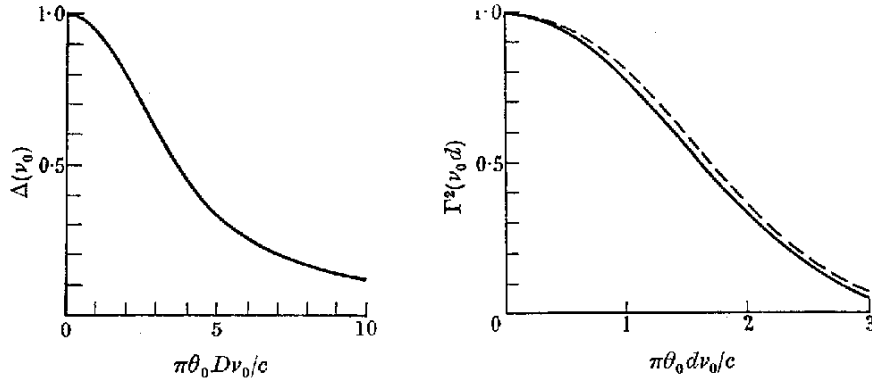


**Fig.1.16.** The behavior of the two functions  $\Delta$  (left) and  $\Gamma^2$  (right), calculated for a circular source of angular diameter  $\theta_0$  viewed by two identical mirrors with circular aperture of diameter  $D$ . The continuous line corresponds to an unresolved star.

Figure 1.17 provides an example of loss of correlation with increasing baseline in the original Narrabri experiment.

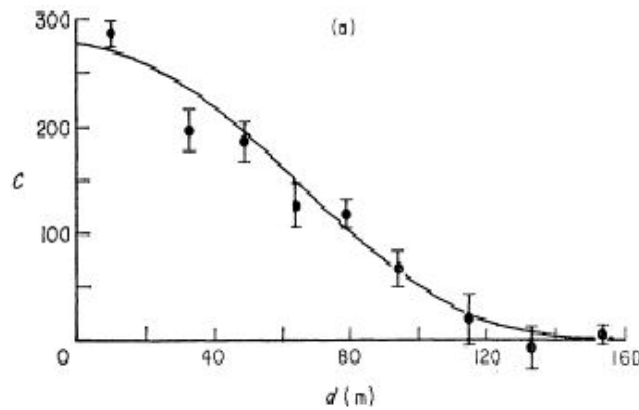


**Fig. 1.17.** Loss of correlation with baseline for Beta Crucis (B0 IV), as measured with the Narrabri interferometer (Hanbury Brown et al. 1967)

#### 1.10.4. Resolution vs. stellar surface temperature

These conditions of unresolved star must be examined in the context of the stellar temperature, because in order to keep constant the apparent magnitude, a cooler star must have a larger diameter than a hotter star. Indeed, the apparent flux is proportional to the solid angle subtended by the star and to the fourth power of its temperature  $T_s$ :

$$l \propto \left(\frac{2R}{2}\right)^2 T_s^4 = l_0 \theta_0^2 T_s^4$$

where  $\theta_0$  is the angular diameter, so that to keep  $l$  constant the apparent diameter  $\theta_0$  must increase with  $(1/T_s)^2$ . Eventually, at any given telescope diameter the star will become resolved below a certain temperature, and the previous equation can be rearranged as:

$$T_s = 2341 \left( \frac{l}{\theta^2} \right)^{1/4} \quad (l \text{ in } 10^{-8} \text{ erg cm}^{-2}\text{s}^{-1}, \quad \theta \text{ in mas})$$

From another point of view, let us take a sequence of stars *having the same angular diameter but decreasing temperatures (and so decreasing fluxes)*: the diameter of the telescope must increase progressively in order to maintain the same S/N. Eventually, the size of the mirrors becomes so large that the star is resolved by the single mirror (and consequently also by the minimum separation of the interferometer), and the S/N rapidly drops. In other words, for stars cooler than a given temperature no gain is given by a further augmentation of the mirror diameter, and for any given temperature there is an optimally large diameter to achieve a given S/N (see Figure 1.18).

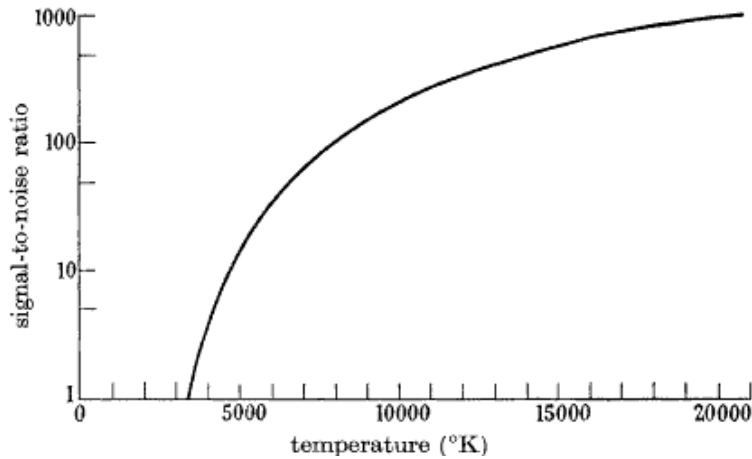


**Fig.1.18.** The original estimate of the S/N as function of the stellar temperature

It can be shown that the factor  $D^2 \cdot \Delta \cdot \Gamma^2$  has a maximum value when:

$$\pi \theta_0 D v_0 \approx 2c \quad \pi \theta_0 D \approx 2\lambda_0 \quad \theta_0 \approx 0.64\lambda_0 / D$$

For main-sequence stars hotter than approximately 3000 K, we can use the relation:

$$\log \theta_0 = +16.95 - 4 \log T_{\text{eff}} - \frac{5800}{T_{\text{eff}}} - 0.2V$$

Let us take for example the diameter of the original Narrabri realization (6.5 m). From the point of view of the single mirror, the resolution of 10 mas is reached for a  $V = 0$  main-sequence star at  $T = 5,000$  K. *All hotter MS stars would remain unresolved, all cooler stars would be resolved*, with a rapid decrease of  $\Delta$ , and therefore of the S/N, with decreasing  $T_{\text{eff}}$ . From the interferometer point of view, the minimum possible separation (13m) corresponds to 5 mas, namely to a  $V = 0$  MS star hotter than 7,500 K. All cooler stars of same magnitude would cause a decrease in  $\Gamma^2$ .

The full aperture of OWL will resolve *all*  $V = 0$  Main Sequence stars cooler than 15,000K (therefore even Sirius and Vega), and *all*  $V=5$  stars cooler than 6,000 K.

The limitations in  $T$  could be overcome by replacing the two mirrors by a *single mirror* in which the light is split to illuminate two (or more) detectors. This can be accomplished either by mounting a beamsplitter near the focus or by constructing the surface of the mirror of a

very large number of small mirrors to be focused individually on either of the two phototubes (an interesting possibility for OWL). This arrangement reduces the interferometer baseline to zero, and the star would be resolved by the mirror itself. Furthermore, this arrangement would allow to increase in successive steps the effective diameter of the mirror, thus measuring the loss of correlation, and therefore the diameter of the star.

### 1.10.5. The effect of atmospheric scintillation

The correlation observed from a point source might be affected in two ways by the propagation through the atmosphere: first, there are additional phase shifts introduced into the light reaching the two detectors, different for the two channels. Second, the amplitudes in the fluctuations of the two photocurrents will be amplitude modulated by the scintillation.

i) Let us consider first the phase scintillation, over a bandwidth narrow enough to ignore dispersion (see also later). We can introduce a *time delay*  $\tau_m$  whose rms value in terms of the standard deviation of the refractive index  $\delta\mu_m$  is given by:

$$\sqrt{\langle \tau_m^2 \rangle} = \frac{1}{c} \sqrt{lL} \delta\mu_m \approx 3 \times 10^{-13} \text{ s}$$

being  $l$  the length of the typical irregularity,  $L$  the total path through the atmosphere, and where the numerical value derives from the reasonable assumptions  $l \approx 1 \text{ m}$ ,  $L \approx 10 \text{ km}$ ,  $\delta\mu_m \approx 10^{-6}$  (local temperature fluctuations of 1 K).

The effect of introducing a time delay in the light reaching one mirror is to reduce the correlation by a factor  $\Delta C$  that can be estimated by the Wiener-Kintchine theorem:

$$\Delta C \approx \frac{1}{\Delta f} \int_0^{\Delta f} \cos(2\pi f \delta\tau) df = 1 - \frac{1}{6} (2\pi \Delta f \delta\tau)^2$$

where  $\Delta f$  is the bandwidth of the correlator. Even raising the rms estimate of the time delay to  $10^{-11} \text{ s}$  (10 picoseconds), the loss of correlation is still less than 1%.

Regarding the dispersion effect, taking the usual formula for the refractive index of the air, it is easy to show that the difference in phase introduced by the entire path through the atmosphere into light waves that are only  $10^9 \text{ Hz}$  apart in frequency is only about 0.5 rad at 400 nm. Any *differential* phase dispersion will be much less.

ii) We consider now the amplitude scintillation. It can be shown that for mirrors larger than 3m and zenith angle not exceeding approximately  $45^\circ$ , the amplitude scintillations at the two mirrors will be practically uncorrelated.

### 1.10.6. The effect of polarization

No interference phenomena can arise from interaction of light beams with mutually orthogonal polarization. In particular, there should be no correlation between the arrival times of two orthogonally polarized beams. This possible decrease of correlation due to partial polarization in one of the two beams (e.g. because a beam splitter has been inserted) must be remembered in any practical experiment. Using two orthogonally polarized beams could be a way to calibrate the instrument.

### 1.11. Possible Modern Realizations of Intensity Interferometry

We have already pointed out that intensity interferometry is realized without light combination, but by correlation of the photon counts on two separate detectors, provided an accurate common time reference is available to both detectors. Given that contemporary electronic techniques are much more powerful than those previously used for the Narrabri instrument, one can envision various modern realizations of intensity interferometry.

#### 1.11.1. Very long baseline optical intensity interferometry?

As an example of possible astrophysical application of a very long baseline optical intensity interferometry, Figure 1.19 shows the intensity-correlation term  $\Gamma^2$  for the Sun at the distance of  $\alpha$  Cen.

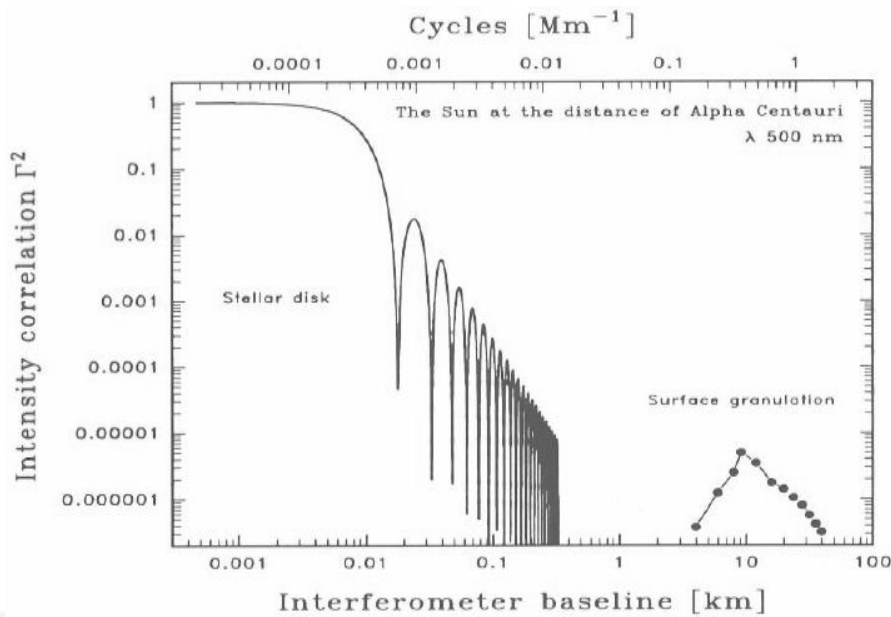


**Fig.1.19.** The resolution of the solar surface at the distance of Alpha Centauri, as seen by km-long optical interferometers.

There are several possible modern realizations of an HBT interferometer:

- with the 4 VLT telescopes. The time distribution would be very simple, it could be insured by a central clock through fibers running in the existing well thermostated tunnels
- with the LBT when completed (it would give us essentially zero-baseline calibration)
- with MAGIC I and II (when completed)
- with OWL, by splitting the light to illuminate two or more detectors.

These possibilities will be further discussed in Chapter 3. The distribution of an accurate time to distant telescopes is discussed in Chapter 4.

### 1.11.2. Combining intensity interferometry with optical heterodyne

Sources of stellar laser emission may be good candidates for small sources with high brightness temperature, which — due to the nature of intensity interferometry — is advantageous for the signal-to-noise ratio. The possibility of using intensity interferometry for detecting stellar laser radiation was actually mentioned already by Lavrinovich & Letokhov (1974/75; 1976).

The recent paper by Johansson & Letokhov (2005) discusses possible means of how the expected spectrally very narrow laser-line components in  $\eta$  Car might be detected. The expected sub-Doppler spectral width of these components is 30-100 MHz (demanding a spectral resolving power of approx.  $10^8$ ), depending on the geometry of the lasing volume. To make measurements with a spectral resolution of  $R > 10^7$ , and an angular resolution better than 0.1 arcsec, they suggest the use of the intensity interferometry coupled with optical heterodyne (mixing the astronomical signal with a frequency-sweeping laboratory laser):

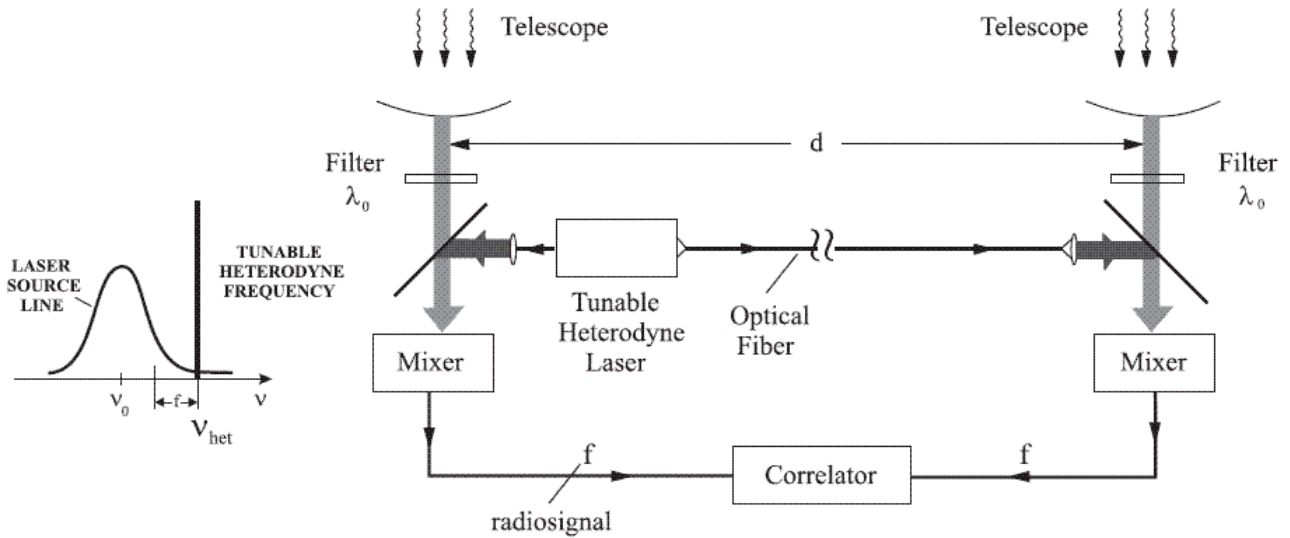


**Fig.1.20.** Proposed setup to identify spatially very small and spectrally very narrow laser emission features in ejecta ('Weigelt blobs') around Eta Carinae: Hanbury Brown-Twiss-Townes optical laser heterodyne intensity-correlation interferometer with two separated telescopes, and a local tunable heterodyne diode laser. One further advantage of the correlation method is that it is insensitive to the inevitable wavelength shifts of spectral lines due to different local velocities in the astrophysical laser source. (Johansson & Letokhov 2005)

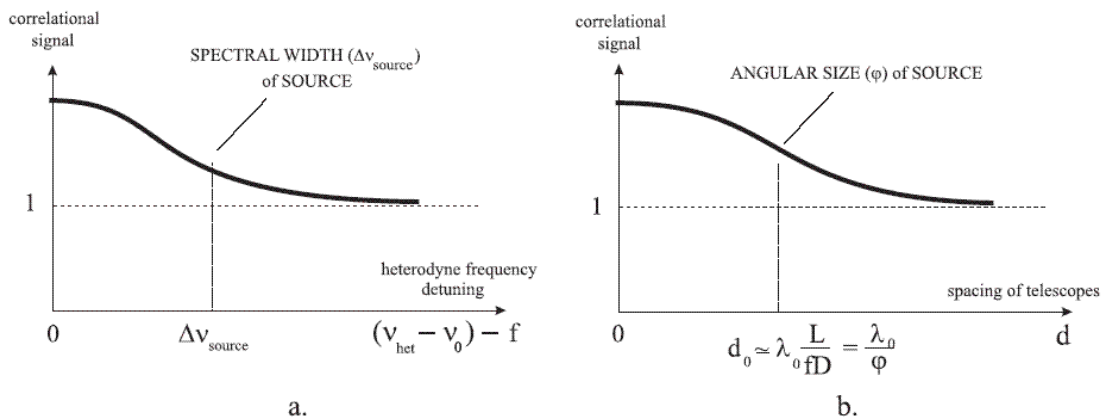


**Fig.1.21.** Expected dependence of the correlation signal intensity as function of (a) the heterodyne frequency detuning and (b) telescope spacing  $d$ . (Johansson & Letokhov 2005)

## 1.12. Intensity-Correlation Spectroscopy

Intensity-correlation (also called intensity-fluctuation or photon-correlation) spectroscopy can be considered as the temporal equivalent of [spatial] intensity interferometry. The “interferometry”, i.e. the cross-correlation of the optical fluctuations, is then performed at the same spatial location, but with a variable temporal baseline (as opposed to variable spatial locations at the same instant of time in the [spatial] intensity interferometer).

Analogous to intensity interferometry, the result of a measurement gives the power spectrum of the source with respect to the baseline over which it has been observed. In the case of the intensity interferometer, information is obtained on the relative power of spatial frequencies covered by the spatial baseline. In the case of the intensity-correlation spectrometer, the result is the relative power of temporal frequencies covered by the temporal baseline.

In any spectroscopic apparatus, the spectral resolution is ultimately limited by the Heisenberg uncertainty principle:  $\Delta E \Delta t \geq \hbar/2$ . Thus, to obtain a small value of the uncertainty in energy,  $\Delta E$ , the time to measure it,  $\Delta t$ , must be relatively great. Methods to increase  $\Delta t$  include the use of larger diffraction gratings, and tilting them parallel to the direction of light propagation in order to increase the time light spends inside the instrument (this is the ultimate reason why echelle gratings give higher resolution than those in lower diffraction orders). Interference filters inside which light travels back and forth many times give high resolution (e.g., Fabry-Perot interferometers with large finesse). Or — as in intensity-correlation spectroscopy — instead of mechanical devices, one can use electronic timing of the light along its direction of propagation. Since this can be made for temporal delays up to one second, say, this enables a spectral resolution corresponding to that of a hardware instrument with physical size equal to one light-second! This enables spectral resolutions of 1 Hz, equivalent to  $R \approx 10^{14}$ , many orders of magnitude beyond those feasible with classical spectrometers.

Resolution	L	T
$1 : 10^5$	5 cm	200 psec
$1 : 10^6$	50 cm	2 nsec
$1 : 10^7$	5 m	20 nsec
$1 : 10^8$	50 m	0.2 $\mu$ sec

**Table 1.1.** Length and time requirements for spectrometers of different resolving power (Pike 1976)

The technique is widely used in various laboratory applications of laser-light scattering, but — as far as we are aware — has not yet been applied in optical astronomy. There are analogs with [auto]correlation spectrometers used for radio astronomy: while the basic physical principles are similar, those build upon the detection of the amplitude of the radio wave, an option not feasible for optical light due to its very much higher electromagnetic frequencies.

Consider light within some optical passband measured with very high time resolution. Intensity fluctuations in this light will arise from the beating together of the various parts of the signal. In an idealized case where the light has components at only the two frequencies  $f$  and  $f + \Delta f$ . Assuming  $\Delta f = 10^{-8}$ , this results in a self-beat pattern, as illustrated in Figure 1.22:



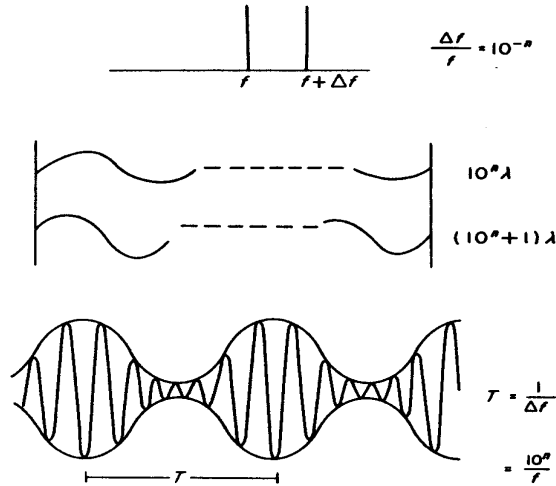


**Fig.1.22.** Length, time, and frequency patterns for a self-beating two-mode spectrum (Pike 1976)

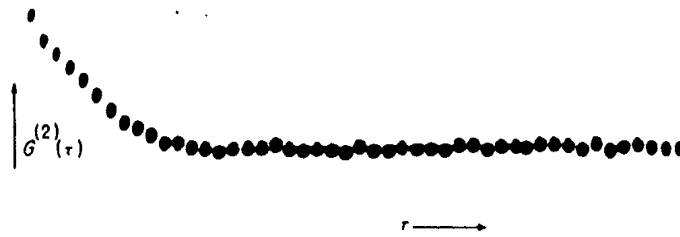


**Fig.1.23.** Example of an early application of intensity-correlation spectroscopy. The temporal auto-correlation function of laser light as scattered from a retinal blood vessel shows a characteristic time of some 5-10 channels in steps of 2 μs delay time. The Doppler broadening leading to this self-beating pattern is caused by a blood-flow velocity of about 1 cm/s. (Pike 1976)

In the general case of an arbitrary spectrum, the power content of spectral features inside the passband can be recovered, analogous to the recovery of the power content of spatial structures in intensity interferometry. The price to be paid for reaching such extreme spectral resolutions is the same as in intensity interferometry: the measurement of second-order coherence is much more expensive in terms of photon flux than a first-order measurement of the phase of light: this is a task for very large telescopes.

For reviews of intensity-correlation spectroscopy principles and applications see Pike (1970; 1976); Degiorgio & Lastovka (1971); Oliver (1978); and Saleh (1978).

*QuantEYE* has the capability to perform intensity-correlation spectroscopy to reach spectral resolving powers of  $\lambda/\Delta\lambda \gtrsim 100,000,000$ , opening up for the first “extreme-resolution” optical spectroscopy in astrophysics. Such resolutions actually are required to resolve laser lines with expected intrinsic widths  $\approx 10$  MHz, such as expected for the circumstellar emission-line lasers around Eta Carinae (Section 2.2.3).

An emission line of width  $\Delta\nu \approx 10$  MHz will be self-beating on timescales on the order of  $\Delta t \approx 100$  ns. Such delay times will easily be handled by *QuantEYE*. Note, however, that broader emissions imply shorter timescales, and thus become gradually more difficult to resolve.

Possibly, the earliest laboratory measurement of a narrow emission line through intensity-correlation spectroscopy was by Phillips et al. (1967) who, not long after the experiments by Hanbury Brown & Twiss, deduced linewidths on the order of 100 MHz, corresponding to correlation times of some nanoseconds.

Analogous to the spatial information extracted from intensity interferometry, photon-correlation spectroscopy does not reconstruct the full shape of the source spectrum, but “only” gives linewidth information. However, this also has advantages in searches for narrow emission-line components: Photon correlations are insensitive to wavelength shifts due to local velocities in the source, thus one does not need to know exactly where within the observed wavelength region there might exist some narrow emission-line components. The signal-to-noise ratios follow similar relations as in intensity interferometry, i.e. not simply scaling with the total photon flux; higher S/N ratios will be associated with sources of high brightness temperatures, such as narrow emission-line components. More technical discussions of error sources, and signal-to-noise ratios are in various papers that appeared around the time laser light scattering became established as a laboratory technique for studying the velocity spread of e.g., exhaust fumes, blood cells, or molecular suspensions: Hughes et al. 1973; Jakeman et al. 1970; Jakeman 1972; Koppel 1974; Saleh 1973; 1978; Saleh & Cardoso 1973.

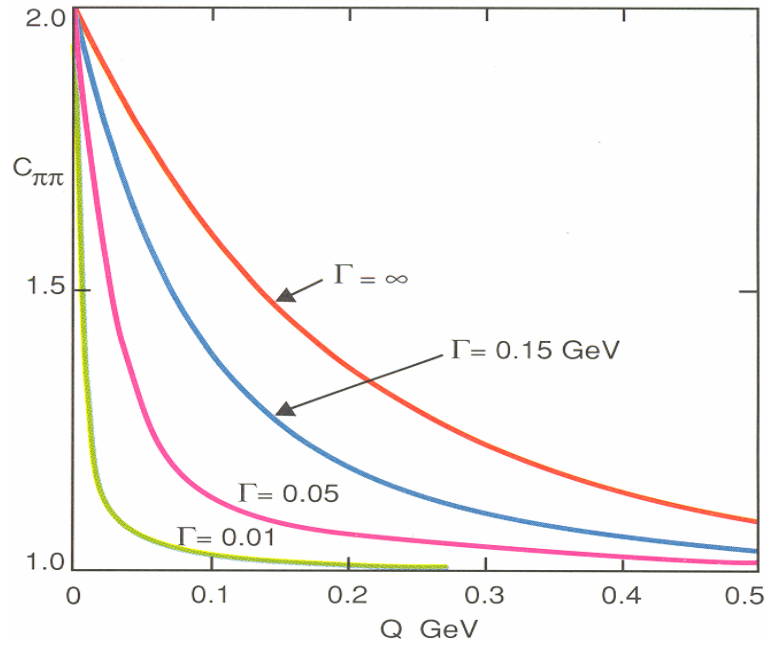
Again similar to intensity interferometry, the method formally assumes Gaussian (= chaotic; thermal; maximum-entropy) photon statistics. For astrophysical sources this could be the case if the emitted light has been somehow randomized, becoming close to thermal. However, if the light is non-Gaussian, photon statistics could be closer to those of a stable wave (such as in laboratory lasers). The analysis of superposed coherent and chaotic radiation could be even more interesting and yield more information; for discussions of such situations, see Aleksandrov et al. (1983), and Vannucci & Teich (1980).

### 1.13. Intensity Interferometry of Non-Photons

In an astronomical context, one naturally thinks of intensity interferometry in terms of correlations between streams of stellar photons. However, it may be illustrative to realize that there exist widespread applications of this interferometric method pioneered by Hanbury Brown and Twiss, although these currently lie outside astronomy. The property being exploited, i.e. the “bunching” in time of photons applies to any other class of *bosons*, particles with integer spin, something that is being applied in high-energy particle physics. The source to be observed is then not a star but perhaps the particles produced in interaction region between high-energy particle beams. The angular size of the source can then be inferred by suitable cross-correlations of intensity fluctuations observed by suitably placed detectors. For reviews, see Boal et al. (1990) and Alexander (2003).

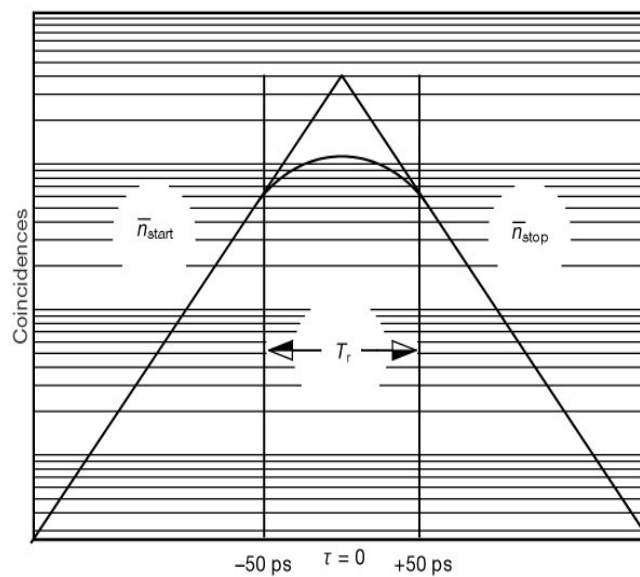
The effort that has been invested in particle applications of intensity interferometry (many hundreds of published papers) is very much greater than that in the past Hanbury Brown – Twiss experiment. Of course, in the laboratory, there are additional degrees of freedom, such as three-dimensional intensity interferometry of time-variable sources. Although it has been outside the scope of this present study to survey this field, it is clear that there exists much valuable experience, and among the many software applications developed for particle intensity interferometry there very likely exist some which could be useful to apply also in the *QuantEYE* context.

Figure 1.24 shows an example of intensity interferometry of pions produced in quark-initiated high-energy jets. With spin = zero, pions are bosons and thus obey the same type of Bose-Einstein statistics as other particles with integer-valued spin, e.g. photons with spin = 1.



**Fig.1.24.** Intensity interferometry of pions in high-energy particle physics: Bose-Einstein correlations in quark-initiated jets. The correlation in momentum space (in angle for pions of equal energy) measures the source size (Bowler 1991)

A somewhat different situation applies to fermions, i.e. particles with half-integral-valued spin, such as electrons with  $S = \frac{1}{2}$ . These obey Fermi-Dirac statistics and follow the Pauli exclusion principle which prohibits two or more particles to occupy the same quantum state. Thus, a gas of electrons or other fermions will show “anti-bunching”, a property “opposite” to the “bunching” characteristic for thermal photons. This is seen experimentally in the laboratory a certain anti-correlation between “nearby” electrons, also showing up as sub-Poissonian counting distributions (i.e. narrower than the Poisson ones that otherwise would have been expected for classical “random” particles”).



**Fig.1.25.** Intensity interferometry of electrons. Time spectra expected for Poissonian processes at infinite time resolution (straight lines), and an antibunched beam at finite resolving time (Kiesel et al. 2002)

It may be essential to appreciate these quantum properties of electrons when planning quantum-optical experiments. The many quantum-statistical properties, and different degrees of bunching in photon streams are “permitted” by their boson nature and the more “permissive” Bose-Einstein statistics.

Although, using common language, one often speaks of photon “detection”, *photons* as such are actually *never* directly detected! Rather, what is being detected and studied is some electrical signal from photo-*electrons* that results from the photon interaction inside the detector. It is a sobering thought that quantum-statistical properties to be measured, e.g. the bunching of several photons in the same quantum state, is a property that can not even in principle be possessed by these electrons. One may wonder how it is possible to at all study boson properties through a medium (electrons) that cannot, not even in principle, carry such properties? For photocathode detectors, the explanation apparently is the very short time (femtoseconds?) required for a photoelectron to exit a photocathode and then be detected as an individual particle.

However, semiconductor detectors are more complex, and have longer timescales for the relaxation of their inner energy levels (e.g., Lim 2002). A further discussion of such possible effects is outside the scope of this study, but we do note that measurements of the quantum statistics of the incoming light may require an adequate understanding of the quantum statistical properties of the detector through which these measurements are to be made.

.

## 2. Quantum Phenomena in Astronomy

### 2.1. Physics of Emission Processes

One can envision applications of nanosecond resolution optical observations to give insight in the physical processes of radiative deexcitation of astrophysical plasmas, fields of study which presently are the exclusive realm of theoreticians.

What is the quantum nature of the light emitted from a volume with departures from thermodynamic equilibrium of the atomic energy level populations? Will a spontaneously emitted photon stimulate others, so that the path where the photon train has passed becomes temporarily deexcited and remains so for perhaps a microsecond until collisions and other effects have restored the balance? Does then light in a spectral line perhaps consist of short photon showers with one spontaneously emitted photon leading a trail of others emitted by stimulated emission? One could search for such amplified spontaneous emission ("laser action") in atomic emission lines from extended stellar envelopes or solar active regions. Such [partial] laser effects have been predicted for celestial sources, for example in mass-losing high-temperature stars, where the rapidly recombining plasma in the stellar envelope can act as an amplifying medium (e.g. Lavrinovich & Letokhov 1974; Varshni & Lam 1976; Varshni & Nasser 1986). Analogous effects could exist in accretion disks (Fang 1981). In the infrared, there are several cases where laser action is predicted for specific atomic lines (e.g. Ferland 1993; Greenhouse et al. 1993; Peng & Pradhan 1994). Somewhat analogous situations (corresponding to a laser below threshold) have been studied in the laboratory. The radiation structure from "free" clouds (i.e. without any laser resonance cavity) of excited gas with population inversion can be analyzed. One natural mode of radiative deexcitation indeed appears to be the emission of "photon showers" triggered by one spontaneously emitted photon which is stimulating others along its flight vector out from the volume.

In principle, quantum statistics of photons should permit to determine whether the Doppler broadening of a spectral line has been caused by motions of those atoms that emitted the photons or by those intervening atoms that have scattered the already existing photons. Thus, for such scattered light, its degree of partial redistribution in frequency might be directly measurable. Although the existence *in principle* of such effects may be clear, their practical observability is not yet known. At first sight, it might even appear that light from a star should be nearly chaotic because of the very large number of independent radiation sources in the stellar atmosphere, which would randomize the photon statistics. However, since the time constants involved in the maintenance of atomic energy level overpopulations (e.g. by collisions) may be longer than those of their depopulation by stimulated emission (speed of light), there may exist, in a given solid angle, only a limited number of radiation modes reaching the observer in a given time interval (each microsecond, say) and the resulting photon statistics might well be non-chaotic. Proposed mechanisms for pulsar emission include stimulated synchrotron and curvature radiation ("free-electron laser") with suggested timescales of nanoseconds, over which the quantum statistics of light would be non-chaotic. In general, photon statistics for the radiation from any kind of energetic source could convey something about the processes where the radiation was liberated. For example, the presence of photon "bubbles" in photohydrodynamic turbulence in very hot stars has been suggested. The bubbles would be filled with light and the photon-gas pressure inside would balance the surrounding gas pressure but due to buoyancy the bubbles would rise through the stellar surface, giving off photon bursts (Prendergast & Spiegel 1973; Spiegel 1976). Obviously, the list of potential astrophysical targets could be made longer.

## 2.2. Cosmic Laser/Maser Sources

### 2.2.1. Non-equilibrium radiation in astrophysics

Emission-line stars such as  $\eta$  Car are promising locations in searching for quantum-optical phenomena in radiation. Light carries more information than is contained in the classical quantities of ‘intensity’, ‘spectrum’ or ‘coherence’. Temporal correlations between successively arriving photons (their degree of ordering) may contain information on how the photons were created in the source (through stimulated or spontaneous emission), and how they have been scattered since. Such properties are studied in the laboratory, and might become observable also in astronomical sources.

The possibility of *laser action*, i.e. an enhanced fraction of stimulated emission in certain spectral lines due to *amplified spontaneous emission*, has been suggested for a number of spectral lines in different sources. Already long ago, it was realized that deviations from thermodynamic equilibrium in atomic energy-level populations could lead to such emission, although the possibility was not taken seriously before the construction of the laboratory microwave maser in 1954, and the visible-light laser in 1960. However, after the discovery in 1965 of the first celestial OH maser at  $\lambda$  18 cm, the astrophysical possibilities become apparent. Cosmic lasers involve the same basic processes as in the laboratory, but of course do not have mirrors in resonance cavities, but rather rely on sheer path-length to achieve amplification. The beams are emitted in narrow angles, and we only observe those beams that happen to be directed at the Earth; the vast majority which do not point towards us, remain invisible.

Laser action normally requires a population inversion in atomic or molecular energy levels. Such deviations from thermodynamic equilibrium can in particular be achieved through selective radiative excitation, or electronic recombination in a cooling plasma. Selective excitation, where another (often ultraviolet) emission line of a closely coinciding wavelength excites a particular transition, overpopulating its upper energy level, is often referred to as *Bowen fluorescence*. Following Bowen (1927), plausible combinations of atomic and molecular lines have been studied by several, e.g., Bowen (1947) and Gahm et al. (1977).

Already long ago, a few authors did touch upon possibility of laser action, but dismissed it as unrealistic or only a mathematical curiosity. Thus, Menzel (1937), when discussing situations outside of thermodynamic equilibrium, concluded “...*the condition may conceivably arise when the value of the integral [of absorbed radiation] turns out to be negative. The physical significance of such a result is that energy is emitted rather than absorbed ... as if the atmosphere had a negative opacity. This extreme will probably never occur in practice.*” (ApJ 85, p.335). However, 33 years later the same Donald Menzel (1970) was a pioneer in proposing laser action in non-LTE atmospheres.

If a strongly ionized plasma is rapidly cooled, population inversion occurs during the subsequent electronic recombination cascade, permitting laser action. This scheme, known as plasma laser or recombination laser, has been studied in the laboratory (e.g., the supersonic expansion of helium plasma from nozzles into low-density media) and is applicable to stars with mass loss. If the electron temperature is sufficiently low, the recombination occurs preferentially into the upper excited states of the ion, which then decay by a radiative and/or collisional cascade to the ground state.

Other mechanisms for creating non-equilibrium populations of energy levels include external X-ray illumination of stellar atmospheres, originating from a hot component in a close binary system (e.g., Sakhbullin & Shimansky 2000).

### 2.2.2. Mechanisms producing astrophysical lasers

Possibly, the earliest modeling in terms of laser action, was for the  $\lambda$  190.9 nm C III intercombination line in the Wolf-Rayet star  $\gamma$  Vel (West 1968), although doubted later (Castor & Nussbaumer 1972). Several infrared atomic transitions with astrophysically favorable parameters for population inversion were identified by Smith (1969), while Menzel (1970) suggested laser action in non-LTE atmospheres by analyzing the microscopic form of the radiative transfer equation. Jefferies (1971) showed that external pumping may not be required for close-lying atomic energy levels with energy separations  $\Delta E$  much smaller than  $kT$ , with  $T$  the kinetic temperature of the gas. Lavrinovich & Letokhov (1975) suggested population inversions for lines such as O I 844.6 nm in the atmospheres of hot Be stars, while Peng & Pradhan (1994) modeled infrared lasers in active galactic nuclei and novae. Selective excitation appears to cause the bright emission of ultraviolet Fe II lines in gas ejecta close to the central star of  $\eta$  Car (Johansson et al. 1996) as well as in the symbiotic star RR Tel (Hartman & Johansson 2000). Masing in the forbidden [Fe XI] 6.08  $\mu$ m line may be common, caused by peculiarities in the atomic energy structure (Ferland 1993). Other authors have discussed infrared lasers in planetary atmospheres, active galactic nuclei, accretion systems and stellar envelopes.

For longer wavelengths, there is a broad literature on millimeter and radio masers, especially molecular ones. Millimeter recombination lines of high levels in hydrogen (H30  $\alpha$ , H50  $\beta$ , and others) are seen towards  $\eta$  Car, apparently affected by maser emission (Cox et al. 1995), as well as in other sources.

Theoretical treatments of astrophysical radiative transfer including laser action have been made by, e.g., Das Gupta & Das Gupta (1991); Fang (1981); Strel'nitski et al. (1996a; 1996b); Varshni & Lam (1976), and Varshni & Nasser (1986). A common conclusion seems to be that while laser action seems possible under many diverse conditions, the amplification of any specific line requires a sufficiently extended region within a rather narrow range of parameter space (pressure, temperature, electron density).

Generally, it appears that radio and microwave masers can be produced more easily (gyrosynchrotron emission, curvature radiation) than those at shorter wavelengths, although there are suggestions for astrophysical lasers even in the X-ray regime, perhaps a recombination laser in hydrogen-like ions around accreting neutron stars (Burdiuzha & Shelepin 1990; Ghosh et al. 1995).

Laser amplification and stimulated emission in the optical region are probably quite common processes in the gaseous media in the vicinity of bright stars. They appear due to processes of the relaxation of excitation of the electronic levels of atoms or ions) in a rarefied circumstellar and interstellar gas.

During the 20<sup>th</sup> century, a lot of astrophysical spectroscopy was carried out, much of which actually was a driving force for the parallel development of atomic physics. Most of the high-resolution spectroscopy which enabled studies of individual spectral lines was carried out for the Sun and brighter stars (indeed, a field upon which rests much of our current understanding of astrophysics as a whole), while studies of line formation physics in other (fainter) types of objects, the development of model atmospheres around accretion disks, quasars, or other classes of fainter sources, have been much more limited. One limiting factor has been the smallness of astronomical telescopes which have precluded high-resolution spectroscopy and detailed physical modeling of faint sources. For example, in order to identify possible mechanisms of small wavelength shifts in quasars (due to line formation processes, changing fundamental constants, or other) probably requires a modeling of their spectral

emission on a level of physical sophistication that is comparable to that of today's spatially resolved and hydrodynamic stellar model atmospheres.

OWL and other ELT's will likely enable such studies, e.g. by providing high-resolution spectra (at  $\lambda/\Delta\lambda = 200,000$ , say) of the spatially resolved structure across e.g. quasar emissions. In many non-stellar sources, the spectral-line emission mechanisms may be in states far from local thermodynamic equilibrium, and thus not likely to be possible to realistically model with purely thermal emission mechanisms. The following discussion highlights examples of spectral-line emission under such non-equilibrium conditions, many of which can be called astrophysical lasers.

In the absence of feedback, the amplifying medium of an astrophysical laser represents an amplifier of spontaneous emission. Because of the large size of astrophysical lasers, the radiation pattern is determined by the geometry of the amplifying region. In the case of a nearly spherical geometry, the radiation should be isotropic.

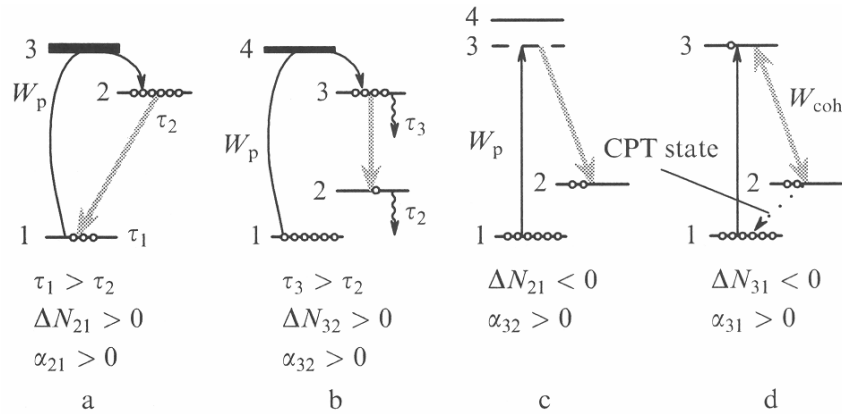


**Fig.2.1.** Methods for obtaining amplification in astrophysical lasers, based on producing the population inversion in three-level (a) and four-level (b) schemes, by means of Raman scattering without population inversion (c), and using the coherent superposition of the states 1 and 2 without population inversion for the levels 2 and 3 (d). To obtain amplification in schemes (a) and (b) requires incoherent pumping with a moderate rate. Scheme (c) requires pumping with very high spectral intensity (not necessarily coherent). Scheme (d) requires coherent pumping at the 3→1 transition. (Letokhov 2002)

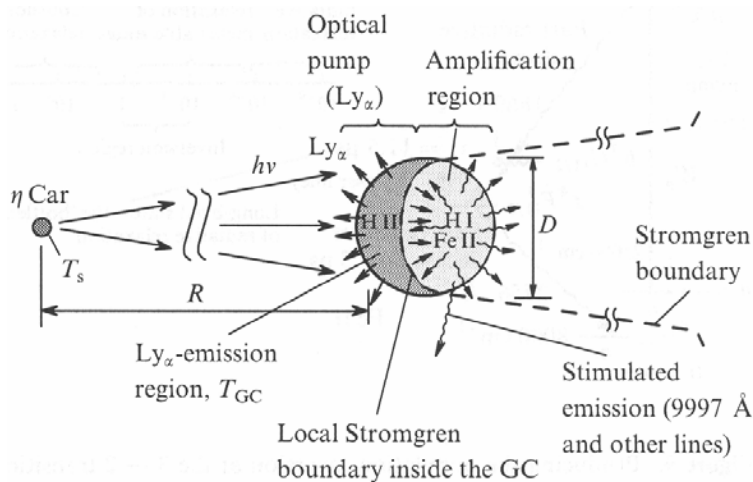


**Fig.2.2.** Model of a compact gas condensation (GC) near the hot bright star  $\eta$  Car with the local Strömrgren boundary between the photoionized (H II) and neutral (H I) regions inside the GC. (Johansson & Letokhov 2002)



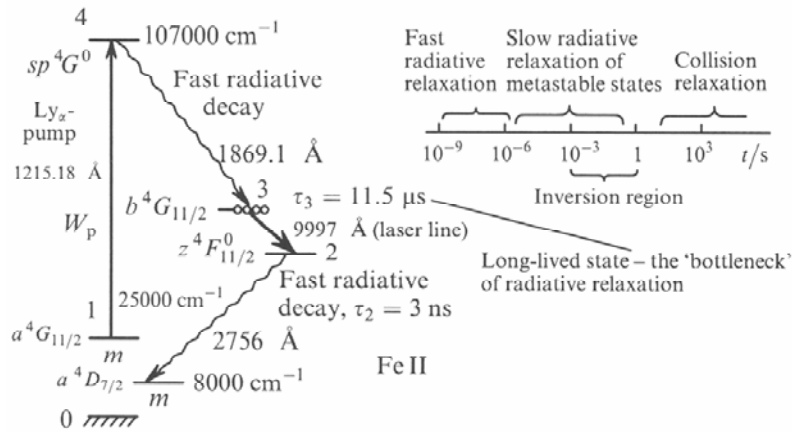


**Fig.2.3.** Producing the population inversion at the 3->2 transition in Fe II upon resonance excitation of the high-lying level 4 followed by a cascade radiative decay to the long-lived ‘pseudo-metastable’ level. Scheme of the population inversion and transitions, and (right) characteristic times of the radiative and collision relaxation of the excited levels of Fe II. (Johansson & Letokhov 2002; Letokhov 2002)

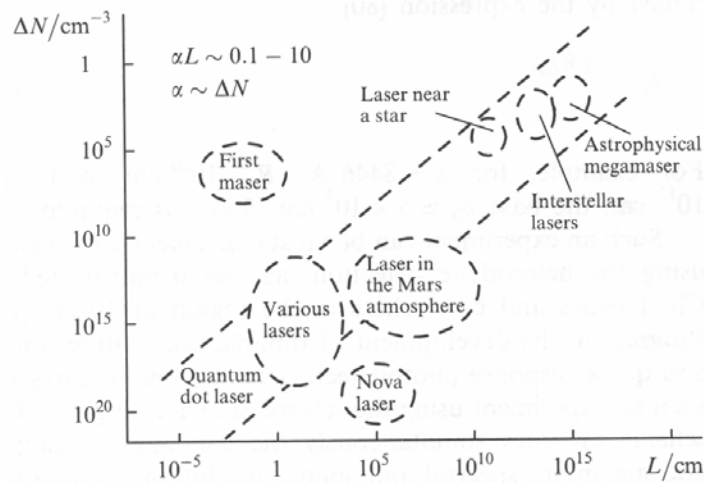


**Fig.2.4.** Various laboratory and astrophysical masers and lasers in the active medium particle density – active medium size diagram. (Letokhov 2002)

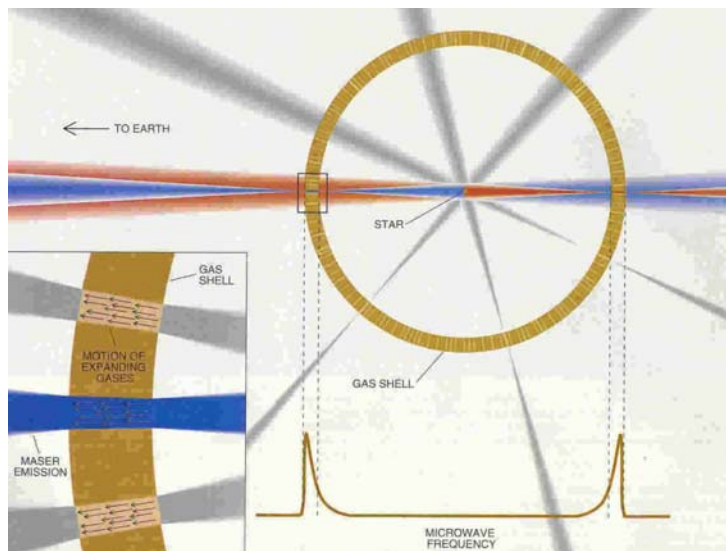


**Fig.2.5.** Schematic of circumstellar maser emission. (Elitzur 1995)

A “random laser” producing monochromatic flashes can be initiated by a few “lucky” photons that remain inside the material for a long time:

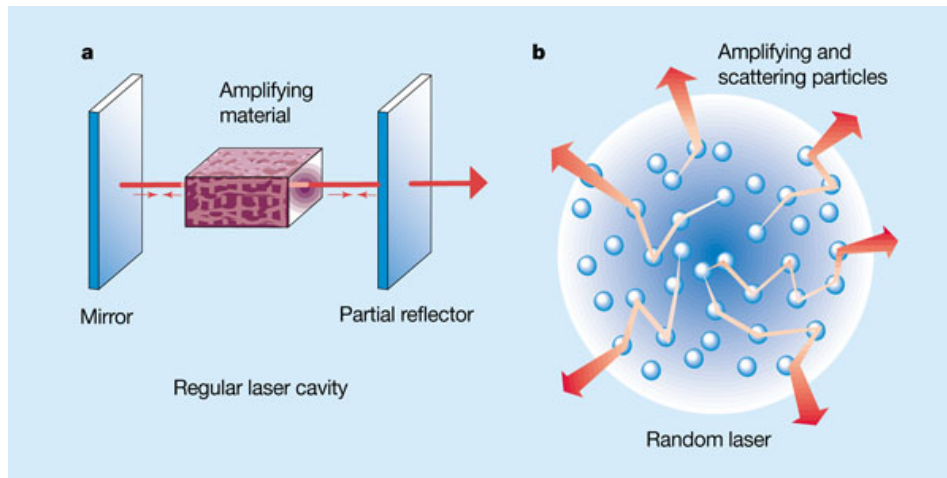


*Fig.2.6. Mechanisms producing a ‘random laser’ (Wiersma 2000)*

### 2.2.3. A case study: Astrophysical lasers in Eta Carinae

Eta Carinae, the most luminous star known in our Galaxy, is some 50-100 times more massive than our Sun and 5 million times as luminous ( $M_{\text{bol}}$  approx=  $-12$ ). This star has now entered the final stage of its life and is highly unstable. It undergoes giant outbursts from time to time; one of the most recent happened in 1841 and created the beautiful bipolar nebula known as the Homunculus Nebula. At that time, and despite the comparatively large distance – 3 kpc –  $\eta$  Car briefly became the second brightest star in the night sky, surpassed only by Sirius.

Eta Carinae is so big that, if placed in our solar system, it would extend beyond the orbit of Jupiter. This large size, though, is somewhat arbitrary. Its outer layers are continually being blown into space by radiation pressure - the impact of photons on atoms of gas. Many stars, lose mass because of such "stellar winds", but in the case of  $\eta$  Car, the resulting mass loss is enormous (about  $10^{-3} M_{\odot}$  or 500 Earth-masses a year) and it is difficult to define the border between the outer layers of the star and the surrounding stellar wind region.

Its circumstellar ejecta: the bipolar *Homunculus*, equatorial disk and three ejected gas clouds (“Weigelt blobs”), at separations 0.1–0.2 arcsec, are resolved by speckle interferometry.  $\eta$  Car is believed to represent an important though short-lived, unstable phase in the life of the most massive stars: the Luminous Blue Variable (LBV) phase. It is an extreme star, even by the standards of LBVs. There is speculation that it may be a binary, though this is by no means certain.

In addition to the many smaller events, Eta Carinae has undergone giant bursts in the last centuries. A Sumerian recording of a ‘new star’ in 3000 B.C. is possibly attributable to  $\eta$  Car (Naeye 1997). In 1837,  $\eta$  Car flared up, peaking second only to Sirius at magnitude -0.8, in 1843. It remained at first magnitude for around 20 years, but has since settled back around 6 to 8. The latest shell event of 1992 was followed by an enhancement of flux in the radio wavelength range and by the reappearance of the stellar source in hard X-rays.

## Homunculus Nebula

The star is now surrounded by a shell of gas ejected in the 1837 outburst, known as the Homunculus Nebula, spectacularly revealed in a famous HST image. The Homunculus is mainly a reflecting nebula comprising some 2 to 3  $M_{\odot}$ , which is apparently produced by a bipolar outflow from  $\eta$  Car, and expanding at around 650 km/sec.

Spanning a scale from 10 to 20-30,000 AU, the star itself and the Homunculus Nebula are thus closely aligned in space. The VINCI on VLTI was able to detect the boundary where the stellar wind from  $\eta$  Car becomes so dense that it is no longer transparent. Apparently, this stellar wind is much stronger in the direction of the long, than of the short axis.

According to mainstream theories, stars lose most mass around their equator because there the stellar wind gets "lifting" assistance from the centrifugal force caused by the star's rotation. However, if this were so in the case of  $\eta$  Car, the axis of rotation (through the star's poles) would then be perpendicular to both mushroom-shaped clouds. But it is virtually impossible that the mushroom clouds are positioned like spokes in a wheel, relative to the rotating star: the matter ejected in 1841 would then have been stretched into a ring or torus.

An assumption is that the star itself, which is located deep inside its stellar wind, is flattened at the poles for the usual reason. However, as the polar areas of this central zone are then closer to the centre where nuclear fusion processes take place, they will be hotter. Consequently, the radiation pressure in the polar directions will be higher and the outer layers above the polar regions of the central zone will get more "puffed up" than the outer layers at the equator. Assuming this model is correct, the rotation of  $\eta$  Car can be calculated. It turns out that it should spin at over 90 percent of the maximum speed possible (before break-up).

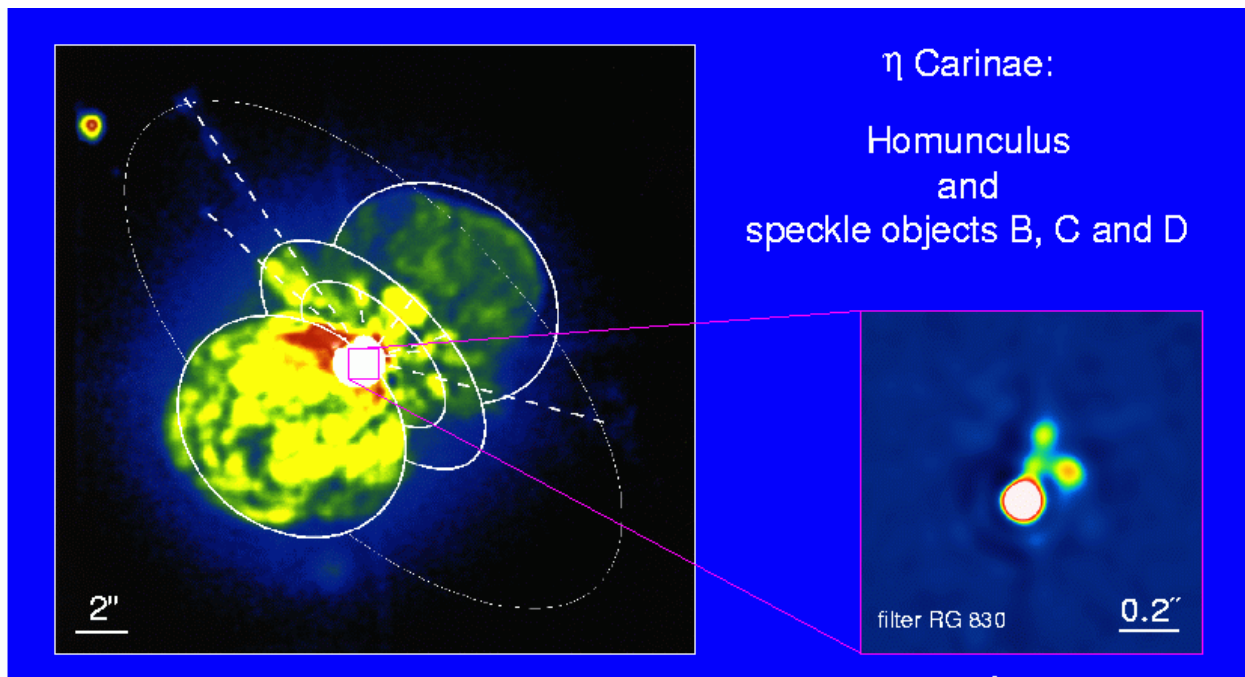


*Fig.2.7. Speckle masking observations of  $\eta$  Carinae (Hofmann & Weigelt 1988)*

At the present,  $\eta$  Car is losing so much mass so rapidly that nothing will be left of it after less than 100,000 years. More likely, though, it will destroy itself long before that in a supernova blast that could possibly become visible in the daytime sky with the naked eye. This may happen "soon" on the astronomical time-scale, perhaps already within the next 10-20,000 years.

### Production of a natural laser in the $\eta$ Car envelope

Quoting Johansson & Letokhov (2004): "Space lasers with optical pumping operate according to a scheme similar to the one suggested for the first laboratory laser 45 years ago by Schawlow and Townes (1958). We believe that laser amplification and stimulated emission of radiation is a fairly common and widespread phenomenon, at least for gaseous condensations in the vicinity of bright stars. This is due to the occurrence of two types of processes (fast radiative and slow collisional) in the very rarefied gaseous condensations, whereby the population of energy levels in atoms (ions) can relax.

These relaxation processes occur on highly different time scales, radiative relaxation operating on a wide time scale of  $10^{-9}$ - $10^{-3}$  s (sometimes even within  $10^{-3}$ -1 s), and collisional relaxation, on a time scale of over seconds (at gas densities  $<10^{10}$   $\text{cm}^{-3}$ ). In the case of photoselective excitation of some high-lying electronic levels of an atom or ion with a complex energy-level structure, radiative relaxation can take place as a consequence of downward transitions with spontaneous emission of radiation, in the course of which there develops an inverse population of some pair (pairs) of levels. If the size of a gas cloud is large enough, large amplification on the inverted-population transition automatically switches on the radiative relaxation channel, which leads to faster stimulated transitions until collisional relaxation becomes important.

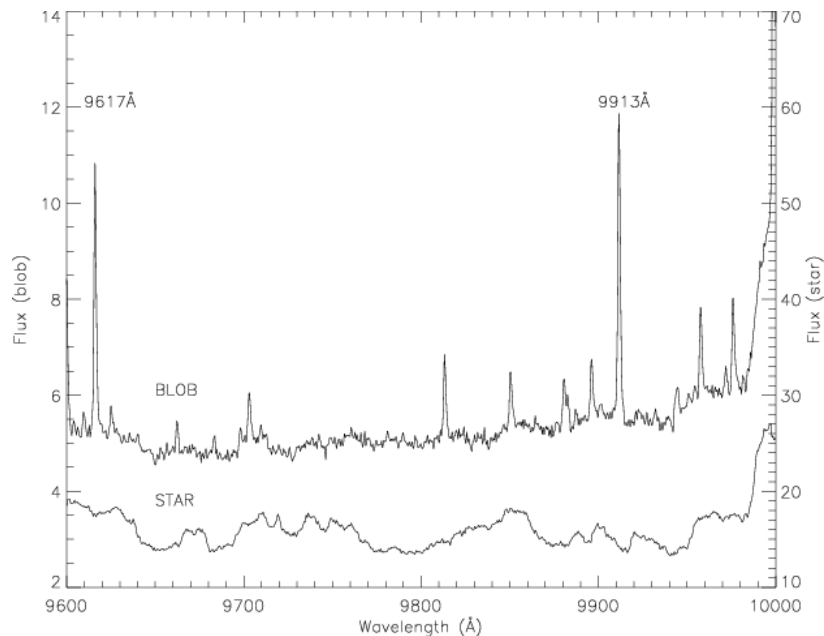


**Fig.2.8.** Comparison of HST/STIS spectra of the central star (flux scale on right axis) and the Weigelt blob B (flux scale on left axis) in  $\eta$  Car with the two lasing lines  $\lambda$  9617, 9913 Å. (Johansson & Letokhov 2004)

Thus, the laser action is an intrinsic characteristic of the radiative cooling of gas clouds near bright stars by stimulated emission for inverted transitions along with spontaneous emission for normal transitions." ... "We report here on the discovery of laser action in the range 0.9-2

$\mu\text{m}$  in several spectral lines of Fe II, which are associated with transitions from "pseudo-metastable" states populated by spontaneous transitions from Ly-alpha pumped Fe II levels. The intense Ly-alpha radiation is formed in the HII region of gas condensations close to the star Eta Car. The laser transitions form together with spontaneous transitions closed radiative cycles, one of which includes the extremely bright 2507/09 Å lines. Closed radiative cycles, together with an accidental mixing of energy levels, may provide an explanation of the abnormal intensities of these UV non-lasing lines. Using the complicated energy level diagram of Fe II we present those peculiar features, which are essential for the inverted population and laser effect: the pumping, the level mixing, and the "bottle neck" for spontaneous decay. The laser action is a new indicator of non-equilibrium and spatially non-homogeneous physical conditions as well as a high brightness temperature of Ly  $\alpha$  in ejecta from eruptive stars. Such conditions are very difficult to probe by existing methods, and we propose some future experiments. The fact, that the lasing near-IR lines appear in the spectrum with about the same intensity as non-lasing lines is discussed and compared with the situation in masers."

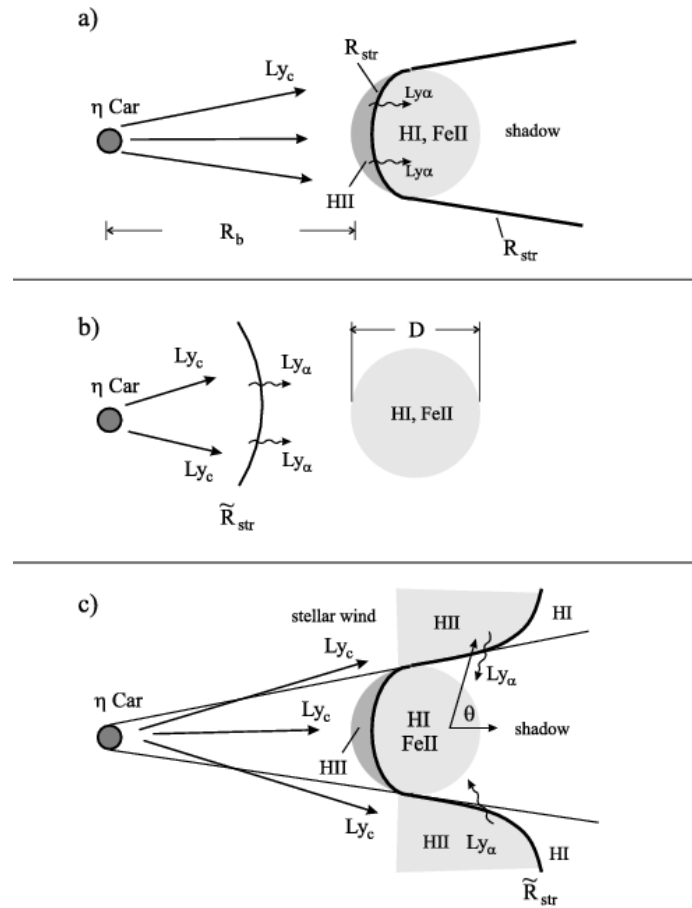


**Fig.2.9.** A schematic model of a Weigelt blob, located near the hot, luminous star Eta Car and subject to the stellar radiation and wind. a) A local Strömgen boundary, between the H II and H I regions is located inside the blob. Stellar radiation in the Lyman continuum photo-ionizes hydrogen only in the front part of the blob. Radiation in the range  $7.6 \text{ eV} < h\nu < 13.6 \text{ eV}$  passes through the H II region and photo-ionizes iron atoms. Intense Ly alpha radiation from the H II region excites Fe II resonantly in the H I region (lasing volume). The Strömgen boundary for the stellar wind b) the stellar wind is optically thick for Ly-continuum, and the blob is a one-component H I medium. Only remote, blue-shifted Ly-alpha radiation from the stellar wind can irradiate the HI region containing Fe II; c) the Strömgen boundary in the wind lies behind the blob, providing intense, red-shifted Ly-alpha photons for efficient excitation of Fe II. (Johansson & Letokhov 2004)

### 2.2.4. Lasers in Wolf-Rayet and symbiotic stars

Symbiotic stars are close binary systems where a hot star ionizes part of an extended envelope of gas from a cooler companion. The combined spectrum of the system shows the superposition of absorption and emission spectral features together with irregular variability.

In the symbiotic star V1016 Cyg, Raman scattering of the O VI lines at 1032 and 1038 Å by the 1s-2p electronic transition in neutral hydrogen (close to the resonance with Ly β at 1026 Å) have been identified. Due to such scattering, the hydrogen atom was found in the 2s state, and the Raman line was observed in the visible region (at 6825 and 7082 Å). This effect was observed under special conditions of symbiotic stars where strong VUV emission lines of highly ionized atoms irradiate the high-density regions of neutral hydrogen. The gain at Raman lines, however, is not very high. (Schmid 1989)

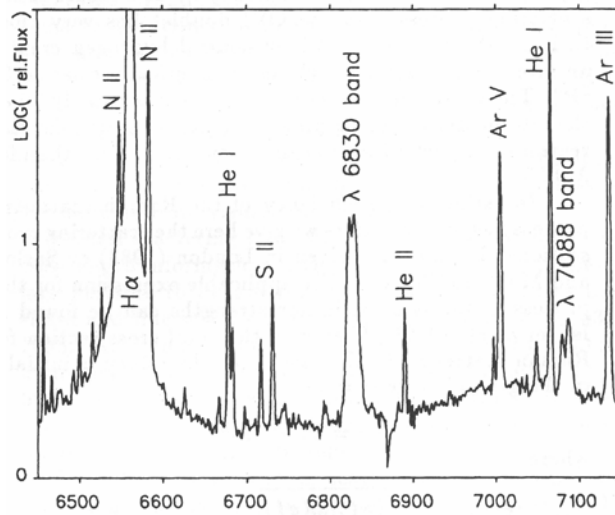


**Fig.2.10.** Raman-scattered emission bands in the symbiotic star V1016 Cyg. (Schmid 1989)

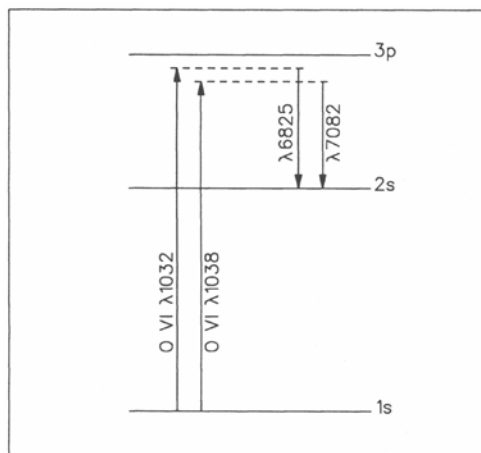


**Fig.2.11.** Energy-level diagram for Raman scattering of O VI photons by neutral hydrogen. (Schmid 1989)

### 2.2.5. Hydrogen lasers/masers in the emission-line star MWC349A

Varshni & Nasser (1986): If an ionized gas is rapidly cooled, population inversions will occur during the subsequent recombination cascade. The scheme is known as a plasma laser or recombination laser. Rapid cooling of a strongly ionized plasma leads to a rapid recombination. If the electron temperature is sufficiently low, the recombination occurs preferentially into the upper excited states of the ion, which then decays by radiative and/or collisional cascade to the ground state. Within the cascade from the upper excited states, population inversions may form among the excited states, depending upon the relative transition probabilities.

Several methods of cooling the plasma have been suggested. Two of these which are of importance for astrophysics are: (a) rapid expansion, and (b) contact with a neutral gas. If mass loss from, e.g., a Wolf-Rayet star is rapid enough, it can lead to rapid cooling. The contact with the interstellar gas can provide further cooling.

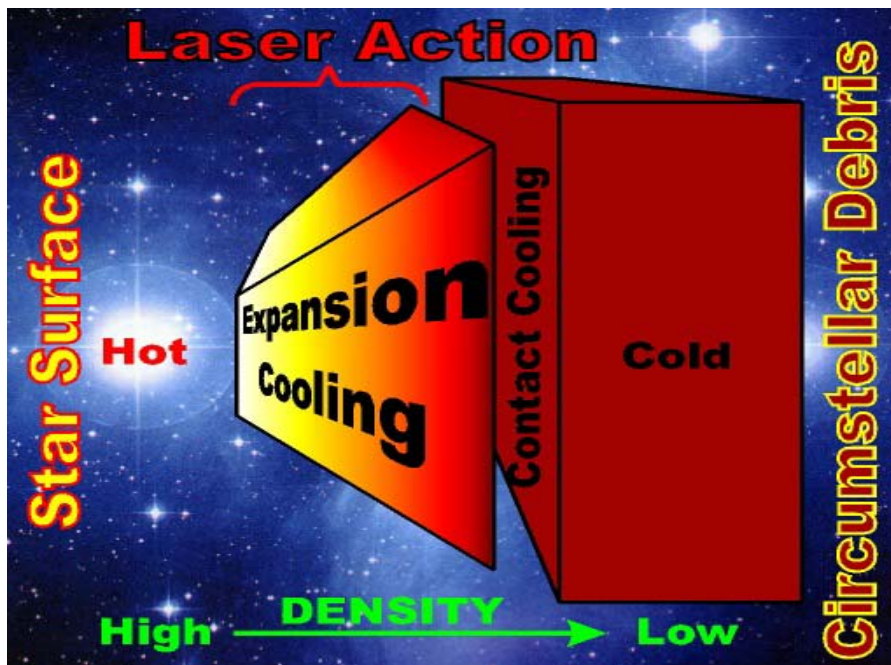


**Fig.2.12.** Plasma dynamics leading to laser action. In hot stellar winds, a hot dense plasma is expanding and cools due to [adiabatic] expansion and/or contact with cold circumstellar gas. Electrons recombine preferentially into the upper energy levels, thus creating population inversions in, e.g., hydrogen atoms. (Talbot 1995)

The unusual IR and radio properties of MWC 349 were discovered in the 1970's. Several models have been proposed, and two seem more likely: a quasi-spherical outflow of ionized gas in the outer part of the circumstellar envelope, and a differentially rotating disk, viewed edge-on, in its inner part. (Gordon et al. 2001)

MWC 349 is a peculiar hot emission-line star, often classified as a B[e] star, somewhat similar to the Herbig Ae/Be stars (the intermediate- or high-mass counterparts to T Tauri stars). It is a very bright infrared source and extremely strong radio star; it has a B0 III companion at 2" separation. The estimated mass of MWC 349 is  $\approx 30 M_{\text{sun}}$  and its distance  $\approx 1.2$  kpc. It possesses a dense neutral Keplerian circumstellar disk (extent  $\approx 300$  AU), and an ionized wind with very low terminal velocity ( $\approx 50$  km/s) which may originate from the disk.

Perhaps the most outstanding features are strong hydrogen recombination line masers at mm and sub-mm wavelengths (H21 $\alpha$  to H35 $\alpha$ ) which are located in the disk at  $\approx 40$  AU. (Quirrenbach & Frink 2001). The emission is interpreted as coming from a region having large electron density in a Keplerian disk at a distance  $\approx 20$ -30 AU from the star. In recent years, maser emission was observed at ever shorter wavelengths – from 1.3 mm to as short as 19  $\mu$ m. These observations are consistent with the masers' originating in a dense plasma created by photoionization of material in a massive Keplerian disk. (Danchi et al. 2001)

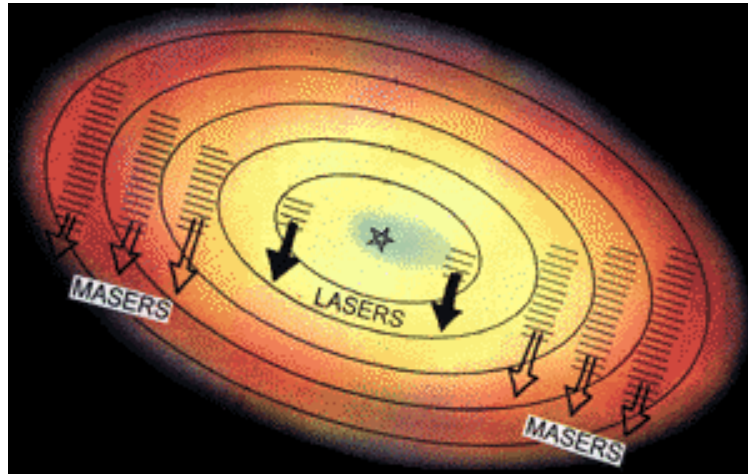


**Fig.2.13.** Circumstellar disk surrounding the hot star MWC 349. Maser emissions are thought to occur in outer regions while lasers are operating nearer the central star. (Kuiper Airborne Observatory press release)

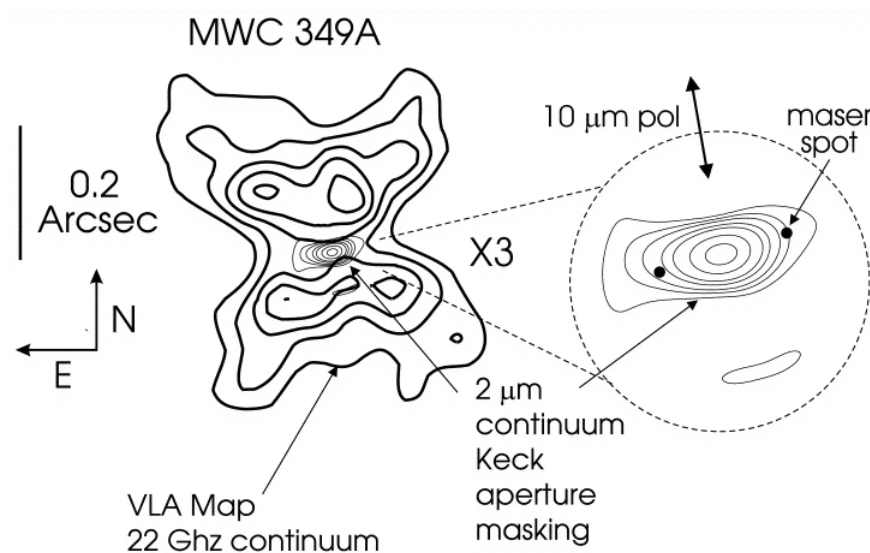


**Fig.2.14.** Superposition of the VLA continuum map at 22 GHz (Martín-Pintado et al. 1993) and the 2  $\mu$ m map from aperture-masking interferometry. The observed near-infrared disk fits neatly into the dark lane of the radio map and is of a size that accounts for the origin of the outflow as coming from material in this disk. To the right is an enlarged view of the 2.2  $\mu$ m disk with a 3 $\times$  magnification, showing its structure in more detail. Also plotted are the recombination line maser spots at 1.3 mm and the 10  $\mu$ m polarization vector. The maser spots are centered on the 2.2  $\mu$ m image; however, this is an assumption, and astrometry is required to place them precisely. (Danchi et al. 2001)



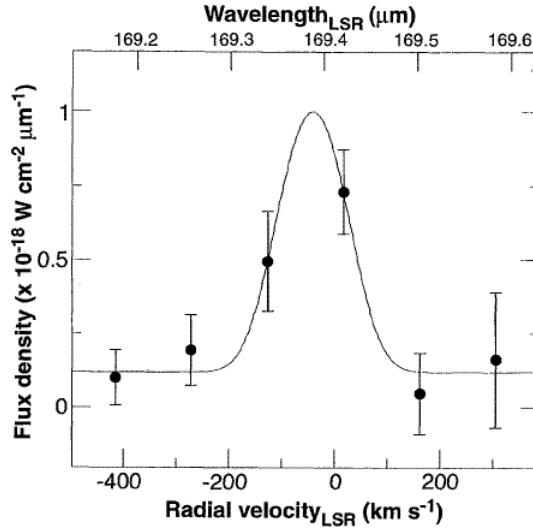


**Fig.2.15.** MWC349A: The H15-alpha spectral flux densities obtained from the Kuiper Airborne Observatory. LSR is the local stellar standard of rest. (Strelitski et al. 1996)

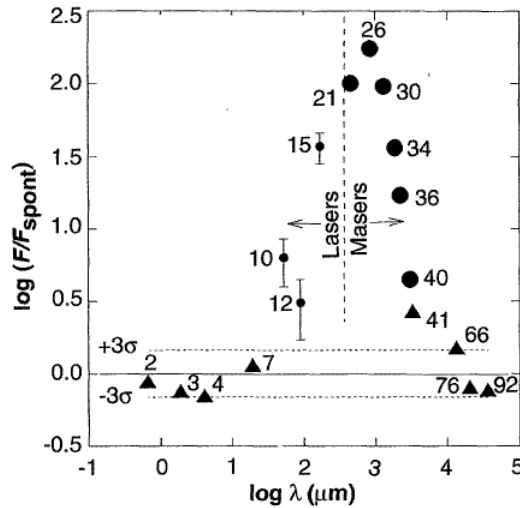


**Fig.2.16.** MWC349A: Log-log plot of the ratio  $F/F_{spont}$  where  $F$  is the observed flux. Large circles indicate masing mm and sub-mm lines; small circles are infrared KAO detections. The numbers are the principal quantum numbers for each line's lower level. (Strelitski et al. 1996)

MWC 349 consists of two apparently close (angular separation  $2.4''$ ) objects: MWC 349A which exhibits a strong emission-line spectrum and IR excess, and MWC 349B, a weak emission-line source which is  $\approx 40\%$  fainter than MWC 349A in the optical region. It has been argued that MWC 349A and B are a physical pair, as they are connected by an arc of emitting matter, and the estimated distance (1.2 kpc) is based on the spectral type and luminosity of MWC 349B (B0 III and  $M_V = -5.0$  mag, respectively). However, other workers have found that the A and B components have different levels of interstellar polarization, suggesting that they are not connected, and that MWC 349A could be a member of the Cygnus OB2 association. Thus, the binary nature of the object is not certain. (Hofmann et al. 2002)

Strong magnetic field in the disk of MWC 349: Using Zeeman observations of the H30 $\alpha$  recombination line maser transition at 1.3 mm, a magnetic field was detected which is

associated with the corona of the circumstellar disk of MWC 349. At a radial distance of 40 AU, where the H30 $\alpha$  maser is located, the line-of-sight component of the field is approximately parallel to the edge-on-disk, and its average strength is 2.2  $\mu$ T (22 mG). The corresponding magnetic energy density is  $\approx$  70% of the thermal energy density of the plasma where the maser emission originates, very likely making the magnetic field dynamically important. The strength of the field at such a large distance from the star makes it unlikely that the field is of stellar origin, possibly it is generated by a local disk dynamo. (Thum & Morris 1999)

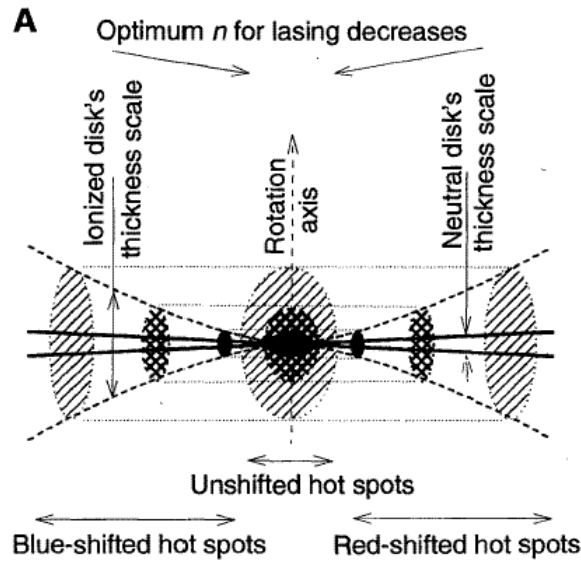


**Fig.2.17.** Proposed structure of the lasing and masing circumstellar disk in MWC349A.  
A: Edge-on view (presumably as we observe it). (Strelnitski et al. 1996)

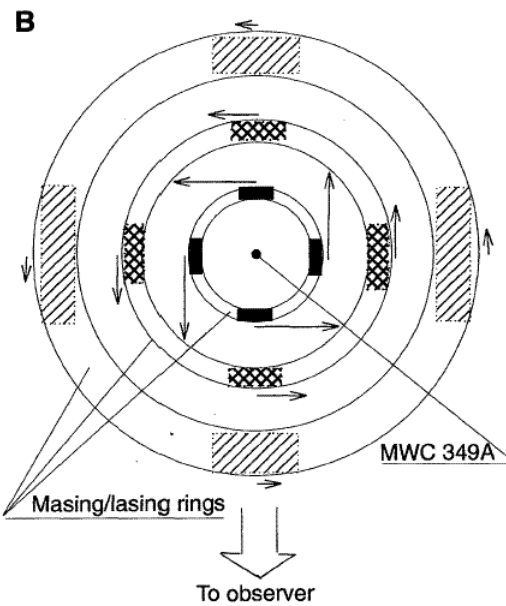


**Fig.2.18.** Proposed structure of the lasing and masing circumstellar disk in MWC349A.  
B: Face-on view (Strelnitski et al. 1996)

### 2.2.6. First masers in the Universe

Hydrogen recombination lasers thus may form as electrons successively recombine into atoms, initially populating the upper energy levels, thus inducing population inversions. [Re]ionization also implies the moving of electrons to higher energy levels, likewise tending to invert the energy-level populations.

This process is also valid for the very early state of the Universe, soon after the Big Bang, at the epochs of recombination and reionization. The physical properties of masing hydrogen recombination lines at  $Z \approx 1000$  have been modeled by Spaans & Norman (1997). They find that if small-scale overdense regions exist, maser action is possible in this phase of cosmological evolution, owing to the expansion of the Universe and the low ambient temperature at decoupling. The paths along which maser amplification is sustained during the epoch of recombination are assumed to be associated with the strong density perturbations required for the development of ionizing sources at  $Z_{(reionization)}$ . Due to the redshift, these spectra might today be observable in the long-wavelength radio region (e.g., with the planned Square Kilometer Array, SKA), but the basic physical processes would be analogous to those observable at shorter wavelengths in today's local Universe.

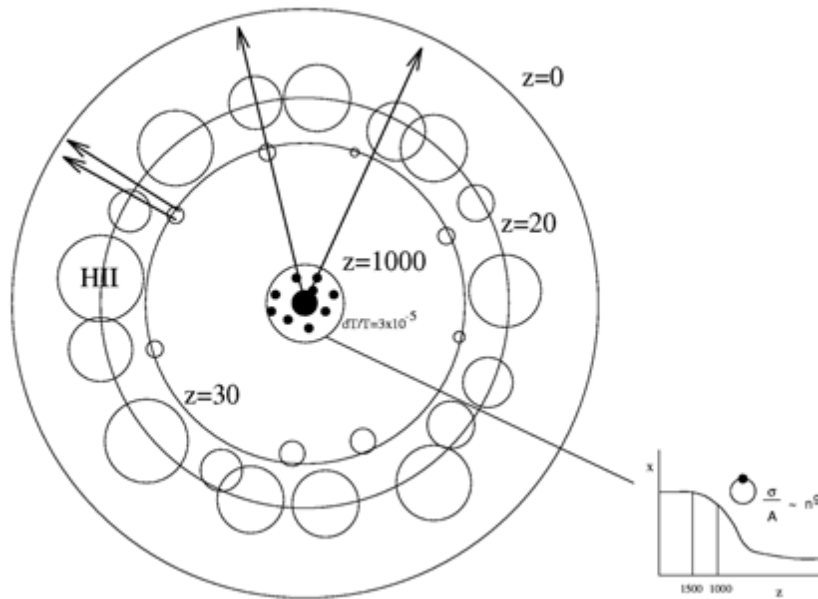


**Fig.2.19.** Sketch of maser mechanisms in the very early Universe. The black inner region denotes the evolution of the universe before decoupling. Arrows indicate maser emission from the epoch of recombination and reionization. The small black dots at recombination indicate small-scale density fluctuations associated with the precursors of ionizing sources at  $z_{ri}$ . The inset shows the variation of the ionization fraction  $x$  with redshift, and the steep dependence of the hydrogen principal quantum number  $n$  on the collisional cross section and the Einstein A-coefficient. Note that some maser spots will interact with H II regions at the onset of reionization. (Spaans & Norman 1997)

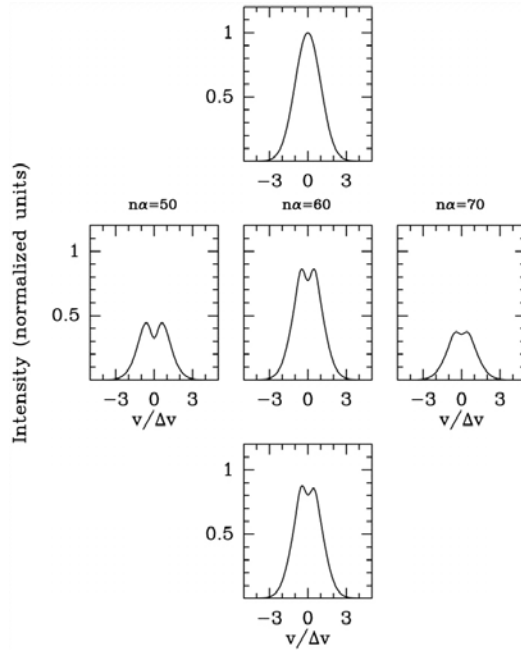


**Fig.2.20.** Three sample maser spots with  $n\alpha = 60$  (top to bottom) produced at  $z \approx 1000$ , if nonlinear regions with  $\delta P/P \approx 10^2$  exist during recombination. The maser radiation interacts with  $H\ II$  regions at  $z_{ri}$ . From left to right the resulting profiles for other frequencies along the same line of sight are shown. The curves correspond to  $z = 0$ . The early stages of reionization lead to absorption features at discrete velocities because the  $H\ II$  regions are small and few. As  $F$  approaches unity and the emission measure decreases, the large  $H\ II$  regions cause shallow line and continuum absorption across the profile. For small  $n$ , the absorption features are more pronounced. The intensity is normalized with respect to the top  $n = 60$  profile. (Spaans & Norman 1997)

Brightness temperatures for individual spots are expected to be on the order of  $10^7$  K.

During propagation, the maser photons will experience Doppler shifts as they climb out of potential wells and traverse time-varying ones. The resulting velocity differences can be measured along various lines of sight and combined to yield  $n$ -point angular correlation functions on the sky. In effect, the power spectrum can be reconstructed. Such measurements may very well provide the most direct determination of the interaction between the photon and baryon fluids prior to last scattering. Given the large brightness temperatures of the maser spots, the sensitivity of these measurements is very high. (Spaan & Norman 1997)

### 2.2.7. CO<sub>2</sub> lasers in planetary atmospheres

Laser/maser emission is not a property that would be exclusive to remote and extreme deep-space environments. The following gives some examples of cosmic laser emission in our planetary-system neighborhood:

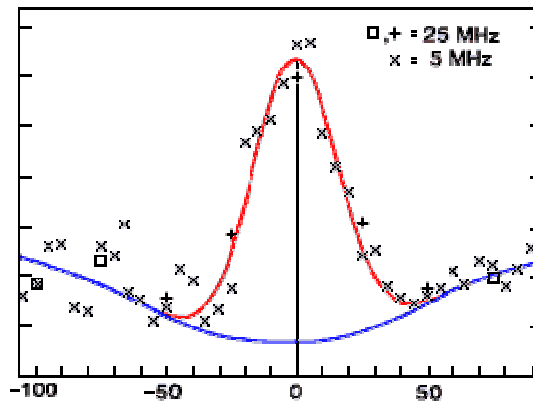


**Fig.2.21.** Spectra of Martian  $\text{CO}_2$  emission line as a function of frequency difference from line center (in MHz). Blue profile is the total emergent intensity in the absence of laser emission. Red profile is Gaussian fit to laser emission line. Radiation is from a 1.7 arc second beam (half-power width) centered on Chryse Planitia (long +41 lat +23). (Mumma et al. 1981)

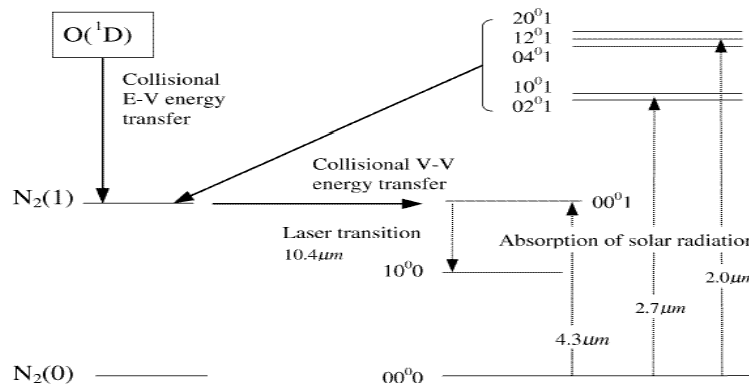


**Fig.2.22.** Vibrational energy states of  $\text{CO}_2$  and  $\text{N}_2$  associated with the natural  $10.4 \mu\text{m}$   $\text{CO}_2$  laser. The figure shows radiative and collisional processes which are involved in the pumping of the relevant  $\text{CO}_2$  state. (Shved & Ogibalov 2000)

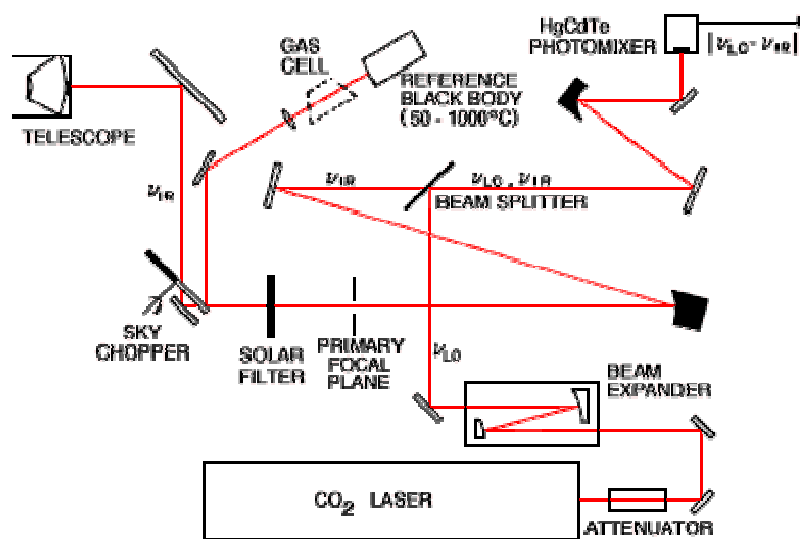


**Fig.2.23.** Goddard Space Flight Center IR heterodyne spectrometer. The  $\text{CO}_2$  laser beam from the bottom ( $\nu_{LO}$ ) is mixed with the input signal ( $\nu_{IR}$ ) coming in from the left. The sensitive IR photodetector produces an electronic signal at the upper right ( $\nu_{LO}-\nu_{IR}$ ) which is further processed by an RF spectrometer (not shown). (Kostiuk & Mumma 1983).

### 2.2.8. Lasers without population inversion?

Stimulated emission does not necessarily require population inversions of atomic energy levels, but can occur in other scattering processes:

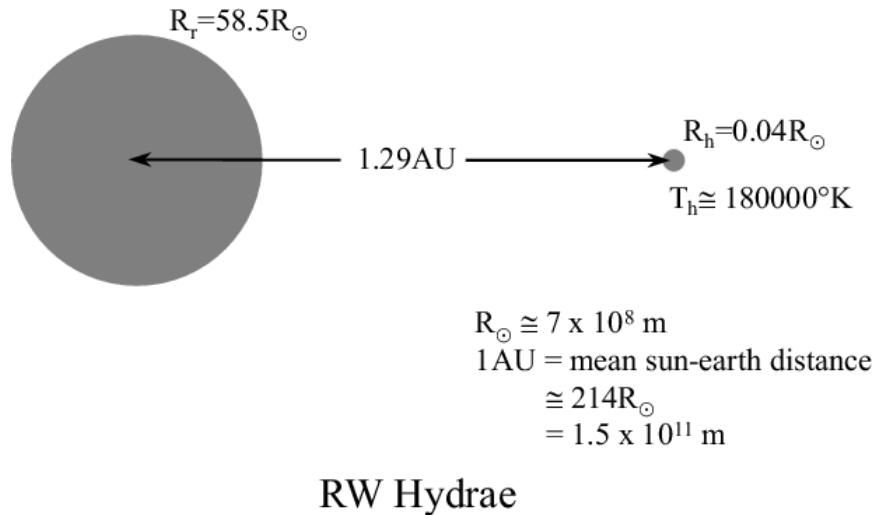


**Fig.2.24.** Sketch of the geometry of the symbiotic star RW Hydrae, based upon measurements presented in Schild et al. (1996); Sorokin & Glowina (2002)

Sorokin & Glowina (2002) suggest “Lasers without inversion” (LWI) as a possible explanation for intense, narrow-band, emissions that dominate the visible and/or far-UV (FUV) spectra of certain astronomical objects. “The optical or far-UV (FUV) spectra of certain objects in space are completely dominated by one or two spectrally narrow emission lines, strongly suggesting that laser action of some kind occurs in these objects. However, the electronic level structures of the atoms/ions producing these emissions preclude the possibility of maintaining population inversions on the electronic transitions involved. In lasers, gain is normally produced on an optical transition that is inverted, i.e. one that has more atoms maintained in the upper than in the lower state, so that stimulated emission can exceed stimulated absorption. However, as a result of discoveries made in quantum electronics over the past 30 years or so, one now knows that there are several ways to make stimulated emission occur on a transition that is not inverted, i.e. to realize a “laser without inversion”. This requires first making the atoms non-absorbing at the lasing frequency, i.e. setting up a condition of ‘electromagnetically induced transparency (EIT)’. Some recently developed EIT techniques for three-level atoms are first reviewed.

A simple model for a space LWI based upon a gas of two-level atoms is then proposed. In this model, transparency results from a form of EIT induced by the presence of an intense, monochromatic, continuous-wave, laser beam tuned to the frequency  $\omega_0$  of the two-level-atom transition. Amplification of light at this same frequency occurs via resonant stimulated hyper-Raman scattering and four-wave mixing, with pumping energy provided by continuum starlight spectrally overlapping the two outer absorption sidebands (‘Mollow bands’) induced by the presence of the beam at  $\omega_0$ . Two specific examples of superintense line emission from space are here considered. These are (a) the H $\alpha$  emission line appearing as a dominant singularity in certain reddened, early-type stars, and (b) the powerful O VI (1032 Å, 1038 Å) emission doublet that dominates the FUV emission spectra of symbiotic stars such as RR Tel.”

### 2.2.9. Nanosecond pulses in pulsars

Nanosecond radio bursts from strong plasma turbulence in the Crab pulsar:

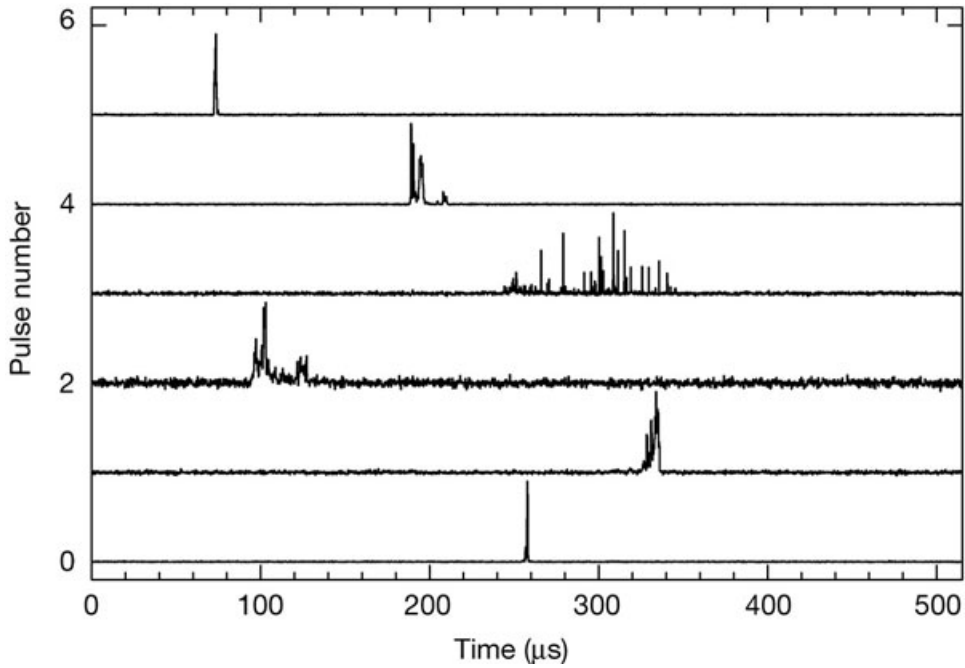


**Fig.2.25.** A sequence of dedispersed Crab giant radio pulses. The arrival time jitter and varied shapes of the total intensity are shown. The time axis origin is modulo one pulsar rotation period. Each pulse has been plotted with a time resolution of 250 ns and is normalized to the same maximum amplitude. The centre frequency is 5.5 GHz and the sampled bandwidth is 0.5 GHz. The resulting time resolution is the reciprocal of the receiver bandwidth, ultimately 1–2 ns. (Hankins et al. 2003)

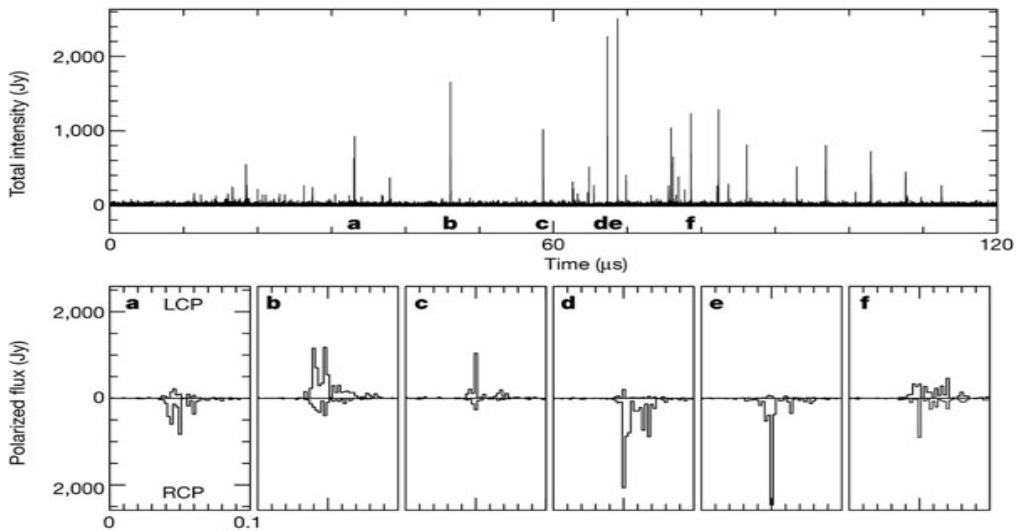


**Fig.2.26.** Intensity, polarization and time structure of radio nanopulses from the Crab pulsar. The upper panel shows details of pulse 3 in Fig. 1, plotted with 2-ns resolution. Sections of 100-ns duration showing the polarized flux from six of the nanopulses, labeled a–f, are plotted below with left circular polarization upward, and right circular polarization downward, also with 2-ns resolution. (Hankins et al. 2003)

## Optical nanopulses?

Shearer et al. (2003) detected a correlation between optical and giant radio pulse emission from the Crab pulsar. Optical pulses coincident with the giant radio pulses were on average 3% brighter than those coincident with normal radio pulses. Combined with the lack of any other pulse profile changes, this result indicates that both the giant radio pulses and the increased optical emission are linked to an increase in the electron-positron plasma density.

This correlation suggests that there might also exist optical nanopulses (however, probably requiring ELT's for their observation).

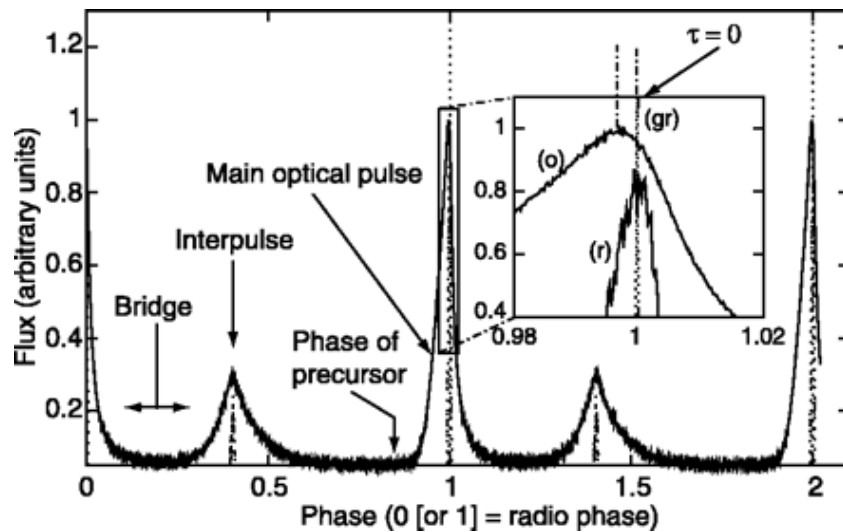


**Fig.2.27.** The Crab pulse profile showing the optical light curve (o), the average radio light curve at 1380 MHz (r), and a single giant radio pulse at 1357.5 MHz (gr). Two periods are shown for clarity. Various pulse parameters have been identified. Also shown is the location of the precursor observed at lower frequencies and the bridge emission seen particularly at higher frequencies. On this scale, the GRP width corresponds to 0.00035 units of phase ( $12 \mu\text{s}$ ), the radio pulse to 0.009 ( $300 \mu\text{s}$ ), and the optical pulse to 0.045 ( $1500 \mu\text{s}$ ). The optical light curve is taken from the second night of observation. The avalanche photodiode (APD) band pass for these observations was from 600 to 750 nm. Phase 0 corresponds to the arrival at the solar system barycenter of the peak radio pulse. The optical light curve for this plot was divided into 5000 phase bins; the optical peak is at  $-100 \mu\text{s}$  with respect to the JBE. (Shearer et al. 2003)

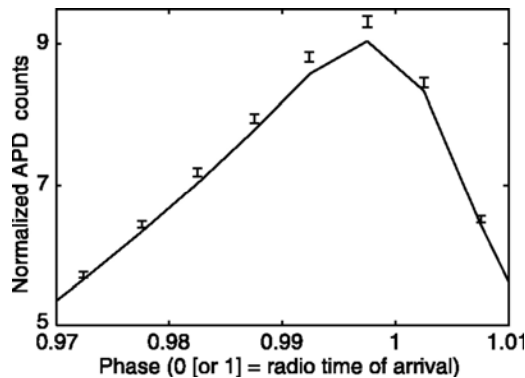


**Fig.2.28.** The mean optical "giant" pulse superimposed (with its error bars) on the average optical pulse. The average pulse is determined from the 40 pulsar periods centered on the GRP, but not including it, from both nights of observation. (Shearer et al. 2003)



### 2.2.10. How short (and bright) pulses exist in nature?

Soglasnov et al. (2004) write: “Giant radio pulses of the millisecond pulsar B1937+21 were recorded with the S2 VLBI system at 1.65 GHz with NASA/JPL's 70 m radio telescope at Tidbinbilla, Australia. These pulses have been observed as strong as 65,000 Jy with widths  $\leq 15$  ns, corresponding to a brightness temperature of  $T_b \geq 5 \times 10^{39}$  K, the highest so far observed in the Universe. The vast majority of these pulses occur in 5.8 and 8.2  $\mu$ s windows at the very trailing edges of the regular main pulse and interpulse profiles, respectively. Giant pulses occur, in general, with a single spike. Only in one case of 309 was the structure clearly more complex. It was estimated that giant pulses occur frequently but are only rarely detected.

When corrected for the directivity factor, 25 giant pulses are estimated to be generated in one neutron star revolution alone. The intensities of the giant pulses of the main pulses and interpulses are not correlated with each other, nor with the intensities or energies of the main pulses and interpulses themselves. Their radiation energy density can exceed 300 times the plasma energy density at the surface of the neutron star and can even exceed the magnetic field energy density at that surface. We therefore do not think that the generation of giant pulses is linked to the plasma mechanisms in the magnetosphere. Instead it is suggested that it is directly related to discharges in the polar cap region of the pulsar.”

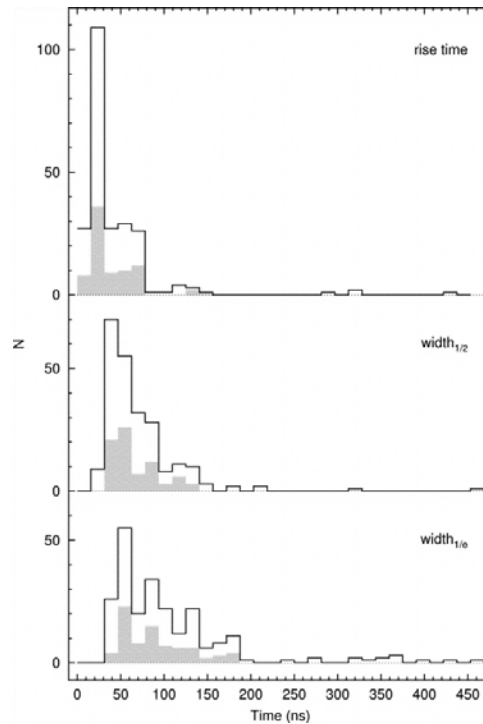


**Fig.2.29.** Statistics of the rise time and the width of giant pulses. The rise time is measured from the  $1/e$  level to the peak of the pulse (top panel), and the width is measured at a level of  $1/2$  (middle panel) and  $1/e$  (bottom panel) of the maximum flux density. The open histograms show the 232 pulses reprocessed in the total 32 MHz band (see text), and the gray-scale histograms show the 76 strong giant pulses with a peak flux density exceeding 1600 Jy. (Soglasnov et al. 2004)

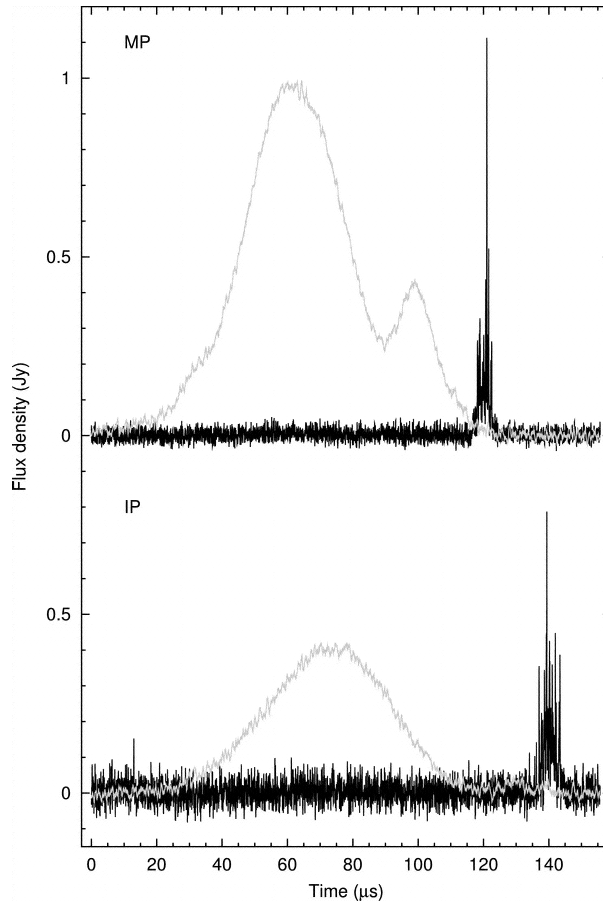


**Fig.2.30.** Longitudes of giant pulses in comparison with those of the components of the average profile. The light gray lines show profiles averaged over the whole observing time of 39 minutes (1,501,344 periods). The solid lines represent a profile averaged over only those periods in which giant pulses were detected, 190 for the main pulse region (MP, upper panel) and 119 for the interpulse region (IP, lower panel). (Soglasnov et al. 2004)

### 2.2.11. Emission in magnetic fields of magnetars

Making a neutron star – and a magnetar – starts (1) with a massive star that has burned up all of its fuel, then (2) collapses and causes a massive explosion, the supernova that blows off the outer layers and (3) compresses the core. Soon, all that is left is a shell of expanding gas (not always this pretty or symmetrical) and a rapidly spinning neutron star at "ground zero." If the original star was spinning fast enough and had a strong enough magnetic field, the neutron star is a magnetar

Possible optical pulsations from magnetars have been suggested. A maser curvature emission mechanism in the presence of curvature drift is used to explain the optical pulsations from anomalous X-ray pulsars (AXPs). The model comprises a rotating neutron star with a strong surface magnetic field, i.e. a magnetar. Assuming the space-charge-limited flow acceleration mechanism, in which the strongly magnetized neutron star induces strong electric fields that pull the charges from its surface and flow along the open field lines, the neutron star generates a dense flow of electrons and positrons (relativistic pair plasma) by either two-photon pair production or one-photon pair creation resulting from inverse Compton scattering of the thermal photons above the pulsar polar cap (PC). The motion of the pair plasma is essentially one-dimensional along the field lines. We propose that optical pulsations from AXPs are generated by a curvature-drift-induced maser developing in the PC of magnetars. Pair plasma is considered as an active medium that can amplify its normal modes. The

curvature drift, which is energy-dependent, is another essential ingredient in allowing negative absorption (maser action) to occur. For the source AXP 4U 0142+61, we find that the optical pulsation triggered by curvature-drift maser radiation occurs at the radial distance  $R(M) = 4.75 \times 10^9$  cm to the neutron star. The corresponding curvature maser frequency is about  $M = 1.39 \times 10^{14}$  Hz, and the pulse component from the maser amplification is about 27 per cent. The result is consistent with the observation of the optical pulsations from AXP 4U 0142+61. (Lu & Zhang 2004)

Source optical/IR	$\nu_{\min,12}^a$ optical/IR	$\nu_M \ll \nu_c^b$	Observation	Model (pulsed)
SGR 1900+14...	2.83	yes	no/no	optical
SGR 1806-20...	3.22	yes	no/no	optical
AXP 1048-5937	2.38	yes	no/yes	optical
AXP 1841-045	2.40	yes	no/no	optical
AXP 2259+586	0.83	yes	no/yes	no
AXP 0142+61	1.15	yes	yes/no	optical
AXP 1708-4009	1.98	yes	no/yes	optical
PSR J1119-6127	1.76	yes	no/no	no
PSR J1814-1744	0.96	yes	no/no	no

<sup>a</sup>  $\nu_{\min,12} = \nu_{\min}/10^{12}$  Hz. <sup>b</sup> Refer to Table 1.

**Table 2.1.** Conditions for a synchrotron maser for the optical pulsation of a magnetar. (Lu & Zhang 2004)

Coherent optical emission from magnetars: Eichler et al. (2002) propose that magnetospheric currents above the surfaces of magnetars radiate coherent emission. Such coherent emission from plasma instabilities in the infrared and optical would probably be pulsed and polarized and have a nonthermal spectrum. Scaling the magnetospheric parameters suggests that the coherent emission from magnetars would emerge in the infrared or optical. the possibility of coherent optical and infrared emission in certain astrophysical situations, such as magnetars. The basis for such a hypothesis is quite simple: Magnetars are expected to have twisted magnetic loops in their magnetospheres, and most of the time, the thermal scale height of their atmospheres is too low to populate the magnetosphere with thermal plasma. On the other hand, magnetospheric currents can easily be drawn out of the surface of the star from at least one of the footpoints. This current can be estimated. The rate of dissipation  $dB/dt$  of the magnetic field can also be estimated; it is presumably the value of  $dB/dt$  that yields a sufficient potential drop across the length of the loop to create enough plasma to short out any larger potential drop. The density of plasma so estimated is many orders of magnitude larger than that in pulsar magnetospheres. If pulsars can radiate coherently in the radio, this frequency being ultimately determined by the plasma frequency in the pulsar magnetosphere, then similar processes could occur in magnetar magnetospheres with the plasma frequency scaled up appropriately.

These estimates suggest that coherent emission can be emitted from the magnetospheres of magnetars in the near-infrared or optical. As the emission is likely to be beamed, in analogy with pulsars, one cannot predict that any given magnetar would be a coherent infrared or optical source, but there are enough in the Galaxy assuming this includes anomalous X-ray pulsars that one or several might be. Because many are in the plane of the Galaxy, the near-infrared might be a good frequency to search for such emission.

The possibility is considered that the recently reported optical emission from the anomalous X-ray pulsar (AXP) 4U 0142+61 is coherent. The high pulsed fraction of the optical emission 0.27, considerably higher than that of the soft X-ray emission is naturally explained by a pulsar-type emission mechanism.

Two conceivable ways to affirm the coherence of an optical signal could be via (1) photon arrival statistics, if the emission happens to consist of high-brightness temperature bursts that stand out above the time average emission, and (2) measurement of temporal correlation of the wave front, if the emission happens to consist of piecewise narrowband wave trains. The former is plausible if the magnetospheric plasma is produced in episodic sparking events. The latter is plausible if the fastest growing mode dominates the plasma instability in any particular layer of plasma.

The optical photon flux at the detector from 4U 0142+61 is on the order of  $10^{-2}$  cm<sup>-2</sup>/s. A 10 m telescope would collect an average of the order, say,  $10^4$  optical photons per second. By analogy to pulsars, micropulses on a timescale of  $10^{-4}$  s or less could carry much of the time-averaged luminosity. Photon bursts significantly shorter than  $10^{-8}$  s might therefore be difficult to explain as being incoherent emission. Although there is no guarantee that the emission proceeds as a series of such short bursts, neither is it out of the question; timescales as short as  $10^{-9}$  s could obtain given outflows on a scale of  $10^6$  cm with Lorentz factors of  $\Gamma \approx 10^{2.5}$ . Such timescales are accessible with photomultiplier detectors. Pulses this short would have to be more intense than  $10^4$  times the average luminosity (implying low duty cycle) in order to have more than one photon per pulse. This too is not predicted with confidence, but is not entirely out of the question.

If the additional constraint of a dipole magnetic field geometry is imposed, we can further argue that optical synchrotron emission, which must arrive from a region with field strength  $10^7/\Gamma$  G, would have to originate some  $10^{8.5} \Gamma^{1/3}$  cm from the star. Then, optical pulses shorter than  $10^{-2}/\Gamma^{5/3}$  s would be hard to explain as synchrotron emission. As  $\Gamma$  is constrained by the above equation, optical synchrotron pulses much shorter than  $10^{-7}$  s would confront this difficulty.

Another way to possibly affirm the coherent nature of the emission is to search for temporal coherence of the wave front, as coherent emission could be piecewise narrow band. Rapid spectroscopy might test for this. For example, splitting the beam and then subtracting one component from the other after one has been delayed by  $\Delta t$  would filter out coherent emission at  $\nu \approx 1/(2\Delta t)$  with a bandwidth of order  $\nu/2$ . If the emission is a sum of narrowband micropulses, then, even if the average frequency varies from one microburst to the next, the photon arrival statistics would be affected on the timescale of the variation of the emission frequency. (Eichler et al. 2002)

### **2.2.12. Maser mechanism for optical pulsations in X-ray pulsars?**

Lu & Zhang (2004): “Based on the work of Luo & Melrose from the early 1990s, a maser curvature emission mechanism in the presence of curvature drift is used to explain the optical pulsations from anomalous X-ray pulsars (AXPs). The model comprises a rotating neutron star with a strong surface magnetic field, i.e. a magnetar. Assuming the space-charge-limited flow acceleration mechanism, in which the strongly magnetized neutron star induces strong electric fields that pull the charges from its surface and flow along the open field lines, the neutron star generates a dense flow of electrons and positrons (relativistic pair plasma) by either two-photon pair production or one-photon pair creation resulting from inverse Compton scattering of the thermal photons above the pulsar polar cap (PC). The motion of the pair plasma is essentially one-dimensional along the field lines. We propose that optical pulsations

from AXPs are generated by a curvature-drift-induced maser developing in the PC of magnetars. Pair plasma is considered as an active medium that can amplify its normal modes. The curvature drift, which is energy-dependent, is another essential ingredient in allowing negative absorption (maser action) to occur. For the source AXP 4U 0142+61, we find that the optical pulsation triggered by curvature-drift maser radiation occurs at the radial distance  $R(\text{num}) \sim 4.75 \times 10^9$  cm to the neutron star. The corresponding curvature maser frequency is about  $\nu_M \sim 1.39 \times 10^{14}$  Hz, and the pulse component from the maser amplification is about 27 per cent. The result is consistent with the observation of the optical pulsations from AXP 4U 0142+61.”

### **2.3. Photon Statistics as a Diagnostic Tool**

In light from any source, there exist temporal correlations between successively arriving photons. Their degree of ordering (the 'entropy' of light) may carry information on the physics of light emission, e.g., how the photons were created in the source, and how they have been scattered since. In thermodynamic equilibrium, photons (being particles with integer spin  $S = 1$ ) follow a Bose-Einstein distribution. However, away from equilibrium, photons may deviate from this distribution (just as classical particles may be non-Maxwellian).

#### **2.3.1. Identifying laser effects in astronomical sources**

Classical indicators for laser/maser action include high line-to-continuum ratios; 'anomalous' intensity ratios among lines in the same multiplet; rapid time variability (perhaps uncorrelated among different lines); small spatial extent, and narrow spectral lines (caused by the amplification of radiation at the line center being higher than in the wings), coupled with theoretical expectations.

Since any region radiating into a specific direction at any moment in time must be very much smaller than the stellar atmosphere, there will exist a large number of independent emission regions, and Doppler shifts from stellar rotation or expanding atmospheres may smear out the integrated line profile, masking the spectrally narrow contributions from individual emission regions. Also, if only a small fraction of the source is lasing, spontaneous emission from the rest may overwhelm the small laser hot-spots when observed with insufficient spatial resolution. Still, the existence of such 'bright spots' could be revealed through phase or intensity interferometry (the latter assuming the photon statistics to be closely Gaussian): Lavrinovich & Letokhov (1975; 1976).

In radio, astrophysical masers have been studied in quite some detail, and some studies have also included considerations of the source statistics. The radiation is generally assumed to arise through processes in which the individual particles radiate independently, and the resulting radiation fields are then Gaussian. This assumption greatly simplifies the radiative transfer equations, although many phenomena can not be well explained by this standard theory, and some attempts to detach from this assumption have been made (Wu 1993). In stimulated emission, the nonlinear gain characteristics may well disturb the Gaussian nature of the original field.

Early efforts to search for deviations from Gaussian statistics in coherent radio sources were made by Evans et al (1972), who studied radiation from OH maser sources, concluding that the statistics were Gaussian within at least some percent. Likewise, Paschenko et al. (1971), and Lekht et al. (1975) found the statistics of OH maser sources to have noiselike signal properties. DeNoyer & Dodd (1982) noted that a way to detect the non-Gaussian

electromagnetic fields in saturated masers would be to perform statistical tests in individual frequency channels; some studies of OH masers, however, did not reveal any such signals.

The claimed first detection of non-Gaussian statistics was reported in the radio emission from some pulsars by Jenet et al. (2001): The statistical properties of the radio emission from four pulsars were studied using high time resolution (100 ns) observations at Arecibo Observatory. Temporally coherent non-Gaussian emission has been detected in three of the four objects. The results were interpreted using a generalized shot noise model, and various basic physical quantities pertaining to the magnetospheric plasma were estimated. However, Smits et al. (2003) in repeating somewhat similar measurements, while also identifying signatures consistent with a coherent signal, conclude that its origin more likely is that from interstellar scintillation, rather than being intrinsic to the pulsars.

### 2.3.2. Modeling photon statistics

Analogous to past observational ventures into previously unexplored parameter domains, the search for phenomena of photon statistics in astronomical light is an explorative project where one does not know beforehand exactly what to expect, nor in which sources. Also — judging from past experience — any more detailed development of relevant astrophysical theory is unlikely until after actual observations are available. Nevertheless, some authors have made efforts towards this direction, and somewhat analogous physical situations could illuminate the challenges to be expected.

The theoretical problem of light scattering in a [macroscopic] turbulent medium is reasonably well studied. In particular, the equations of transfer for  $I^2$  and higher-order moments of intensity have been formulated and solved (e.g. Uscinski 1977). A result that is familiar to many people implies that stars twinkle more with [moderately] increasing atmospheric turbulence. The value of  $I$ , i.e. the total number of photons transmitted may well be constant, but  $I^2$  increases with greater fluctuations in the medium. The quantum mechanical problem of scattering of light against atoms is somewhat related, except that the timescales involved are now those of the coherence time of light.

Theoretical treatments of astrophysical radiative transfer have so far concentrated on the first-order quantities of intensity, spectrum and polarization, and not on the transfer of  $I^2$  and higher-order terms. There are a few notable exceptions, however, like the analytical solution of the higher-order moment equation relevant for radio scintillations in the interstellar medium (Lee and Jokipii 1975; Lerche 1979a; 1979b) and attempts to formulate the quantum mechanical description of the transfer of radiation, including non-Markovian effects (i.e. such referring to more than one photon at a time) in a photon gas (Macháček 1978; 1979), the transfer equation for the density matrix of phase space cell occupation number states (Sapar 1978; Ojaste & Sapar 1979), or the need to introduce concepts from non-linear optics (Wu 1993). Other relevant efforts include those by, e.g., Cooper et al. (1982), and Streater et al. (1988), and there must be many relevant papers in laboratory quantum optics. However, as opposed to the laboratory case, the often complex nature of astronomical sources may not lend itself to simple such treatments, and there does not yet appear to exist any theoretical predictions for specific astronomical sources of any spectral line profiles of higher-order than one (i.e. the ordinary intensity versus wavelength).

It appears that the equations for radiative transfer must be written in a *microscopic* form, i.e. considering each radiation, excitation, and scattering process on a photon-to-atom[s]-to-photon level, rather than treating only statistically averaged light intensities, opacities, etc. While it could be argued that the many radiation sources in any astronomical object would tend to randomize the emerging radiation (erasing the signatures of non-equilibrium processes), the

number of independent sources that contribute to the observed photon signal in any given short time interval is actually very limited. If 1000 photons per millisecond are collected, those can originate from at most 1000 spatially distinct locations, which during that particular millisecond happened to beam their radiation towards the Earth. Perhaps, such 1000 photons would originate from only 900 sources, say, in which case some insight in the source physics could be gained through measurements of photon statistics.

There exist other types of quantum phenomena known in the laboratory, which conceivably might be detected in photon statistics also from some astronomical sources. These include emission cascades which could show up in cross correlations between emission successively appearing in different spectral lines, or various collective effects of light-emitting matter (“superradiance”, i.e. several *atoms* emitting together, perhaps in pulsar nanopulses?).

## 2.4. Photon Orbital Angular Momentum

There exist other effects of quantum optics which perhaps might be exploited in astronomy. One of these is orbital angular momentum: One single photon arriving from a given direction, of any given wavelength, still can have hundreds of different states since it may carry different amounts of orbital angular momentum. Although known in principle since already long ago, it has only very recently that this photon property has been more widely appreciated (not least for applications in quantum computing and quantum communication since it implies that a photon may carry not only one bit, but at least a full byte of information). Some astronomical applications have already been suggested, but whether these can be realized still remains to be seen. Although measurements of Photon Orbital Angular Momentum (POAM) are not yet foreseen in the current design of *QuantEYE*, this Section describes this quantum-optical effect, both for completeness, and as a background for a possible later discussion.

Photons have many properties: Electromagnetic radiation carries momentum and its linear momentum is associated with radiation pressure, while the angular momentum is usually associated with the polarization of the optical beam. Only quite recently has it been more widely realized that individual photons may carry also orbital angular momentum, OAM (besides the “classically” known angular momentum associated with photon spin and polarization), a property which now can be measured also for individual photons. This OAM in the direction of propagation is characterized by an integer  $\ell$  in units of  $\hbar$ , so that an absorber placed in the path of such a beam will, for each photon absorbed, acquire an angular momentum  $\ell\hbar$ . The transfer of angular momentum of light to a material body has been measured first by Beth in the 1930’s then demonstrated in several basic experiments and found also new applications in nanotechnology.

The integer  $\ell$  gives the OAM states of the photon and determines – in a quantum information context – how many bits of information that can be encoded in a single photon.

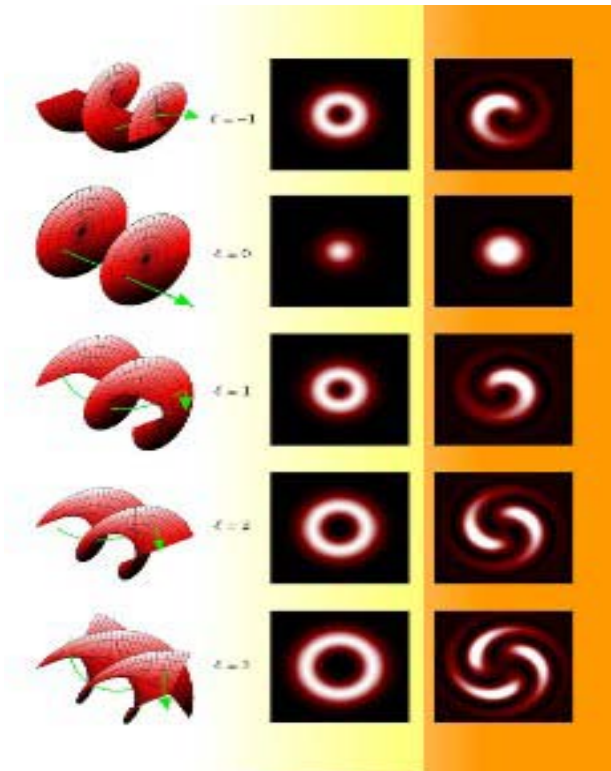


**Fig. 2.31.** Up, left: for any given  $\ell$ , the beam has  $\ell$  intertwined helical phase fronts. For helically phased beams, the phase singularity on the axis dictates zero intensity there. The cross-sectional intensity pattern of all such beams has an annular character that persists no matter how tightly the beam is focused. (Padgett et al. 2004)

**Fig.2.32.** Below:  $\ell =1$  mode and the corresponding Gaussian mode from a laser source crossing a fork hologram. Right: The optical vortex in white light from a thorium lamp before and after having compressed the wavelength dispersion by the hologram. (Tamburini et al. 2005).

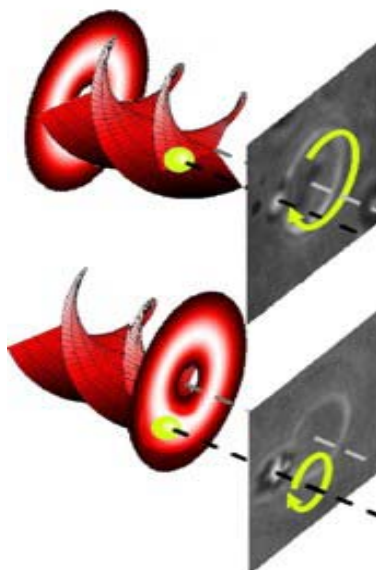
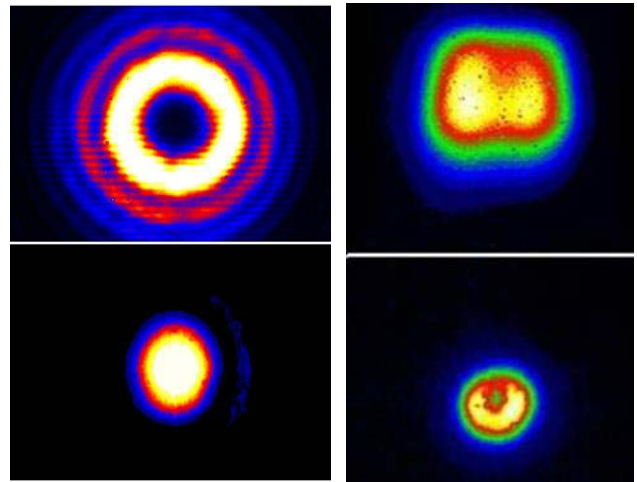


**Fig.2.33.** Technological applications of OAM. At microscopic level, interactions have been observed with helical beams acting as optical tweezers. A small transparent particle was confined away from the axis in the beam's annular ring of light. The particle's tangential recoil due to the helical phase fronts caused it to orbit around the beam axis. At the same time, the beam's spin angular momentum caused the particle to rotate on its own axis. (Padgett et al. 2004). This effect is used in the realization of optical tweezers.



**Imposing and Measuring Orbital Angular Momentum:**

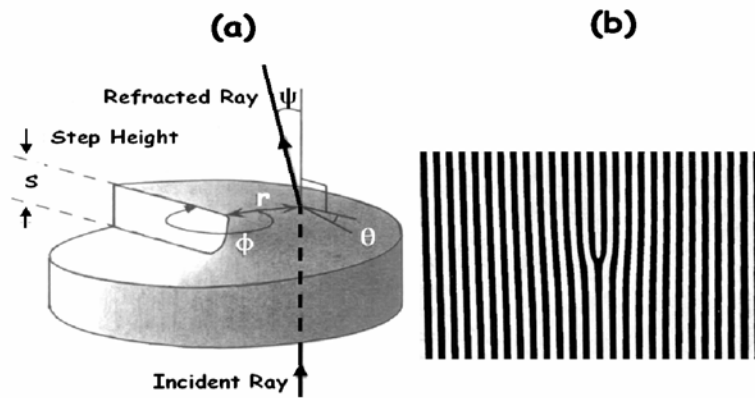


**Fig.2.34.** The technique used to generate beams carrying OAM from a Gaussian beam is to insert in the optical path a phase modifying device, like a spiral phase plate (a) or the so-called fork hologram (b) shown in the picture below. These devices have the ability to imprint a certain vorticity on the phase distribution of the incident beam.

The characterization of different orbital angular momenta present in a light beam, instead proceeds either thanks to Dove-prism Mach-Zehnder interferometer or to rotation of phase profiles realized with cylindrical optics or spiral phase plates as in the figures below.

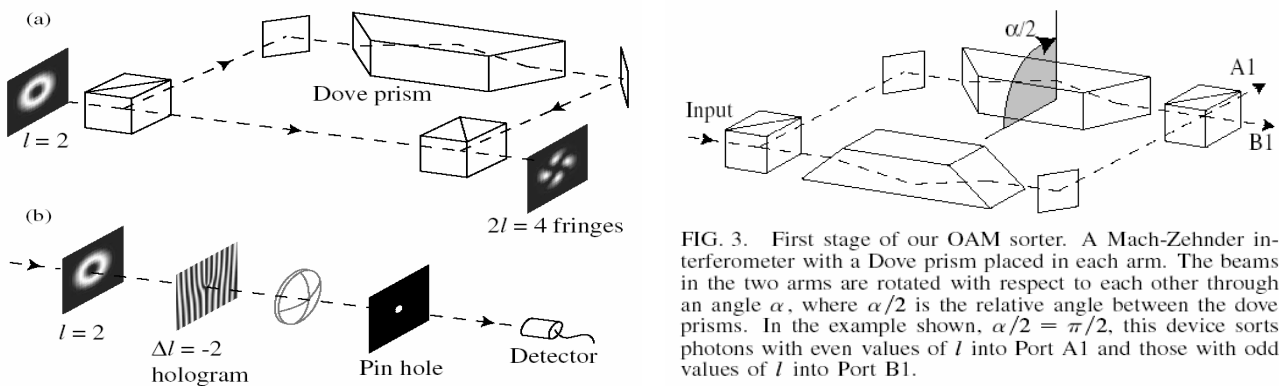


**FIG. 3.** First stage of our OAM sorter. A Mach-Zehnder interferometer with a Dove prism placed in each arm. The beams in the two arms are rotated with respect to each other through an angle  $\alpha$ , where  $\alpha/2$  is the relative angle between the dove prisms. In the example shown,  $\alpha/2 = \pi/2$ , this device sorts photons with even values of  $l$  into Port A1 and those with odd values of  $l$  into Port B1.

**Fig.2.35.** Dove-Prism Mach-Zehnder interferometer (Leach et al. 2002)

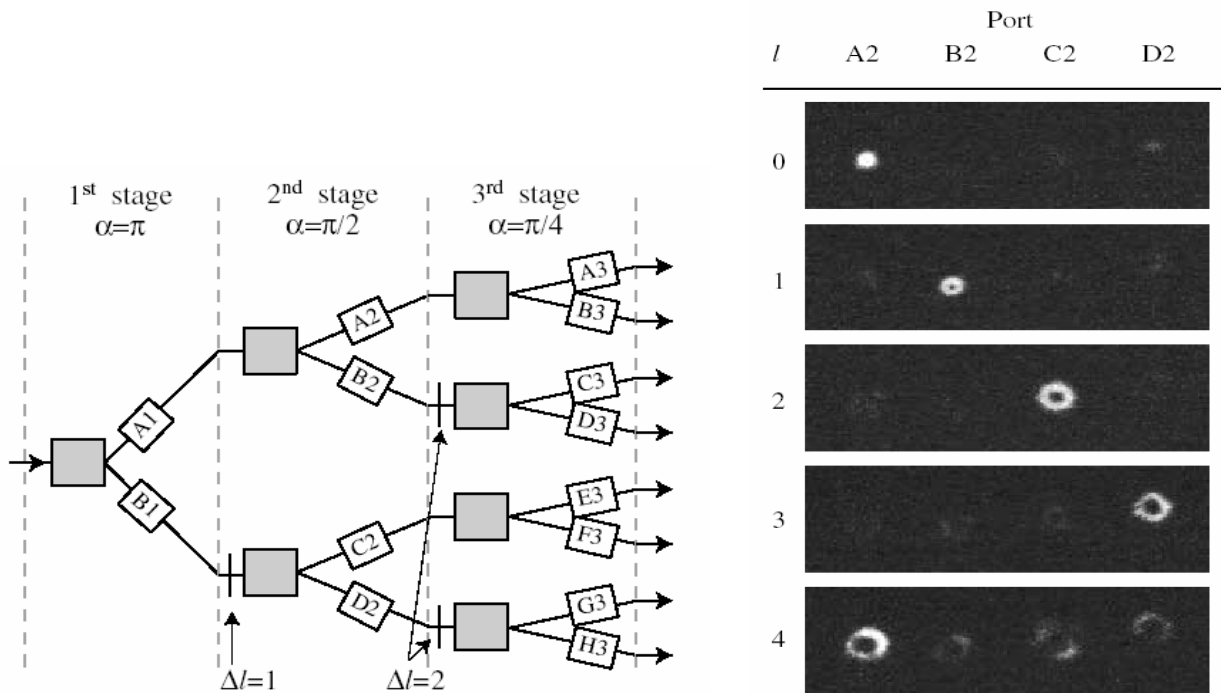


**Fig.2.36.** Another technique used to determine POAMs is to use a cascade of phase rotators to build the spectrum of all the different components of  $\ell$  present in a pencil of light. Here is reported the results of a 2-stage sorting scheme. The four ports correspond to modes with the values  $\ell = 0,1,2,3$ , resp. (Leach et al. 2002)

Since, in the laboratory, photons can now be prepared with  $\ell$  up to the order of 300, it implies that single photons may carry [at least] 8 bits of information, of considerable interest for quantum computing, and a main reason for the current interest in these phenomena. Of course, in an astronomical context, the question arises whether, and in which astronomical sources photons with such properties might be produced?

Light from astronomical sources can also be manipulated at the telescope. Interference of light with orbital angular momentum produces a dark spot on the optical axis (irrespective of how tightly it is focused), but normal intensities outside. By suitable manipulation of starlight, one might induce different amounts of angular momentum to light from the central star, relative to its nearby exoplanet, thus enhancing the observable contrast by several orders of magnitude. In a sense, such light may thus act as its own coronagraph. In the first experimental setup at the telescope recently tested Tamburini et al. (2005), used a holographic element with a single edge dislocation, also called a fork-hologram grating to generate OAM in the light and remove the light emitted from the central bright star. This results in a screw phase dislocation on the beam axis that gives us the characteristic phase structure of these beams with an azimuthal index of  $\ell$ .

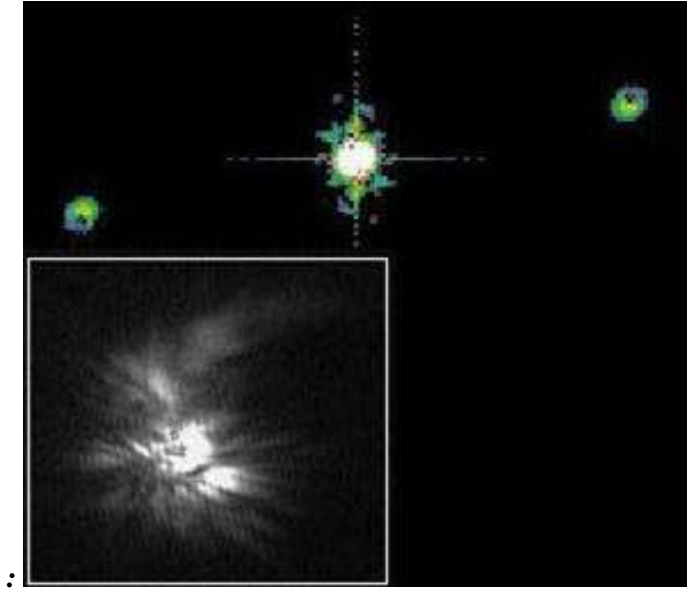


**Fig.2.37.** First tests at the telescope with light from stars: the collimated light from Arcturus (inset below) and the collimation test with the L-G modes obtained from a FFT transform of the hologram image after spatial filtering of the light to obtain an optical vortex with the light from Arcturus, taken at the Asiago 122-cm telescope.

In the laboratory, photons with non-null orbital angular momentum are produced in laser cavities. This could happen also in astrophysical sources where laser and maser processes are present. In the optical band, for example, laser modes with well-defined POAM might be produced in systems like Eta Carinae. Astronomical observations illustrate the existence of large density inhomogeneities in the interstellar medium on small scales closeby maser and laser sources. Interstellar and circumstellar masers tend to be associated with shocked domains. These peculiar clumpy associations of matter can originate particular cavity modes which can characterize the POAM of the emitted photons.

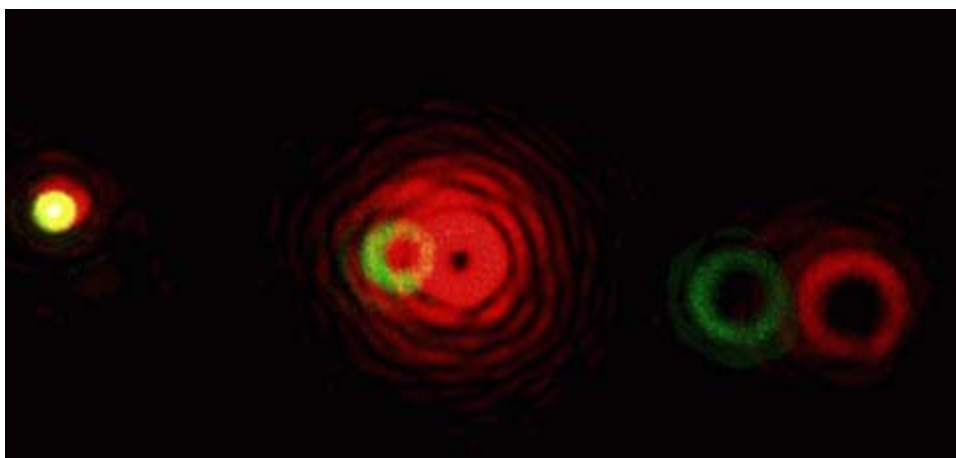


**Fig.2.38.** Cavity modes of a green (546 nm) and red (632 nm) laser sources. From the left POAMs  $\ell = 0$ ,  $\ell = 1$ , and  $\ell = 2$ .

In addition to the creation “in situ” of photons with non-null POAM, photons traveling to the Earth may cross regions of interstellar material that may well have discontinuities, impressing POAM on transmitted electromagnetic waves. These effects can be sizeable because the refractive index  $n$  of the interstellar medium is substantial.

The radiation emitted by luminous pulsars and quasars may also encounter density discontinuities in traversing the immediate surroundings of these respective sources which can act as a fork hologram.

Transfer of POAM by Kerr black holes: The transfer of angular momentum of a relativistic rotating body to single photons with a change of POAM to each single light quanta has not been discussed in detail; since now no significant works have been written in this subject. Following Harwit, a sort of Lense-Thirring effect due to spacetime dragging, could impose additional orbital angular momentum to the photons emitted in or crossing regions located in the ergosphere of a Kerr-Newman black hole. Teukolsky first looked in detail at the interaction of electromagnetic radiation with Kerr black holes. Mashoon (1973) soon thereafter pointed out that electromagnetic radiation scattered off black holes would absorb some of the hole’s angular momentum. More recently Falcke, Melia & Agol (2000) have discussed observations to detect the shape of a dark shadow in the immediate vicinity of a rapidly rotating black hole.

Angular momentum transfer from a Kerr black hole might be expected to induce a helical form on an incident wave, just as produced by a holographic or spiral phase plate, except that the angle would be independent of wavelength.

Another introduction to the light's orbital angular momentum is by Padgett et al. (2004). A general discussion of the astronomical potential of light with OAM is by Falcke et al (2000); Harwit (2003), Mashoon (1973), Tamburini et al. (2005), and Teukolsky (1972). For a discussion of high-contrast imaging using such light, see Swartzlander (2001), and for a discussion of means for detecting photons with different OAM, see Leach et al. (2002).

## **2.5. Quantum Gravity Effects?**

One may also consider studying the possibility of identifying the interactions between gravitation and photon quantum states.

Special relativity asserts that physical phenomena appear the same for all inertially moving observers. This symmetry, called Lorentz symmetry, relates long wavelengths to short ones: if the symmetry is exact it implies that spacetime must look the same at all length scales. Several approaches to quantum gravity, however, suggest that there may be a Lorentz violating microscopic structure of spacetime, for example discreteness, non-commutativity, or extra dimensions. One might be able to determine in more detail the strong constraints on Lorentz violations in the production of a maximum electron speed less than the speed of light with Crab nebula (Jacobson et al. 2004). Currently there isn’t any effective quantum theory of gravity which could provide exact parameters to observe.

The preliminary stage would consist on a theoretical approach aimed to identify possible effects of quantum gravity in the light traveling from very far objects at cosmological

distances. We would like to determine, or put a better limit on, the cumulative effects of Planck-scale phenomenology on light propagation by observing distant supernovae. These quantum gravity effects may cause a loss of phase of radiation emitted at large distances from the observer. When adaptive optics is working we could also analyze quantum gravity effects in very distant objects, which would be affected by a blurring effect on their PSFs. What is of interest for us is the so-called distance fuzziness effect. If spacetime is coarse-grained, as supposed from Planck-scale physics, a pencil of light would be blurred after a journey in spite of the small size of Planck scale. Coarse-grained spacetimes will give a natural error in metrology and in wavefront propagation. Recently several authors pointed out that the systematic accumulation of such effects during the long journey of a photon propagating through a spacetime could lead to observable consequences. Practically a distant observer could see this effect by analyzing the point spread function (PSF) of very distant pointlike sources such as supernovae.



### **3. Observational High-Speed Astrophysics**

Since the advent of high-speed astronomical instrumentation, numerous discoveries and studies have been made with resolutions of seconds and milliseconds. The topics include optical and X-ray pulsars; lunar and planetary-ring occultations; rotation of cometary nuclei; cataclysmic variable stars; pulsating white dwarfs; flickering high-luminosity stars; X-ray binaries; accretion-disk instabilities; gamma-ray burst afterglows, and many more. A standard textbook on the subject is: "*High speed astronomical photometry*" by Brian Warner (1988). Appendix 3 below surveys current and recent high-speed instrumentation worldwide, also giving numerous samples of astrophysical objects and processes that are being studied with that very instrumentation.

#### **3.1. Examples of High-Speed Phenomena**

It is far outside the scope of this instrumentation study to survey all the astrophysical issues or problems that can be studied with high-speed instrumentation. However, as a few examples of different classes of relevant problems, in this Section we describe some current issues in a few such subfields: the study of rapid variability in compact binaries; the detection of exoplanets near their parent star; and the study of distant solar-system objects.

##### **3.1.1. Time domain and reprocessing:**

###### **High-frequency phenomena in optical and infrared**

The performance achievable with OWL can open new scenarios in the time-domain window. High energy astrophysics, the physics of binary systems, the physics of compact objects such as neutron stars and black holes and plasma astrophysics are likely to be driven into a new perspective.

Together with OWL, this challenge will require as a fundamental tool a new generation of detectors developed with the aim of characterizing the quantum-mechanical properties of the light emitted by a celestial source by counting, analyzing and giving evidence to photon correlation statistics and their distribution in the space, time and energy domains. The information encrypted in light, needed to understand high-energy phenomena, is in fact much more extensive than the intensity or polarization only. The use of quantum techniques makes possible the analysis of the decoherence of the information contained in a pencil of light due to the environment in which the source is embedded. The information is the correlation in the photon bunching. This will give new, crucial information about the physical characteristics of the surrounding medium.

For example, the micro-to-nanosecond time scale of the photon emission fluctuations obtained in the high-energy window are compared with those obtained in the optical band of a pulsar embedded in a nebula to obtain information about the nebula itself (Gil 1985). Common envelopes of binary systems or electron gas trapped in the magnetosphere of a compact object are another example. OWL performances will allow astronomers to obtain enough information to correlate tiny and fast luminosity variations in optical and IR band with those observed in the X-rays.

Previous experimental results are quite encouraging and show that OWL could give a real contribution in the investigation of rapidly variable astrophysical phenomena, such as non-thermal ultrafast phenomena and reprocessed thermal fast phenomena.

In addition to ultrafast photometry, OWL could finally make possible the analysis of multi-photon correlation in astrophysical sources. Fast astrophysical phenomena have been detected mainly in the X- or gamma-ray bands. The first millisecond X-ray variability phenomena from accreting compact objects were discovered with the Rossi X-ray Timing Explorer. In X-ray binaries (XRBs) the material transferred from the donor star falls inspiralling around the central compact object and is heated up at very high temperatures, emitting X-rays. XRBs are close binaries that contain a relatively un-evolved donor star and a neutron star or black hole that is thought to be accreting material through Roche-lobe overflow. Material passing through the inner Lagrangian point moves along a ballistic trajectory until impacting onto the outer regions of an accretion disk. This material spirals through the disk, losing angular momentum, until it accretes onto the central compact object. X-rays are emitted from inner disk regions via thermal bremsstrahlung with an effective temperature of  $10^7$ - $10^8$  K. The X-ray flux depends on the mass transfer rate, which in turn depends on the structure of the disk and its ability to transport angular momentum. In XRBs the structure of the accretion disc is significantly affected by irradiation.

The closer the gas is to the central object, the higher is its temperature and usually the fastest is its time variability. This is the reason why the fastest astrophysical phenomena have been mostly observed in the X-ray window. Three typical signatures are observed from low-mass X-ray binaries containing low-magnetic-field neutron stars: millisecond pulsations, burst oscillations and kiloHertz quasi-periodic oscillations. Models for these new phenomena involve the neutron star spin and orbital motion closely around the neutron star and rely explicitly on our understanding of strong gravity and dense matter.

OWL will operate in the wavelength range of 0.32-12  $\mu\text{m}$ . Most of the optical and IR light in XRBs is thought to arise in regions surrounding the central source through the reprocessing of the X-rays. Reprocessing of X-rays into optical and infrared photons occurs in the accretion streams and at the surface of the companion star. The hard X-ray photons can penetrate below the photosphere and be thermalized, rising the temperature of the optically emitting gas, whereas the soft X-ray photons are responsible for the production of the observed emission line spectrum. In general, it is important to determine what is the limiting timescale above which reprocessing may leave some tiny traces of the variability observed in the X-ray flux also in the optical and IR reprocessed light, preserving the initial photon statistics like bunching, antibunching and high-order correlations. In some cases the fast variability, observed at high energies, has been seen to induce also a variability in the reprocessed signal, showing characteristic time delays with respect to the X-ray variations (caused by the light-time travel between the X-ray source and the illuminated spots where reprocessing takes place). The light travel times arise from the time of flight differences for photons that are observed directly and those that are reprocessed and re-emitted before traveling to the observer and depend on the geometry of the system.

Much of the optical emission in XRBs, and in particular in Low Mass X-ray Binaries, arises from reprocessing of X-rays by material at some distance from the central compact object. The disk is highly ionized and out-shines the donor star. Light travel times within the system are of the order of 10 seconds. The dynamical timescales in the accretion discs in interacting X-ray binaries span the interval from minutes to milliseconds as the gas spirals inwards. Fluctuations on short dynamical timescales (sub-second timescale) have been observed in X-rays by some satellites. The shortest variability observed is of the order of 0.1-1 ms, supposed to be the characteristic time for gas moving close to a 10 km neutron star. An example is the  $\sim 1100$  Hz quasi-periodic oscillation discovered in Sco X-1 by Van der Klis et al. (1996).

Optical variability may thus be delayed in time relative to the X-ray driving variability by an amount characteristic of the position of the reprocessing region in the binary and the geometry



of the binary. The optical emission may be modeled as a convolution of the lightcurve of the X-ray emission with a time-delay transfer function.

This time delay is the basis of an indirect imaging technique, known as echo tomography (reverberation mapping), to probe the structure of accretion flows on scales that cannot be imaged directly, even with current interferometric techniques. Echo mapping has already been developed to interpret lightcurves of Active Galactic Nuclei (AGN), where time delays are used to resolve photoionized emission-line regions near the compact variable source of ionizing radiation in the nucleus (e.g., Horne et al. 2004).

In AGN the timescale of detectable variations is days to weeks, giving a resolution in the transfer functions of 1-10 light days. In XRBs the binary separation is c.a. light seconds rather than light days, requiring high-speed optical and X-ray lightcurves to probe the components of the binary in detail. The detectable X-ray and optical variations in the lightcurves of such systems are also suitably fast.

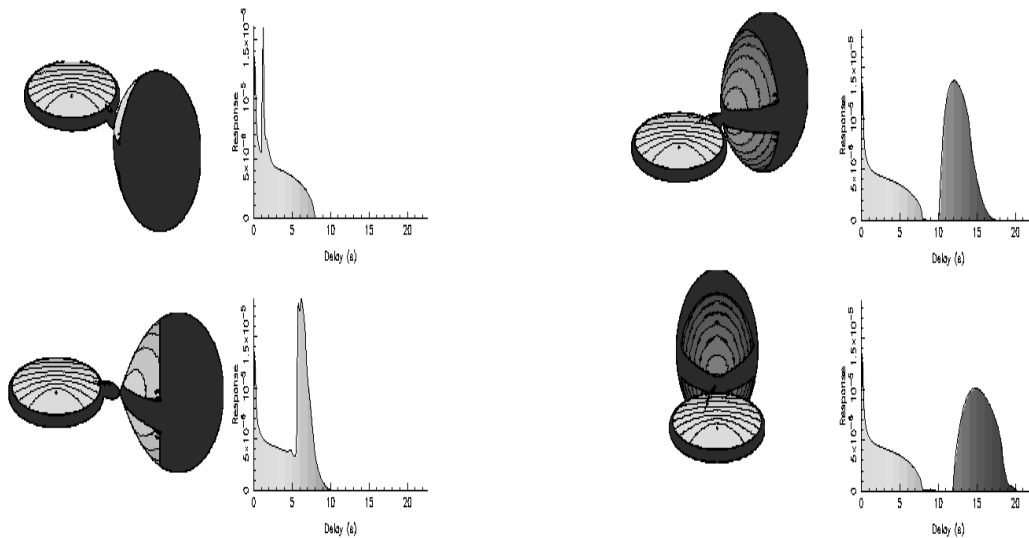


**Fig.3.1.** Model of an X-ray binary, based on typical binary parameters for a LMXB. Iso-delay surfaces projected onto the irradiated surfaces of the binary are shown. Right, the associated time delay transfer functions, showing the relative contributions from the regions highlighted in the model X-ray binaries. (O'Brien et al. 2002). Here the geometry plays an important role in the time delay due to the flight time of photons.

Optical emission from X-ray binaries with low mass companion stars (Low Mass X-ray Binaries, LMXBs) is in general dominated by the reprocessing of the X-rays in the accretion disk and/or the donor star (e.g. Van Paradjis & McClintock 1995; Chakrabarty 1998). Evidence for reprocessing of X-rays in LMXBs has been found from the detection of quasi periodic oscillations in the range 0.001-10 Hz in both the optical and X-ray bands (e.g. GX 339-4, Motch et al. 1983), the correlated X-ray and optical outbursts in X-ray bursters (Lewin, van Paradjis & Taam 1993) and the coherent optical pulsations (0.1-10 s) detected in some LMXB pulsars (Her X-1, 4U 1626-67, GX 1+4; see Figure 3.2). In these objects the optical light curve results from a convolution of the X-ray light curve with a function representing the spatial distribution of matter in the system (response function). The reprocessed optical signal is delayed and smeared out with respect to the incident X-ray signal (e.g. Pedersen et al. 1982; O'brien et al. 2002). Besides the geometrical delay/smearing time  $t_{\text{geom}}$  there is also an additional physical delay/smearing time  $t_{\text{tran}}$  associated to radiative transport effects (time

that a X-ray photon takes to be absorbed and re-emitted as an optical photon in the reprocessing medium). Typical values of the geometrical and physical delay/smearing times are

$$t_{\text{geom}} \sim r_{\text{repr}}/c \sim 0.1\text{-}10 \text{ s}$$

$$t_{\text{tran}} \sim N l /c < 0.5 \text{ s}$$

where  $r_{\text{repr}}$  is the characteristic size of the reprocessing site ( $10^{10}\text{-}10^{12}$  cm; outer accretion disk, surface of the companion star), and  $l$  and  $N$  are the photon mean free path and the average number of path lengths traversed by a photon before emerging from the reprocessing medium (the time to absorb the incident X-ray photon is typically smaller; see e.g. Pedersen et al. 1982). The X-ray irradiation causes also X-ray heating of the reprocessing medium, thereby increasing the temperature of the optically emitting gas (e.g. Chakrabarty 1998; Frank et al. 2002). If X-ray photons are thermalized, an X-ray heated star with (unirradiated) effective temperature  $T_{\text{eff}}$  will have a temperature

$$T_{\text{irr}} = [T_{\text{eff}}^4 + L_X(1-A)/4\pi r^2]^{1/4}$$

where  $L_X$  is the X-ray luminosity of the central source,  $A$  the albedo and  $r$  the distance between the star and the X-ray source. Thus, optical emission occurs at the X-ray heated temperature  $T_{\text{irr}}$ . Because of the large geometrical/physical smearing times, the traces of X-ray rapid variability (above  $\sim 10\text{-}100$  Hz) in the reprocessed optical emission of LMXBs are essentially washed out. An early search for large amplitude high frequency phenomena in some X-ray binaries was carried out by the MANIA collaboration, obtaining 15-20% upper limits on the relative variability strength of  $10^{-3}\text{-}10^{-2}$  s oscillations (Beskin et al. 1979; Shvartsman, Beskin & Pustil'nik 1989; Shvartsman et al. 1989). In particular, a cut-off in the optical variability of the LMXB Cygnus X-2 was observed at a timescale  $t_{\text{min}} \sim 10\text{-}30$  s (Beskin et al. 1979).

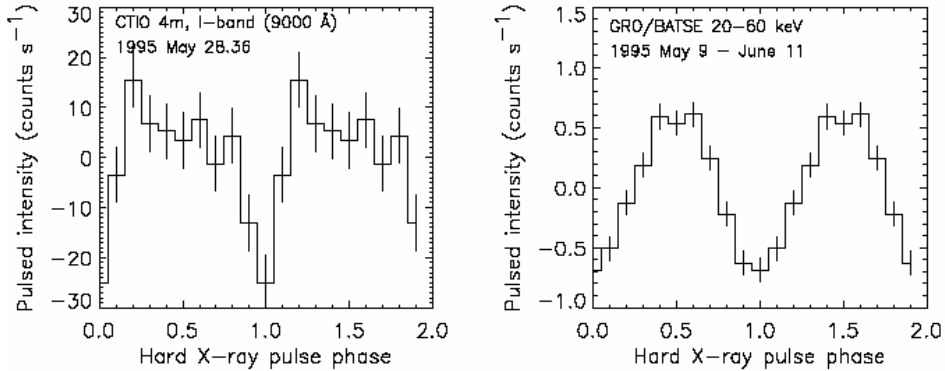


**Fig.3.2.** Pulse profiles in the I and X-ray (20-60 keV) bands as a function of X-ray pulse phase for the LMXB pulsar 4U 1626-67 (from Chakrabarty 1998). A coherent pulsation at 7.67 s is detected in both bands, caused by rotation of the highly magnetized accreting neutron star. The optical pulsation can be understood as a reprocessing of the pulsed X-ray emission in the accretion disk.

At lower frequencies, typically in the mHz regime, fluctuations in the X-ray and optical light appear to be related. An example is the case of the Soft X-ray Transient and Black Hole Candidate GRO J1655-40. O'Brien et al. (2002) analyzed this process by using a transfer function which describes the difference in light travel time (time delay), due to the difference in path lengths, between the X-ray source and the reprocessing regions in the binary. The optical variability lags the X-ray variability with a mean time delay of  $19.3 \pm 2.2$  sec, showing

that the outer regions of the accretion disc are the dominant reprocessing site in this system. This correlation is lost during outburst. In fact, according to recent reprocessing models, the disc at maximum is so thick that the outer disc and companion star are not irradiated efficiently. The observed disk thickening has the effect of almost entirely shielding the companion star from irradiation at this stage of the outburst. Therefore, high flickering and possible correlation between optical/X-ray due to reprocessing may be damped by the thick outer disc.

A final comment on X-ray reflection is made. At first instance, the surface of the accretion disk can be modeled as a semi-infinite slab of uniform density gas, irradiated from above by a continuum X-ray spectrum produced in the disk corona via thermal Comptonization. The hydrogen and helium are fully ionized, but all metals are neutral. This is a crude approximation to the situation found in a “cold” AGN accretion disk. An incident X-ray photon can be Compton scattered by the free-electrons mainly from HII and HeIII. The photon can be photoelectrically absorbed by one of the neutral atoms with different photoionization processes (for a recent up-to-date calculation of the full radiative coupling in two-phase models of accreting black holes see, e.g., Malzac et al. 2005).

If the spectrum is emitted from an accretion disk close to a black hole, we should also consider the effects on the reflected X-ray spectrum of distortions due to relativistic effects, namely the Doppler effect, relativistic aberration, and gravitational light-bending/red-shift. The reprocessing of soft X-ray emission lines in black-hole accretion disks has been studied by means of Monte Carlo codes accounting for Compton scattering and photoabsorption followed by recombination. Mauche et al. (2004) investigated the radiation transfer of Ly-alpha, He-alpha, and recombination continua photons of H- and He-like C, N, O, and Ne produced in the photoionized atmosphere of a relativistic black hole accretion disk.

### 3.1.2. Galactic X-ray binaries

Rapid variability in High Mass X-ray Binaries: Jernigan et al. (2000) report the discovery of kilohertz fluctuations, including quasiperiodic oscillations (QPOs) at  $\sim 330$  Hz (260-407 Hz) and  $\sim 760$  Hz (671-849 Hz) and a broadband kilohertz continuum in the power-density spectrum of the high-mass X-ray binary pulsar Centaurus X-3. These observations of Cen X-3 were carried out with the Rossi X-Ray Timing Explorer (RXTE). The fluctuation spectrum is flat from millihertz to a few hertz, and then steepens to an  $f^2$  behavior between a few hertz and  $\sim 100$  Hz. Above 100 Hz, the spectrum shows the QPO features, plus a flat continuum extending to  $\sim 1200$  Hz and then falling out to  $\sim 1800$  Hz. These results required co-adding three days of observations of Cen X-3.

Multidimensional radiation hydrodynamics simulations of optically thick plasma flow onto the magnetic poles of an accreting neutron star show that the fluctuations at frequencies above 100 Hz are consistent with photon bubble turbulence and oscillations (PBOs) previously predicted to be observable in this source.

Rapid variability in Low Mass X-ray Binaries: The rapid (100-1000 Hz) variability phenomena observed in Low Mass X-ray Binaries are essentially of five types: (i) kHz quasi periodic oscillations (QPOs) in neutron star (NS) binaries, representing the fastest variability observed in X-ray binaries; (ii) Hectohertz QPOs in NS binaries; (iii) High Frequency QPOs in black hole (BH) binaries; (iv) ms oscillations in the persistent emission of accretion-powered pulsars; (v) ms oscillations during Type I X-ray bursts in NS binaries. For a recent and complete review on rapid variability phenomena in X-ray binaries we refer to van der Klis (2006). The last two types of QPOs range between 200 and 400 Hz and provide a direct measurement of the angular velocity of the NS.

- kHz QPOs (e.g. van der Klis et al. 1996) are observed in the two types of known low magnetic field, low mass X-ray binaries (LMXBs) containing NSs, the so called *Z sources* (presumably accreting close to the Eddington limit) and the *atoll sources* (weaker luminosity objects). These QPOs manifest a rather rich phenomenology. Two peaks (usually referred to as the upper and lower kHz QPOs,  $\nu_u$  and  $\nu_l$ ) occur in the power density spectrum of the X-ray flux and move up and down in frequency together in the 200-1200 Hz range, in correlation with the source spectral state. The several 100-Hz peak separation  $\Delta\nu = \nu_u - \nu_l$  is typically within 20% of the NS spin frequency, or half that, depending on source, and usually decreases by a few tens of Hz when both peaks move up by hundreds of Hz.
- NS hectohertz QPOs (e.g. Ford & van der Klis 1998) are observed only in *atoll sources* in most spectral states with a frequency  $\nu_{\text{hHz}}=100\text{-}200$  Hz. As mentioned above, their frequency is approximately constant (and quite similar across sources).
- BH high frequency QPOs are the fastest variability observed in BH binaries (Remillard et al. 1999) and are observed in well defined transitional states. As for the NS Hectohertz QPOs their frequency is approximately constant. The frequencies of these QPOs  $\nu_{\text{BHF}}$  range from 100 to 450 Hz, and sometimes harmonically related frequencies have also been seen.
- ms pulsars are NSs that are thought to have been spun up by mass accretion from a stellar companion (Chakrabarty et al. 2003). A total of 11 such objects have been identified, including SAX J1808.4-3658, the first accreting ms pulsar to be discovered (Wijnands & van der Klis 1998). Coherent pulsations are detected with a frequency in the range 270-619 Hz, produced by rotational modulation of the NS emission. They provide a direct measurement of the NS spin frequency. Bursts of periodic or quasi periodic variability are also observed in these sources (Wijnands et al. 2003).
- ms oscillations during Type I X-ray bursts are transient phenomena observed in 10 LMXBs only during the short (1-10 s) duration of a burst (e.g. Strohmayer et al. 1996). Chakrabarty et al. (2003) firmly established burst oscillations as nuclear-powered pulsations tracing the spin of accreting NSs, corroborating earlier evidence. The frequency range of these oscillations is indeed between 300 and 600 Hz.

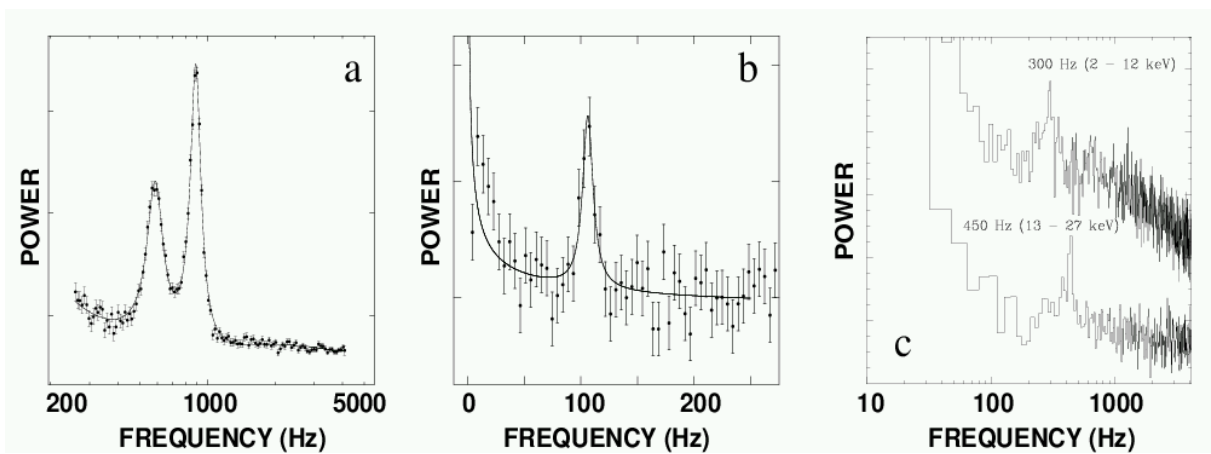


**Fig.3.3.** (a) Twin kHz QPOs in the LMXB Sco X-1 (van der Klis et al. 1997). (b) Hectohertz QPO in the LMXB 4U 0614+09. (c) High frequency QPO in the BH binary GRO J1655-40 (Strohmayer 2001). Figure from van der Klis (2006)

In the following we will focus on the first three types of oscillations, observed during the persistent emission in NS or BH systems. Examples of power spectra showing these three types of QPOs are shown in Figure 3.3.

Different interpretations of the characteristic frequencies of the rapid variability observed in Low Mass X-ray Binaries are present in literature (see e.g. the beat-frequency model for kHz QPOs: Miller et al. 1998; the relativistic precession model for kHz QPOs: Stella & Vietri 1998, Stella et al. 1999; the model of discoseismic oscillations of the accretion disk for NS-hectohertz QPOs and BH-high frequency QPOs: Kato et al. 1998, Titarchuk et al. 1999; the relativistic resonance model for NS-Hectohertz QPOs and BH-high frequency QPOs: Abramowicz & Klu'zniak 2001). All the models for kHz QPOs involve plasma motion in the strong field region around a NS and in nearly all of them the QPOs originate in the accretion disk.

In most models, one of the characteristic frequencies (usually the highest frequency of the system, e.g. the upper kHz QPO  $\nu_u$  in NS systems) is identified with the Keplerian frequency  $\nu_K$  at some preferred radius in the disk  $r_K$ . In Schwarzschild spacetime, it is

$$\begin{aligned} \nu_K &= (1/2\pi)(GM/r_K^3)^{1/2} \sim 1200 \text{ Hz } (r_K/15 \text{ km})^{-3/2} (M/1.4 M_\odot)^{1/2} \\ &\sim 200 \text{ Hz } (r_K/90 \text{ km})^{-3/2} (M/10 M_\odot)^{1/2}. \end{aligned}$$

Modulation of radiation produced by matter moving near to the central compact object is then expected to produce oscillations in the observed flux in the ms range, consistent with what is observed. Besides azimuthal motion, matter moving around the central compact object may undergo small radial and vertical displacements resulting in a corresponding radial/vertical oscillation. In strong field gravity, in general, the radial and vertical epicyclic frequencies  $\nu_r$  and  $\nu_\theta$  associated to these motions are different from the azimuthal (Keplerian) frequency. Because of this, the periastron and nodal line of the orbit advance at the characteristic frequencies  $\nu_p = \nu_K - \nu_r$  and  $\nu_n = \nu_K - \nu_\theta$ . In principle, all these frequencies may give rise to detectable features in the power spectrum of X-ray binaries (e.g. Stella & Vietri 1998), although the mechanism through which this might occur is unknown.

One may think to use rapid variability in X-ray binaries to probe strong field effects in General Relativity (GR). One of the most definite predictions of GR is that, for sufficiently compact objects, there exists an innermost stable circular orbit (ISCO) below which stable circular motion is no longer possible. In Schwarzschild spacetime

$$\begin{aligned} r_{\text{ISCO}} &= 6 GM/c^2 \sim 12.5 \text{ km } (M/1.4 M_\odot) \\ &\sim 90 \text{ km } (M/10 M_\odot). \end{aligned}$$

An apparent leveling off of the upper kHz QPO frequency  $\nu_u$  as a function of count rate, flux or other indicator of the accretion rate may signal that matter has reached the ISCO. From this one may also derive a direct measurement of the mass of the compact object. Although evidences of this kind have been reported (see e.g. Zhang et al. 1998), none of them is conclusive. From the assumption that at least one of the observed QPOs is the signature of matter moving in Keplerian motion in a strong gravitational field, one can also derive important limits on the radius-mass diagram of the accreting NS in these systems (Miller, Lamb & Psaltis 1998). Taking into account the detailed structure of the NS and spacetime around it (Morsink & Stella 1999, Markovic' 2000), it is possible to derive accurate constraints on the allowable equations of state of matter at supra-nuclear density.

### ***High-frequency phenomena in the optical band?***

The characteristic temperature of radiation emitted by matter in the vicinity of a NS or a BH falls in 0.1-100 keV range and hence the X-ray band remains the privileged band for studying rapid variability in these systems. However, it is important to explore any possibility that might exist to observe high frequency phenomena in X-ray binaries in the optical domain, especially considering the unprecedented opportunity offered by the extremely large collecting area of OWL and the availability of a dedicated timing instrument. Clearly, the possibility of exploring the characteristic frequencies of matter moving in the vicinity of NSs and BHs with OWL is not in competition with any possible X-ray timing mission, because the X-ray band is the natural window for observing these systems. However, optical measurements might allow us to supplement the information derived from X-ray observations, with the huge advantage of not having to confront with the typical restrictions (exposure time, mission duration) imposed by space missions.

A crucial issue to address is the way in which high frequency phenomena at optical wavelengths, including QPOs, might be produced. Although, in general, this depends on the specific model (and emission mechanism) assumed to produce them, some general arguments about the sensitivity to QPOs of these types may be given. We note that looking for QPOs above 1 kHz in the X-ray *reprocessed* emission is ruled out because of the geometrical/physical smearing taking place in the reprocessing site (outer accretion disk, surface of the companion star), which has a typical size of  $10^{10}$ - $10^{12}$  cm. A search for large amplitude rapid variability in some X-ray binaries was carried out by the MANIA collaboration with the 6 m telescope, however only obtaining 15-20% upper limits on the relative variability strength of  $10^{-3}$ - $10^{-2}$  s oscillations (Beskin et al. 1979; Shvartsman et al. 1989ab).

Of course, there may be many phenomena in low-mass X-ray binaries where the optical emission has a different origin than the reprocessing of X-rays. One example is in Figure A3.20 below, where the optical variability in the black-hole candidate XTE J1118+480 turned out to be more rapid than the fluctuations in X-rays, showing that its origin cannot be the reprocessing of the latter.

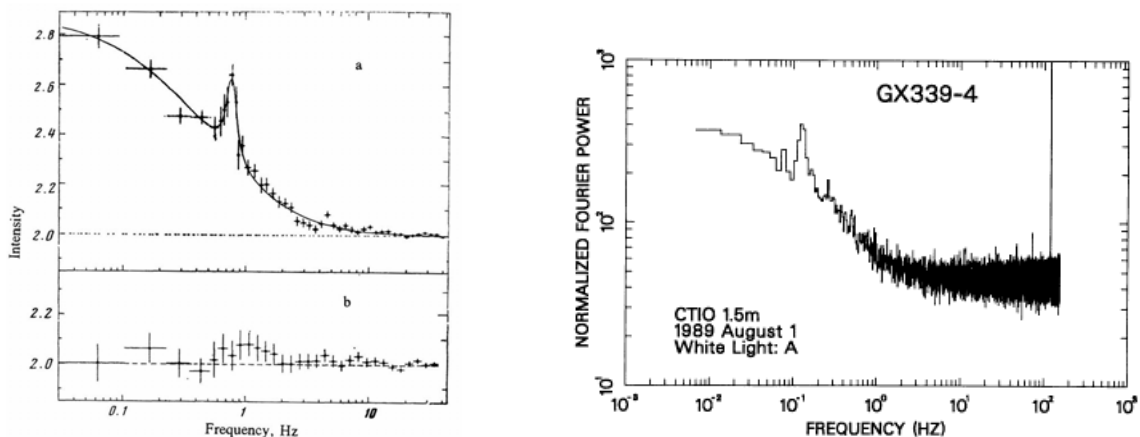


**Fig.3.4.** *Quasi-periodic oscillations in the low-mass X-ray binary GX339-4, observed in both X-rays and in the optical. Left: Two different activity states at different epochs, observed in 3-25 keV X-rays from GRANAT (Grebenev et al. 1991). Right: The same source in white-light optical (Imamura et al. 1990). Already with a photon-count rate of only some 500 Hz, obtained with a PMT photometer on a 1.5 m telescope at an epoch when the source was faint ( $m_v = 17.7$ ), the 8 second quasi-periodic oscillations of width 0.03 Hz stand out clearly after a 2-hour integration. The count rate with QuantEYE will be 10,000 times greater, increasing the Fourier power a factor of  $10^8$ ! Other optical observations of this black-hole candidate have indicated periodicities down to 1.13 milliseconds (Imamura et al. 1987).*

We have performed a preliminary calculation on the possibility of detecting a QPO in the Rayleigh-Jeans tail of the thermal emission from the innermost part of the accretion disk. For a QPO with a root mean square (rms) amplitude of  $\sim 15\%$  in the X-ray band and the typical parameters of a high/low luminosity LMXB, we find that the corresponding rms in the optical band would be  $10^{-6}$ - $10^{-5}$  (taking into account the optical emission of the donor star and that of an irradiated accretion disk). In order to have an  $n = 3\sigma$  detection of such a QPO (rms  $r \sim 10^{-5}$ , width  $\Delta\nu \sim 100$  Hz) with a reasonable exposure time  $T \sim 10^5$  s, the required net source count rate is  $S = 2 n r^2 (\Delta\nu/T)^{1/2} \sim 6 \times 10^9$  counts  $s^{-1}$  (neglecting the background). For an instrument like OWL, with an effective collecting area  $A \sim 100$  m<sup>2</sup>, this count rate corresponds to  $m_v \sim 13$ , consistent with the apparent magnitude of bright Galactic X-ray binaries.

### 3.1.3. Finding exoplanets through dark speckles

Labeyrie (1995) and Boccaletti et al. (1998) have expounded a method to image exo-planets with a large telescope equipped with a good adaptive optics system, through ‘dark-speckle’ coronagraphy. This method therefore is a combination of speckle interferometry and adaptive optics.

The method exploits the light cancellation effect occurring in random coherent fields according to the Bose-Einstein statistics. Although adaptive optics can reconstruct the Airy peak, and possibly the first few rings in the focal plane image of a bright star, the degree of correction cannot be good enough to remove the fluctuating speckles in the surrounding zone of the Airy pattern.

Destructive interference in the stellar light occasionally causes a dark speckle to appear here and there; however, at the position of the planet’s own faint Airy peak, the darkening cannot be as deep as in the generic position. Adaptive optics indeed will keep the peak of the planet Airy disk at a fairly constant intensity. A strategy for detecting exo-planets thus consists in mapping the occurrence of speckles darker than a given threshold intensity corresponding to the planet’s intensity: the exo-planet would emerge as a bright spot from a much darker surrounding.

An ideal detecting system would consist of a multi-pixel fast photon counting camera, with spatial resolution comparable to the dark spots (much smaller than the speckle size, say  $10 \times 10$  px per speckle) and temporal resolution better than the lifetime of the speckle, say 1 ms.

A monochromatic system would be desirable, because otherwise the speckles are smeared by the chromatism of the system. In addition to the obvious solution of acquiring a series of monochromatic exposures, there are other possible solutions, e.g. by using a Wynne chromatic lens providing a dispersion inversely proportional to the wavelength, followed by a field grating producing a dozen or so of almost monochromatic speckles. But this is only an example.

Boccaletti et al. (1998) provide an expression for the S/N ratio (SNR) slightly different (and 50% more conservative) from the original one given by Labeyrie (1995). The total exposure time  $T$  needed to achieve a given SNR can be expressed as:

$$\text{SNR} = \frac{N_*}{R} \sqrt{\frac{\tau_c T}{j + \frac{\tau_c N_*}{G}}}$$

where:

$N_*$  = number of detected photons per second

$R$  = ratio star/planet brightness (typically  $10^9$ )

$G$  = gain of the adaptive optics (the ratio of the Airy peak to the halo of speckles, typically  $10^6$ , so that  $R/G = 10^3$ )

$\tau_c$  = sampling time (e.g. 1 ms)

$j$  = number of px per speckle

A detailed analysis shows that  $j$  must obey the following optimal relation:

$$j = \frac{(\lambda/D)^2}{s^2} = \frac{(\lambda/D)^2}{1.27^2 \varepsilon (\lambda/D)^2} = 0.62 \frac{R}{G}$$

where:

$s$  = the size of the pixel over which the light is integrated,  $s \approx 1.27\sqrt{\varepsilon} \frac{\lambda}{D}$

$\varepsilon$  = threshold of detection,  $\varepsilon \approx G/R$ .

Therefore:

$$T = \left( \frac{\text{SNR}}{N_*} \right)^2 \frac{R}{G} \frac{1}{\tau_c} (0.62R^2 + \tau_c N_* R)$$

*Example:* system parameters:  $R = 10^9$ ,  $D = 8$  m,  $G = 10^6$ ,  $\tau_c = 10$  ms,  $q_e = 0.2$ . To achieve  $\text{SNR} = 5$  for a  $V = 2.5$  mag star through a bandpass of 100 nm, an exposure time of 2.7 h is necessary. This value improves with the diameter, with the sampling time and with the square root of the quantum efficiency.

One has to notice the crucial parameters of the detector, which must have a high number of pixels, small dimension of the px size in comparison with the speckle size, and be extremely fast.

### 3.1.4. Occultations by the Moon, asteroids, and Kuiper-Belt objects

We present some considerations on geometrical and temporal characteristics and on the astrometrical and astrophysical information (size of the occulting body, limb darkening and even distance of the occulting stars) that OWL could derive from observing occultations by the Moon, main-belt asteroids and KBOs. The values of occultations is not only for providing ‘astrometric’ information (diameters, duplicity, etc., see for instance Schmidtke et al. 1989). Occultations can indeed be a powerful instrument for astrophysical considerations. For instance, Gies et. al. (1990) obtained low-resolution spectra with a time sampling rate of 7 ms of the H-alpha emission line in the spectrum of the Be star Pleione. See also Richichi (2004ab).

The Fresnel diffraction fringes produced by occultations have a typical length  $x$  and angle  $\psi$  given by:

$$x = \sqrt{\frac{\lambda d}{2}} \quad , \quad \psi = \sqrt{\frac{\lambda}{2d}}$$

where  $\lambda$  is the wavelength of the light and  $d$  is the distance Earth-screen.



<b>Moon</b>	0.5 $\mu\text{m}$	1.0 $\mu\text{m}$	5.0 $\mu\text{m}$	10.0 $\mu\text{m}$
$x$ (m)	10	14	32	45
$\psi$ (arcsec)	0".005	0".007	0".016	0".022
$\tau$ (sec)	0.012	0.017	0.038	0.053
<b>Main Belt Asteroids</b>				
$x$ (m)	273	383	857	1210
$\psi$ (arcsec)	0".00019	0".00027	0".00059	0".00084
$\tau$ (sec)	0.018	0.0256	0.058	0.081
<b>KBO</b>				
$x$ (m)	1220	1710	3833	5411
$\psi$ (arcsec)	0".000043	0".000060	0".00013	0".00018
$\tau$ (sec)	0.1776	0.216	0.39	0.512

**Table 3.1.** Fresnel fringe length, angular size and crossing times

Table 3.1 gives several values of  $x$ ,  $\psi$  and of the typical crossing time of a Fresnel fringe calculated for the Moon ( $d = 3.8 \times 10^5$  km, considering a typical velocity  $v = 0.9$  km/s), for bodies in the asteroidal main belt ( $d \sim 3 \times 10^8$  km,  $v \sim 15$  km/s), and for bodies in the Kuiper belt ( $d \sim 6 \times 10^9$  km,  $v \sim 25$  km/s), for five wavelengths spanning the OWL interval (0.5  $\mu\text{m}$ , 1  $\mu\text{m}$ , 5  $\mu\text{m}$ , 10  $\mu\text{m}$ ).

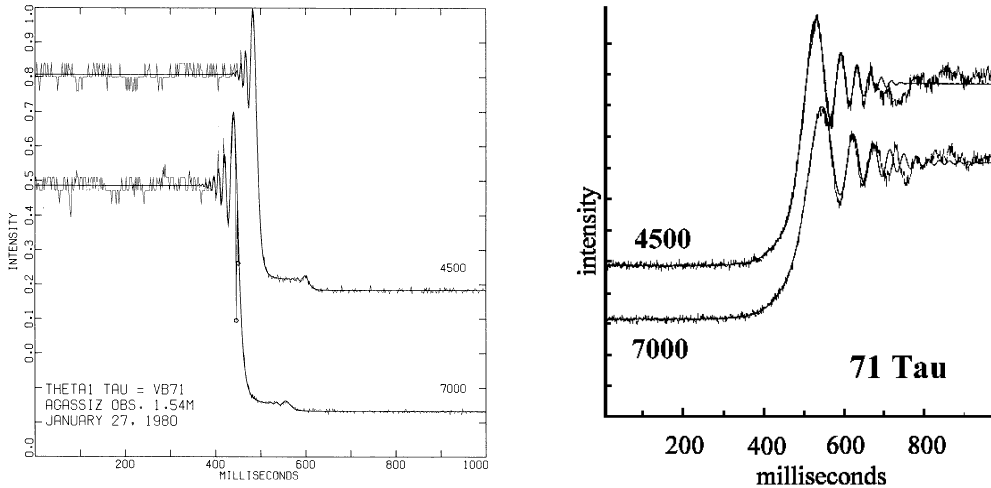


**Fig. 3.5.** Two examples of lunar occultations, left immersion, right emersion. The scale on the abscissa is in milliseconds. Notice the presence of fine details in the light curves that would warrant better time resolution.

Notice that the timescales of occultations are comparable for the three cases, from 0.01 to 0.5 seconds, requiring a resolution at least ten times better, but that for the Main Belt asteroids and for Kuiper-belt objects, OWL is always much smaller than the Fresnel scale length, even in visible light.

Therefore, at first sight, OWL is too large for the Moon, even in the far IR. The full aperture of OWL will smear the Fresnel pattern over the aperture. However, the size of OWL can play to our advantage, as shown by Takato (2003) using the technique of subapertures (*pupil segmentation*). He shows that the optimum pupil size for lunar occultations is from 2 to 4 m; therefore pupil segmentation of OWL can provide an unprecedented sensitivity for very high spatial resolution of polarization and spectrophotometric properties of the celestial source. In particular, following Richichi (1993), OWL will be a powerful tool in the detection of faint companions of a star (exoplanet or brown dwarfs) during lunar occultation: the study of the diffraction pattern and superposition phenomena with a 100m class telescope will allow the detection of a companion 13-15<sup>th</sup> magnitudes fainter than the central star.

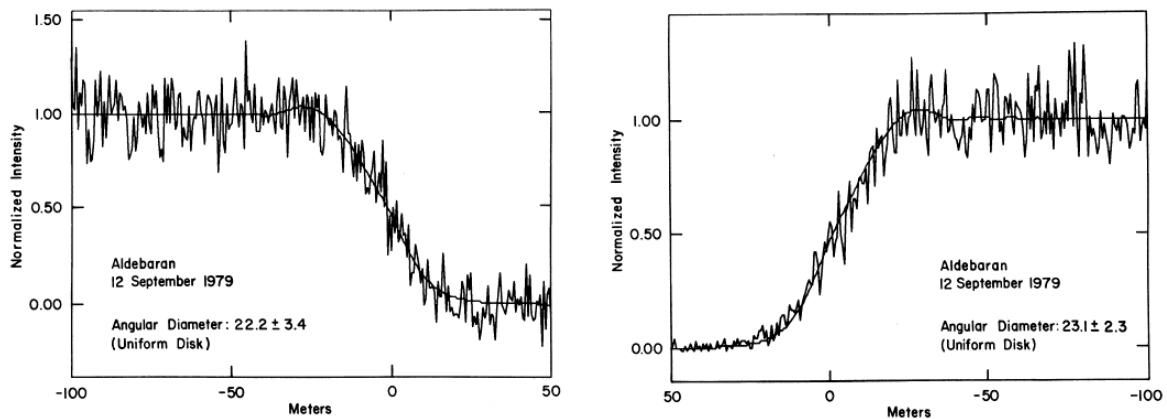


**Fig.3.6.** Determining the diameter of Aldebaran from lunar occultations. Observational traces with theoretical best-fit superimposed; left: immersion; right: reappearance. The scale on the abscissa is in meters on the Earth surface. (Radick & Africano 1981)

Star occultations by *main-belt asteroids* occur frequently: about 300 asteroids occultation events by background stars up to 12<sup>th</sup> magnitude are foreseen each year, see <http://sorry.vse.cz/~ludek/mp/world/mpoccl.txt>. Given their large distance, the asteroidal shadow pattern on the Earth is similar to its size (from few to hundreds km). The probability to have an occultation over a particular Observatory dramatically increases going to fainter background stars, and therefore OWL will have several occultations each day. Moreover, the fact that the Fresnel scale is larger than the OWL aperture means that atmospheric intensity scintillation – a parameter that actually may be a limiting one in occultation measurements – will be much better averaged out over a large OWL aperture, compared to a smaller telescope.

The *KBO occultations* give an accurate diameter evaluation, and allow to search for possible atmospheres and for binary companions. The number of *geometric* occultations of stars with angular radius  $\Phi_*$ , and with an inclination  $I$  on the ecliptic plane, by KBOs of angular radius between  $\varphi$  and  $\varphi+d$ , observed during an interval  $\Delta t$  can be written as:

$$n_{occ} = 2\delta(\varphi, i)(\varphi + \Phi_*)v\Delta t$$

where  $\delta(\varphi, I)$  is the density and  $v$  is the velocity of KBOs in the sky plane. To apply this formula, it must be considered that:

**The density of KBOs is poorly known**, because the faint magnitudes of these objects limit the size of directly detectable objects to few kilometers. Recent observations provide an estimate of  $\sim 10^{11}$  objects larger than 1 km, located between 30 and 50 AU, near the Ecliptic plane. Assuming that the differential size distribution varies as  $\rho^q$  (with the index  $q = 3$  to 4) down to decameter-sized objects, we expect a *number of valid occultations* (i.e. a  $4\sigma$  event) between a few to several tens per night, if we may obtain an r.m.s. signal fluctuation  $\sigma \leq 1\%$ , by observing stars close to the ecliptic plane having an angular radius  $\leq 0.01$  mas.

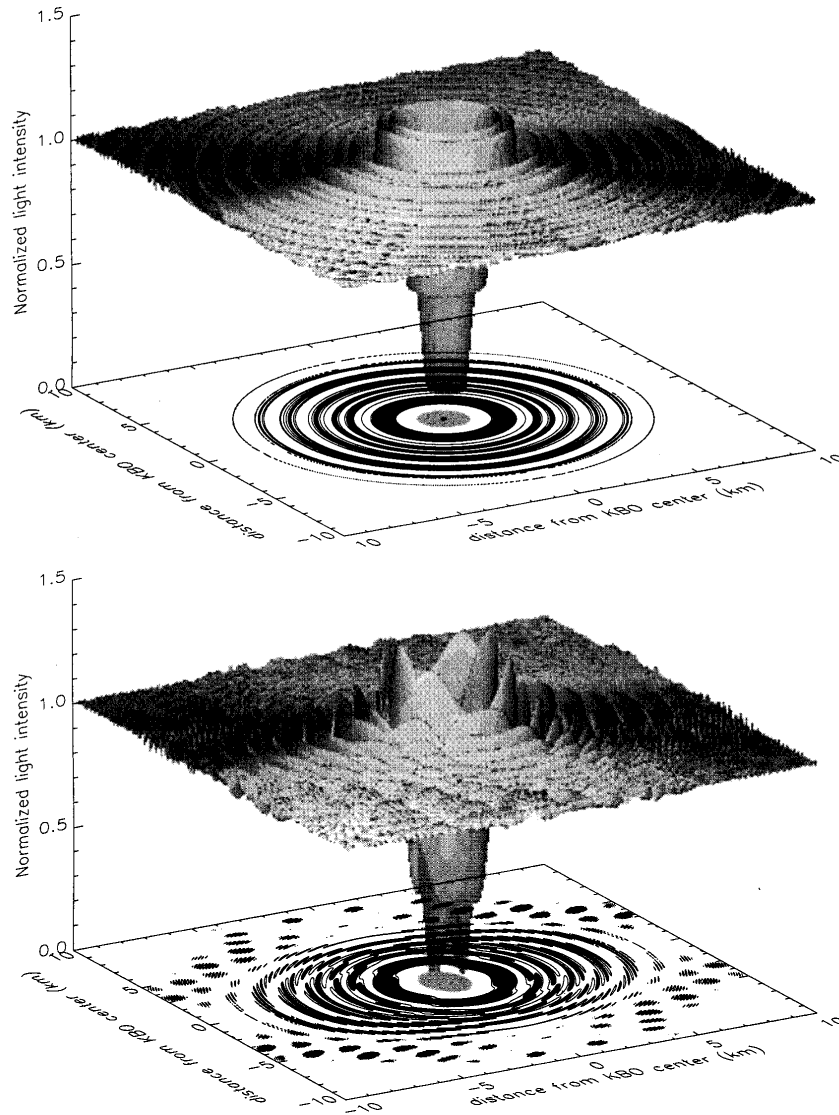


**Fig.3.7.** The shadow pattern of a 1-km radius Kuiper-Belt Object in front of a point star. The two horizontal axes are in km, and the vertical axis is the normalized stellar flux. Top: Circular KBO; Bottom: Irregular and elliptical object. The grey central spot indicates the geometrical shadow of the KBO. (Roques & Moncuquet 2000)

**The diffraction** is an important parameter and occurs when the diameter of the occulting star (projected at the KBO distance) is of the order of 1.2 km (the KBO Fresnel scale in the visible). The diffraction reduces the depth of the event but increases the size of the shadow, which is much larger than the geometrical shadow.

The *star size is a critical parameter*, because the occultation profile is smoothed on the stellar disc. Occultations of large stars by under-kilometer KBO do not generate a detectable decrease of the stellar flux. Typical star radii are between  $3 \cdot 10^{-3}$  to 1 mas. Projected at 40 AU, this corresponds to 0.1 to 30 km in radius. Blue stars are the best candidates, because for a given magnitude, they have the smaller angular diameter.

$m_V$	8	10	12	14
M5 V star	50 km	20 km	8 km	3 km
F5 V star	4 km	2 km	700m	100m
O5 V star	800 m	300 m	100m	50m

**Table 3.2.** Apparent stellar radii projected at 40 AU, for stars of increasing magnitude

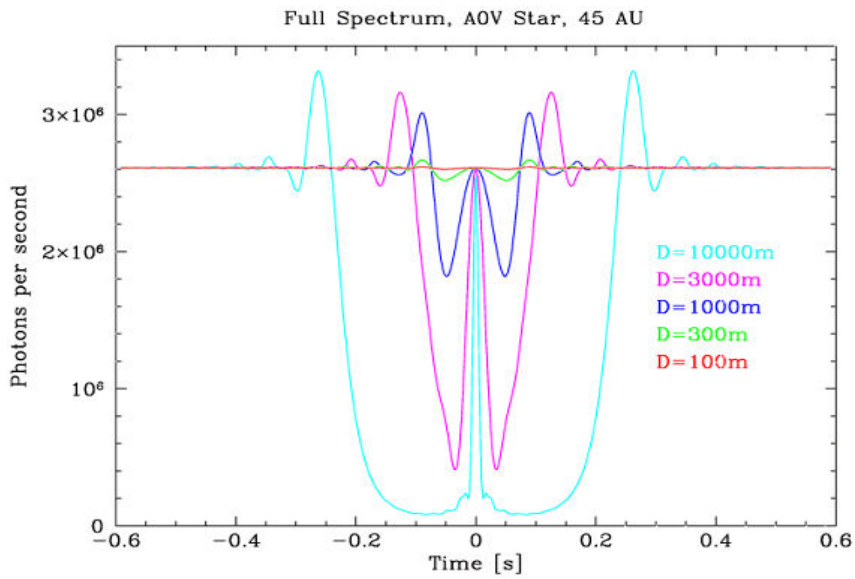


**Fig.3.8.** Kuiper-Belt object occultation pattern as function of the KBO diameter (from 10 to 0.1 km) for an A0 V star at 45 AU

The *S/N ratio of the light-curve limits the detection*. If the star is brighter than magnitude 12, the noise on a high time resolution light-curve is dominated by scintillation, which affects the stars independent of their brightness. The r.m.s. signal fluctuation observed with a telescope with a diameter  $D$ , at an altitude  $h$  above the sea level can be written as (Young, 1967; Dravins et al. 1998):

$$\sigma = S_0 D^{-2/3} X^{3/2} e^{h/H} \sqrt{\frac{\tau_c}{2}}$$

where  $X$  is the airmass,  $\tau$  is the integration time,  $H$  is taken to be 8 km,  $S_0$  is a constant equal to 0.09 for conditions of good seeing,  $D$  is in centimeters and  $\tau$  is in seconds.

For  $\tau = 0.05$  second, the r.m.s. fluctuations on a 2-m class telescope is roughly  $2 \cdot 10^{-2}$  for optimal conditions. This allows us to detect sub-kilometer objects. *The 100-meters class telescopes allow to reach  $\sigma \approx 10^{-3}$  with good margins, and then to detect about 30-40m radius KBOs.*

Moreover, if an *occultation is observed at different wavelengths*, the profiles are different and their comparison could give information on the Fresnel scale, and then *on the distance* of the occulting object.

It can be concluded therefore that high time resolution photometry with OWL of main-belt asteroids and KBO occultations will provide plenty of good science. Lunar occultations instead would need a fuller discussion, including operational constraints, before the usefulness of such a large telescope can be established.

### 3.2. Advantages of the Optical





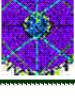
Rapid astrophysical events (e.g. quasi-periodic oscillations, flashes, pulsars) are seen at various wavelengths. Although X-rays might originate in hotter structures closer to the compact object, the *optical* appears to be the best for studying the *most rapid* phenomena. The number of photons per second (and especially per millisecond!) is much greater from the optical parts of the sources (observed with large telescopes), than that from their X-ray parts, observed with foreseen space instruments. (Indeed, X-ray observations are more often characterized by kilosecond observing times than by kilohertz count rates!)

Another optical advantage is the feasibility to ultimately detect *quantum phenomena* in radiation. Some effects are easier to see in radio (e.g. the bunching of photons appears as "wave noise"), but a limit is set by the practical difficulties of photon counting at wavelengths beyond the infrared.

### 3.3. Advantages of Great Light-Collecting Power

Very large optical telescopes permit *enormously more sensitive* searches for high-speed phenomena in astrophysics, such as those expected from instabilities in accretion flows onto compact objects, or in the fine structure of photon emission.

For very high time resolution, classical light curves are of little use. Measurements have to be of autocorrelations, power spectra, or other statistical properties of the arriving photon stream. All such statistical functions depend on a power of the average intensity that is *higher than one*. For example, an autocorrelation (obtained by multiplying the intensity signal by itself, shifted by a time lag) is proportional to the *square* of the intensity. This dependence makes large telescopes *very much more sensitive* for the detection of rapid variability than ordinary-sized ones.

Telescope diameter	Intensity $\langle I \rangle$	Second-order correlation $\langle I^2 \rangle$	Fourth-order photon statistics $\langle I^4 \rangle$
 3.6 m	1	1	1
 8.2 m	5	27	720
 4 x 8.2 m	21	430	185,000
 50 m	193	37,000	1,385,000,000
 100 m	770	595,000	355,000,000,000

**Table 3.3.** Comparisons between the observed signal of source intensity ( $I$ ), its square and fourth powers, for telescopes of different size. The signal for classical quantities increases with the intensity  $I$ ; the signal in power spectra and similar functions suitable for variability searches, as  $I^2$ ; and that of four-photon correlations as  $I^4$ , as relevant for quantum-statistical studies. The current (and future) advent of very large telescopes enormously increases the potential for quantum optics, and high-speed astrophysics in general.

Specifically, the signal for second-order (two-photon) intensity correlation increases as the recorded intensity squared, while the signal for a four-photon correlation equals the probability that four photons are recorded in rapid succession, and thus increases with the fourth power of the intensity. Table 3.3 summarizes this dependence for some telescope sizes.

These large numbers may appear unusual when compared to the more modest gains expected for classical types of instruments, and initially perhaps even difficult to believe. Such numbers are, however, well understood among workers in non-linear optics. The measured  $\langle I^4 \rangle$  is proportional to the conditional probability that four photons are recorded within a certain time interval.  $\langle I^4 \rangle$  itself is, strictly speaking, not a physical observable: either one detects a photon in a time interval, or one does not.  $\langle I^4 \rangle$  therefore has the meaning of successive intensity measurements in rapid succession:  $\langle I(t) \cdot I(t+dt) \cdot I(t+2dt) \cdot I(t+3dt) \rangle$ . In an experiment where one is studying the multi-step ionization of some atomic species, where four successive photons have to be absorbed in rapid succession, one indeed sees how a doubling of the light intensity causes a 16-fold increase in the ionization efficiency. Or indeed, for light of identical intensity, how the efficiency increases if the illuminating light source is changed to another of the same intensity but with different statistical properties, i.e. a different value of  $\langle I^4 \rangle$ .

But it does not stop there. The prospect of improved detectors will further increase the efficiency in a multiplicative manner. E.g. an increased quantum efficiency in the visual of a factor 3, say, or in the near infrared a factor 10, will mean factors of 10 and 100 in second-order quantities, while the signal in fourth-order functions will improve by factors 100 and 10,000, respectively. These factors should thus be multiplied with those already large numbers to give the likely gains for large telescopes equipped with future detectors, as compared to present ones.

Due to analogous steep dependences on intensity, the research field of non-linear optics was opened up for study by the advent of high-power laboratory sources. In a similar vein the advent of very large telescopes could well open up the field of very-high-speed astrophysical variability, and bring astronomical quantum optics above a detection threshold.

### 3.4. Advantages of Large Telescope Area

Besides providing a great light-collecting area, the geometrical extent of very large telescopes is advantageous in averaging out effects of atmospheric intensity scintillation. Although it is not possible to precisely predict the amount of scintillation in very large apertures (due to the uncertainty in outer scales of atmospheric turbulence; local properties of the observatory site, etc.), the general trend should follow that in Figure 3.9, where observed scintillation in a series of small apertures has been fitted to the expected theoretical run for larger ones:

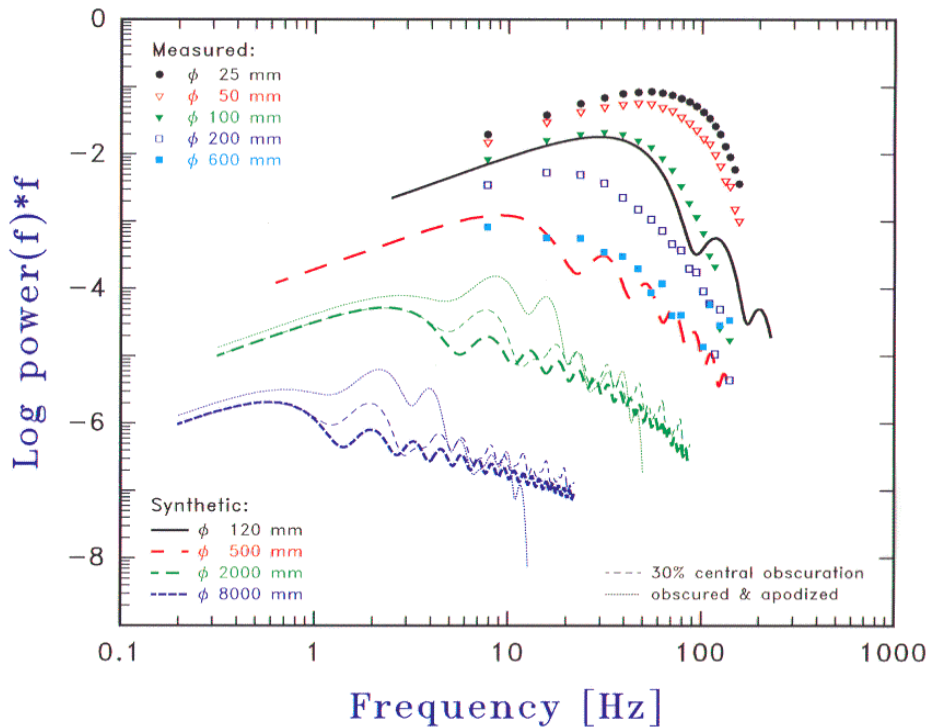


**Fig.3.9.** Power spectral content of scintillation in different apertures, i.e. the amount of integrated power, as function of frequency. Observations in small apertures made on La Palma were fitted to a sequence of models for large apertures. This plot illustrates where in the spectrum the power is located. For smaller apertures, the power distinctly shifts towards higher frequencies. This trend continues until aperture diameters around 5 cm, where the structures in the "flying shadows" begin to get resolved. (Dravins et al. 1998).

Spatial averaging thus strongly decreases the power in large apertures. However, the aperture of OWL (nor of any other current ELT project) is not completely filled due to its segmented mirrors with gaps between mirror segments. Small apertures (or small gaps) do preferentially filter out the smaller and more rapid scintillation components, and thus will make the scintillation signature more complex than that of a filled aperture. Some aspects of

this appear feasible to observationally investigate already now, using large optical flux collectors (cf. Sect. 5.7.3). For a broad overview of scintillation in optical astronomy, see Dravins et al. (1997ab; 1998).

### 3.5. Using Optical Flux Collectors

With the ELT generation still some years away, a number of “precursors” may be identified that may permit experimental studies of at least some aspects of ELT observing.

A number of large flux collectors have been constructed for the study of cosmic gamma-rays though the detection of atmospheric Cherenkov-light flashes. Others have been developed as solar flux collectors for the purpose of energy research or for concentration of radiant energy. Some among these appear relevant for some classes of experiments. Their large collecting areas permit to realize photon-count rates on ELT-like levels, and the identification of background or noise sources on micro- or nanosecond levels (though the angular resolution is quite poor, and only very few astronomical objects can realistically be observed), while their optical construction (typically with hexagonal segmented mirrors) are similar to most ELT concepts and permit, e.g., experimental studies of atmospheric intensity scintillation over such hexagonal-structured apertures.

#### 3.5.1. *MAGIC* on La Palma

The 17-meter diameter *MAGIC* [*Major Atmospheric Gamma Imaging Cherenkov*] telescope at the Roque de los Muchachos observatory site on La Palma, is the world’s largest single telescope to observe atmospheric Cherenkov light from high-energy gamma rays. It begun operations in 2004. The telescope has a parabolic mirror,  $f/D \approx 1$ , built up of 943 individual 50 x 50 cm<sup>2</sup> aluminum elements. An active mirror control performs fast corrections of the residual mirror deformations. The image quality is such that each individual mirror segment generates an image of approximately 5 mm FWHM.

<http://wwwmagic.mppmu.mpg.de/introduction/>

*MAGIC* provides a central 'empty' pixel which could be adapted to various optical experiments. A second telescope (*MAGIC II*) of similar size is being planned at the same La Palma site. In principle, *MAGIC I* and *MAGIC II* might be connected for experiments in intensity interferometry.

***Optical observations with flux collectors:*** Because of the limited angular resolution (approx. 6 arcmin), the contribution from the background sky is considerable (approx 13 magnitudes brighter than one square arcsecond of sky, i.e. approx 8 mag for a background level of 21 mag). Therefore, it is only practical to observe either very bright objects, or such with a characteristic variability. Among the latter, the Crab pulsar is outstanding (although its background is further enhanced by light from the Crab nebula), and it has been successfully observed with several flux collectors. Its observation simultaneous with the Cherenkov light studies also has a direct relevance since one wishes to know the precise phase in the pulsar cycle when some gamma-rays are detected.



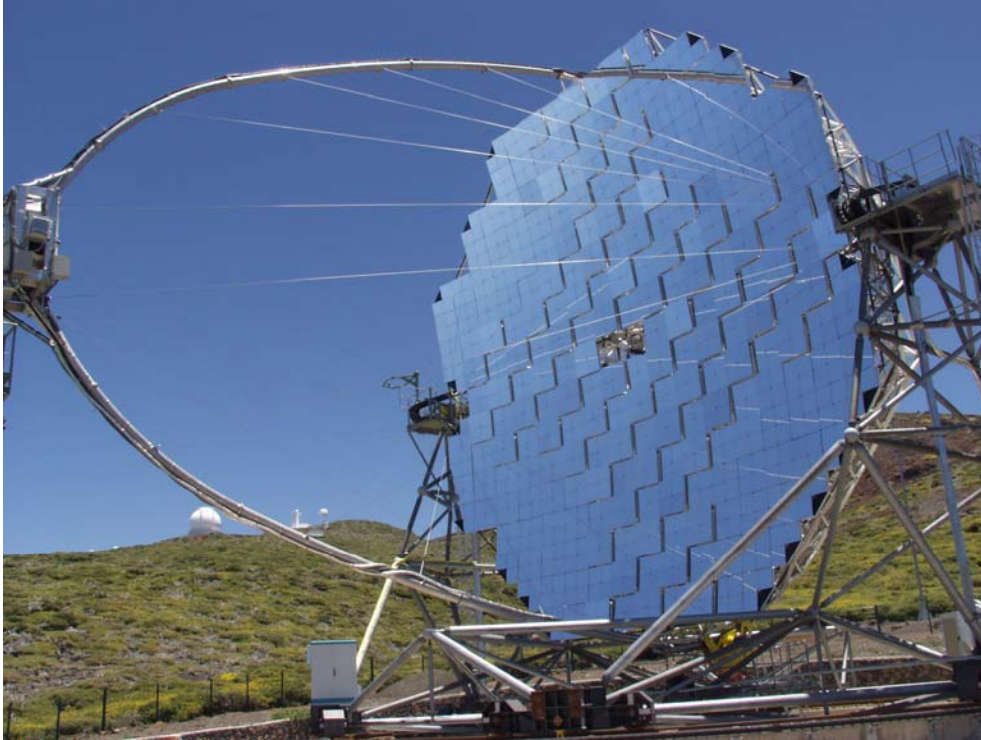


*Fig.3.10. MAGIC on La Palma.*



*Fig.3.11. MAGIC focal-plane detector system: The camera has “pixels” of 0.1 degrees in the central section, up to 1.2° radius, and a ring of 0.2° pixels extending to 1.8° radius. The camera detectors are hemispherical photomultiplier tubes, operated at low gain in order to prevent damage from the night-sky background or during operation in moonlight.*

The optical pulse from the Crab pulsar was detected already by the HEGRA array (precursor to MAGIC on the same La Palma site): E. Oña-Wilhelmi et al. (2004); and has also recently been observed also with MAGIC (Fabrizio Lucarelli, Universidad Complutense, Madrid; private comm., 2005).

### ***Simulated observations of Crab pulsar with MAGIC***

Simulated Crab pulsar measurements on MAGIC may be used as an illustration of potential observations with large flux collectors.

The count rate is given by

$$R = \int F_\lambda \cdot A \cdot \eta \cdot \beta \cdot Q_\lambda d\lambda, \quad (1)$$

where  $F_\lambda$  is the spectral flux distribution,  $A$  is the telescope main mirror area,  $\eta$  is the mirror reflectivity,  $\beta$  is the “light-guide” efficiency, and  $Q_\lambda$  is the detector quantum efficiency. The total count rate  $R_{tot}$  (in photoelectrons per second, phe s<sup>-1</sup>) is the sum of the object count rate  $R_{object}$  and that of the background  $R_{background}$

$$R_{tot} = R_{object} + R_{background}. \quad (2)$$

For observations of the Crab pulsar  $R_{background}$  is the sum of the contributions from the *light of the night sky* (LONS) and from the Crab *nebula*,

$$R_{background} = R_{LONS} + R_{nebula}. \quad (3)$$

The estimated optical count rates from the various contributors observed with MAGIC’s central pixel are according to Oña-Wilhelmi *et al.* (2004):

$$\begin{aligned} R_{object} &= 3.7 \cdot 10^6 \text{ phe s}^{-1} \\ R_{nebula} &= 3.5 \cdot 10^9 \text{ phe s}^{-1} \\ R_{LONS} &= 1.3 \cdot 10^8 \text{ phe s}^{-1} \end{aligned}$$

which gives  $R_{background} = 3.63 \cdot 10^9 \text{ phe s}^{-1}$ . Thus, the total pulsed contribution from the object is almost three orders of magnitude lower than that of the background.

The signal-to-noise ratio (SNR) set by Poissonian noise in a photometric signal can be estimated by

$$\text{SNR} = \sqrt{N} = \sqrt{R \cdot t_{sample}}, \quad (4)$$

where  $N$  is the number of counts and  $t_{sample}$  is the sample time. We are here neglecting the smaller noise contributions from the detector and the source itself.

- 1) For the present calculations, a maximum background count rate is set to the maximum count rate of a plausible digital detector at the central pixel of MAGIC:  $R_{\max background} = R_{\max} = 10 \text{ MHz}$ . Since the total photon flux is much higher, this number would increase for more powerful detector systems.
- 2) The constructed Crab pulsar intensity signal, which has a profile looking like the mean pulsar light-curve, is normalized to the background level:

$$R_{normobject}(t) = \frac{R_{object}(t)}{R_{background}} \cdot R_{\max}$$

- 3) The SNR of  $R_{\max background}$  is calculated as:  $\text{SNR} = \sqrt{R_{\max} \cdot t_{sample}}$ , where  $t_{sample} = 1 \cdot 10^{-6} \text{ s}$  is the sample time of the intensity measurement.

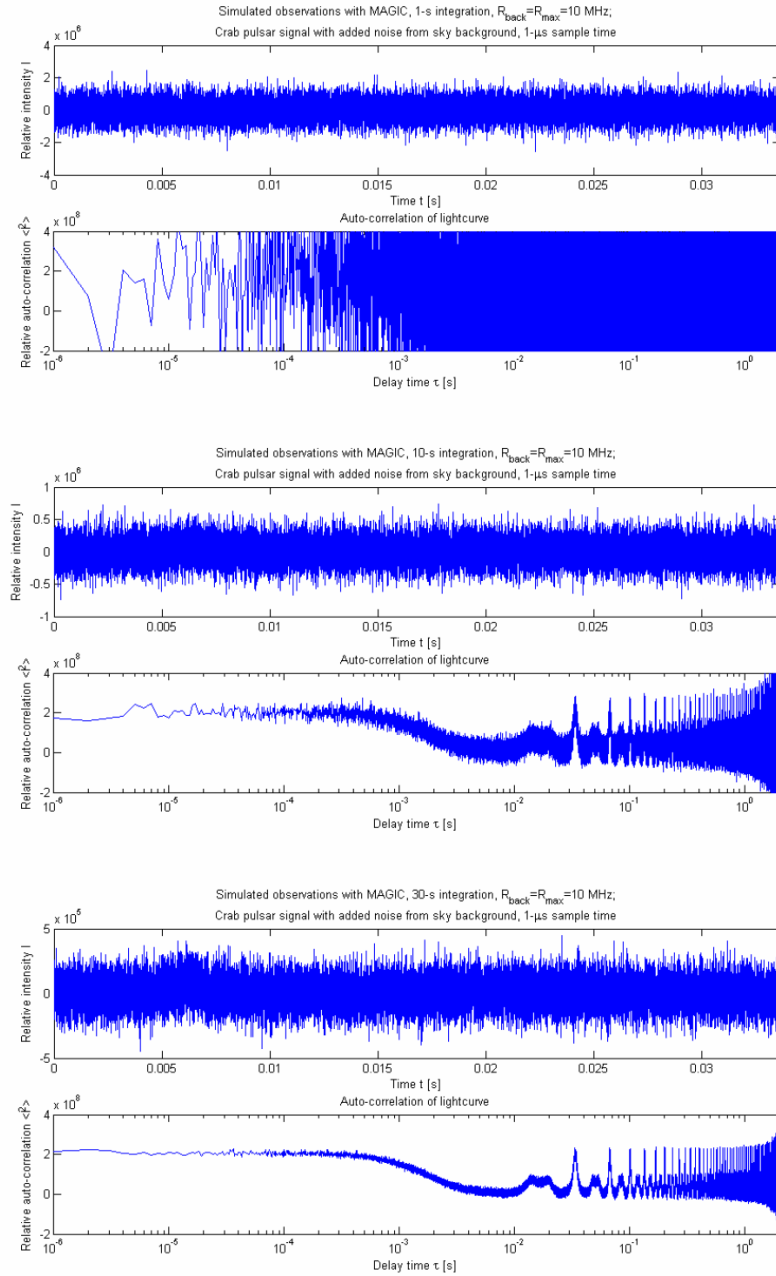


**Fig.3.12.** Simulated observations of the Crab pulsar with the MAGIC 17-m flux collector, for integrations over 1, 10 and 30 seconds. The top curves are the folded intensity profiles, folded with the pulsar 33 ms period (only in the bottom panel does a hint of the pulsar main pulse appear). The bottom curves show the temporal autocorrelation which has various structures: each peak identifies some particular timescale of variability. The sharp peak at 33 ms (and its harmonics) is the pulsar period; the peaks around 13 and 20 ms are the time differences between the main and secondary, and between the secondary and main peaks, respectively; while the rise towards shorter times is a measure of the sharpness of the peaks, etc. The signal was assumed sampled by a 10 MHz-counting detector, with the relative ratios between the pulsar, the Crab nebula, and the sky background taken from Oña-Wilhelmi et al. (2004). Since the signal from the pulsar is only some  $10^{-6}$  of the background, integrations over many hundreds of pulsar periods are required before a sensible autocorrelation signal appears. Nevertheless, it appears clear that a good signal can be retrieved down to microsecond timelags within reasonable integration times (a few hours, say). For such observations, the main aims would perhaps not primarily be to study the pulsar as such, but rather use the pulsar signature as a representative background against which to survey observational constraints (e.g., atmospheric phenomena). Nevertheless, it can not be excluded that already such flux-collector observations could give some insight into possible phenomena on very short timescales, perhaps optical giant pulses if such would exist on microsecond scales.

- 4) The background noise  $R_{backnoise}(t)$  is generated by creating a random sequence  $N_{rand}(t)$  of numbers from a normal distribution with mean zero, variance one, and standard distribution one, and then calculating:

$$R_{backnoise}(t) = \frac{N_{rand}(t) \cdot R_{max}}{SNR \cdot \sqrt{\frac{T}{0.0336}}}, \text{ where } T \text{ is the integration time.}$$

- 5) The Crab pulsar signal with added noise from the sky background,  $R_{normobject}(t) + R_{backnoise}$ , is then plotted.
- 6) The auto-correlation function of the integrated signal is calculated with an “unbiased” normalization, which means that the raw correlation value is divided by the total number of correlated intensity elements minus the number of lags for that particular delay time.
- 7) The power spectrum of the plotted noisy intensity signal is calculated as the Fourier transform of the auto-correlation function, and both are then plotted.

### 3.5.2. The H.E.S.S. observatory in Namibia

The H.E.S.S. observatory in Namibia is, in a sense, the southern-hemisphere equivalent of MAGIC. H.E.S.S. is a system of imaging atmospheric Cherenkov telescopes for the investigation of cosmic gamma rays in the 100 GeV energy range. The name H.E.S.S. stands for High Energy Stereoscopic System, and should also remind of Victor Hess, who received in 1936 the Nobel prize in physics for his discovery of cosmic radiation. H.E.S.S. is located in Namibia, near the Gamsberg, an area well known for its excellent optical quality. The first of the four telescopes of Phase I of the H.E.S.S. project went into operation in 2002; all four were operational in 2003, and were officially inaugurated in September, 2004.

The initial four H.E.S.S. telescopes (Phase I) are arranged in form of a square with 120 m side length, to provide multiple stereoscopic views of air showers. The telescope mirrors have diameters around 12 m, each has an area of 108 m<sup>2</sup>. The cameras have 960 PMT photon detector elements, each subtending an angle of 0.16 deg (10 arcmin) angle, using 29 mm, 8-stage photomultiplier tubes (PMTs) with borosilicate windows, equipped with Winston cones to improve light collection.

The optical Crab pulsar has been observed also using one of the H.E.S.S. telescopes: Franzen et al. (2003).

HESS project: <http://www.mpi-hd.mpg.de/hfm/HESS/>

In the world, there exist some additional optical Cherenkov gamma-ray-flash observing telescopes, although MAGIC and H.E.S.S. appear to be the ones with the currently largest apertures.

### 3.5.3. The Pierre Auger observatory in Argentina

The southern Pierre Auger Observatory is presently under construction in Argentina. It combines two complementary air shower observation techniques; the detection of particles at ground and the observation of associated light flashes generated in the atmosphere. Experimentally, this is being realized by employing an array of 1600 water Cherenkov

detectors, distributed over an area of 3000 km<sup>2</sup>, and operating 24 wide-angle Schmidt telescopes, positioned at four sites at the border of the ground array. The Observatory will reach its full size in 2006.

The main elements of the aperture system are the 2.2 m diaphragm including a corrector ring (not installed at each telescope, yet) and an UV transmission filter made of MUG-6 glass. The light is reflected by segmented 13 m<sup>2</sup> spherical mirrors. The focal plane of the mirror is instrumented with a camera arranged in 20x22 pixels. Thus, each of the 440 PMTs (XP 3062 of Photonis) of a camera views approximately 1.5 × 1.5 of the sky. The PMT signals are continuously digitized at 10 MHz sampling rate with a dynamic range of 15 bit in total. An FPGA based multi-level trigger system records traces out of a random background of 100 Hz per pixel.

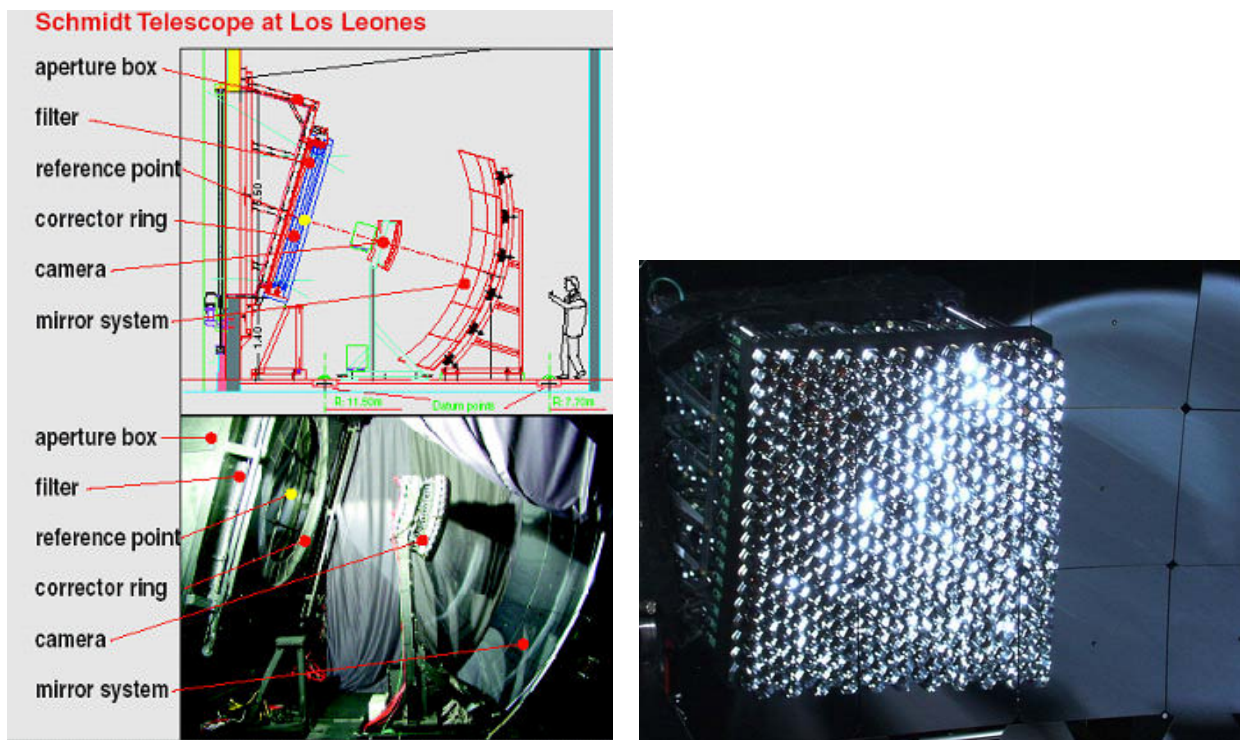


*Fig.3.13. The Pierre Auger Schmidt telescopes and focal plane cameras.*

The Fluorescence Detectors are producing light curves at 435 nm for ca. 200 stars with a time sampling of 100 ns. (Ambrosio et al. 2005). The Pierre Auger experiment, thanks to its high time resolution, high collection area of blue photons, very long baseline characteristics and of the careful atmospheric monitoring at distant locations, could be highly interesting for experiments in intensity interferometry, or other aspects of high-time resolution astronomy.

Pierre Auger Observatory: <http://www.auger.org/>

### 3.5.4. Solar flux collectors

There further exist a number of large, and very large optical flux collectors, built for solar flux collection, either for research in solar energy utilization, or as devices to obtain high temperatures by radiation only. Although the optical quality is generally modest (i.e., by astronomical telescope standards), their collecting areas are huge, in some cases even significantly larger than that of OWL. Some authors have considered the feasibility of using some of these for astronomical observations, and some demonstration observations of a few bright stars have actually been made with these facilities.

An evaluation of the possible use of solar flux collectors for optical SETI is by Covault (2001), while Ribak et al. (2003) propose to convert PETAL (*Photon Energy Transformer & Astrophysics Laboratory*), a 25-m diameter solar flux collector on the Negev desert plateau in southern Israel, into an astronomical facility.



**Fig.3.14.** *Four solaire (CNRS), Odeillo, Pyrénées*

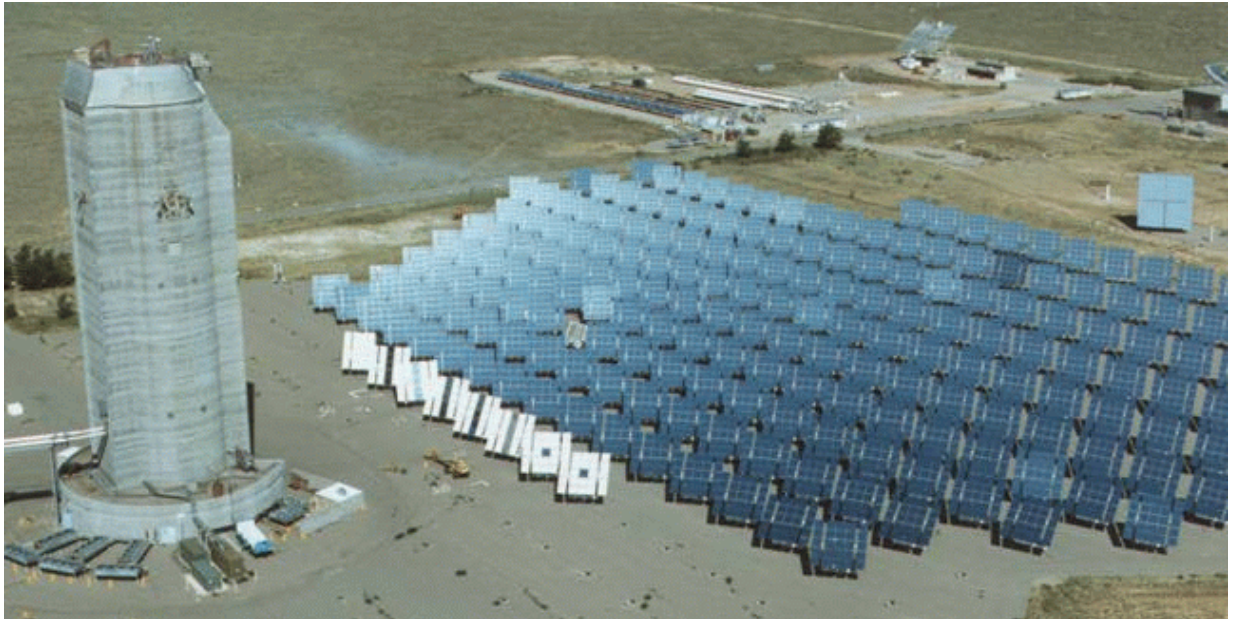


**Fig.3.15** National Solar Thermal Test Facility, Sandia Laboratories, Albuquerque, New Mexico.  
Heliostat area: approx. 30,000 m<sup>2</sup>





## 4. Instrumental Requirements

### 4.1. Optical and Near-IR Detectors for Nanosecond Astrophysics

The following paragraph gives a condensed overview of available and futuristic detectors for photon counting. Given the great interest for photon counting detectors, this survey is by no means complete. Photomultipliers (PMTs) and Single-Photon Avalanche Photodiodes (SPADs) have been examined in detail, while also other detector types have been surveyed (hybrid photo detectors; other cathode-based detectors such as streak cameras; energy-resolving detectors (STJs, TESs); L3CCD; counting boards and systems, etc. Some information on these is given also elsewhere, e.g. in Appendix A3. However, they do not enter in the present condensed version of the detector survey.

#### 4.1.1. Photomultipliers

Photomultipliers (PMTs) are excellent detectors for measuring the time characteristics of very weak and extremely short-duration light pulses (sub-nanoseconds, rates exceeding 1 GHz). PMTs have high bandwidth and noise-free gain on the order of  $5 \times 10^6$ . This makes them ideal for the detection of extremely low light or short pulses of light. In the context of our study it is useful to recall some characteristics of the time response:

- Anode pulse rise time: elapsed time between the 10% and 90% amplitude point of the leading edge of the anode current pulse with the *photocathode fully illuminated*. A decrease of the rise time can be obtained by illuminating a small portion of the cathode. The rise time can also be affected by the amplitude of the pulse (the higher the amplitude, the longer the rise time, usually not more than a factor of 2 in the linear regime). Excessive high dark current caused by high ambient temperature or extraneous electric fields near the tube also tend to increase the rise time.
- FWHM: period of anode current pulse at its half amplitude points
- Anode pulse fall time: elapsed time between the 90% and 10% of the trailing edge (generally longer than the rise time).
  - The fastest performances are obtained with *single photoelectrons* (Single Electron Rise time, SERT). Notice that in this condition the profile of the trailing edge shows a typical 'ringing' effect not visible on multielectron currents.

#### ***Hamamatsu PMTs***

Hamamatsu offers a most complete range of *head-on* and *side-on* photomultiplier tubes from 3/8" to 20" in diameter. Many of the detectors can operate at high frequencies and are capable of capturing events of short duration or at extremely low light levels. Image intensifiers, ion, electron detectors and microchannel plates (MCP) are also available. Many types of detectors can be customized to a specific application. Two Hamamatsu web sites have been consulted:

- 1) <http://usa.hamamatsu.com/en/products/electron-tube-division/detectors/photomultiplier-tubes-pmts.php>
- 2) <http://www.hpj.co.jp/Eng/products/ETD/pmte/pmte.htm>

This second site contains useful documents, e.g.:

*Construction and Operating Characteristics*

*Typical Spectral Response:* examples for transmission mode tube are given in Figure 4.1.

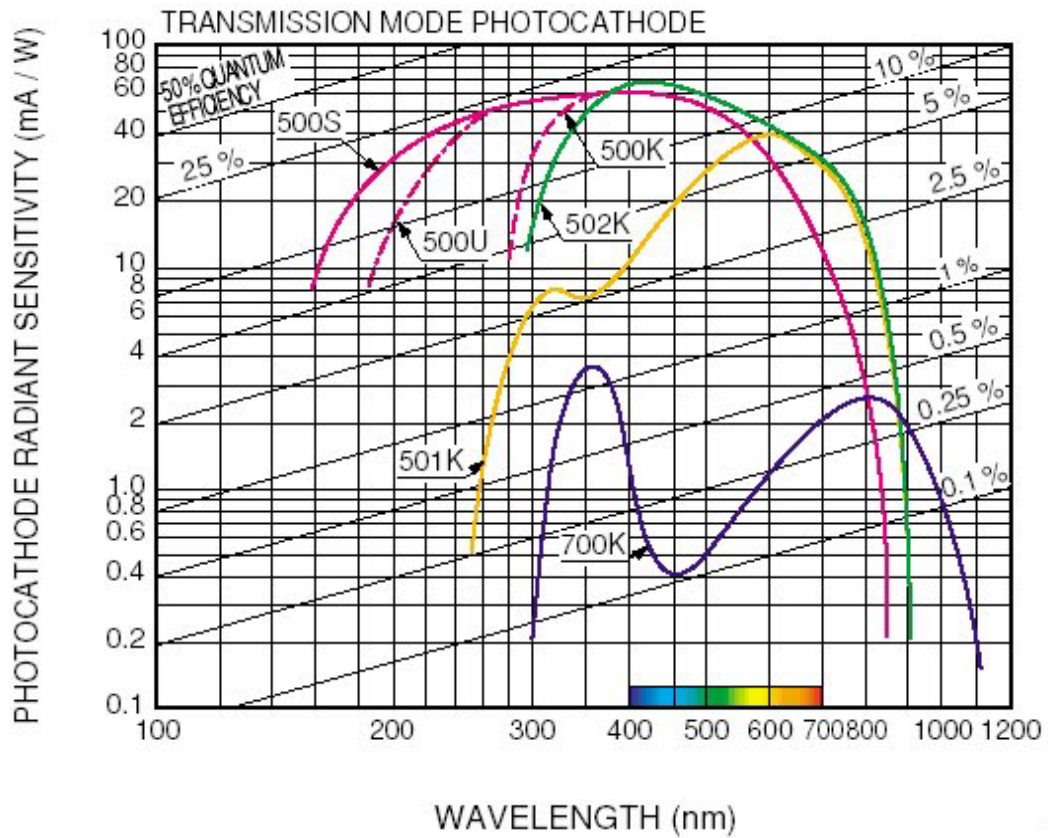


**Fig.4.1.** Typical efficiencies of Hamamatsu PMTs, both reflection and transmission. Peak values in the visible are around 25%.

A new product is a highly sensitive semitransparent NIR photomultiplier for the near Infrared (950-1700 nm) *PMT R5509-43 / R5509-73* (see Figure 4.2), capable of photon counting by a novel photocathode technology. Adaptors for optical fiber or monochromator are available as an option.

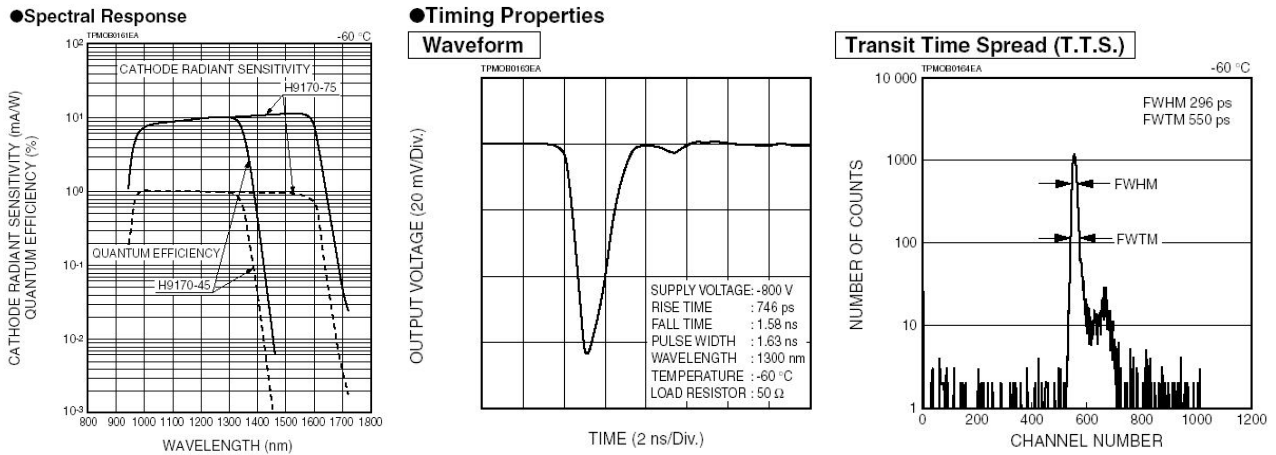


**Fig.4.2.** The QE and timing properties of the Hamamatsu near-IR PMTs

**Burle Electron Tube PMTs** (<http://www.burle.com/>): This firm provides several types of PMTs, both in *Transmission Mode Type* and in *Reflection Mode Type*. It could be considered in a final decision stage, if PMTs are selected.

#### 4.1.2. Avalanche photodiodes

**Generalities:** A distinction must be made between ordinary avalanche photodiodes (APD), namely p-n junctions biased near the break-down voltage but below it, and single-photon avalanche diodes (SPAD) which are biased *above* it (see Cova et al. 2004). However, quite often the two terms are confused. In APDs, avalanche multiplication is exploited to produce linear amplification of the primary photogenerated electric signal. In a way, they are similar to PMTs, but with an intrinsic positive feedback in the amplification due to the avalanche process. Hence, whereas PMTs provide a gain around  $10^6$  and moderate fluctuations, the mean value of gain in APDs with acceptable fluctuations is lower than  $10^3$ . Their performance as single photon detectors is therefore poor.

SPADs instead operate *not as amplifiers but as bi-stable circuits, analogous to the Geiger-Muller counters of ionizing radiation* (hence, SPADs are also termed *Geiger-mode* avalanche diodes). In the quiescent state the SPAD is biased at voltage  $V_a$  above the breakdown voltage  $V_{BD}$ , and no current flows (OFF-state). When even a single charge carrier is injected into the high field region, it is strongly accelerated and can impact and generate a secondary electron-hole pair, starting a self-sustaining avalanche multiplication process. The current then rapidly grows until the space charge effect limits its value to a constant level (in the milli-ampere range), proportional to  $(V_a - V_{BD})$ . *The fast onset of the current marks the time of arrival of the photon that generated the initial the initial charge carrier.* The device remains in this ON-state until the avalanche is quenched by an external circuit. An avalanche pulse current with *standard amplitude* has thus been produced (it doesn't make sense therefore to speak of gain). The detector is insensitive to any subsequent photon arriving in the time interval from the avalanche onset to the voltage reset (*detector dead time*).

Regarding *quantum efficiency*, it depends on several factors, and in particular on the difference  $(V_a - V_{BD})$ . Typical curves are shown in the following.

Regarding *noise*: Free carriers are thermally generated also in absence of illumination and produce dark current pulses, analogous to the dark current in PMTs. Cooling however is not

very effective because tunnel-assisted generation is not reduced by lowering the temperature. At any rate, it is possible to obtain SPADs with less than  $10^3$  dark counts/s at room temperature. The noise is further enhanced by impurities and crystal defects, which produce deep energy levels acting as minority carrier traps. The released carriers can re-trigger the avalanche, thereby generating correlated afterpulses. The feature of the avalanche quenching circuit can play an important role in reducing the afterpulses, for instance by enforcing a longer hold-off time after each avalanche pulse, of course at the expense of increasing the dead time. If the hold-off time could be increased to say 500 ns, the afterpulsing effect could be reduced to less than 1%. It is also worth pointing out that excessive cooling increases the afterpulse effect by exponentially increasing the lifetime of the deep energy levels.

Hence, to reduce the afterpulsing probability in a SPAD operating at cryogenic temperature a very long dead time is necessary: tens of microseconds or more. *This is a main drawback of SPADs intended to operate in the infrared.*

Regarding *photon timing*: the onset of the avalanche pulse is correlated with the arrival time of the photon, but the delay is not constant, being subject to statistical fluctuations. The typical delay distribution shows that after a main peak of duration say 70ps, there is a long tail whose amplitude and duration are wavelength-dependent, due to different penetration length. *This is a further remarkable drawback when the light source is not monochromatic.* The timing performance of any particular SPAD device must therefore be accurately assessed.

**Arrays of SPADs (SPADAs):** Si-SPAD array detectors are a realistic possibility, with a rapid progress of the technology, at least for those applications where certain degree of cross talking among the pixels can be tolerated. The main contrary factors for arrays are:

- the *fill factor* is quite low, typically  $< 10\%$ , the active areas have to be separated by "dead zones". To improve the fill factor, optical devices, like lenslets and/or fibers, must be employed.
- the *cross-talk* between cells can not be avoided in principle, especially for large individual cell size. Notice, that the dangerous cross talk is optical, *photons do propagate inside the wafer.*
- each detector has to have its own, *individually matched*, electronic circuit.
- it would be difficult, if not impossible, to maintain *the timing stability* and resolution equal for all the sensitive cells of an array.

**SPADs for the infrared:** In order to detect photons with wavelength longer than 1.1  $\mu\text{m}$ , germanium and compound semiconductor must be employed, and the detector must be cooled, often to cryogenic temperature. The trap concentration is high and their lifetime at low temperature can exceed 10  $\mu\text{s}$ . On the other hand, time gating can be made very efficient. Photon timing has been achieved better than 80 ps. *The detection efficiency can reach 40%.* There is such an interest in these devices for communication purposes that the situation is likely to improve in the near future (*see also the paragraph on the Czech Technical University group*).

### ***Characteristics of commercially available SPADs***

#### **PerkinElmer: Single Photon Counting Module SPCM-AQR Series**

General site: <http://www.perkinelmer.com/opto/>

## SPAD sites:

<http://optoelectronics.perkinelmer.com/catalog/Category.aspx?CategoryName=APD+Module>  
<http://optoelectronics.perkinelmer.com/catalog/Category.aspx?CategoryName=APD+Array>

## Single-Module Description

<http://optoelectronics.perkinelmer.com/content/Datasheets/SPCM-AQR.pdf>

The SPCM-AQR is a self-contained module which detects single photons of light over the wavelength range from 400 nm to 1060 nm, a range and sensitivity which often outperforms photomultiplier tubes. The SPCM-AQR-1X utilizes a unique silicon avalanche photodiode which has a circular active area whose peak photon detection efficiency *over a 180  $\mu\text{m}$  diameter* exceeds 70% at 650 nm. The photodiode is both thermoelectrically cooled and temperature controlled, ensuring stabilized performance despite changes in the ambient temperature. The SPCM-AQR module can count to speeds exceeding  $10^7$  c/s for the SPCM-AQR-1X. There is a "dead time" of 50 ns between pulses.

*Single photon arrival can be measured with an accuracy of 350 ps FWHM.*

## Features

- Mean Count Rate: 5 MHz (Above this point, dead time will increase due to diode self-heating)
- Peak Light Intensity:  $10^4$  photons per pulse and pulse width less than 1 ns.
- Peak Photon Detection Efficiency @ 650 nm: 70% typical (see Figure 4.3.)  
(400 nm 2%; 650 nm 90%; 830 nm 92%; 1060 nm 18%).

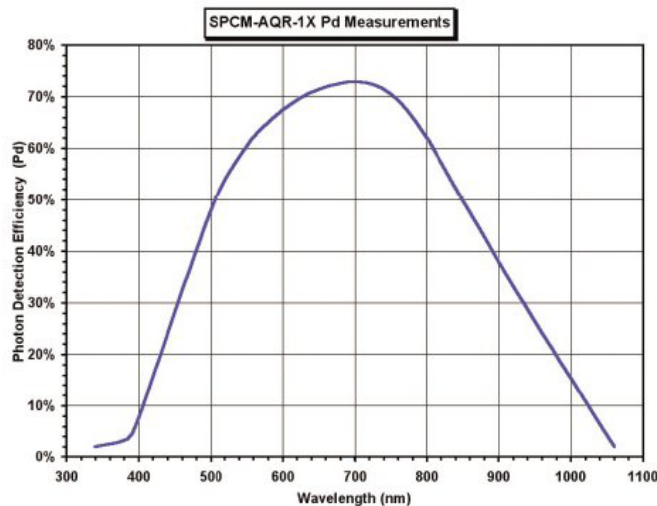


**Fig.4.3.** The QE of the typical PerkinElmer SPAD

- Dark count on selected device (SPCM-AQR-16) 25 counts/second
- Active area: SPCM-AQR-1X: 175  $\mu\text{m}$
- Timing resolution: 350 ps FWHM
- Fiber connection option

## Light emission during photon detection

One peculiarity of silicon avalanche photodiodes is that as an incoming photon is detected a small amount of light is emitted from the avalanche region. The light emitted has a broad

spectral distribution. In most cases this is not a problem. However, it can cause some confusion if another detector is monitoring light, or if the optical system is such that light emitted from the SPCM-AQR is reflected back onto itself. If these photons return 30 ns after the initial event, they will be detected.

### Saturation

The count decreases at higher incoming light levels. The count at which the output rate starts to decrease is called the saturation point. As an extreme example, if the module is exposed to intense light the count rate will fall to zero. Precautions should be taken to avoid any excessive light level that will damage the SPCM module.

**Cost:** The cost depends strongly on how low a dark count is required, and is in the range of approximately 5,000 to 20,000 €.

**Array 1x4: The PE 4-channel photon counting array SPCM-AQ4C** (see Figure 4.4.)

See manual at:

<http://optoelectronics.perkinelmer.com/content/Datasheets/SPCM-AQ4C.pdf>



*Fig.4.4. The PerkinElmer SPCM-AQ4C 4-channel photon counting array*

### Micro Photon Devices

<http://www.microphotondevices.com/products.asp>

Their modules are available with different features:

- 20  $\mu\text{m}$ , 50  $\mu\text{m}$  and 100  $\mu\text{m}$  active sensing area diameter

- Peltier-cooled and uncooled (20  $\mu\text{m}$  only)

- Timing resolution 250 to 50 ps (with additional timing board installed in the module to enhance timing performance)

- Dead time 70 ns.

The typical quantum efficiency is shown in Figure 4.5.

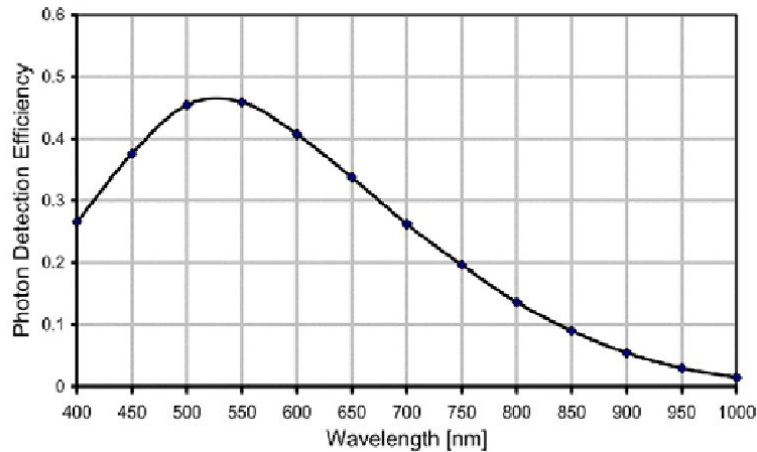


*Fig. 4.5. The QE of a SPAD from Micro Photon Devices*

The dark current of the 100  $\mu\text{m}$  device can be kept lower than 1000 c/s.

### **The Czech Technical University in Prague**

[http://space.fjfi.cvut.cz/web/prochazk/doc/Photon\\_counting\\_detectors/](http://space.fjfi.cvut.cz/web/prochazk/doc/Photon_counting_detectors/)

The company responsible for the commercial issues is:

PESO Consulting, Att. Peter Soucek, Prague; <petr.soucek@ctgroup.cz>.

The Prague group concentrated on three main areas of interest:

- Avalanche photodiode (APD) design for single photon counting: new semiconductor materials have been used to extend the spectral sensitivity of the detector from X-rays up to the near infrared spectral region, while maintaining low dark count rate at acceptable active area apertures in the range 20–350  $\mu\text{m}$  and high timing resolution in the range 3 ps to 3 ns.
- Active quenching and gating circuit design and construction: the circuit has been tailored to specific applications including laser ranging, Lidar, time resolved spectroscopy, space born ranging, and optical sensors.
- Measurement techniques development for solid state photon counter applications.

### **Silicon SPADs**

Si-SPADs have been developed mostly for satellite ranging applications (SRL), implementing a novel concept of Pico Event Timer (PET). A portable demo (P-PET) has been installed in several SLR stations (Graz, Wetzell WLRS, Wetzell TIGO, Bern, Herstmonceux).

To reduce the dark count rate, the Si-SPAD has been housed with three-stage evacuated thermoelectric (TE) cooling (Figure 4.6), which enables chip operating temperatures of  $-70^{\circ}\text{C}$ . A compact detector package has been developed, consisting of a 200 mm diameter SPAD K14 chip, three-stage thermoelectric cooling, an active quenching and gating circuit and collecting optics. It accepts a collimated beam 12mm in diameter. The dark count rate is below 10 kHz, timing resolution is 50 ps FWHM and the stability is 1 ps/h. The entire package has dimensions 50×50×130 mm, and the total mass is 300 g. The heat generated by the thermoelectric cooler and by the circuit is passively radiated by the housing surface, and totals 2 W. The detector active area can be exposed to optical pulses of up to  $10^9$  photons, which

represents about 1 nJ of energy in nanosecond long pulses, without chip damage. The chip, operating or non-operating, can be exposed to direct sunlight without chip damage.

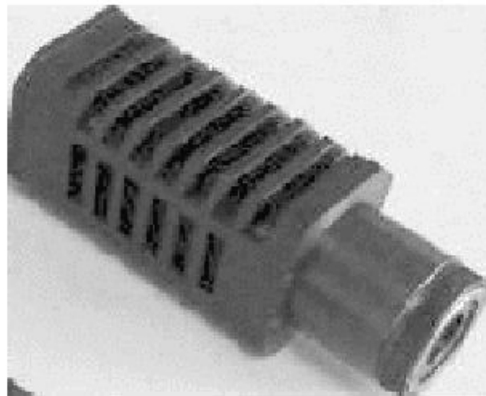


*Fig.4.6. The Czech Technical University Si-SPAD*

### **Germanium SPADs**

More recently, the Prague group has been involved in Infrared, Germanium based SPADs (Ge, Ge-Si, Ge-As, Ga-As, Ga-P, InGaP). The quantum efficiency at 1.5  $\mu\text{m}$  is quoted around 40%.

The germanium based single photon detector is of general interest for several applications: time-resolved spectroscopy, laser-induced fluorescence, optical time domain reflectometry, laser ranging and other applications aimed at developing a large aperture single photon counter for the near infrared spectral region. Several applications including laser ranging, ultimately require an active area diameter of not less than 100  $\mu\text{m}$ . The echo signal detector in the laser ranging system limits the field of view of the entire optical system. For example, a satellite laser ranging station equipped with a 1.5m diameter telescope and a 100  $\mu\text{m}$  diameter detector has a field of view of the entire receiver of 8 arcsec. This is the minimum for satellite laser ranging and free space optical communication applications, as well. Germanium has been the favored semiconductor material for APD structures for near-infrared detection from the point of view of available active apertures of 80–200  $\mu\text{m}$ . For photon counting operations, germanium APDs have to be cooled to 77 K.

Germanium photon counters are operated in an active quenched and gated mode. The quenching circuit has been optimized for germanium SPADs and is called AQGC-STD. It permits operation of the APD in a Geiger mode biased 0.5 to 3.5 V above breakdown voltage. To cool the germanium APD, a cryostat was designed with active quenching electronics built inside.

The germanium based detector package has been applied to the satellite laser ranging on the so-called ‘eye safe wavelength’ of 1540 nm. The example of the time-correlated photon counting data is depicted in Figure 4.7. The laser pulse was 32 psec long at 747 nm, the resolution of the timing chain was 20 psec. The germanium SPAD had an active area diameter of 100  $\mu\text{m}$ , was cooled by liquid nitrogen to 77 K, and biased 3.5 V above breakdown voltage.



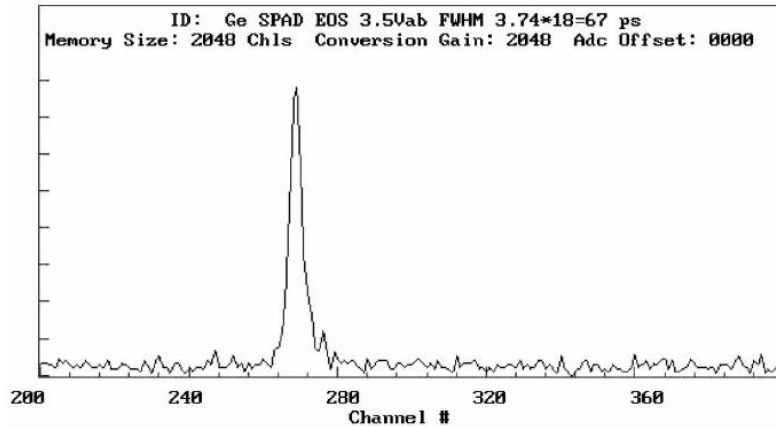


**Fig.4.7.** Timing resolution of the Ge-based SPAD. Time-correlated photon counting data illustrating the germanium SPAD timing resolution. Horizontal scale: channel number with 18 ps/channel. Vertical scale: number of counts in the range 0-1000 counts/channel. 100  $\mu\text{m}$  diameter diode, 77 K. FWHM = 67 ps.

### ***id Quantique***

<http://www.idquantique.com/>

In December 2004, *id Quantique* has launched two single photon counters for the visible range, namely the id100 and id150. According to the firm, these compact and affordable single-photon detection modules exhibit best-in-class timing resolution (40 ps), high detection efficiency (up to 40%) over a wide spectral range (350 – 900 nm), low dead time (70 ns) and low dark count rate (200 Hz). At the heart of these modules are novel silicon APDs operated in Geiger mode and designed specifically for photon counting applications. *The active area of the detector is however of only 20  $\mu\text{m}$ .*

*The id150 is the first 1 $\times$ 10 linear array on the market.* The active area of each pixel is 15  $\mu\text{m}$ , with a center-to-center pitch of 50  $\mu\text{m}$ .



**Fig.4.8.** The *id Quantique* visible SPD and SPAD linear array

This firm offers also near-IR Single Photon Detection Module (SPDM-IR). The id 200 single photon detection module is meant for photon counting at telecom wavelengths.

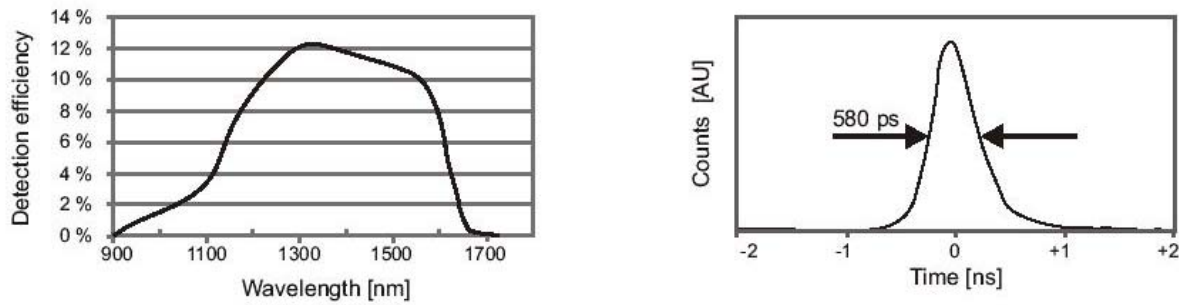


*Fig.4.9. Spectral response (left) and temporal response (right) for the id Quantique near-IR detector.*

**École Polytechnique Fédérale de Lausanne** (<http://aqua.epfl.ch/> )

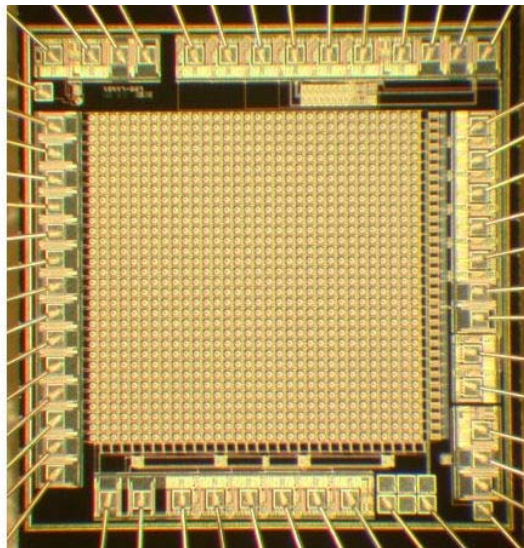


*Fig.4.10. The 32×32 SPADA of the École Polytechnique Fédérale de Lausanne*

**SensL** (<http://www.sensl.com/>)

SensL is associated with the National Microelectronics Research Centre at the University of Cork. SensL's Silicon photon counting sensors are based on a new shallow junction Geiger-mode avalanche photodiode technology. Advantages in this detector structure include increased sensitivity to blue-red wavelengths, increased response time (timing jitter) to fast optical signals and low internal operating voltages.

#### *PCMPlus – Intelligent Photon Counting Module*

The PCMPlus module is the first “intelligent” Photon Counting system on the market. It is a self contained module with integrated sensor, power supply, cooling and a full microprocessor control system. The module can be remotely configured by PC (serial or USB link). The user can optimize the sensor performance (e.g. quantum efficiency, dark count, amplification, operating temperature) for a particular application. A novel counting function makes it possible for the electronics to count the photon pulses within a defined time window and

output the result via the USB port. A mode switching option is also available whereby the sensor will switch from photon counting (Geiger) mode to avalanche (linear) mode at high light intensities. The mode switching function in effect gives a sensor a wide dynamic range, from single photons to normal light intensities. An output signal indicates which mode the system is operating in at any particular time. The counting function means it is not necessary to have external counting electronics with the PCPlus thereby simplifying the overall photon counting architecture. It is possible to integrate the PCPlus into a full PC controlled system without any additional or electronic interface cards.

## Features

- Low internal operating voltage (< 40V). Single wall mounted power supply provided
- Excellent timing resolution
- Excellent quantum efficiency at blue/red wavelengths
- Integrated Peltier cooling
- Active quench circuit – integrated in module
- Configurable via PC (user optimization of quantum efficiency, dark count, amplification and operating temperature for specific applications)
- Integrated counter (no counting electronics needed)
- Mode switching: avalanche <-> Geiger mode (thereby extending the dynamic range)
- Not damaged by excess/ambient light
- Compact size/portable
- Custom sensor design & specialized packaging to customer specification available

## Specifications

Operational voltage (internal) < 40 V

Power supply 5 V & 15 V from single wall-mounted power supply

Module size 74 mm (width) × 34 mm (height) × 115mm (length)

Quantum efficiency 45% @ 650 nm (See Figure 4.11)

Spectral range 400–850 nm (See Figure 4.11)

Timing jitter (TTL) ≤ 150 ps FWHM (See Figure 4.11)

Dead time ≤ 75 ns

Sensor size (diameter) 10, 20 or 50µm circular (custom shapes and higher specifications available on request)

Dark counts @ 25°C: 10 µm < 10 counts/sec, 20 µm < 500 counts/sec, 50 µm < 5000 counts/sec

Dark count cooled @ -20°C: 10 µm < 1 count/sec, 20 µm < 50 counts/sec, 50 µm < 500 counts/sec

Afterpulse probability low

Cooling: Peltier cooling (sensor is hermitically sealed) – configurable via PC

Impact of ambient light/bright light none (no damage)

Remote configuration voltage above breakdown voltage, amplification, operating temperature, dead time

Parameter optimization dark count, afterpulse probability, quantum efficiency

Outputs photon detected: TTL Geiger/avalanche mode: TTL

Inputs gate (signal to initiate and stop pulse counting)

Coms USB and serial (for module programming and data output)

Optical interface free space or optical fiber (with FC or other connector)

Core sensor technology silicon (CMOS Compatible)

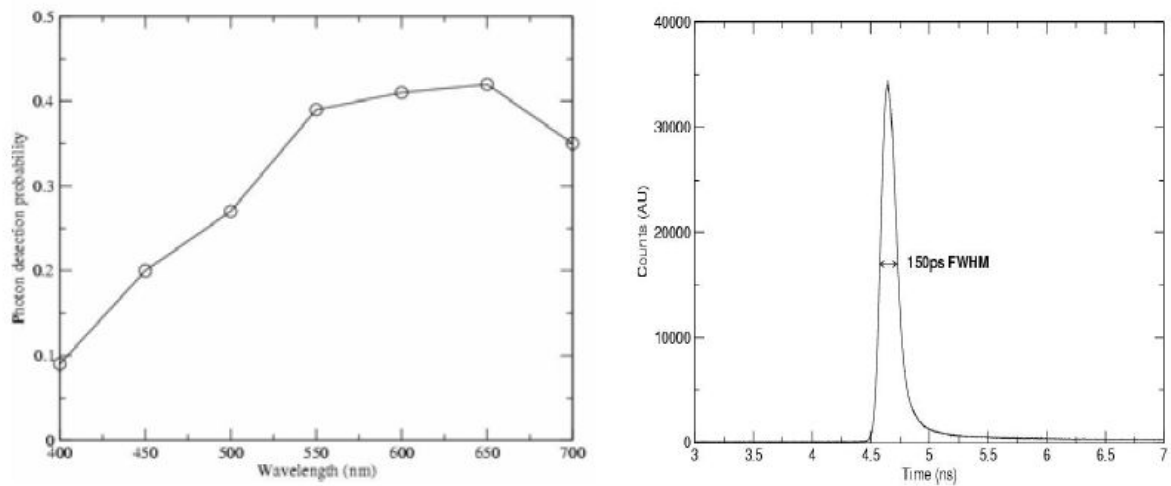


**Fig.4.11.** *SensL data. Left: Photon detection probability vs. wavelength; Right: Timing resolution*

Future developments promise to be even more apt to quantum astronomy needs (see [http://www.sensl.com/Miniturisation\\_Product\\_Options\\_V2.0.pdf](http://www.sensl.com/Miniturisation_Product_Options_V2.0.pdf))

*SensL* is pursuing options to exploit its unique technology and to augment its photon counting module (PCM) product series. This includes 1D and 2D arrays of photon counting sensors on a single chip, integrated passive and active quench and readout circuitry. Samples of 5×5 to 6×6 and 1×10 and 1×20 arrays are available on request in various device geometries. Larger array sizes are in development and can be customized to meet specific applications. Off chip passive or active quench circuitry can provide a new level of integration not possible with competing technologies. This reduces the power supply requirements since a Peltier cooler for each photon counter is not required, it is possible to have one Peltier cooler for the entire array.

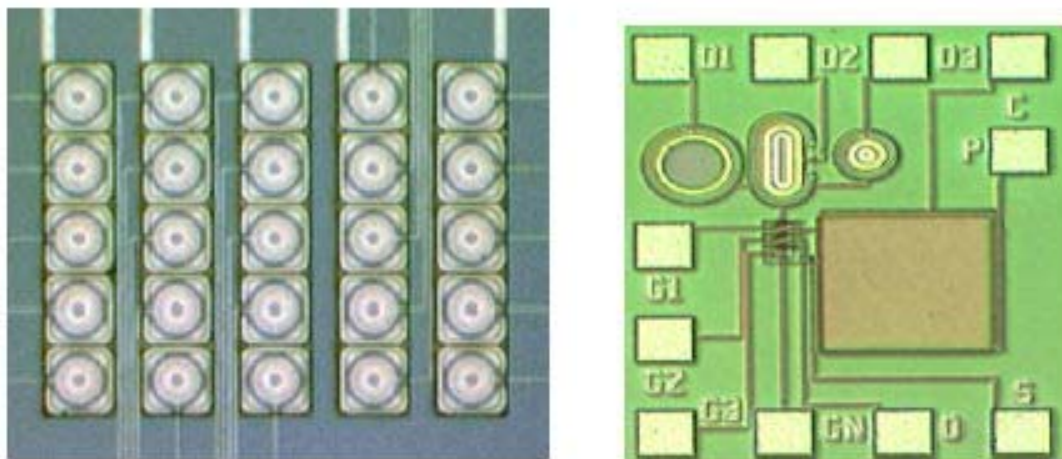


**Fig.4.12.** *SensL 2D arrays and an example of integrated quench circuit*

A unique feature of the *SensL* device design is that it is possible to operate it in linear mode below the breakdown voltage, i.e. in avalanche mode instead of the normal Geiger mode operation (namely in the APD, not SPAD regime). The device can be tailored for operation in this regime and fully integrated APDs with full readout circuitry have been manufactured.

Work is ongoing to provide 64×64 and 128×128 arrays of *linear mode detectors* and integrated readout circuitry.

## Hamamatsu

<http://www.hamamatsu.com/> :

“While Avalanche photodiodes are limited to gains below 200, they have excellent quantum efficiency in the near infrared include the S8890 and S9251 series. Low bias infrared sensitive avalanche photodiodes have typical breakdown voltage of 150V. We make APDs with visible sensitivity as well. Technical data and operation of silicon avalanche photodiodes can be found in “Characteristics and Use of Si APD”. The article “Light Levels and Noise, Guide Detector Choices” is useful in determining if an APD is an appropriate detector. For ease of use we recommend an APD module that incorporates an APD, power supply and amplifier in one package. APD arrays are also available. APD's are also widely used in high-energy physics experiments.”

Hamamatsu offers Si APDs with active areas ranging from 0.2mm to 5.0mm in diameter, hermetically sealed in metal packages. Applications for APDs include optical fiber communication, spatial light transmission, low-light-level detection, high speed bar code reader, laser radar and biomedical devices.

**Note:** *These are not SPADs, but APDs!*

## The Lincoln Lab SPAD Array

For completeness we quote a project of the Lincoln Lab to produce SPAD arrays. However, the product is likely not to be available outside that project.

See the papers [http://www.ll.mit.edu/news/journal/pdf/13\\_2aull.pdf](http://www.ll.mit.edu/news/journal/pdf/13_2aull.pdf) (Aull et al. , 2002), which discuss the properties of Geiger-mode avalanche photodiodes (APDs) and their use in developing an imaging laser radar (ladar), and presents ongoing work at Lincoln Laboratory on three-dimensional (3D) imaging with arrays of these diodes, and the integration of the arrays with fast complementary metal-oxide semiconductor (CMOS) digital timing circuits. See also Heinrichs et al. 2003.

The Lincoln Lab arrays find application for instance in the APOLLO project lead by Tom Murphy, UCSD (a 3.5 m telescope for lunar laser ranging located on Apache Point), which is described in:

<http://www.roa.es/14workshop-laser/#Presentations>  
<http://physics.ucsd.edu/~tmurphy/apollo/apollo.html>

Other details are given in the Appendix Section A3.8

## ST Microelectronics, INAF Astronomical Observatory and CNR, Catania

<http://www.st.com/stonline/>

Figure 4.13 shows an ST array of 5×5, 40 μm active area, 240 μm pitch. The quantum efficiency is very high, but it can be raised even more with proper coating. For more details, see Belluso et al. (2005).

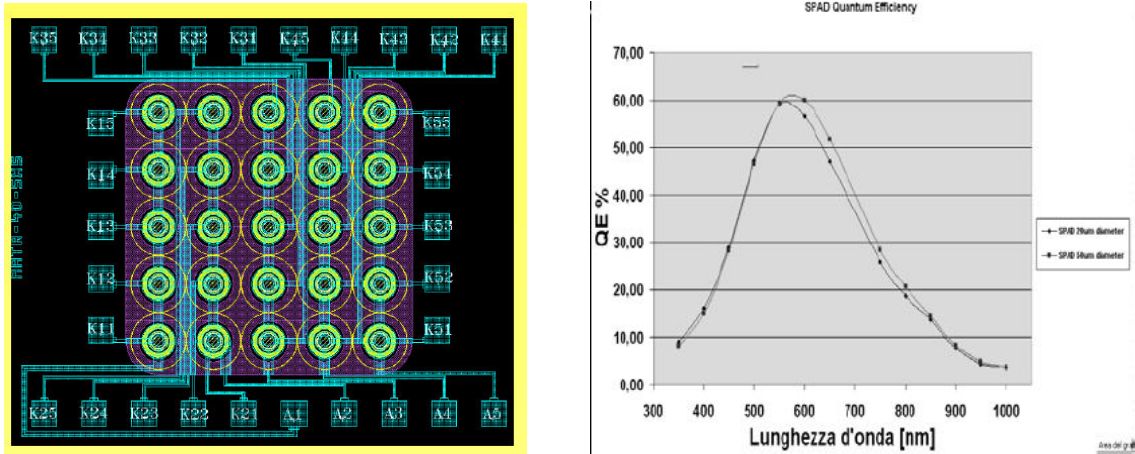


Fig.4.13. ST Microelectronics SPAD array

### 4.1.3. Futuristic detectors

The field of sensors is rapidly evolving, and several laboratory products might come to the market before the entrance in operation of OWL. An interesting paper, mostly concerning detectors useful for communication purposes, is the one by Sobolevski (2004).

#### Possible future classes of detectors

Some thinking is in progress concerning possible future types of qualitatively different detectors for astronomy. Detectors with extremely high intrinsic spectral resolution ( $R = 10,000$  or more) have been demonstrated: Graff et al. (1995); Keller (2000); Keller et al. (1995); Rosselet et al. (1995).

However, there are many more potential future detectors for astronomy:

#### “Ultimate” limits to photon detection?

Possible phase detection of optical light (e.g., with carbon nanotubes acting as electromagnetic antennas at optical wavelengths)?

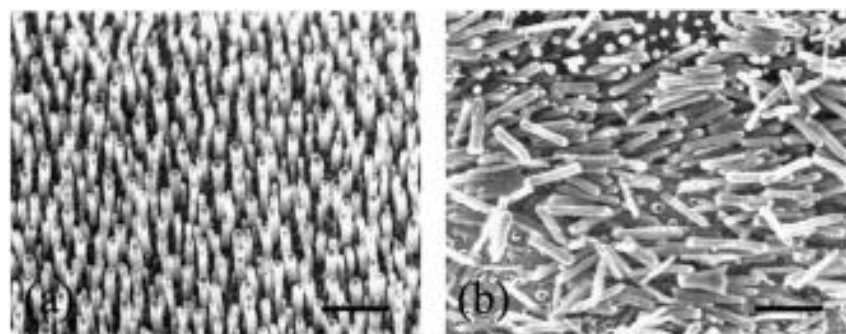


Fig.4.14. Aligned (a), and (b) random arrays of multiwalled carbon nanotubes. Scale bars: 1  $\mu$ m. (Wang et al. 2004)

Applying methods from quantum optics, there is even the possibility of non-destructive photon detection, i.e. detecting a photon through quantum entanglement without annihilating them): Nogues et al. (1999).

## 4.2. Time Tagging and Time Distribution

Quantum Astronomy raises the need to determine the arrival time of photons (briefly, to *time-tag* the photons) with an accuracy of 100 ps or better (goal 1 ps), namely from  $10^{-10}$  s (maximum allowed) to  $10^{-12}$  s (goal), in a continuous manner for the entire duration of the observations, be it seconds, minutes, even hours. To give a number, suppose we want to keep an accuracy of 10 ps for 1000 s, then we need a clock stability of  $10^{-14}$ .

This paragraph contains some considerations about the possibilities to measure and distribute this very accurate time. Furthermore, it will briefly discuss future developments, like optical clocks, space facilities distributing to ground observers sets of photons with predetermined well controlled statistical properties (thermal source, laser, entangled photons), clock synchronization by means of novel quantum devices such as entangled photons.

Two different scenarios can be considered:

- a) single telescope operation: a local device is needed, be it a signal coming from a H-maser clock inside the observatory, or remotely via fiber or air or satellite.
- b) interferometric operation, with two detectors on two distant telescopes having to be synchronized to a common central clock, as routinely done in VLBI operations.

In both cases, the start time must be connected to the UTC via e.g. a GPS signal (or a GALILEO signal in the future), e.g. in order to have a synchronization with experiments taking place in other bands, but since then onward, the observatory clock must insure the requested precision for the entire duration of the data acquisition.

Initially, we considered three solutions for the local clock:

- 1) Hydrogen Masers (H-M), both active and passive
- 2) Cesium (Cs)
- 3) Rubidium (Rb)

with the following approximate pricing figures:

Active H-M, € 4,000,000; Passive H-M, € 100,000; Cs, € 70,000; Rb, € 10,000.

It was quickly concluded that only the active H-M offers the required stability, with passive H-M still acceptable. Rb could be considered only as an economic solution useful for an initial assessment of a prototype.

### ***Common terminology***

We recall some terms usually employed in time metrology, mostly taken from the US National Institute of Standards and Technologies (NIST) web site:

<http://tf.nist.gov/timefreq/general/glossary.htm>

**Stability vs. Accuracy.** *Stability* is an inherent characteristic of an oscillator that determines how well it can produce the same frequency over a given time interval. Stability

doesn't indicate whether the frequency is right or wrong, but only whether it stays the same. The stability of an oscillator is usually specified by a statistic such as the *Allan deviation* (see later) that estimates the frequency fluctuations of the device over a given time interval. Some devices, such as an OCXO (Oven Controlled Crystal Oscillator), have good short-term stability and poor long-term stability. Other devices, such as a GPS disciplined oscillator (GPSDO), typically have poor short-term stability and good long-term stability. The relationship between accuracy and stability is illustrated in Figure 4.15:

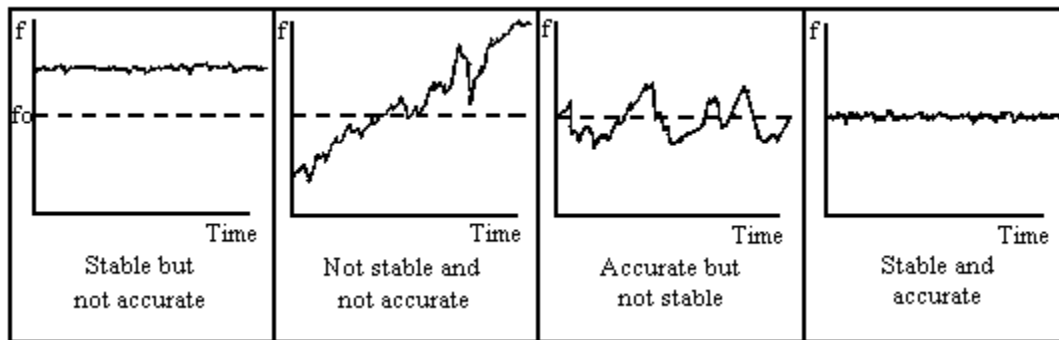


**Fig.4.15.** Accuracy vs. stability

In recent years, the term *uncertainty* has been given preference over accuracy when a *quantitative* measure is stated. Accuracy is often used in a qualitative sense. For example, we might say that a time measurement has an uncertainty of 1 microsecond, and that the accuracy of the measurement is very good.

**Allan Deviation** is a log-log plot of frequency *stability*. This statistic is sometimes called the Allan variance, but since it is the square root of the variance, its proper name is the Allan deviation. The equation for the Allan deviation is;

$$\sigma_y(\tau) = \sqrt{\frac{1}{2(M-1)} \sum_{i=1}^{M-1} (y_{i+1} - y_i)^2}$$

where  $y_i$  is a set of frequency offset measurements that consists of individual measurements,  $y_1, y_2, y_3$ , and so on;  $M$  is the number of values in the  $y_i$  series, and the data are equally spaced in segments  $\tau$  seconds long. The Allan deviation is also used to identify types of oscillator and measurement system noise.

**Active vs. Passive Frequency Standard.** An *active* frequency standard is an atomic oscillator, usually a hydrogen maser, whose output signal is derived from the radiation emitted by the atom.

A *passive* frequency standard is an atomic oscillator whose output signal is derived from an oscillator frequency locked to the atomic resonance frequency, instead of being directly output by the atoms. Unlike active frequency standards, the cavity where the atomic transitions take place does not sustain self-oscillation. *Most commercially available atomic oscillators are passive frequency standards.*

Another very useful source of information is the *Bureau International des Poids et Mesures (BIPM)* located near Paris, France. The task of the BIPM is to ensure worldwide uniformity



of measurements and their traceability to the International System of Units (SI). The BIPM averages data from about 50 laboratories (including NIST) to produce a time scale called International Atomic Time (TAI). When corrected for leap seconds, TAI becomes Coordinated Universal Time (UTC), or the true international time scale. The BIPM publishes the time offset or difference of each laboratory's version of UTC relative to the international average. For example, the BIPM publishes the time offset between UTC and UTC(NIST). The work of the BIPM makes it possible for NIST and the other laboratories to adjust their standards so that they agree as closely as possible with the rest of the world. For more information, see <http://www.bipm.fr>.

### ***Characteristics of commercially available clocks***

We provide in the following some results from a quick (and certainly not complete) market survey.

**Symmetricom** ( <http://www.symmttm.com/> )

Symmetricom designs, manufactures and markets hydrogen, cesium and rubidium standards, and quartz oscillators in numerous configurations for multiple applications. They also design and manufacture the supporting electronics, software and packaging for their products.

One of their H-maser models is the MHM 2010™, with stand-alone cavity switching auto tuning. This technique enables the MHM 2010 to deliver long-term stability normally only attributed to the most stable of cesium atomic standards. The data sheet is: MHM 2010: Active hydrogen maser:

<b>STABILITY</b>	
• Allan deviation (measured in 1Hz bandwidth):	
1s	2.0E-13
10s	5.0E-14
100s	1.3E-14
1000s	3.2E-15
Floor*	3.0E-15
• Long term:	<2.0E-16 per day*
• Auto tuning:	no external reference required
* Achieved after extended period of unperturbed, continuous operation.	

***Table 4.1. Hydrogen maser performance***

The paper: The Long-Term Stability of the U.S. Naval Observatory's Masers gives an account of the many H-M clocks owned by the US Naval Observatory, and all built by Symmetricom.

**Oscilloquartz** (<http://www.oscilloquartz.com/>)

This firm offers a variety of H-M and Cs clocks. Oscilloquartz provides also a useful document comparing cesium clock and hydrogen maser:

[http://www.oscilloquartz.com/file/pdf/Ap19Cs\\_vs\\_H1.pdf](http://www.oscilloquartz.com/file/pdf/Ap19Cs_vs_H1.pdf) .

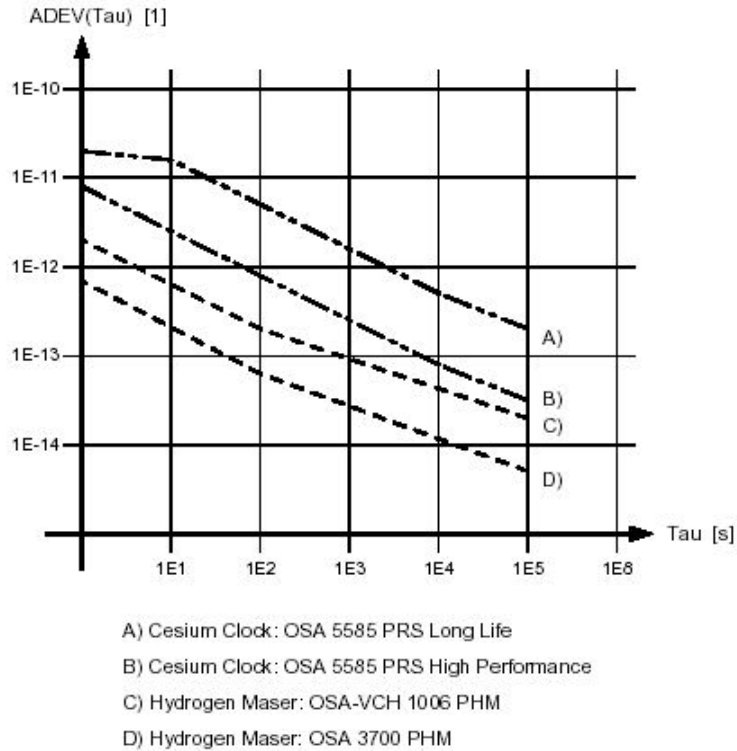


**Fig.4.16.** Cs vs. H maser short-term stability. The panel shows the Allan deviation as a function of the observation time interval for two Cs and two H-maser clock models. For an OTI less than 1 day, ADEV expresses the short time stability.

H-M are clearly superior on the short time scale, and this is their main advantage.

**Agilent** (former HP, <http://www.home.agilent.com/USeng/nav/-11567.0/pc.html>)

The Agilent 5071A primary frequency standard is the first Cs standard to specify its stability for averaging times longer than a day. The frequency accuracy is  $5 \times 10^{-13}$ , the long-term stability is better than  $1 \times 10^{-14}$ .



**Fig.4.17.** The Agilent cesium clock model 5071A

See in particular the Technical Note **BIPM Clock Data** of 2005-03-30.

### ***Dual Telescope Operations***

For this case, what can become of great importance if the feasibility of the optical VLB intensity interferometry is established, we have considered how to distribute a common time from a central station. Information received from several experts insure that there are several possibilities to distribute a time accurate as quantum astronomy demands, if the two telescopes can be connected via fibers, or are in direct view (such would be e.g. the case of the VLTs) and can be reached via lasers or microwaves. Well experimented methods of transmission and error correcting codes exist.

As a recent example, we quote the paper *Time Transfer by Laser Pulses between Ground Stations*, by Yang Fumin and collaborators (2004). Two stations, A and B, were located in same room and a mirror for reflecting the laser beams was set up at 250 meters away. Both stations were equipped with hydrogen masers that were directly compared by a SR-620 timer continuously. It is shown by the comparison results that the standard deviation of the mean of the clock differences determined by laser pulses is 24.1 ps for a 100 s interval, and the relative stability of frequency for two masers is  $1.8 \times 10^{-13}/200$  s. The uncertainty of measurement for the relative frequency differences by laser link for two masers is  $4 \times 10^{-15}$  during 6000 seconds. The comparison result by laser link is very coincident with the direct timing method.

The term **One Way Time and Frequency Transfer** indicates a measurement technique used to transfer time and frequency information from one location to another. As shown in Fig.4.18, the reference source, A, simply sends a time signal to the user, B, through a transmission medium.

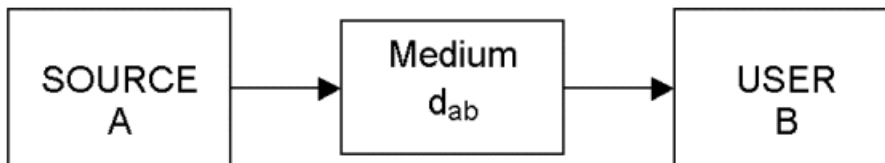


**Fig.4.18.** *The one-way time and frequency transfer technique*

The delay  $d$  over a transmission path is at least 3.3 microseconds per kilometer. If high accuracy time transfer is desired in a one-way system, the physical locations (coordinates) of the two clocks must be known so that the path delay can be calculated. For frequency transfer, only the variability of the delay (the path stability) is important.

To overcome the limitation of the OWTFT technique, the Two-Way Time and Frequency Transfer (TWSTFT) has been introduced. TWSTFT indicates the two-way technique implemented on satellites. TWSTFT differs from other methods of satellite time and frequency transfer in that signals are both transmitted to, and received from, the satellite. Many of the systematic errors present in receive-only time transfer methods, for example GPS common-view, are either eliminated or very substantially reduced. There is a presentation of Two-Way Satellite Time and Frequency Transfer (TWSTFT) on the UK National Measurement Laboratory website: [http://www.npl.co.uk/time/twstft\\_intro.html](http://www.npl.co.uk/time/twstft_intro.html) . It is useful to recall in this context the main characteristics and limitations of the GPS system.

## ***The GPS***

GPS satellites broadcast a timing signal on a phase modulated L-band carrier along with information identifying the time for which the tick corresponds. The satellites broadcast a time code referenced to the clock on the satellite, but there is also information enabling the user to obtain an estimate of GPS system time as well as UTC (USNO). The user's receiver may then compare the arrival time of the GPS signal to the local clock with a Time Interval Counter (TIC). The major challenge is to account for the propagation delay. The geometrical delay is obtained from the receiver's location (which can be obtained from the GPS system) and from the broadcast satellite positions. Major sources of timing error are the geometrical delay, the effect of the ionosphere and troposphere on the propagation time, multipath, and hardware delays. Currently, the GPS system provides time to the general public with *uncertainties measured in nanoseconds*. With a well-designed receiver system the user can obtain the time to better than 100 ns in a few minutes, and to about  $\pm 10$  ns with a 24 hour average (and a good local clock). The receiver's *location* can, in principle, be known to a few centimeters (cm), though this takes considerable effort. Users interested in ns accuracy must know their position to within a few meters. The broadcast satellite positions are only accurate to a few meters, and therefore also limit the accuracy of the geometrical delay to only 3 to 6 ns.

The ionosphere and troposphere also have a significant impact on propagation delay. Ionospheric delays can range from a few nanoseconds at night in the vertical direction to hundreds of nanoseconds during the day at low elevation angles. The navigation message broadcast by the satellites contains a model of the ionospheric delay, but this may be accurate to only within a factor of two. There are ways to improve the ionospheric correction with direct measurements using the *two-frequency method* or with code and carrier phase measurements. The accuracy with which the delays and delay variations are removed depends on how much effort one is willing to put into the task. The total excess delay introduced by the troposphere is in the range of tens of nanoseconds, and can generally be corrected to an uncertainty of a few nanoseconds. Multipath errors can be as large as tens of nanoseconds. Hardware instabilities and inaccuracies will generally be a few nanoseconds or larger. Many of these errors have a daily, or diurnal cycle, and can be averaged down if the users local clock is sufficiently stable over 24 hours.

The only relativistic effect that is included in GPS time transfer is the Sagnac delay. This is calculated from the positions and relative velocities of the two stations and can be as large as 200 ns. The uncertainty in the Sagnac effect is small compared to other sources of error.

## ***Other satellite systems***

To better exploit bandwidth spectrum and to ease interconnection between different operators, telecom operators have always looked for an independent infrastructure able to distribute in real time an accurate and stable clock reference. In addition to telecom operators, a wide range of disciplines would benefit from the availability of such an infrastructure. This is not the case as of today; available solutions are mostly spin-off of positioning systems as GPS (despite the diffusion of GPS-based receivers, it is worth reminding that GPS is a military system and not under European control), and offer limited guarantees in terms of accuracy, stability and reliability. The planned Galileo Navigation System, as a civil navigation system, is expected to improve the situation, although the Time distribution function will not be the primary system function (see later).

The **ESA Patent 407 (T&FD system, Giunta et al. 2004)** has been designed to overcome these limitations. The T&FD system concepts are based on the innovative principle to

distribute a very accurate ground-based time reference by means of a satellite network. This is done by synchronizing a low performance on-board oscillator (slave clock) with a very accurate ground time reference (master clock) and then distributing the space clock time to ground users.

Figure 4.19 shows the overall time & frequency distribution system architecture. The system concept can be broadly summarized in the following points:

- A state-of-the-art atomic clock located on ground in the Master Clock Station (MCS) is used as time reference. A backup station is provided for availability reasons in order to take the role of MCS in case of its failure.
- A less accurate clock is embarked on a satellite. The on board clock is synchronized to the ground-based time reference, thus inheriting the accuracy and stability features of the ground one and can be used as reference for the following time and frequency dissemination process.
- The radio link connecting the ground stations and the space-based time reference is operated using existing communication techniques
- After satellite clock synchronization the time/frequency reference is provided to the users:

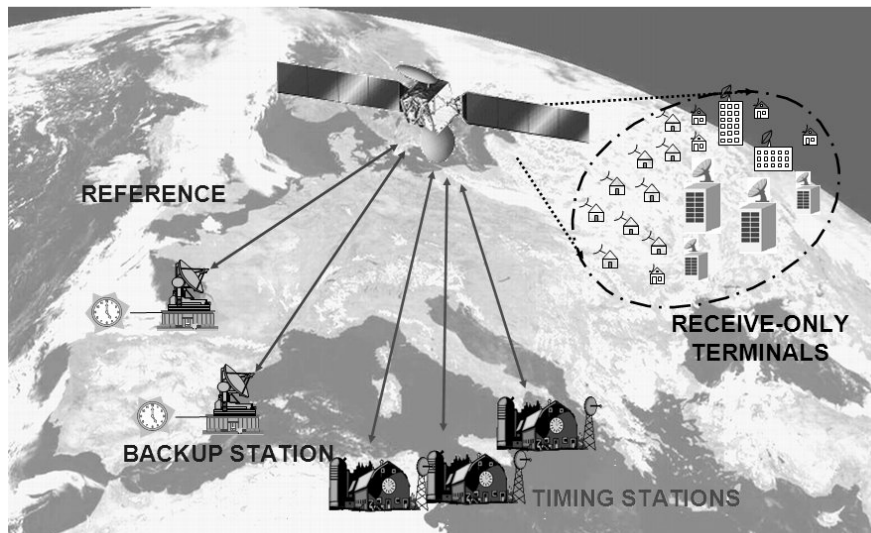


*Fig.4.19. Time & frequency distribution system architecture*

Another recent experiment, called **T2L2** (Time Transfer By Laser Link, Ravet et al. 2004), allows the synchronization of remote clocks on Earth, and the monitoring of a satellite clock, with a time stability of the order of 1 ps over 1000s and a time accuracy better than 100 ps. The principle is based on the propagation of light pulses between the clocks to synchronise (see Figure 4.20).

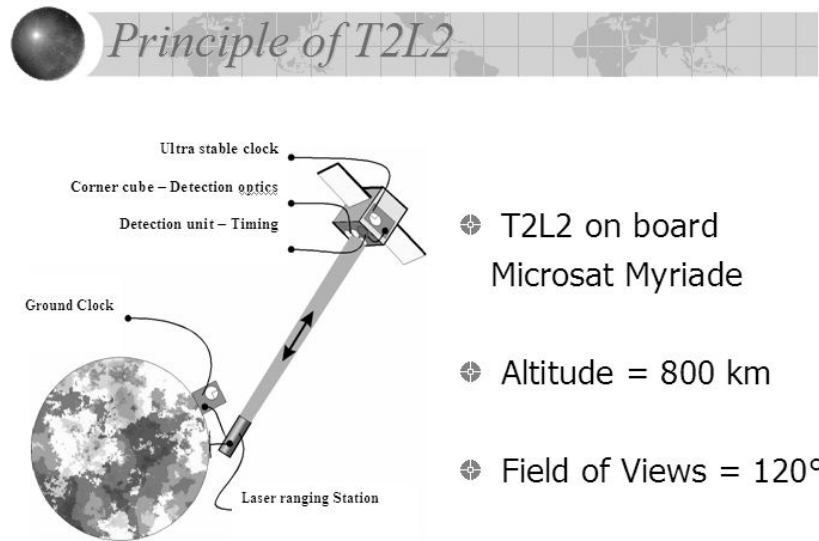


**Fig.4.20.** *The T2L2 scheme*

The ground segment is a satellite laser ranging station with a special instrumentation able to time light pulses accurately as compared to the ground clock to synchronize. The satellite payload comprises an optical package, and a time tagging unit connected to the space clock. T2L2 was proposed for both low and high altitude, respectively in the framework of the CNES micro-satellite Myriade and in the framework of Galileo. The phase B study of the space segment was concluded at the beginning of 2004. This study permitted to design an instrument having a mass in the range of 10 kg and a power consumption of 40 W. It comprises the following elements:

- A detection unit based on an avalanche photo-diode working in a Geiger mode.
- A time tagging unit able to time the photo-diode output in the satellite clock time scale with a precision better than 3 ps.
- A high index corner cube (100 mm diameter) having a large field of view.

### ***A reference system of statistical photon distributions***

Quantum astronomy will require the comparison of the statistical distributions of the acquired photons with well determined and calibrated distributions. The determination of second and higher order correlations, of properties such as photon bunching and antibunching, etc. would greatly benefit from the availability of a well known source above the atmosphere. The emerging science of quantum communication leads naturally to the near-future availability of such sources. Reference is made to studies performed under ESA Contract (*QSpace*, Asplemeyer et al. 2003), and *Quantum Communication in Space*, (Rarity et al. 2003), and to two proposals submitted to ESA by Weinfurter et al. (2005) and by Zeilinger et al. (2005).

The space segment (in the immediate, LEO satellites, but likely in the future GEO satellites) will consist of telescopes capable to send continuum light, laser light and entangled photons. The same laser can be used to produce 'normal' light and entangled photons.

### Optical Clocks

The optical transition frequencies of single ions or collections of laser-cooled atoms are emerging as the most stable and accurate frequency sources. Their high frequencies, however, make it difficult to count cycles as required for comparisons to the current cesium microwave standard. Now, femtosecond technology provides a promising means for making this difficult connection. For instance, recent developments in Research Laboratory of Electronics (RLE) at MIT open the opportunity of building optical clocks with accuracies superior to the current microwave standard — which dates back fundamentally to 1967 — by *several orders of magnitude* (see [http://www.rle.mit.edu/rleatmit/2003may\\_article01.htm](http://www.rle.mit.edu/rleatmit/2003may_article01.htm) ). Such improved clocks would find widespread applications in measurements of the highest precision and should greatly improve the resolution of today’s guidance and global positioning systems. The opportunity to greatly increase timing precision arises from recent advances in ultrashort-pulse modelocked lasers and in ultracold atom and ion physics. A major feature of the RLE program is the close integration of research efforts to apply femtosecond comb technology to ultraprecise atom spectroscopy, in a sense, creating a femtosecond comb bridge between the microwave domain and the optical domain.

Figure 4.21 gives an idea of future possible improvements in clock relative accuracy, and Table 4.2. the theoretical limit.

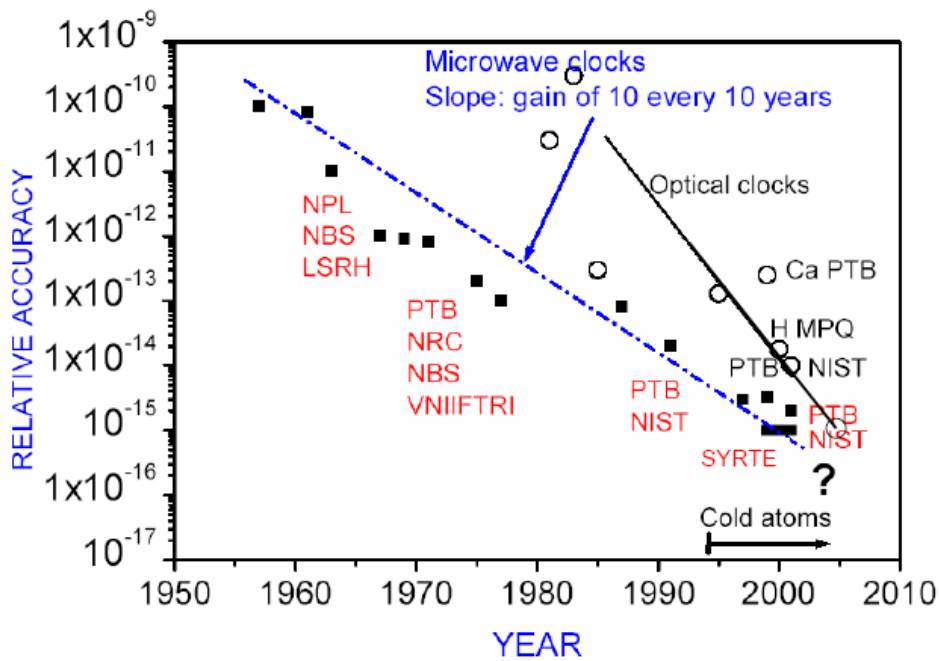


Fig.4.21. Clock accuracy improvement

Frequency stability :

$$\sigma_y(\tau) = \frac{\Delta}{\pi\omega_0\sqrt{N_{\text{det}}}}\sqrt{\frac{T_c}{\tau}}$$

Microwave fountain:  $\sigma_y(\tau) \sim 10^{-14}\tau^{-1/2}$

Optical fountain at the quantum limit  $\sigma_y(\tau) \sim 10^{-18}\tau^{-1/2}$

**Table.4.2.** *The theoretical quantum limit to clock accuracy*

The European Space Agency is looking with great interest to optical clocks. It organized the 1st *ESA International Workshop on Optical Clocks*, in June 2005 at ESTEC, Noordwijk. As a most important astrophysical application of space high accuracy timing, we quote the gravitational wave experiment LISA. See for instance in:

[http://qm-space.onera.fr/talks/RT13\\_P.Lemonde.pdf](http://qm-space.onera.fr/talks/RT13_P.Lemonde.pdf)

### ***Clock Synchronization via Entangled Photons***

As a further example of quantum technologies that might bring substantial improvement into the field of clock synchronizations, we quote the use of entangled photons. See:

<http://www.aip.org/pnu/2000/split/pnu499-2.htm> ,  
<http://www.aip.org/pnu/2004/split/701-2.html>.

Synchronizing clocks using entangled particles has been proposed by two independent teams. J. Dowling, then at JPL, proposed entangling two particles and sending them to the locations that need to be synchronized. In a separate scheme, I. Chuang of IBM proposed that two users at remote locations exchange a series of particles that serve as quantum wristwatches. These new schemes may circumvent traditional problems of synchronization, such as distortions in radio signals sent from a GPS satellite to a user. However, entanglement-based synchronization calls for technical advances. Physicists at the University of Maryland have confirmed the idea by doing an experiment in which two entangled photons are sent respectively to two detectors 3 km apart. The two clocks were synchronized within a picosecond (Valencia et al. 2004)



## 5. *QuantEYE* Conceptual Instrument Design

This Chapter expounds the present conceptual design of *QuantEYE*, which must be capable to measure the photon first, second- (and possibly higher-) order correlation functions from point-like sources as its primary scientific goal. The signal for such quantum phenomena, involving the correlation between two (or more) photons, increases proportionally to the *square* (or higher power) of the *light intensity*, and thus to the *square* (or higher powers) of the *telescope area*, making extremely large telescopes as OWL *much more sensitive* for the detection of such photon correlations than 8-m or 10-m ones.

As a second goal, the instrument must allow scientific applications where the area increase permits high time resolution studies simply impossible with 8m-10m telescopes, on time scales much shorter than possible with other existing technologies (e.g. L3CCDs, TES, STJs, etc.), namely from the nanosecond up to the millisecond. The present concept of *QuantEYE* allows measuring periodic or impulsive phenomena with time scales from nanosecond to millisecond by a posteriori integration of the counts.

### 5.1. *QuantEYE* Requirements and Identified Solutions

#### 5.1.1. Time tagging accuracy and duration of operation

Quantum effects are fully developed over *timescales of the order of the inverse bandwidth of light*. For example, using a 0.1 nm (1 Å) bandpass filter in the visible domain (a frequency bandwidth of approximately  $10^{11}$  Hz at  $6 \times 10^{14}$  Hz), the quantum effects are developed on timescales of  $10^{-11}$  seconds (10 picoseconds); enlarging the bandwidth to 1 nm would require a time resolution of  $10^{-12}$  seconds (1 picosecond).

With present day technology, we consider realistic to perform photon counting in continuous mode with a time tagging precision better than 100 ps. *Therefore, the present technology is capable to reach near the sought time domain of quantum phenomena.*

Furthermore, given the accuracy of available clocks ( $\sim 1 \times 10^{-14}$  with hydrogen masers), the continuous operation of photon counting can be extended up to *several hours*, before the accuracy of the clock starts to deteriorate the timing uniformity below the 100 ps level.

Given the strong interest of many applications (e.g. particle physics, telecommunications) to improve on those performances, it is likely that in few years the development of new detectors and optical clocks can push the time resolution into the picosecond region for several hours of continuous operation.

Regarding the secondary scientific goals: by reducing the time tagging request to the ten nanosecond level and higher, continuous counts longer than 10 hours are allowed with no difficulty.

#### 5.1.2 Spectral range and choice of detectors

The spectral range chosen in this study is from 400 to 900 nm, where existing single-photon detectors (in particular SPADs) insure a QE better than 40% on a substantial fraction inside that range, a very good timing accuracy (better than 100 ps), a very low dark count rate (of the

order of 100 Hz), as well as small power demands, and easy cooling. SPADs represent a modern technology, of great interest for different applications, with the capability to improve even further in all areas, and in particular in that of future large arrays.

Their main limitations are the dead time of approximately 75 ns after each photon pulse, a non-negligible afterpulsing (approximately 0.5% of cases), and the small light-sensitive area, typically from 25 to 200  $\mu\text{m}$  diameter.

A table of commercially available SPADs and graphs of their quantum efficiencies was presented in Chapter 4. In Table 5.1 we recall the characteristics of two different detectors, namely those of PerkinElmer and Micro Photon Devices. Their quantum efficiencies are shown in Figure 5.1.

Producer	QE	Active area dimensions [ $\mu\text{m}$ ]	Fiber Optics coupling	Max count rate [MHz]	Dark count [Hz]	Time tagging [ps]	Dead time [ns]
PE	Very high, extended to the near IR	175	Yes	10	25-500	350	50-60
MPD	> 40% at 500 nm	25, 50, 100	Yes	10	< 100 for 50 $\mu\text{m}$ active area, cooled to $-20^{\circ}\text{C}$	< 100	70

*Table 5.1. Comparison Chart of two SPADs*

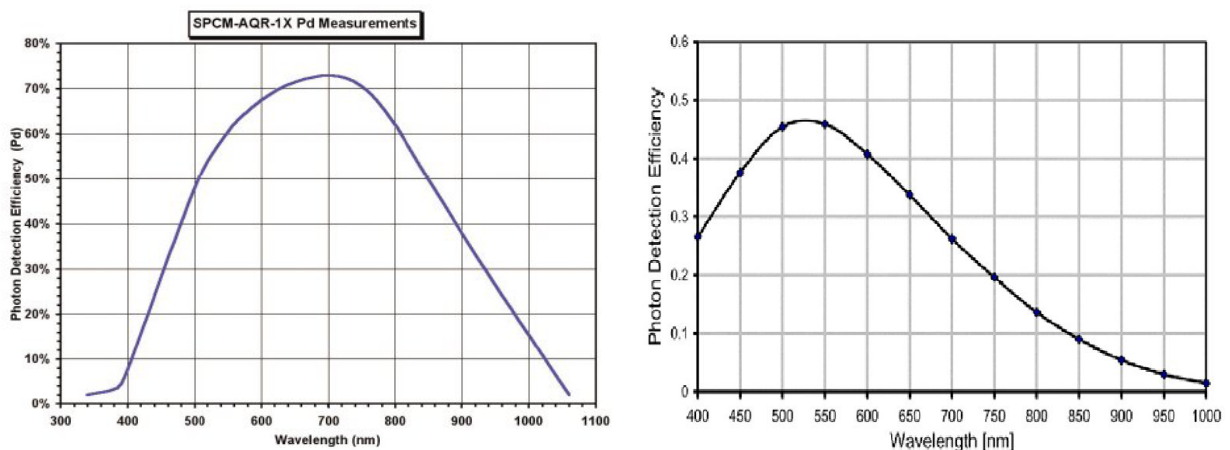


*Fig. 5.1. Quantum efficiencies of sensors from PerkinElmer and Micro Photon Devices*

Table 5.1 contains only some of the several parameters needed to make a final choice. For instance, the PE unit has a *large after-pulse probability*, a non negligible linearity correction is needed above 500 kHz, it can be damaged by strong light levels, etc. Furthermore, the

availability of the PE technology in 10 years appears doubtful. There are instead good hopes that the other devices (MPDs, SensL, STM Microelectronics, etc.) can raise their QE in the visible. In conclusion, we have concentrated our attention on a MPD-type detector.

For our application, the small area is to be preferred because of better time tagging accuracy, lower dark count and lower afterpulsing. An indicative value for the detector dimension, on which we have based our further considerations, is 50  $\mu\text{m}$ . A single focal reducer coupling directly the 100m OWL pupil to the 50 micrometer detector appears impossible to produce and align. However we have found a viable optical solution, as detailed in the following.

The alternative of an instrument with Near IR response *is not considered in this document, essentially because of the higher dark count of the present-day detectors*. However, the field of photon counting detectors in the near-IR is in rapid evolution, essentially thanks to quantum telecommunication needs (spectral range 800 – 1800 nm) so that it might be useful to reassess the situation in the near future. In particular, *correlation spectroscopy* in that band might receive a big impetus if these expectations are substantiated.

### 5.1.3 Optical design requirements

The optical design must be able to satisfy the primary and secondary scientific goals with existing technology (even if pushed to the limit). The main difficulties with present-day high-speed photon counting detectors are: a) their small area, making it exceedingly difficult to couple them directly to the 100 m pupil, b) the unavailability of good CCD-like detector arrays, c) the dead time of each detector after a photon detection.

We have identified a baseline solution capable to overcome these difficulties, in which imaging is not provided, and *QuantEYE* behaves as a fixed aperture photometer capable to cope with a very broad range of photon rates, from say 1 Hz up to 1 GHz. This baseline solution of *QuantEYE* is expounded in detail in Section 5.3. Several variants of this baseline are also considered, and the main trade-off studies are identified. Some considerations have been given also to an imaging solution.

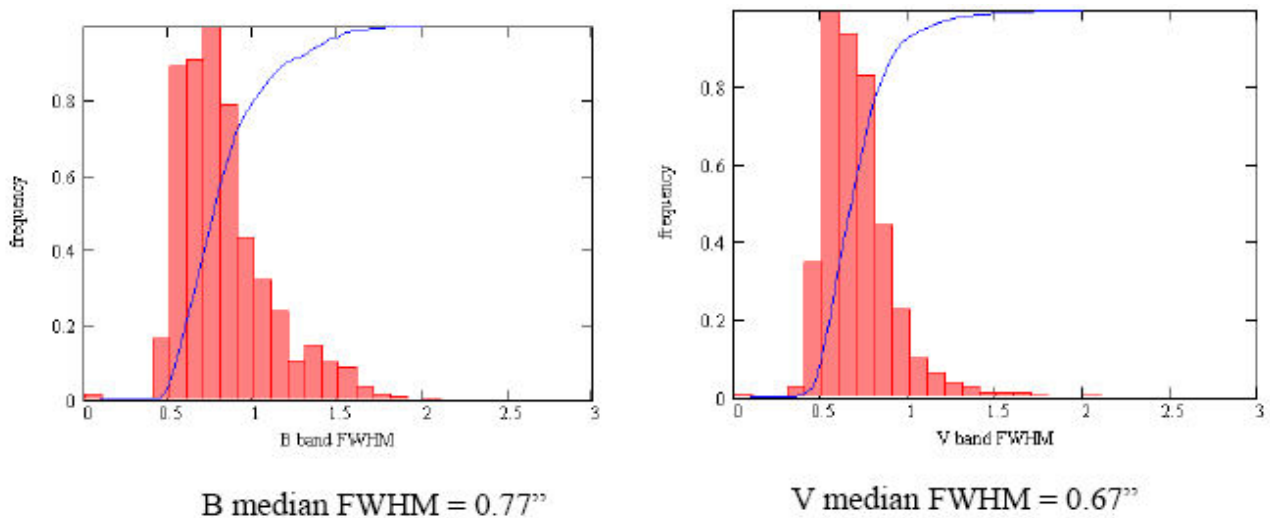


**Fig.5.2.** The seeing distribution at Paranal (ESO).

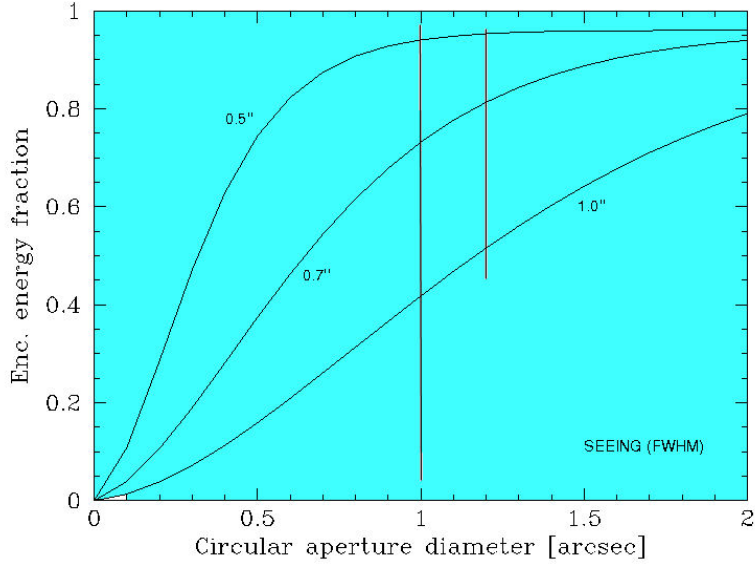


**Fig. 5.3.** Seeing and encircled energy

The baseline design assumes that a substantial fraction of the stellar flux is concentrated in a disk of  $1'' = 2.93$  mm at the OWL focus. To estimate the fraction of nights satisfying this requirement, given that the site of OWL is still unspecified, we have used the seeing statistics at Paranal (see Figure 5.2). In the case of a PSF generated from Kolmogorov turbulence, the 50% encircled energy EE50 is related to the FWHM by:  $EE50 = 1.17$  FWHM. The median values at Paranal are therefore: EE50 in B =  $0''.90$ , EE50 in V =  $0''.78$ .

We will show in a later paragraph that the sky is not the limiting factor for the primary scientific goal. Therefore one could study the possibility to increase the FoV; we have already shown that an extension to  $1''.2$  is feasible (see later). One could think of even larger FoV, but indeed the preferred solution is requesting from OWL a simple adaptive optics device.

V	$b = 0^\circ$	$b = 10^\circ$	$b = 30^\circ$	$b = 60^\circ$	$b = 90^\circ$
12	0.11	0.03	0.07	0.03	0.03
13	0.37	0.32	0.17	0.08	0.07
14	1.00	0.81	0.37	0.17	0.14
15	2.50	1.90	0.77	0.32	0.25
16	5.99	4.21	1.47	0.56	0.44
17	13.64	8.73	2.61	0.92	0.70
18	29.03	17.05	4.38	1.45	1.09
19	58.45	31.83	7.11	2.21	1.65
20	117.17	57.65	10.99	3.30	2.43
21	234.86	99.50	15.92	4.81	3.45

**Table 5.2.** Expected number of bright stars in the 3-arcmin scientific field of view (radius  $1.5'$ );  $b$  is the galactic latitude. The number of stars is derived from a standard model of the stellar Galaxy (Cox 2000)

In order to correct as much as possible the effects of telescope disturbances, varying sky transparency and of other factors affecting the entire FoV, a second identical but movable head is foreseen in addition to the primary detection head. This second head must be movable in the focal plane, in order to measure at the same time a suitable reference star, on a total travel inside the scientific fields of OWL (3 arcmin diameter). This second head carries its own focal reducer, set of filters, polarizers and detectors. The optical performances have been shown identical to those of the unit on axis. Table 5.2 shows the expected average number of stars in the scientific field of 3', for the different galactic latitudes.

It is seen that to find at least one star, we have to reach the 14<sup>th</sup> visual magnitude near the Milky Way plane, the 18<sup>th</sup> visual magnitude near the galactic pole. The numbers take into account the (small) central field that is forbidden because of the presence of the central unit.

#### **5.1.4 Filters and polarizers**

To satisfy the primary scientific goals, the instrument must have the capability to isolate narrow spectral regions, and define the linear polarization.

Narrow-band filters can be selected to cover interesting emission lines (e.g. those in Eta Carinae) and adjacent continuum. To satisfy the secondary scientific goals, broad (e.g. BRVI) and intermediate band filters are needed. A set of linear polarizers can be used in conjunction with the previous filters. A mechanical solution capable to store more than a dozen of filters is sketched in the following. More considerations about narrow band filters are provided in Section 5.9.

#### **5.1.5 Electronic acquisition and data storage**

To satisfy the primary and secondary scientific goals, *QuantEYE* will acquire long strings of data (e.g. several Terabytes per hour). The total storage unit will have a minimum capacity of 50 Terabytes, and it will be connected to an a-posteriori analysis system with a high bandwidth transport channel (fiber optics communications).

In order to perform the scientific analysis of the acquired data, the a-posteriori processing unit could be a cluster of CPUs. Specific parallel algorithms will work together, optimizing the computations of the high order correlation functions between the time tagged photons.

Furthermore, *QuantEYE* will perform real time correlation functions among different detectors (on-line correlation unit). The number of detectors to be analyzed in real time will depend on the computational power of reprogrammable logic circuits and processors, which is connected to the technological progress of CPUs, ASICs and FPGAs.

The solution identified in the frame of current technology is presented in Section 5.5.

## **5.2. Requirements set by *QuantEYE* on OWL**

The main requirements from OWL are the corrector and the active optics system, necessary to ensure the isochronism of the wavefront over the whole scientific field of 3 arcmin diameter.

A fast adaptive optics system is not mandatory, although even a modest degree of correction (e.g. tip-tilt) insuring that a larger fraction of the energy is concentrated inside a disk of 0.5''

diameter over the whole scientific area would greatly improve the photometric performances of *QuantEYE* (Figure 5.3).

Indeed, the possible effect of a full and fast adaptive optics system must still be investigated (see Section 5.11 on Instrumentation Physics).

An atmospheric dispersion corrector is not absolutely mandatory from OWL because the primary scientific goal requires very narrow bandwidths (0.1 – 2 nm), although it will be required for broad-band measurements and for correlated measurements between different wavelengths (cf. Table 5.3).

B	391 – 489 nm	730 mas
V	505 – 595 nm	290 mas
R	590 – 810 nm	350 mas
I	780 – 1020 nm	190 mas

**Table 5.3.** Typical atmospheric dispersion values at  $z = 45^\circ$  at 2400 m above sea level

Growing strategy: *QuantEYE* does not set particular specifications on the order to fill the aperture, because the main requirement is for total available area. Already at year +10, the effective diameter of OWL will exceed all other astronomical telescopes and even relevant light collectors.

The temperature control of the instrument room should be to  $\pm 1^\circ\text{C}$  (TBC).

A high-speed communication system to/from *QuantEYE* and the control room: Gigabit Ethernet, FC (fiber channel) links will be necessary in order to transfer the amount of data inside the storage unit of *QuantEYE*.

Active hydrogen maser clock in an environment controlled technical room or instrument control room; a pair of optical fiber links to this clock room.

### 5.3. Optical Design

The optical design of the proposed *QuantEYE* instrument is driven by two main factors, namely first the OWL telescope characteristics and performances, and second, the planned detector.

- The 100m aperture f/6 OWL telescope, fully corrected for geometric aberrations and limited by seeing in the absence of an adaptive optics system (which is not strictly necessary for this instrument), concentrates a good fraction of the light within a 1" image, over a fairly satisfactory percentage of the observing time. Taking into account the telescope 600 m focal length, 1" corresponds to a 3 mm diameter spot at the OWL focus.
- The planned detector is a SPAD. A 50  $\mu\text{m}$  format size (diameter, circular shape) has been assumed as baseline for the optical design. In order to limit as much as possible the loss of information owing to the detector dead time, it has been envisaged to distribute the light over a "distributed array" composed by no less than  $10 \times 10$  single SPADs (with the added benefit of raising the maximum count rate of the whole unit to 1 GHz).

### 5.3.1. Baseline: A non-imaging solution

The previous considerations and assumptions have several consequences.

First of all, a CCD-like *imaging system is not directly applicable* (in the sense of locating a SPAD array detector on the OWL focus) because the present technology does not allow the realization of a detector array with *contiguous* sensitive cells. At present, the best SPAD “arrays” consist of active cells greatly separated by dead zones (the main problem in realizing very close active cells is the cross-talk, if high speed detection is required).

Since a direct imaging system is not presently possible, a re-imaging has to be realized to send the image on the 50  $\mu\text{m}$  size SPADs. This has an immediate consequence, due to fundamental optics: defining  $y$  and  $y'$ , respectively, the one-dimensional size of the object and of the image, and  $\theta$  and  $\theta'$  the relative beam semi-aperture angles, the Lagrange invariant says that the magnification of an optical system is given by  $m = y/y' = \tan\theta' / \tan\theta$ . Owing to the  $f/6$  OWL telescope aperture ( $2 \tan\theta = 1/6$ ) and the object size, this basic principle implies that the beam aperture at the SPAD should be  $f/0.1$  ( $2 \tan\theta' = y \cdot 2 \tan\theta / y' = 3000 \cdot (1/6) / 50 = 10 = 1/0.1$ ). This value is unreachable with normal optics: so it is not conceivable to realize an optical system re-imaging the 3 mm (1 arcsec) OWL spot on a single 50  $\mu\text{m}$  size SPAD. Therefore, a different way of collecting the photons has been adopted,

The idea we have developed as *baseline solution* is to re-collimate the beam after its focus, and to subdivide the system pupil into  $N \times N$  sub-pupils, where  $N^2$  is the number of used SPADs. Since the sub-pupil size is  $N^2$  times smaller than the whole pupil, it will be much easier to act independently on each one of them, and to focus the light on the respective SPAD. In effect, since each SPAD collects light from a  $N^2$  time smaller aperture, by the Lagrange invariant in one dimension, the aperture of the beam at the detector is relaxed to  $f/1$  ( $2 \tan\theta' = y \cdot (2 \tan\theta / N) / y' = 3000 \cdot (1/60) / 50 = 1$ ). In this way, since the detector “distributed array” is essentially sampling the telescope pupil, a system of  $N^2$  parallel smaller telescopes is realized, each one acting as a fast photometer (i.e. with no imaging capability).

Each SPAD collects the light coming from a single smaller telescope. Since these smaller telescopes work in parallel and have the same Field of View, each SPAD collects light from the whole FoV of the system. In the case of a 1” FoV, which is projected on a 3 mm diameter spot on the OWL telescope, since the SPAD size is 50  $\mu\text{m}$ , a system (de)magnification  $m = y/y' = 50/3000 = 1/60$  is necessary to project the light from the OWL focus to the SPADs.

A conceptual schematic of the instrument satisfying the previous requirements is shown in Figure 5.5: the beam diverging from the OWL focus with an  $f/6$  aperture is collimated by a suitable collimator, and then sampled by a  $10 \times 10$  array of square section lenses. These lenses have an  $f/1$  aperture, which is a fairly limiting, but still acceptable value to feed the optical fibers eventually needed to bring the image on the SPAD detectors. To obtain the required  $1/60$  (de)magnification, this system has to satisfy the relation  $f_c/f_l = 60$  where  $f_c$  is the collimator focal length and  $f_l$  is the array lenses focal length.

The lenslet array needed to realize this system cannot be a “standard” one, because the present off-the-shelf lenslet arrays have poor optical quality, at least over the whole required 400-900 nm spectral range, and there is a very limited availability of arrays with *fast* lenses as required. So, an *ad hoc* lens array with square section lenses of 10 mm side must be realized.

The 10×10 mm square size has been chosen to allow the feasibility of the single lenses and their mounting on an array structure. In principle, different sizes are possible, by changing the collimator size and correspondingly the values of  $f_c$  and  $f_i$ . Smaller lenses could be a better solution for reducing the total envelope of the instrument, but the problems in realizing them and mainly in realizing the array structure and the lens mounting are not worthwhile the effort.

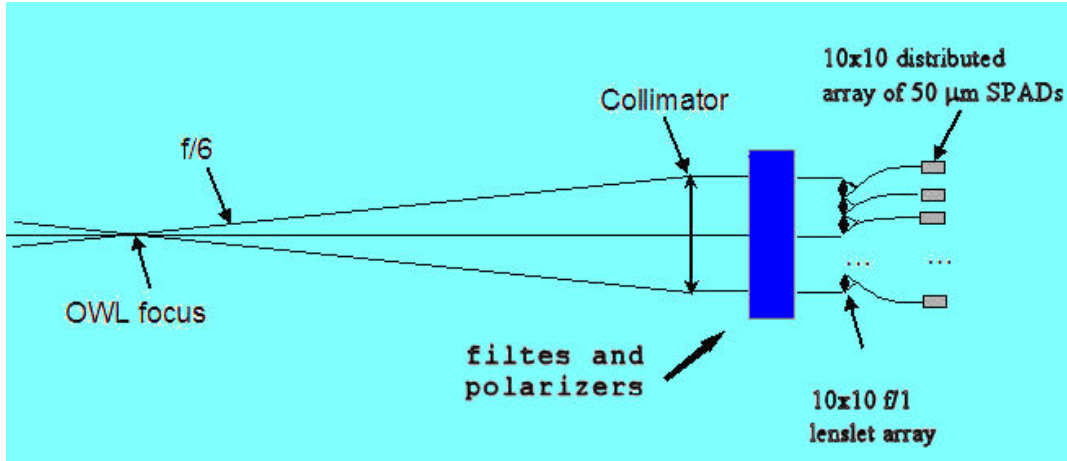


**Fig. 5.4.** Schematic of the optical design of the proposed instrument. Notice that the very narrow filters are better placed in the parallel section of the beam following the collimator. Therefore it would be simpler to have a single filter carrying unit, placed in the parallel beam section.

Given the lens size and number, it is immediate to see that the collimator must have a 100 mm diameter. A *refracting* collimator of this size does not easily offer acceptable optical quality, because of a large amount of chromatic aberration. So, an *all-reflective Cassegrain collimator* has been adopted.

In Figure 5.4 we have inserted the filters and polarizers in the parallel section of the beam, after the collimator. An alternative choice is after the OWL focus and before the collimator. In this position the beam size is very small (less than 7 mm diameter), so that a single filter wheel could host all the necessary filters; a second wheel would be necessary for the polarizers. This solution however has some disadvantages:

- owing to the small area of the intercepted beam, great care has to be taken in assuring the maximum quality of the filter surface flatness, to avoid significant wavefront distortion.

- to avoid a focusing mechanism in *QuantEYE* when changing filter, each filter must be realized with a suitable optical thickness.

- when a ray impinges from the air on a filter with an incidence angle  $\theta$ , the filter bandwidth central wavelength has a shift with respect to the normal incidence case:

$$\lambda_{\theta} = \lambda_o \left[ 1 - \left( \frac{n_{air}}{n_{filter}} \right)^2 \sin^2 \theta \right]$$



Assuming a filter refractive index  $n_{\text{filter}} = 1.5$ , at an incidence angle  $\theta = 4.8^\circ$  (marginal angle for the  $f/6$  aperture) the wavelength shift is equal to 0.3%. For a filter centered say at 500 nm, this corresponds to a shift of about 1.5 nm. In practice, this result says that if a very narrow band ( $\Delta\lambda = 0.1$  nm) interferential filter is used, the bandwidth degrades to about  $\Delta\lambda = 0.8$  nm (FWHM), which is not acceptable. So only wide-band filters and polarizers, which are not so sensitive to this bandpass degradation, can be located right behind the OWL focus. Narrow-band filters have instead to be placed along the collimated beam path, namely after the collimator, where the beam cross section diameter is about 90 mm.

For simplicity, in the following we shall assume that *all filters are placed in the parallel beam section*. This not only implies the need of relatively large interferential filters, but also of the necessary room for a suitable system exchanging these filters. Different solutions are possible, for instance 2 or 3 rather cumbersome filter wheels, or a “stack” of filters located on the side on the collimator. The first solution is fairly conventional, but would require some extra room around the collimator that would limit the useful scan area of the second head (see in the following); the second solution needs a slightly more complex mechanism, but leaves more room around the collimator. Both solutions are feasible, and quite likely others could be thought of. The decision among the various possibilities can be left to further stages. In the present concept we have chosen a simple 'stack' of filters close to the collimated beam.

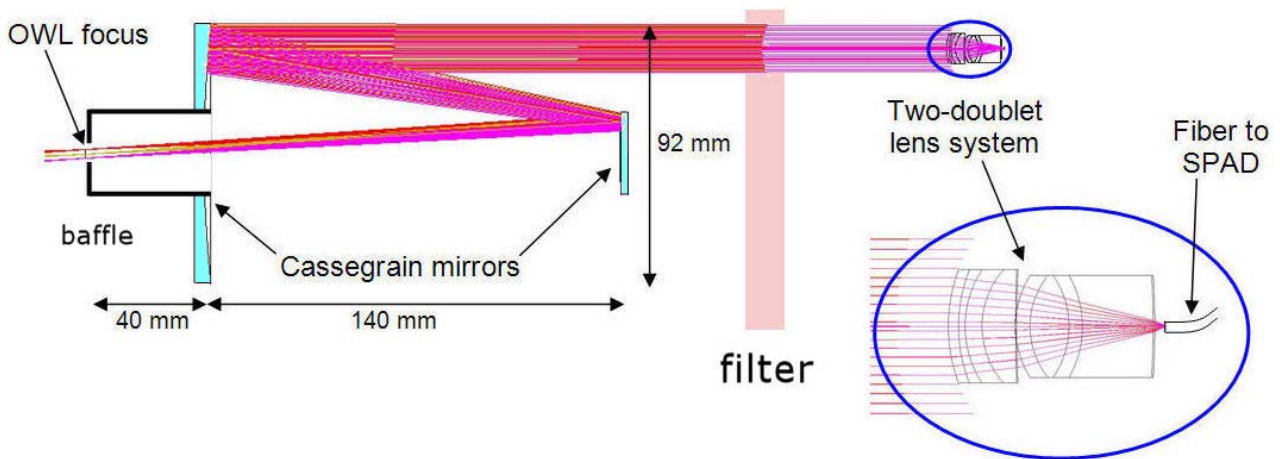


**Fig. 5.5.** Current solution of focal reducer plus lenslet array. Each lenslet is an  $f/1$  system of four square lenses (all spherical surfaces). At the focus of each lenslet there is an optical fiber.

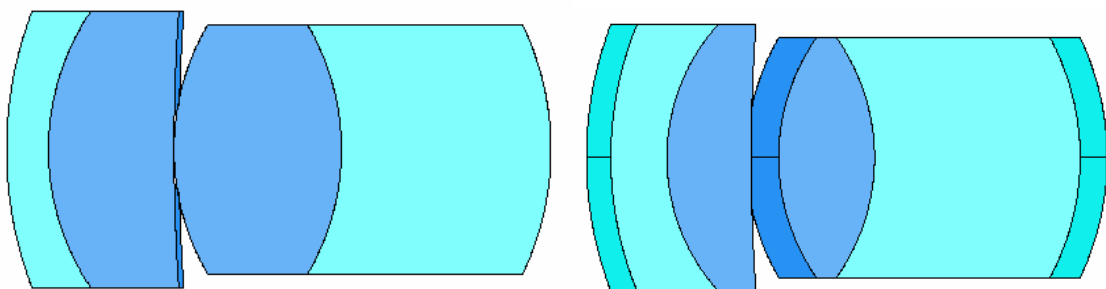


**Fig. 5.6.** Two different views of the two-doublet lens system: on the left, an axial cut view; on the right, the projection of lens system on one side. The different colors represent the two different glasses used for the lens; the horizontal segment on the right figure indicates the curved surface of the glass.

Comment	Radius	Thickness	Class	Semi-Diameter	Conic
OWL FOCUS	Infinity	180.000000		1.450722	0.000000
CASSEGRAIN M1	180.000000	-140.000000	MIRROR	14.085193	-4.000000
CASSEGRAIN M2	400.000000	250.000000	MIRROR	45.606059	-1.000000
		0.000000	-	0.000000	
LENS1:BEGIN	14.145120 V	1.500000	SF11	10.000000 U	0.000000
END - LENS2:BEGIN	9.000000	4.500000	BAFN10	8.574148	0.000000
END	71.776191 V	0.000000		8.932592	0.000000
LENS3:BEGIN	9.035611 V	6.000000	BAFN10	7.486074	0.000000
END - LENS4:BEGIN	-9.000000	7.510238 V	SF11	6.218910	0.000000
END	-10.503855 V	1.000000		1.832405	0.000000
IMAGE	Infinity			0.121377	0.000000

**Table 5.4.** Optical parameters of the proposed optical instrument.

In conclusion, the *baseline* optical design is the one shown in Figure 5.5: A classical Cassegrain telescope with 600 mm focal length and 100 mm diameter ( $f/6$ ) collimates the light from the OWL focus, and then the beam is intercepted by a two-doublet lens array system with a  $10 \times 10$  mm<sup>2</sup> section and 10 mm focal length ( $f/1$ ). For simplicity, this figure shows only a single lens of the whole array. A different view of the two-doublet lens system is shown in Figure 5.6.

The optical parameters of the system are summarized in Table 5.4 (filters have not been considered in this optical design):

- the telescope has a Cassegrain configuration: the first mirror diameter is 28 mm, the second mirror diameter is 92 mm, and the distance between the two mirrors is 140 mm.
- the surfaces of the lenses have been chosen *spherical* to have an easier manufacturing; the thickness of the first doublet is 6 mm, while the thickness of the second is 13.5 mm. Both doublets use SF11 and BaFN10 glasses, which are standard products.
- the system focus is located 1 mm behind the vertex of the last glass surface.

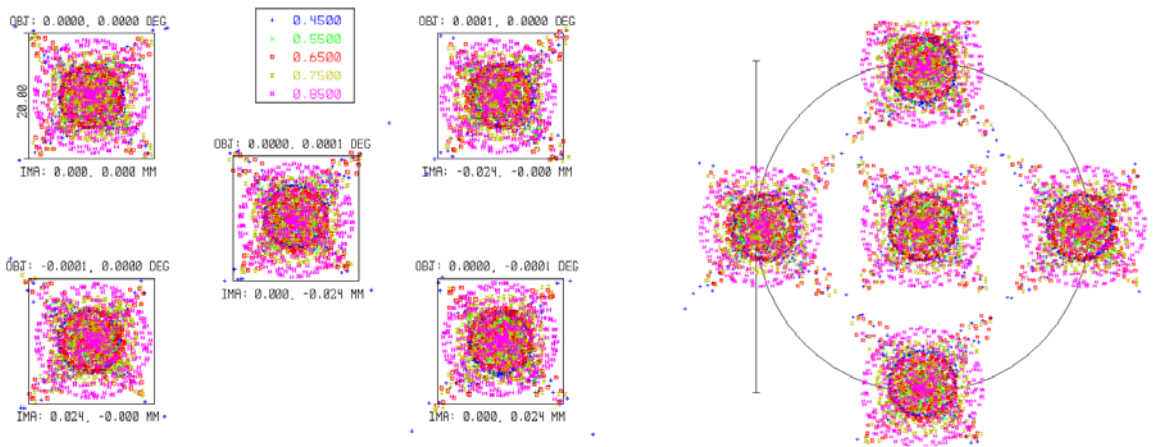


**Fig. 5.7.** Spot diagrams of the proposed optical design. On the left, the spots at the center and at the edges of the 1° field of view are compared with a 20 μm square box. On the right, the same spots are located in the focal plane and are compared with a 50 μm circle, representative of the fiber core: A 1° extended source would fill the circle. The spectral range is 450-850 nm.

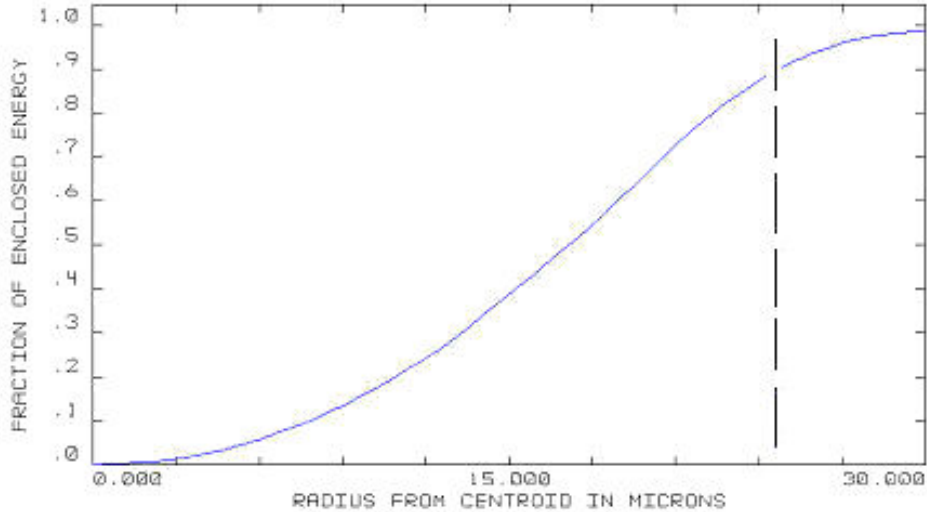


**Fig. 5.8.** *Extended source encircled energy plot: percentage of energy falling within a circle of given radius for a **uniformly** illuminated 1" extended circular source. The vertical dashed line indicates the radius of the fiber core.*

The optical performance of the system is shown in Figure 5.7. The five spot diagrams refer to four fields at the edges and one field at the center of the 1 arcsec total field of view. They are located in the focal plane in a way to fill the fiber acceptance core.

In Figure 5.8 the plot of the extended source encircled energy is shown. It is possible to see that about 90% of the 1" source energy falls within the 50  $\mu\text{m}$  diameter of the fiber core. In this simulation, the extended source is assumed to have a uniform intensity; in the real case in which the illumination distribution is of Gaussian type, we expect a still higher percentage of energy flux entering the fiber.

It must be underlined that the opto-mechanical design can still be optimized. One critical point is the tight tolerance on the lens-fiber alignment. To relax this point, we are evaluating if it is more convenient to bring the lens focus coincident with the last lens surface. This is possible simply modifying the lens, with the additional advantage of having a slightly better optical performance. The mechanical analysis on the lens focus – fiber interface, will define if this can be an optimal solution.

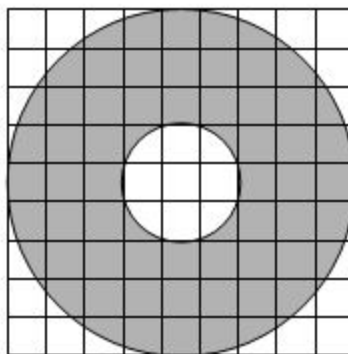


**Fig. 5.9.** *Schematics of a possible sectioning of the collimated beam by means of the lens array. Note that some lenses do not collect radiation: they can be used to monitor the “dark” statistics*

Figure 5.9 shows preliminary schematics of how the collimated beam exiting the Cassegrain collimator can be sectioned by the lens array. Nine lenses and 9 detectors are not reached by light, and four are only marginally interested. Therefore the number of really active SPADs is around 90, not 100. The difference at the moment is not significant for the statistical considerations performed in the Section on linearity and limiting magnitude. The number of ‘blind’ lenses and detectors can be minimized. However, 5 ‘blind’ detectors could be useful in any case, to give an indication of the “dark” statistics at the four corners and at the center of the FoV.

A very schematic concept of what can be the opto-mechanical lens mounting is shown in Figure 5.10. A critical point of this subsystem is the fiber link between the lens system focus and the SPAD. Contacts we had with fiber producers assure that there is no problem in providing 50  $\mu\text{m}$  core multimode (given the short length, multimode fibers are fully adequate) pure silica fibers with numerical apertures as low as 0.6 (corresponding to  $f/0.66$ ). So, the only real concern of this subsystem is relative to the mechanical interface between the lens focus and the fiber, and between the fiber and the SPAD. This is a critical point owing to the tight tolerances of the system.

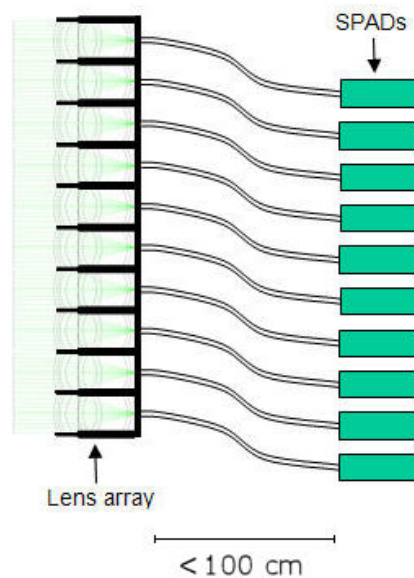


**Fig. 5.10.** Example of a possible mounting of the lens array feeding the SPADs by the fibers. NB: Lenses and SPADs are not scaled for their actual size. The length of the fibers (all of equal length) can be of 50 to 100 cm at most.

#### 5.3.1.1. Variants of the non-imaging solution

Some variants are possible with respect to this baseline design: here follows the list of the most important ones.

- **Tapering the fibers.** According to information received from fiber providers, it is possible to get fibers with a tapering factor of 3:1. This would allow a fiber with a 150  $\mu\text{m}$  diameter core on the doublet lens focus side and a 50  $\mu\text{m}$  diameter core on the SPAD side. This solution would allow a much easier fiber-to-lens relative alignment. However, a fiber core size increase implies a proportional decrease of the acceptance angle, because of the Lagrange invariant. In our case, increasing the fiber core diameter from 50  $\mu\text{m}$  to 150  $\mu\text{m}$

implies an acceptance angle  $f/3$ ; therefore, it is necessary to change the lens design, making it an  $f/3$  system. But again, owing to the Lagrange invariant, reducing by three times the lens numerical aperture means enlarging by three times the image: this brings the image size produced by the lens to  $150\ \mu\text{m}$ . In practice, tapering the fibers does not really give an advantage in terms of collected flux, because the ratio between image and fiber core size always remains 1:1. The only, but absolutely not negligible, advantage of this option is some relaxation in the relative alignment tolerance between lens focus and fiber.

Therefore, since this option is really important to ease the mechanical accommodation of the system, we have studied a small variation of the lens system optical design that would allow us to implement this option when a deeper study on fiber characteristics and quality will demonstrate its feasibility. Essentially, the only modification to the baseline is the lens design, as shown in Figure 5.11 and described in Table 5.5. In addition to the mechanical advantage, it will become easier to manufacture the lenses. Moreover, the system optical performance is slightly better (see Figures 5.12 and 5.13), with the difference of focusing now on a  $150\ \mu\text{m}$  (instead of a  $50\ \mu\text{m}$ ) spot.

In practice, with a few minor variations to the opto-mechanical design of the baseline system, it would be possible to implement this option.

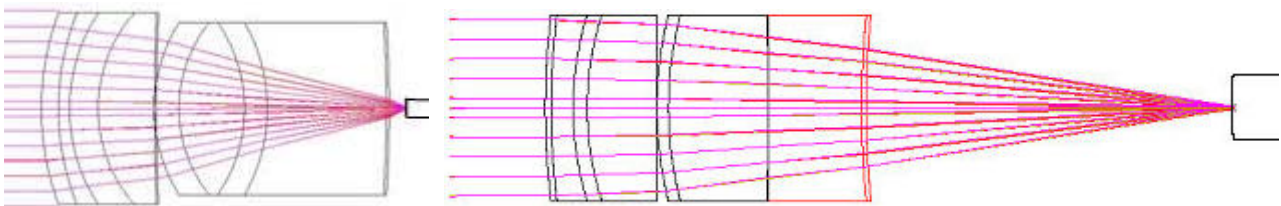


**Fig. 5.11.** Lens design and focus location if using 3:1 tapered fibers (right) vs. the baseline solution (left).

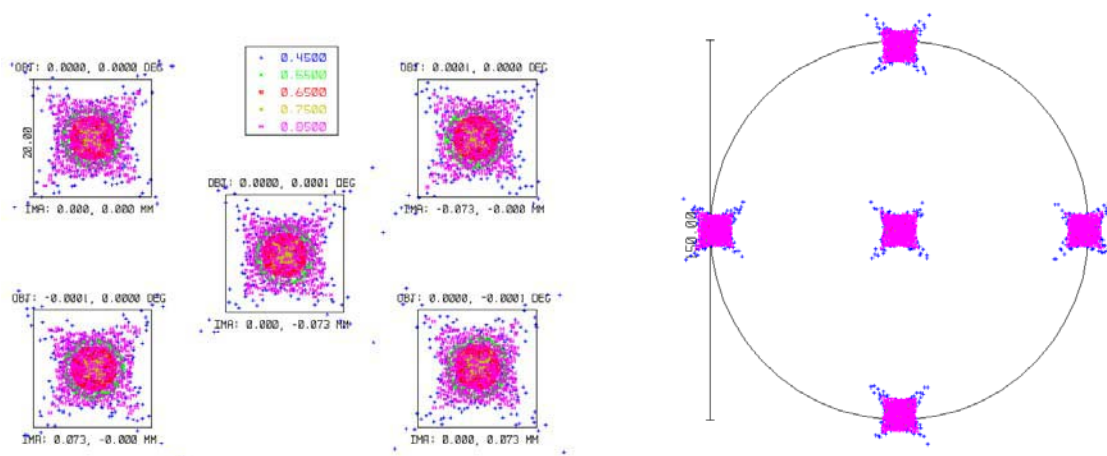


**Fig. 5.12.** Spot diagrams if using 3:1 tapered fibers. On the left, the spots at the center and at the edges of the 1" field of view are compared with a  $20\ \mu\text{m}$  square box. On the right, the same spots are located in the focal plane and are compared with a  $150\ \mu\text{m}$  circle, representative of the fiber core: a 1" extended source would fill the circle. The spectral range is 450-850 nm.

OWL FOCUS	Infinity		180.000000			1.450683	0.000000
CASSEGRAIN M1	180.000000		-140.000000	MIRROR		14.083090	-4.000000
CASSEGRAIN M2	400.000000		250.000000	MIRROR		45.599145	-1.000000
			0.000000	-		0.000000	
LENS1:BEGIN	40.000000		1.500000	SF11		10.000000	U 0.000000
END - LENS2:BEGIN	16.968663	V	4.500000	BAFN10		9.645705	0.000000
END	Infinity		0.000000			9.533724	0.000000
LENS3:BEGIN	20.448186	V	6.000000	BAFN10		9.259674	0.000000
END - LENS4:BEGIN	-400.000000		5.000000	SF11		8.257070	0.000000
END	50.000000		20.057833	V		6.877049	0.000000
IMAGE	Infinity					0.162045	0.000000

Table 5.5. Optical parameters of the optical design if using 3:1 tapered fibers

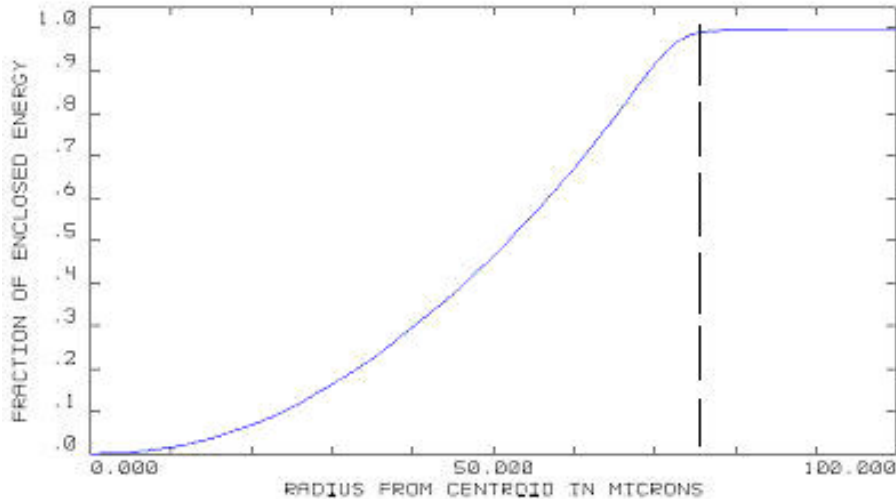
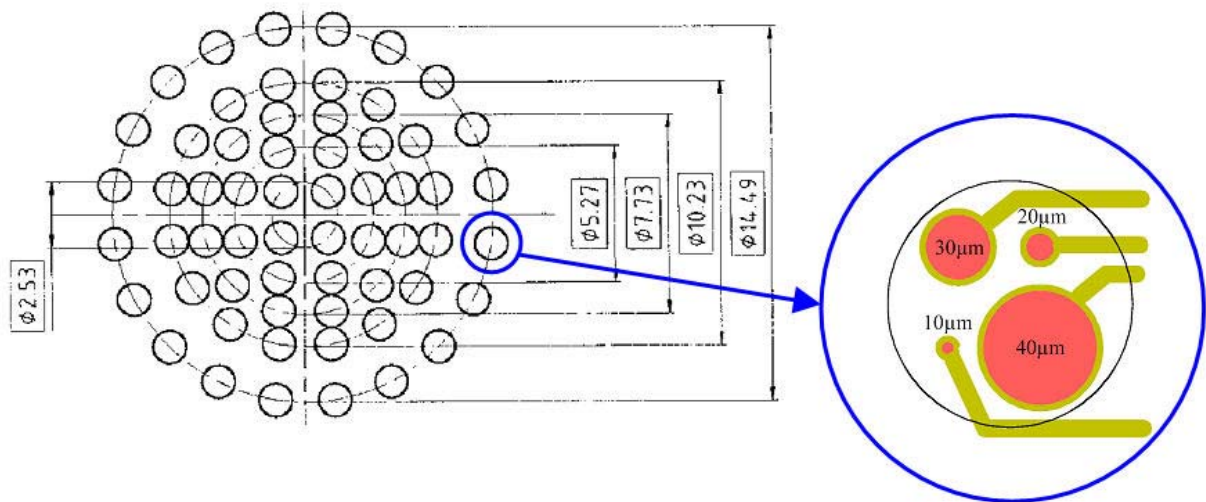


Fig. 5.13. Extended source encircled energy plot if using 3:1 tapered fibers: percentage of energy falling within a circle of given radius for a uniformly illuminated extended circular source, spectral range 400-850 nm. The vertical dashed line indicates the radius of the fiber core.

- Enlarging the field of view to 1.2 arcsec.** This option would allow collecting a higher percentage of the stellar flux. To achieve this enlargement, two solutions are possible: in the first, the collimator does not change, but the lenses have to work with an  $f/0.83$  aperture, namely with a shorter focal length (8.3 mm). The aperture system makes more difficult the provision of suitable fibers (however, already available), and still more critical the opto-mechanical interface.

In the second solution, the collimator is changed, bringing its focal length to 720 mm and consequently the diameter of the collimated beam to 120 mm (the collimator is always working at  $f/6$ ). Then, each lens of the array remains the same as before (a square of  $10 \times 10$  mm<sup>2</sup>,  $f = 10$  mm), but their number is increased to  $12 \times 12$  to cover the whole aperture. Therefore, this second option is easier to be implemented, at the expense of a slightly larger dimension of the unit. Obviously, tapered fibers could be adopted also in this case.

- **Avoiding the optical fibers.** This option appears not easily feasible with the present technology, but it is reasonable to think that it will be in the near future. The SPAD technology is indeed greatly advancing in the realization of ‘granular’ arrays, as already mentioned. One example of this is the SPADA detector, presently under realization for the adaptive optics MACAO system for VLT, in which a 60×4 SPAD array has already been built (see Figure 5.14). Although this detector has different characteristics from the one we are interested in, it shows that the technology to realize separated SPADs on the same silicon substrate is available. From contacts we had with SPAD producers, it seems that locating 50  $\mu\text{m}$  SPADs separated by 10  $\mu\text{m}$  (a distance which would bring essentially to zero the cross-talk between the detectors) is not a real problem. More difficult is to have a single 100  $\mu\text{m}$  diameter wafer with all the detectors on it, but this problem could be overcome using a wafer mosaic. If this is feasible, it would be possible to match the lens focus with the SPAD head, *removing the fiber link*. This would simplify the system, making it more robust and efficient.



**Fig. 5.14.** Schematic of the SPAD detector array. The detector has 60 “pixels” each one consisting of four different-size SPADs.

However, from the opto-mechanical point of view, if tapered fibers are available this solution may no longer be so attractive.

#### 5.3.1.2. Further advantages of the non-imaging solution

We wish to underline three further advantages of the non-imaging, pupil-slicing solution:

- Subdividing a filter in the parallel section in two or more subfilters, so that different detectors see differently colored light. In the limit, each lens could have a different filter in front. This option would allow the simultaneous observation of one object at two or more spectral bandwidth, giving some spectral capability to the system. Obviously, this is possible at the expenses of a reduced flux per each “spectral” channel.
- Changing one or more SPADs, e.g. if effective photon counting devices in the near IR become available. Then one could change the entire train filter+lens+fiber+detector, and count simultaneously in the visible and near IR. In the limit, one could think of 100

individual channels corresponding to 10×10 10-m telescopes simultaneously looking to the same star with 100 different spectral channels.

- Realizing 10×10 simultaneous HBT interferometers, again through several color filters.

### 5.3.2. An imaging solution

Finally, some consideration has been given to the possibility of realizing an “imaging” detector, and to what could be the necessary technological developments.

A first obvious development would be the capability of realizing a SPAD array with no dead area between the sensitive portions. Once this detector is available, it could be simply located on the OWL focus to obtain the requested scientific return.

Since this ideal array seems far from being realized, with “almost” present-day technology one can think of different possible solutions. In the following we expound two designs we have considered:

(1) Use a 10×10 microlens array (300×300  $\mu\text{m}^2$  section each) located at the OWL focus, acting as *field* lenses; this first array needs to be followed by a second 10×10 microlens array of the same section but different focal length acting as *relay* lens. Figure 5.15 shows a schematic of this system: instead of “real” lenses, the so called “paraxial” lenses (drawn as a straight line: they behave as *ideal* lenses of a given focal length, and do not introduce any aberration) have been simulated for simplicity.

The field lenses, located on the OWL focus and collecting a 0.1×0.1 arcsec<sup>2</sup> field of view, have a 1.8 mm focal length; each of them sends the light on the relay lens, which has the same size and a focal length of 0.26 mm, which focuses the beam to 0.3 mm distance. Owing to the suitable demagnification of the system, the spot size on the focus of this ideal system has a 50  $\mu\text{m}$  diameter, as schematically shown in Figure 5.16, where only the extreme and the central fields have been considered. At this point, the light can be collected either by fibers bringing the light on the detectors, or by a matrix SPAD detector, if available.

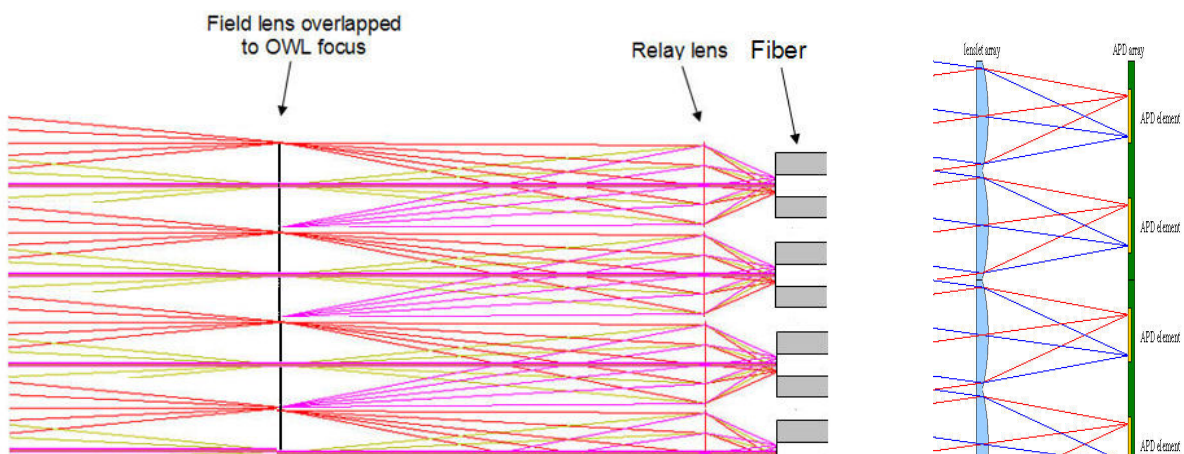


**Fig. 5.15.** Example of a possible scheme for an imaging detector. Left: A number of “channels” of the two 10×10 lens arrays coupled to a fiber. We have used in the simulation the so-called “paraxial” lenses. Right: A possible solution to couple the light directly to a matrix detector.



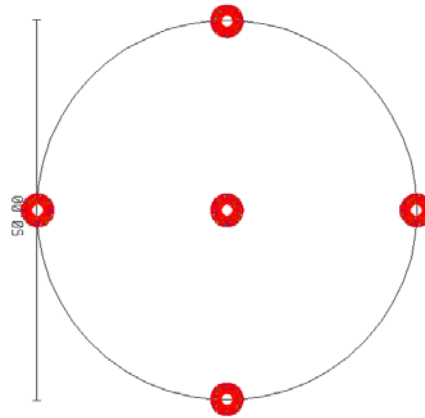


**Fig. 5.16.** Spot diagram of the focus of the ideal imaging system; only the extreme and the central fields are represented. The circle represented has a  $50\ \mu\text{m}$  diameter.

This design has two main problems:

(a) The first is the availability of the microlens array, because these lenses can only be manufactured as an “array” (not as single lenses and then integrated to form the array): this implies that the lens shape control is rather poor, and that there are many limitations in realizing the desired lens surface shape. Moreover, the large required spectral range implies the need of a complex ‘lens’ (at least one doublet for the field lens, and probably two doublets for the relay lens: in addition, the latter lens has an extremely short focal length compared to its size, making very critical its shape), or of several interchangeable arrays optimized for shorter spectral ranges.

(b) The second problem is the matching of the lens array foci with the detectors. Unless a matrix SPAD for direct coupling is available, the fiber matching would be extremely critical because of the size of the system. This is due to the fact that the foci are separated by  $300\ \mu\text{m}$ , and the fiber cladding is probably of only slightly smaller size.

**(2)** Use a  $30\times 30$  matrix of SPADs, in which the  $50\ \mu\text{m}$  active area heads are center-to-center spaced by  $100\ \mu\text{m}$ . In this case, an optical system of  $30\times 30$  microlens array ( $100\times 100\ \mu\text{m}^2$  section each), acting as field lens, can be located on the OWL focus; then, a second  $30\times 30$  microlens array ( $100\times 100\ \mu\text{m}^2$  section each), acting as relay lens, focuses the light on the SPAD active areas. This SPAD array can be considered as an evolution of the SPADA detector.

This solution is a sort of evolution of the previous one, in case the detector array is available. This design would eliminate the problem of interfacing the lenses with the SPADs through the fibers, so simplifying the global design. Unfortunately, it suffers of the same limitations described for the previous case: that is not only the detector availability, but also the capability of providing the required lenslet array (that in this case would be still more critical).

As a general comment, an imaging solution should consider how it would be possible to insert very narrow filters without degradation.

### 5.3.3. The second optical head

To monitor spurious effects (introduced either by the atmosphere through intensity scintillation, meteor flashes, cosmic ray Cherenkov flashes etc., or by the telescope through the adaptive optics, guiding errors, structural resonances, thermal vibrations etc.), a second moveable optical head, equal to the main fixed one, has been foreseen, with the capability to be pointed to a reference object in the 3 arcmin OWL scientific FoV (see Figure 5.17).

The *QuantEYE* main head is located on-axis with the OWL central ray. The second head will move around the main head with a suitable mechanism within the available FoV (see Figure 5.18). The optical performance of OWL is such that the focal spot at 1.5 arcmin from the axis is still extremely small. We have verified that the optical performance of the second optical head everywhere inside this FoV remains extremely good, with no additional aberration.

As shown in Figure 5.18, the location of the second head is somehow limited by the envelope of the main head, whose size also permits to include the filter holder.

The concept of using a second optical head is valid also for the imaging solution.

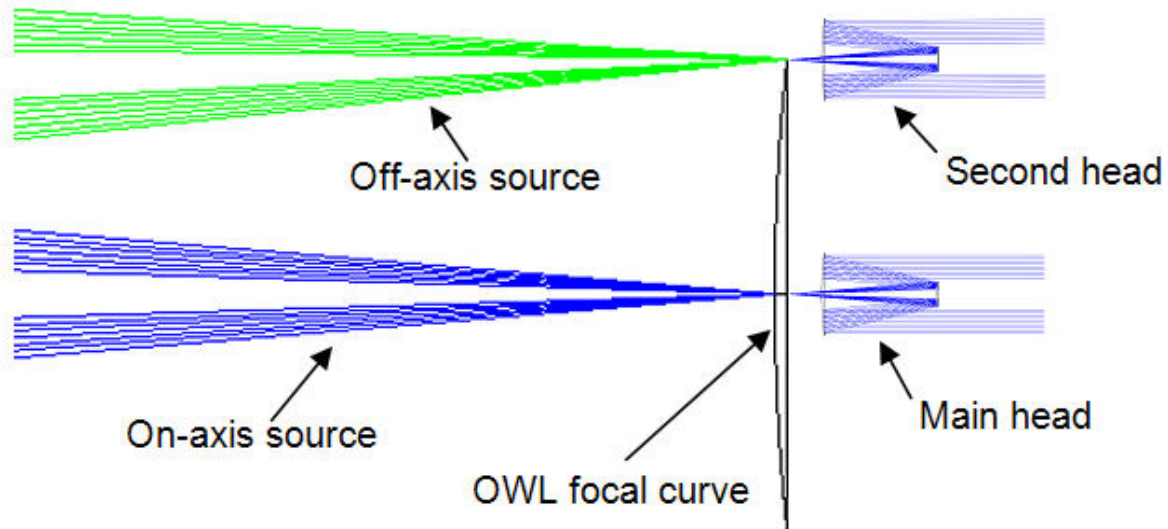


**Fig. 5.17.** Schematic representation of the main and second optical head positioned on the OWL focus. The main head works on-axis, while the second head can move inside the 3-arcmin scientific FoV.

### Calibration unit

A *calibration unit*, to inject arc, thermal and laser light into the detector unit, through the entrance aperture is also foreseen. The light can be injected into the collimator either via movable mirrors or movable fibers.

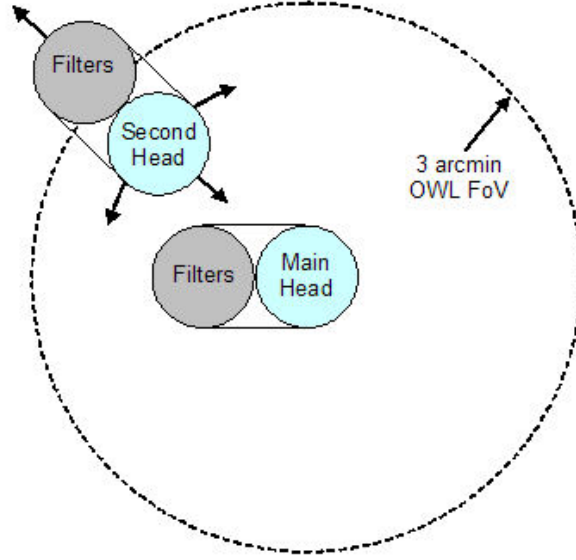


**Fig. 5.18.** Schematic top-view representation of how the OWL FoV is occupied by the two optical heads. *QuantEYE* will fit inside the inner 534.2 mm diameter. For a more realistic view, the filter stack on the side of the collimator is also represented. The arrows on the second head indicate its possible movements on the OWL focal surface.

#### 5.4. Photon Budget and Limiting Magnitude

The following numbers are indicative only, because no great precision is required at this stage.

From the calibration of Vega:

$V = 0$  corresponds to  $f(5556 \text{ \AA}) = 3.44 \times 10^{-9} \text{ erg}\cdot\text{cm}^{-2}\cdot\text{s}^{-1}\cdot\text{\AA}^{-1} = 3.44 \times 10^{-8} \text{ W}\cdot\text{m}^{-2}\cdot\mu^{-1}$  (outside the atmosphere)

In photon flux, recalling that the energy of a photon is  $E = 1.98610 \times 10^{-8} / \lambda(\text{\AA}) \text{ erg}$ , we have:

$N_{\text{ph}, A}(V=0) \approx 1000 \text{ ph}\cdot\text{cm}^{-2}\cdot\text{s}^{-1}\cdot\text{\AA}^{-1}$  at 5556 \AA (or else,  $N_{\text{ph}, \text{Hz}} \approx 1 \times 10^{-8} \text{ ph}\cdot\text{s}^{-1}\cdot\text{cm}^{-2}\cdot\text{Hz}^{-1}$  at  $5.4 \times 10^{14} \text{ Hz}$ )

The average atmospheric extinction is estimated as 0.2 mag ( $\approx 20\%$ ), so that:

$N_{\text{ph}, A}(V=0) \approx 800 \text{ ph}\cdot\text{cm}^{-2}\cdot\text{s}^{-1}\cdot\text{\AA}^{-1}$  at 5556 \AA (or else,  $n_{\text{ph}, \text{Hz}} \approx 8 \times 10^{-9} \text{ ph}\cdot\text{s}^{-1}\cdot\text{cm}^{-2}\cdot\text{Hz}^{-1}$  at  $5.4 \times 10^{14} \text{ Hz}$ )

Over the OWL aperture ( $\approx 7.3 \times 10^7 \text{ cm}^2$ , including obscuration), with an assumed overall reflectivity of 0.6, Vega would produce a photon rate of:

$$A \cdot R^6 \cdot N_{\text{ph}, A} = 7.3 \times 10^7 \times 800 \times 0.6 = 3.50 \times 10^{10} \text{ ph}\cdot\text{s}^{-1}\cdot\text{\AA}^{-1} = 35.5 \text{ ph}\cdot\text{ns}^{-1}\cdot\text{\AA}^{-1}$$

With quantum efficiency  $\text{QE} = 0.4$ , and a filter (plus fibers if present) transmission  $T = 50\%$ , the count rate would be:

$$Q = QE \cdot T \cdot A \cdot R^6 \cdot N_{\text{ph}, \text{\AA}} = 0.4 \times 0.5 \times 7.3 \times 10^7 \times 800 \times 0.6 = 0.70 \times 10^{10} \text{ c} \cdot \text{s}^{-1} \cdot \text{\AA}^{-1} = 7.0 \text{ c} \cdot \text{ns}^{-1} \cdot \text{\AA}^{-1}$$

For simplicity, let us consider 10×10 detectors (the real number  $N$  of active SPADs will be closer to 90 than to 100, and at any time after one detection it will decrease to  $N-1$  for the duration of the dead time) and let us divide this count rate over 10×10 individual heads: the maximum individual count rate from Vega is  $0.07 \text{ c} \cdot \text{ns}^{-1} \cdot \text{\AA}^{-1}$  (count rate 0.07 GHz), and the average time between the arrival of two photons on the same detector is 14.3 ns.

Inserting a polarizer, and assuming that the flux from Vega is totally unpolarized, the previous count rates must be divided by 2, and the average time between the arrivals of the two photons is doubled to 28.6 ns.

Again for simplicity, in the following we shall assume that the dead time of each SPAD is 100 ns (actually, the dead time for selected SPADS can be as low as 70 ns, the maximum count rate is then 14 MHz, and the linear regime would start at slightly brighter magnitudes).

As is well known, the proper statistical analysis of photon counting is exceedingly intricate. A deep insight about quantum theory of photoelectric detection of light can be found in the quoted book by Mandel and Wolf (*Optical Coherence and Quantum Optics*, Chapter 14), where topics such as coincidence detection and counting statistics are discussed in precise examples: coherent states, laser light and partially/polarized thermal light. The detection and characterization of a specific quantum phenomenon would require the complete quantum mechanical solution of the field + detector interaction, which is strictly dependent on the actual characteristics of the SPADs.

The more conventional problem of detecting *fast variability* in a peculiar object using photon counting, has been treated in several places, and many statistical tools have been developed in the past literature. Previous experiments in the astronomical context (e.g. MANIA, see Appendix 3) derived the correlation functions from the counting statistics, either with custom developed statistical techniques or from second moment of the photoelectron counts, which contains information about the correlation function of the measured events.

We have summarized some of these considerations in Appendix 1.

For the present report we have given only some representative estimates, using the previous assumptions, of linearity regime, limiting magnitude and data string length.

#### 5.4.1. Linear regime

First, we wish to check the linear regime of *each individual* SPAD.

The relevant Poisson formula is:  $\Pi(x) = \frac{\langle n \rangle^x}{x!} e^{-\langle n \rangle}$ ,

where  $\langle n \rangle$  is the average number of counts in the unit time. Assume as before a dead time of 100 ns for each detector, so that 100 ns becomes in this context the time unit.

For each *individual* detector unit, the average count rate from Vega in this unit time is  $\langle n \rangle \approx 3.5$ , and the exponential is  $\approx 3.0 \times 10^{-2}$ . Thus, the probability of receiving 0, 1, 2, 3, ... photons in 100 ns is as in Table 5.6.

Notice the strong non-linearity of the detector for the brightest magnitudes. Even at the 5<sup>th</sup> mag,  $P(2)/P(1) = 0.02$ , which is certainly not negligible with respect to the primary application of detecting deviations of second order effects from a Poisson distribution.

V	P(0)	P(1)	P(2)	P(3)	P(2)/P(1)	P(3)/P(1)
0.00	3.02E-02	1.06E-01	1.85E-01	2.16E-01	1.75E+00	2.04E+00
2.50	7.05E-01	2.47E-01	4.32E-02	5.04E-03	1.75E-01	2.04E-02
5.00	9.66E-01	3.38E-02	5.91E-04	6.90E-06	1.75E-02	2.04E-04
7.50	9.97E-01	3.49E-03	6.10E-06	7.12E-09	1.75E-03	2.04E-06
10.00	1.00E+00	3.50E-04	6.12E-08	7.14E-12	1.75E-04	2.04E-08
12.50	1.00E+00	3.50E-05	6.12E-10	7.15E-15	1.75E-05	2.04E-10

*Table 5.6. Poisson probabilities*

#### 5.4.2. Limiting magnitude

Primary scientific goal (quantum effects)

For the primary scientific application (measurement of second and higher order correlation functions), *a very narrow bandwidth is required, and no time integration of counts is allowed.*

In order to calculate the limiting magnitude, the following naïve considerations set a first limit:

- the entire 10×10 detector is able to produce up to 1 count every nanosecond, time tagged to better than 100 picoseconds. After one pulse, any SPAD will stay ‘dead’ for 100 nanoseconds.

- at  $V = 0$ , through a 1 Å bandpass and a linear polarizer, the count rate *over the whole detector (10×10 SPADs)* is  $C(0) = 3.5 \text{ c} \cdot \text{ns}^{-1} \cdot \text{Å}^{-1}$

- the dark count of each individual SPAD is assumed  $100 \text{ c} \cdot \text{s}^{-1} = 10^{-7} \text{ c} \cdot \text{ns}^{-1}$ , or else  $D = 10^{-5} \text{ c} \cdot \text{ns}^{-1}$  in total.

- the night sky is equivalent to one  $V = 20$  per arcsec<sup>2</sup>. Contribution from other sources, e.g. Cherenkov light from cosmic rays, scattered moonlight, is ignored. The night sky is negligible in the following considerations. Notice that with 1Å bandpass the dark count, not the sky, is the limiting factor.

Therefore, the count rate from a star becomes equal to the count rate from the dark when:

$$C(0) \times 10^{-0.4V} = D$$

namely at  $V = 13.86$ .

This result simply means that in order to perform a meaningful statistical analysis (through correlation functions or other complex procedure), a long string of counts must be accumulated for stars fainter than the 12<sup>th</sup>, as estimated in the following paragraph.

### 5.4.3. Integration times

To roughly estimate how long the integration time (and consequently the data string length) might be to fulfill the primary scientific goal, we have followed two different roads.

(a) First road, we apply the conventional photometric considerations. Suppose we count for 1 second. The conventional  $S/N$  ratio over the whole detector becomes:

$$\frac{S}{N} = \frac{C(0) \times 10^9 \times 10^{-0.4V}}{\sqrt{C(0) \times 10^9 \times 10^{-0.4V} + D \times 10^9}} \quad (\text{per second})$$

with the result ( $C(0) = 3.5$ ,  $D = 10^{-5}$ ) :

$S/N = 583$  at  $V = 10.0$ ,  $S/N = 165$  at  $V = 12.5$ ,  $S/N = 30$  at  $V = 15.0$ ,  $S/N = 3$  at  $V = 17.5$ ,  $S/N = 0.3$  at  $V = 20.0$ .

Therefore, in order to reach a  $S/N = 100$  at any magnitude, the length  $L$  of the strings would be:

$V = 10.0$	,	$L =$	0.03 seconds
$V = 12.5$	,	$L =$	0.4 seconds
$V = 15.0$	,	$L =$	11 seconds
$V = 17.5$	,	$L =$	845 seconds
$V = 20.0$	,	$L =$	81,900 seconds

a result which sets an effective limit around the 18.5<sup>th</sup> magnitude.

(b) Second road, we calculate the exposure time needed to ascertain the deviation of the observed statistics from a strict Poisson distribution. In other words, we want to check if the observed 2 or 3 photon coincidences in the unit time are significantly different from what is expected from a Poisson distribution of the stellar (plus dark) counts.

Indeed, the non-imaging solution was conceived in order to avoid the dead-time problem and to permit the study of coincidences to better than 1 nanosecond. Recall the dead time effect: if two photons impinge on the same SPAD within 100 ns (as before, for simplicity we have carried out the calculations assuming 100 ns as dead time for each individual detector), then the SPAD would produce only one count. If one SPAD gives a count at a certain instant, any other count in the same time bin of 1 ns must come from another SPAD (there are 99 of them). This second count can be a good photon from the star, or a dark count photon. If a third count arrives in the same time bin, then it must come from one of the other 98 SPADS, etc. At this stage of a very rough analysis, there is no point to distinguish  $N$  from 100, and 98 from 99 or 100. Therefore, statistically at least, we should be able to count almost all pairs or triplets of photons, even if arriving within 1 ns. ***This is why the baseline solution of QuantEYE is sensitive to quantum effects.***

Therefore, a very rough calculation has been performed, namely to determine the time needed for finding at least two or three counts in the same time bin if the statistics is strictly Poissonian, simply as  $1/P(2)$  and  $1/P(3)$  over the  $10 \times 10$  SPADs array. The results are in Table 5.7.

V	T(2) s	T(3) s
10.00	1,63E-02	1,40E+02
12.50	1,63E+00	(1,40E+05)
15.00	1,63E+02	(1,40E+08)
17.50	1,63E+04	(1,40E+11)
20.00	(1,63E+06)	(1,40E+14)

**Table 5.7.** Time needed to detect quantum effects.

We take these numbers as the *maximum interval of time* needed to ascertain the deviation from a strictly Poisson distribution. If the photons come in bursts, then the exposure time would correspondingly decrease

The two roads give essentially the same approximate results. Is it possible to improve on these figures, in order to analyze fainter magnitudes? One can think of:

- i) selecting SPADs with smaller dark counts
- ii) carefully characterizing the statistics of the noise of each SPAD, and see if there are features allowing a distinction between dark, sky and *bona-fide* stellar photon counts. The worst case is if the three contributions have the identical power spectrum.
- iii) implement dedicated statistical algorithms

(b) Secondary scientific goals

In this case we can use larger bandwidth and integrate the counts.

In the following we have set a bandwidth of 20 nm, removed the polarizing filter, assumed a sky of  $V = 20/\text{arcsec}^2$  and integrated the counts from 10 ns to 3 hours. The results are in Table 5.8, which shows the exposure time needed to achieve a given S/N.

Notice that the integration is performed *post-facto*: *QuantEYE* has indeed a tremendous linear range, probably unparalleled by any other instrument. Furthermore, it preserves the arrival times of each individual photon to better than 100ps for more than 3 hours.

V	S/N = 100	S/N = 10	S/N = 3
5.0	1 $\mu$ s	10 ns	1 ns
10.0	100 $\mu$ s	1 $\mu$ s	100 ns
15.0	10 ms	100 $\mu$ s	10 $\mu$ s
20.0	4 s	40 ms	4 ms
25.0	3 h	100 s	10 s
27.5		3 h	1000 s
30.0			>10 h

**Table 5.8.** Limiting magnitude of *QuantEYE* when time integrating

In this case, the already quoted statistical devices (e.g. those used by the MANIA group) can be applied.

Given the possible interest to utilize *QuantEYE* with slices of the pupil, we have also calculated the limiting magnitude per single detector, through a 1 Å bandwidth and linear polarizer, as in Table 5.9.

Regarding the secondary scientific goals, the limiting magnitude is faint enough to cover all foreseen applications (accretion disks, occultations, microlensing, etc.) down to the 28<sup>th</sup> magnitude.

V	1 ms	1 s	100 s	1 h	3 h
5.0	19	592	5915	35491	61473
7.5	5.9	187	1868	11209	19414
10.0	1.8	58	583	3500	6062
12.5		16	165	990	1714
15.0		3.0	30	181	313
17.5			3,4	21	36
20.0			0,4	2.1	3.6
22.5				0,2	0.4

*Table 5.9. Single SPAD S/N through a 1 Å filter and linear polarizer*

## 5.5. Data Acquisition

In this Section we outline a *QuantEYE* acquisition system that uses present day technologies.

Future technologies are likely to appear. Furthermore, the application of quantum information in the post processing of the data could become very interesting. In Section 1.1, the conceptual importance of the *qubit* was highlighted, and it was pointed out that in the next years a quantum computer will most likely be available. Using a quantum computer, or a hybrid quantum-classical computer, some complex operations could become much easier. For example, the Grover quantum algorithm would permit searches in a large database much faster than the classical search algorithm. Another example is the quantum Fourier transform (see also Section 5.12).

However, for the solutions adopted in the present paragraph, these future developments are not required. The proposed system has several features in common with large detectors for neutrinos or for the particle accelerators like the Large Hadron Collider (CERN).



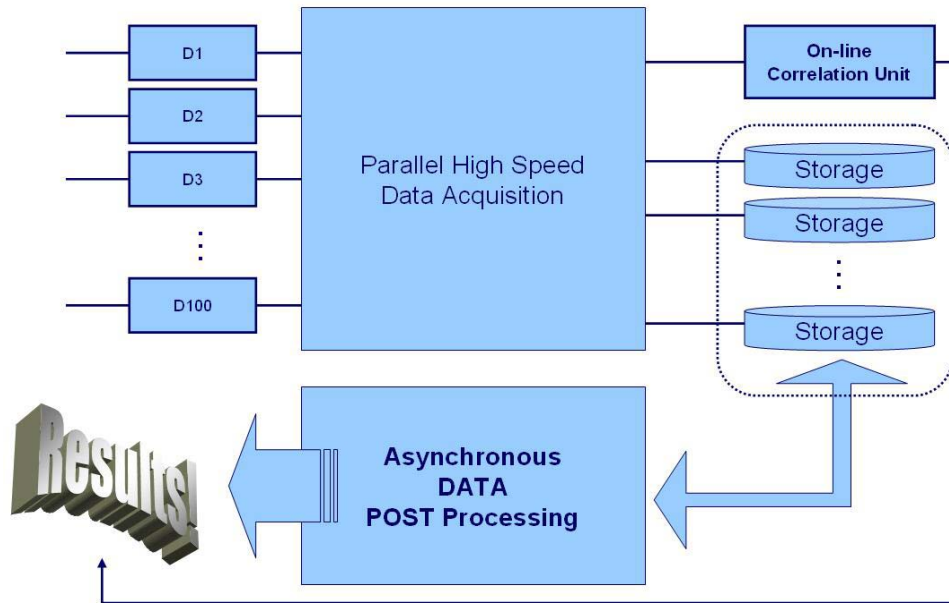


*Fig. 5.19. The high-level data acquisition system*

The system, from a high level point of view, can be sketched like in Figure 5.19, where five different macro-blocks are indicated:

- Detector electronics
- Signal detection and clocking unit
- On line correlation unit
- Data storage unit
- Post processing data analysis system

The amount of data in the storage unit is very much extended, and the optimal analysis procedure is not yet defined. For this reason, we favor the solution of an asynchronous post processing, in order to guarantee data integrity and future scientific investigation.

In order to explain the acquisition electronics, it is useful to introduce two items, namely the TDCs (Time to Digital Converters), and the hydrogen maser clock reference.

### **5.5.1. Time-to-digital converter (TDC)**

The electronic system must count events at high speed rates. One solution is counting the arrival times of the photons with the so called TDC (Time to Digital Converter). TDCs are used in the range of 1 nanosecond down to the picosecond range. The first TDC's were developed for scientific and research purposes as a combination of time-to-analog (TAC) and analog-to-digital (ADC) converter.

Thanks to CMOS technology, it is possible to integrate fully digital TDCs into a single chip. The high precision – down to 14 ps – in combination with the large dynamic range (up to 30 bits, but they can operate also in continuous mode), the high stability over temperature and supply voltage and the possibility of a low cost production thanks to the CMOS technology, make them the first choice for industrial applications.

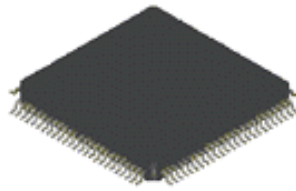


*Fig. 5.20. TDC-GPX from Acam-Messelectronic*

TDCs usually operate as follows: when a START signal arrives, the TDC starts to count the clicks of a very high speed internal oscillator (precision in the order of 20 ps) until a STOP signal arrives. A single input line must be used in order to have the START and STOP signal collapsed together.

Commercial acquisition boards are usually equipped with TDCs. An example useful for our application is the GPX chip from Acam-Messelectronic GmbH. The TDC-GPX (see Figure 5.20) can be configured in order to work in continuous mode, assuring 8 channels with 81 ps resolution.

### 5.5.2. Clock reference and time precision

Given the great number of TDCs needed for *QuantEYE* (for example 100), one needs to synchronize them with a common time reference. This clock reference must keep the desired precision for all the length of the experimental run. The solution is an active hydrogen maser (H-M) clock.

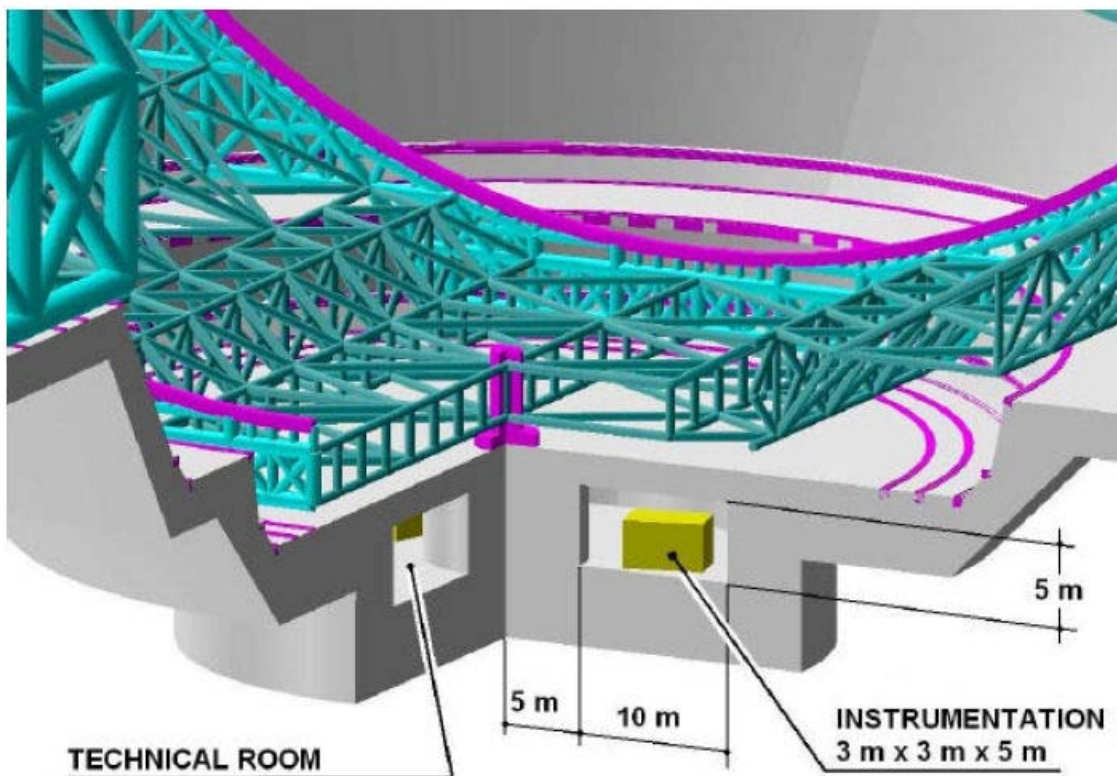


*Fig. 5.21. Possible locations for the active hydrogen maser*

This clock is usually large, heavy and sensitive to changes of its orientation with respect to gravity and to magnetic fields. We request therefore to install it in a dedicated temperature and humidity controlled room, far from the on-telescope electronics, as in Figure 5.21.

With commercial electronics, the reference clock signal can be transported from the generator to the *QuantEYE* room, with the help of optical fibers and a transmitter and receiver unit usually supplied by the H-maser vendors (Figure 5.22). A UTC receiver (GPS, or Galileo when available, or other UTC satellite receivers) can be installed inside the main *QuantEYE* room, in order to set a universal time reference for each observing run.

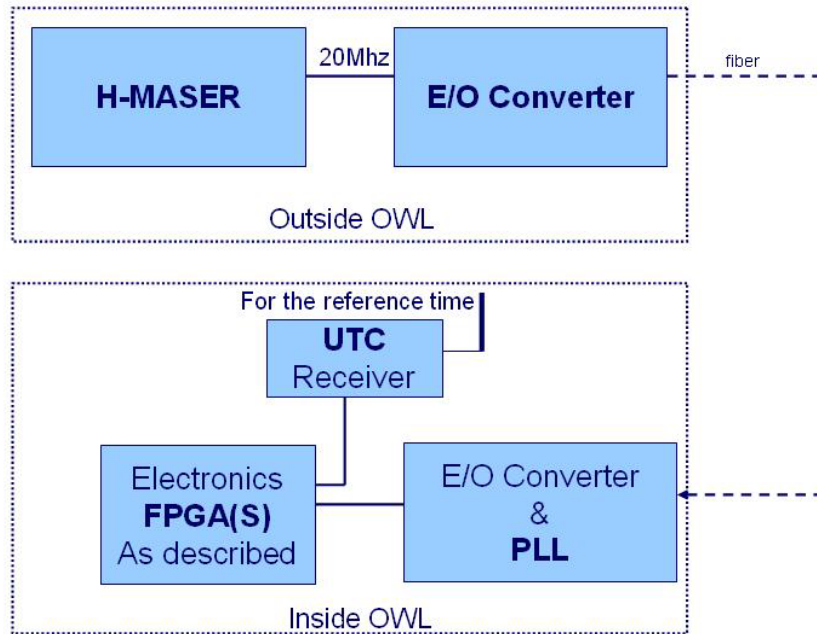


*Fig. 5.22. Reference time distribution with the hydrogen maser in a separate laboratory*

## 5.6. Electronics

One of the main constraints in designing the electronics for the acquisition system is the performance of the SPAD detectors. The baseline optical solution is based on an array of  $10 \times 10$  SPAD detectors, each with a dead time of 100 ns (maximum count rate 10 MHz). The  $10 \times 10$  detectors in parallel are able to produce up to 1 GHz counts (Figure 5.23).

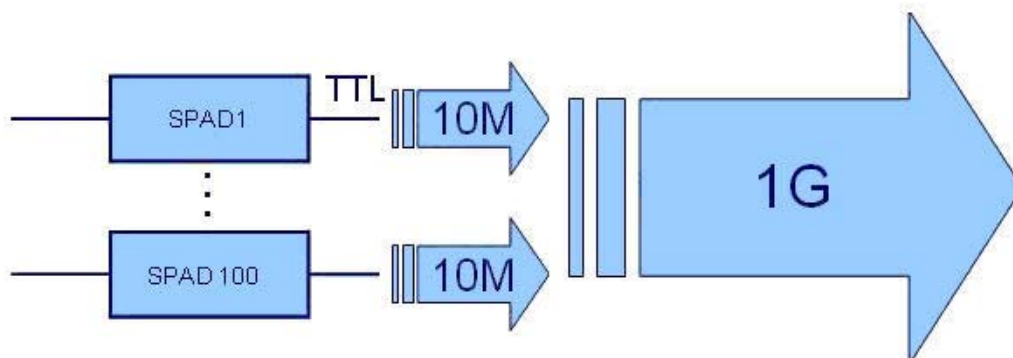


*Fig. 5.23. The  $10 \times 10$  flux collector solution.*

Two possible scenarios will be described in the following paragraphs:

1. a flux collector followed by ad hoc electronics development and programming
2. a flux collector followed by off-the-shelf standard technologies taken from a particular supplier.

### 5.6.1. Scenario (1): *Ad hoc electronics*

Using 4-input line devices as the previously described ACAM chip (Figure 5.24), the system electronics will require 25 TDC in parallel. Each TDC will count 4 signals coming from 4 SPADs. In order to synchronize all the TDCs, it is necessary to develop a “start-stop” electronics producing 25 synchronization signals, taking a reference clock from the input side. Those signals will come to the synchronization input line on each TDC. The reference clock can be a slow squared period signal (typically 20 MHz), very precise and stable during the entire length of the observing run. This reference is provided by the H-M clock. The “start-stop” electronics can be designed with the help of a FPGA (Field Programmable Gate Array), or of an ASIC (application-specific integrated circuit), and will have a synchronization unit provided by a PLL (phase-locked loop) electronics with the same precision of the reference clock. A possible solution is shown in Figure 5.24.

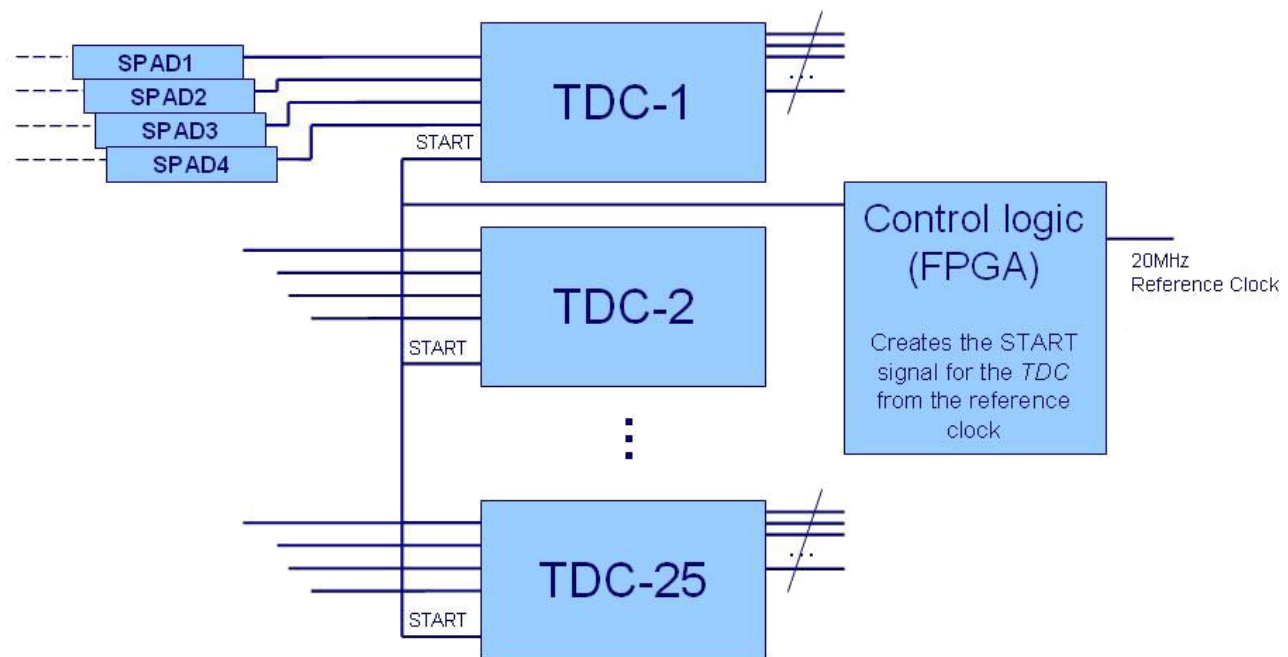


*Fig. 5.24. The use of 25 TDCs for QuantEYE's acquisition system*

At the output of each TDC there is the photon arrival time taken from 4 SPADs and written in a data output BUS. With present technologies (see ACAM, for example), this bus is a 27 bit parallel bus working at 40 MHz (128 Mbytes/s).

It is important to point out that in *QuantEYE* we want to keep as much information as feasible, in order to do optimal correlations in time and space. To do so, we have to store all

the coming information from each TDC. This is possible using ULTRA-SCSI II or SATA micro-controllers, which can provide transfer rates up to 300-400 Mb/s in writing hard drives.

Not considering any type of compression, the amount of data is very large, but not prohibitive, even with present-day technologies. For example, in the case of a run of 15 minutes on a very bright star, *QuantEYE* will store a total of 3 TBytes; it will need one hard drive of 180 GB capacity for each one of the 25 lines; see Figure 5.25:

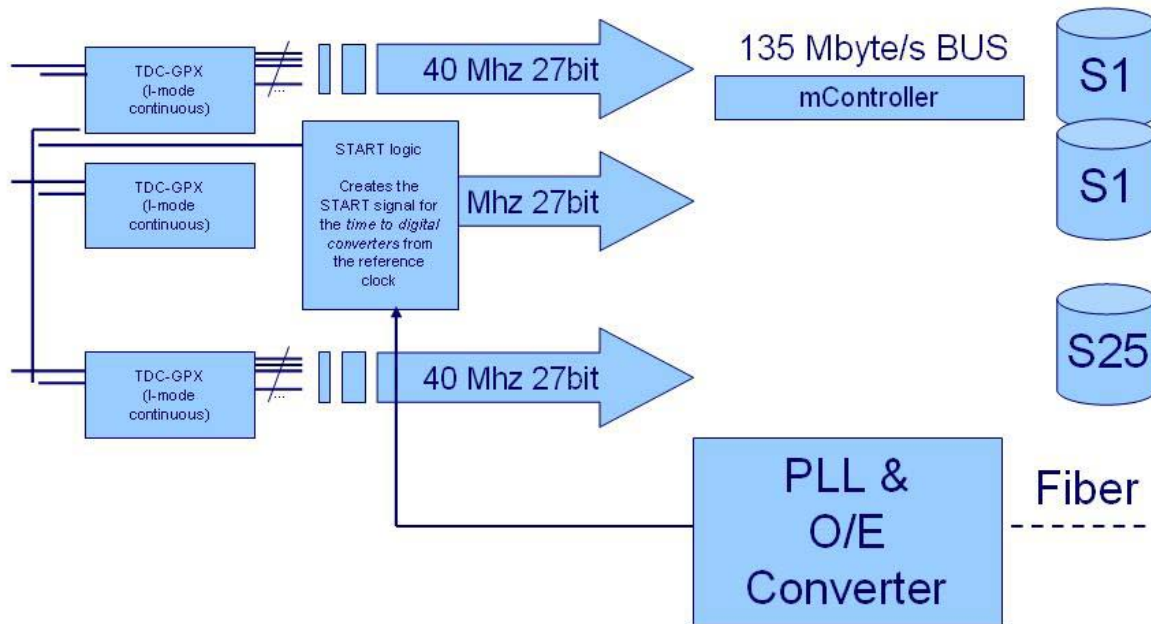


**Fig. 5.25.** Data storage and final acquisition capacity

#### Post Processing and on-line correlation unit

The very large amount of data will require great computational power inside the post-processing unit. Usually, this unit is a well dimensioned workstation or, better, a cluster of workstations working together. Nowadays a viable technology could be the clustering of Intel Itanium 2, AMD Opteron or Apple G5 nodes interconnected with gigabit Ethernet LAN. However, this area is in constant evolution, so we do not want to specify which technology and hardware architecture will be used in the future.

We suggest then to introduce, after the signal detection and clocking unit, an electronic unit demanded to calculate some correlation functions in a continuous and direct mode (on-line mode). Using FPGAs (or specific ASICs), it will be possible to calculate autocorrelations and correlations between different lines coming from the SPADs. The number of lines that this electronics can be process will depend obviously on the computational power of the FPGAs.

#### 5.6.2. Scenario (2): Commercial solutions

For the sake of completeness, we now discuss *QuantEYE* electronics composed of commercial solutions. Several vendors keep on the market modular systems initially devised for big experiments for nuclear and particle physics (as already pointed out, our system has several

technical features in common with systems used at CERN). For instance, the Italian firm CAEN S.p.A. has a VME Family of TDCs acquisition boards. Their VX120N model is capable of 25 ps resolution with 32 multi-hit start-stop lines, as shown in Figure 5.26:

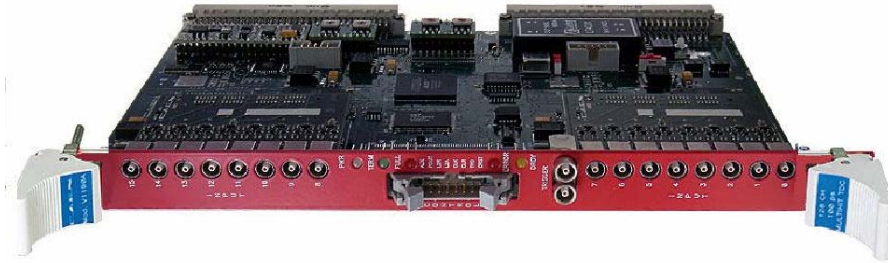


*Fig.5.26. The VX1290N CAEN board.*

It is important to stress that any commercial solution must be “tuned” to the *QuantEYE* specific requirements with the help of the producer.

### **5.7. Mechanical and Electrical Characteristics**

We present in the following figures (Figures 5.27, 5.28, 5.29, 5.30) a number of renderings meant to provide a visual impression of *QuantEYE*. The relative dimensions are approximately correct, but not optimized. A list of bare dimensions is given in Table 5.10.

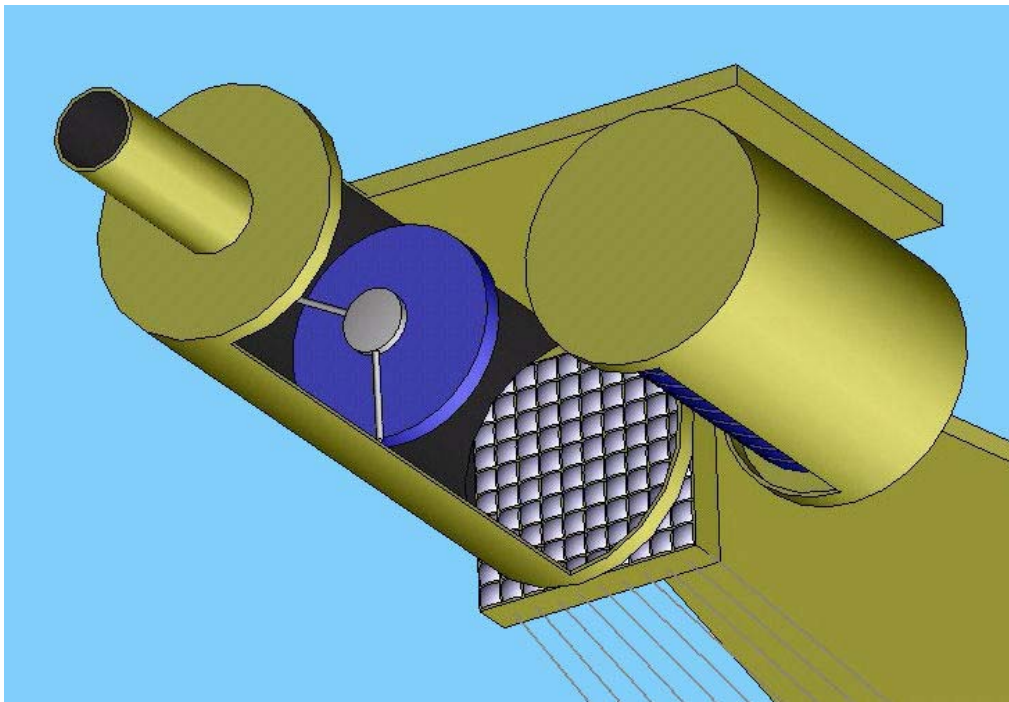


*Fig. 5.27. Schematics of the optical head (from the top left to the bottom right): baffle, collimator, lenslet array, filter magazine, fiber bundle.*

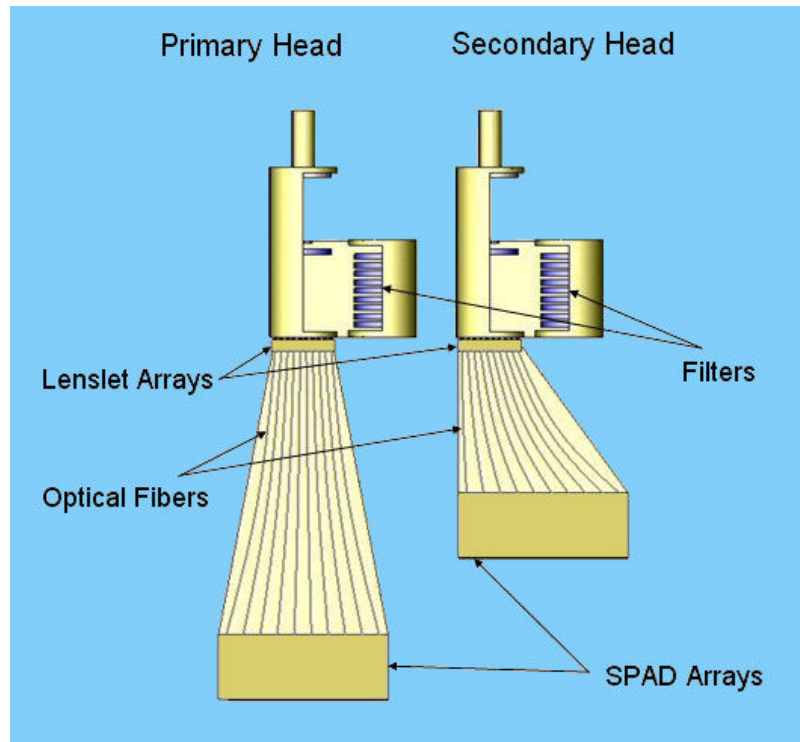


**Fig. 5.28.** Schematics of the two heads, the fixed one (left) and the moving one (right). The different mechanical configuration and dimensions are meant to indicate that the moving head cannot interfere with the fixed one, and must have a greater mechanical rigidity.

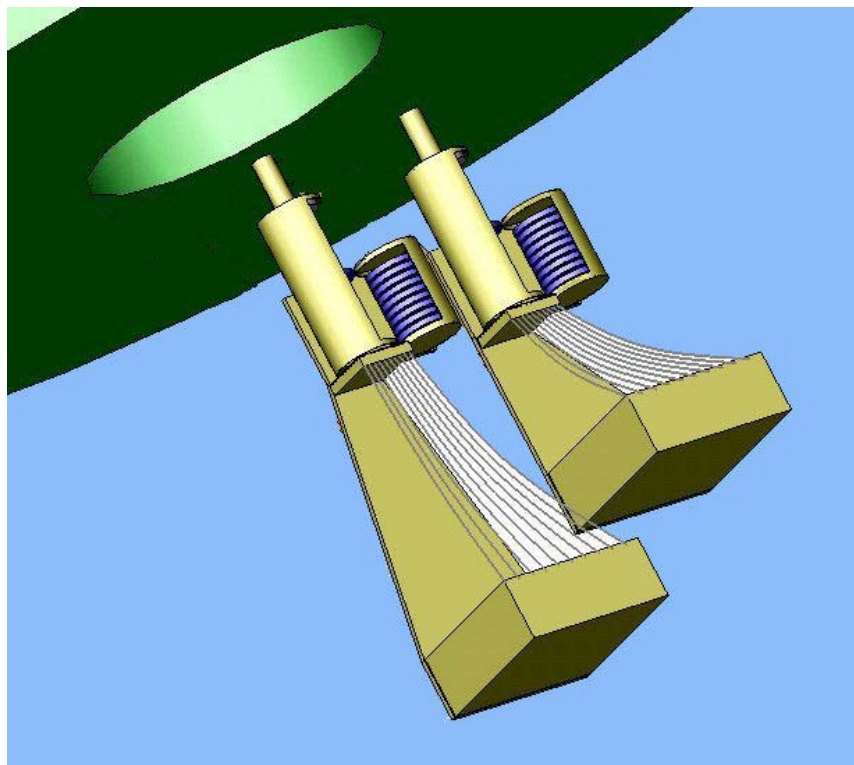


**Fig.5.29.** The moving head (on the right) explores the scientific field of OWL. Interface to the OWL derotator is not shown.

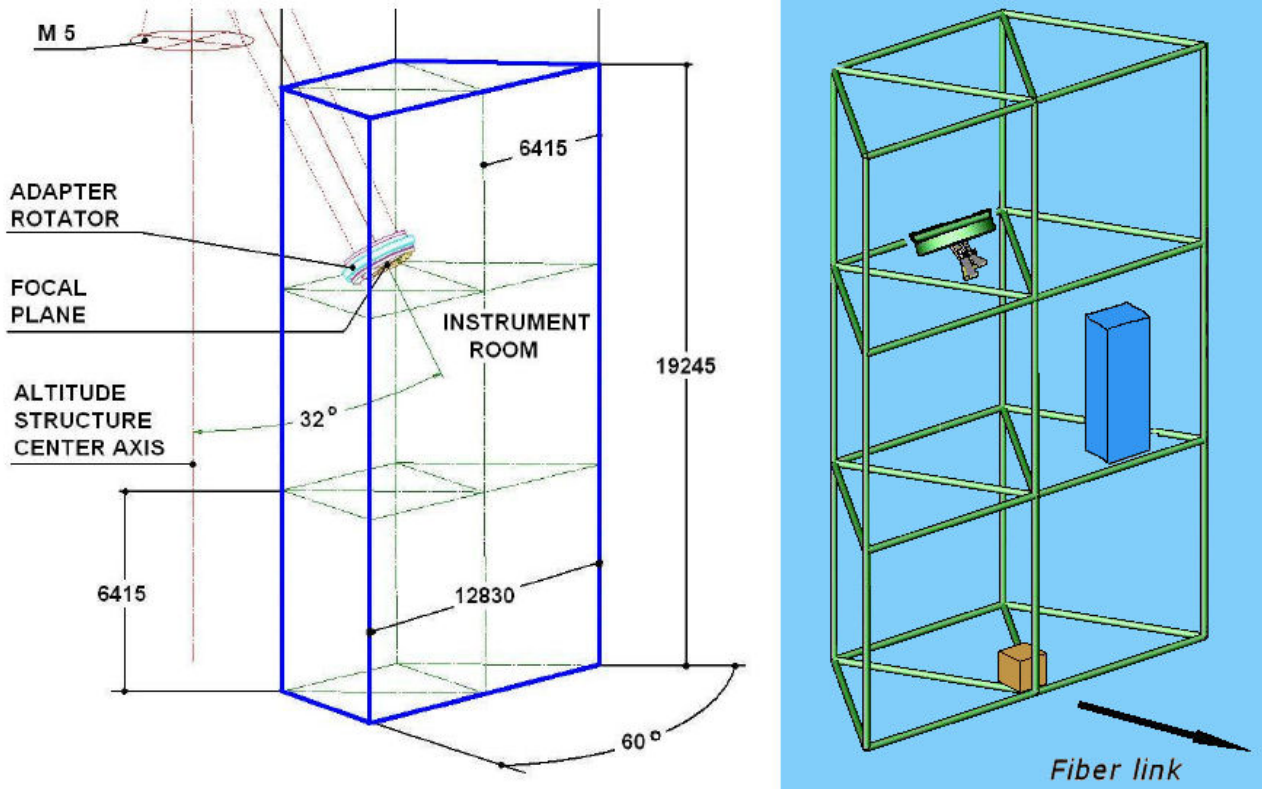


*Fig. 5.30. Schematics of the total volume of QuantEYE.*

The following sections provide some further details.

### **Detector heads**

The weight of the optical components (focal reducer, filter magazine and lenslet array) and their structure could weight less than 20 kg. A simple mechanism is foreseen to insert and remove the filters. The electrical power is around 10 W.

The detector box: as a reference, we have used the mechanical and electrical characteristics of a 50  $\mu\text{m}$  SPAD. The 100 detectors can be arranged on a box of 10 $\times$ 10 SPAD units, optimizing the mechanical design and keeping a sufficient space for ventilation purposes. The box will contain also the TDCs, the micro-controllers for the communication between the head and the storage unit, and finally the electronics of the on-line correlation unit. The total weight of the box (excluding cabling) could be around 50 kg. The total power (including cooling) is 100 W.

The interface to the telescope could weigh 20 kg.

The second detector head is identical to the first one, but it must be moveable over the scientific field with great precision. Therefore it requires fine optomechanics, highly precise positional reading, greater mechanical rigidity, greater weight (150 kg) and greater power (say 200 Watts).



---

Overall Dimensions - Primary		
head	Length×Height×Width [mm]	1040×315×340
Overall Dimensions - Secondary		
head	Length×Height×Width [mm]	790×315×300
Baffle	Outer Diameter [mm]	40
	Length [mm]	100
Telescope	Outer Diameter [mm]	120
	Length [mm]	300
Mirror_1	Outer Diameter [mm]	30
	Thickness [mm]	4.3
Mirror_2	Outer Diameter [mm]	100
	Internal Diameter [mm]	20
	Thickness [mm]	14.3
Distance Mirror_1-Mirror_2	Length [mm]	140
Filters box	Outer Diameter [mm]	120
	Length [mm]	160
Individual Filter	Outer Diameter [mm]	100
	Thickness [mm]	10
	Length×Height×Thickness [mm]	
Lenslet Array		100×100×20
	Length×Height×Thickness [mm]	
SPAD Array		300×300×115
	Length×Height×Thickness [mm]	
Electronic and Storage Box		1500×1500×1500
	Length×Height×Thickness [mm]	
Calibration Unit		300×300×150

---

*Table 5.10. A list of approximate dimensions of the several sub-systems*

### **Total weight and power**

Total weight attached to the derotator:

total weight (max): 20+50+20 +150 ≈ 240 kg .

total power (max) ≈ 310 W.

### **Storage and electronics crate**

In order to arrange a typical array of 50 hard drives of 200 GB each one, we foresee to arrange them into a multi-purpose rack. Using present technologies, some specifications are:

Dimensions: 190×60×100 cm (Height × Width × Depth)

Weight: 200 kg

Power: 1500 W

Input Current: Typical 3A – Maximum 20A

### Calibration unit

It must contain a thermal source, an arc, a laser, possibly one or two neutral density filter, an optomechanical system to feed both primary and moving heads.

Weight 20 kg, power 200 W

### Complete system view

The two Figures 5.31 and 5.32 show a complete view of the electronics and data analysis system of *QuantEYE*.

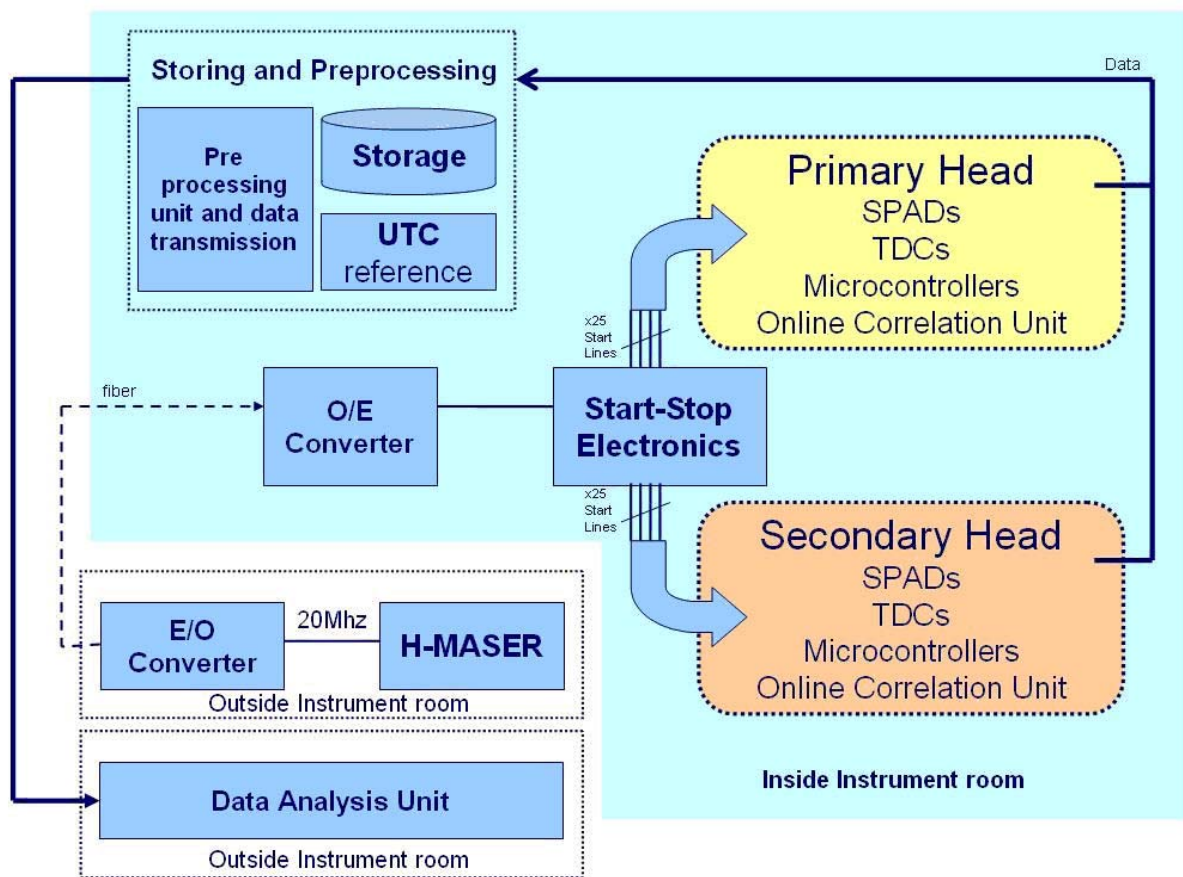


**Fig. 5.31.** A block diagram of the main components of *QuantEYE* (except the optical calibration unit)

The main characteristics of the setup are:

- 1) Inside the instrument room:
  - a. Two instrument heads composed by:
    - i. Optical components and SPADs
    - ii. Electronics for the time to digital conversion
    - iii. Electronics for the output of data (time tagging information)

- iv. Online correlation unit for the real time analysis of signals coming from the detectors. The number of real-time signals will depend on the computational power of this electronics.
  - v. the calibration unit (not shown)
  - b. O/E Converter: this optical to electrical converter will deliver the 20 MHz high precision clock coming from the H-maser located outside the instrument room.
  - c. Start-Stop Electronics: this piece of hardware and software will create the controller signals for the TDC as already explained.
  - d. Storing and Preprocessing Units:
    - i. Storage
    - ii. UTC reference system: it will be a GPS or GALILEO or other suitable receiver connected with an external antenna
    - iii. Pre-processing and data transmission unit. It will format the data inside the storage system and send it toward the final analysis.
- 2) Outside the instrument room:
- a. Active hydrogen maser with the E/O converter: the 20 MHz clock coming from the maser will be converted in optical laser pulses and then sent to the *QuantEYE* room through an optical fiber
  - b. Data analysis unit: the main workstation where scientist and technicians will control and configure the entire system and then precede to the post processing of all the data. It will also provide an interface for the on-line correlation unit.

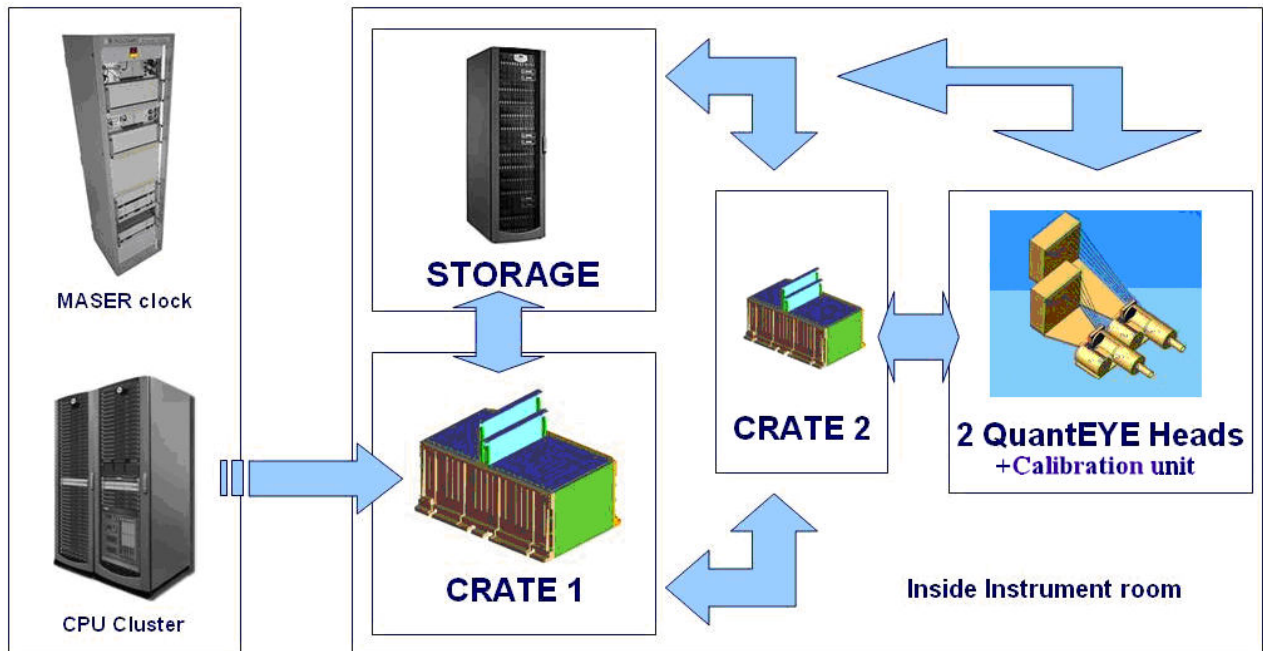


**Fig. 5.32.** The main subsystems of *QuantEYE*

## 5.8. Cost Estimates

The cost of QuantEYE is an ill-defined element, for several reasons: the interfaces must still be defined, the site has not been selected, the sharing of costs with ESO is not known, the technology is in continuous evolution etc. Therefore the following provides a rough estimate based on a 5 year development time with a substantial contribution in manpower and laboratory equipment from research institutes attributed only partly to *QuantEYE*.

A consortium of four European institutes, each providing 5 men for 5 years is foreseen:

***Manpower (5 years × 4 institutes × 5 persons): 100 FTE's***

Regarding the other elements, here is a preliminary estimate:

Item	Cost (k€)
Optics (collimators, filters, fibers, calibration unit)	500
Detectors (development and testing, laboratory equipment)	1500
Electronic Boards	400
Mechanics and Controls	400
Data Storage, CPU cluster	300
Controls and Data Analysis Software	300
Active Hydrogen Maser*	400
External Consultants, Travel, Documentation, Management	600
<b>Total [k€]</b>	<b>4400</b>

\* in an instrument like OWL, the hydrogen maser could be an observatory facility, as is presently the case at all VLBI stations.

## 5.9. Technical Issues in Current Design

Here is list of identified issues requiring further study:

***Custom-built lens array with minimum inter-lens dead area***

***Tapered fibers***

***Large-dimension very narrow band filters***

The need to have very narrow and large filters deserves some consideration, but it does not appear beyond existing technology. For instance, Figure 5.33 shows the transmission of a 1.5 Å wide filter with 50% peak transmission and 12.5 mm diameter, which we use with the 1.5m Matera telescope for quantum communication and quantum astronomy purposes.

According to the filter producer, the filter can be moved to cover the range of *QuantEYE*, and reach the 10 cm dimension. With proper thermal control, the peak wavelength can be tuned to the appropriate radial velocity of the object to be observed.

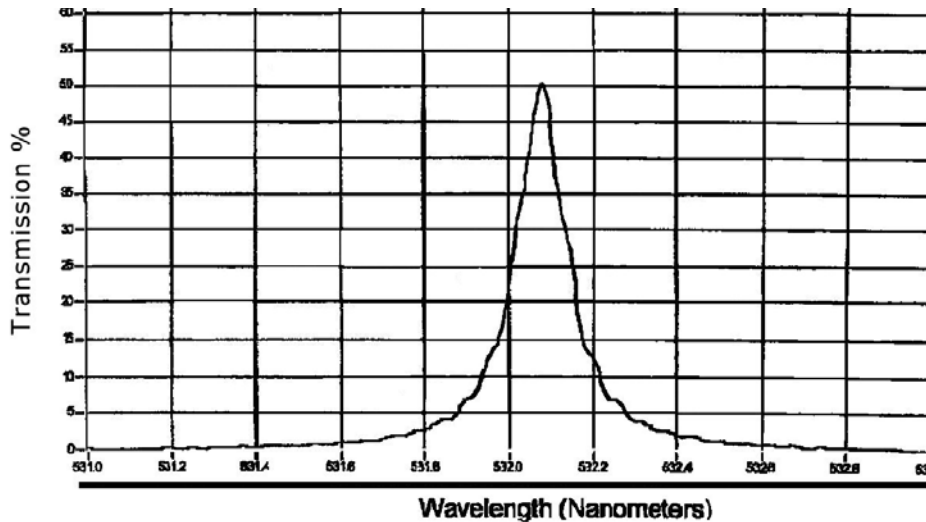


*Fig. 5.33. A narrow-band filter used at the 1.5m Matera telescope with a SPAD device*

### ***Mirror coatings and spurious polarization introduced by the telescope***

The final mirror of the corrector (M6) is tilted by  $16^\circ$  thus providing a  $32^\circ$  rotation of the optical axis after reflection. If it were coated by aluminum, one could fear some non-negligible polarizing effect (of the order of 11%).

However, the coating of OWL could be a *protected silver* layer. Regarding silver, information can be taken from <http://www.emf-corp.com/pdf/EMF-SilverCoatings.pdf>, <http://www.majestic-coatings.com/coating-p-silver.html> ).

Unfortunately, no precise information about the polarization characteristics of silver protected coatings has been obtained as yet.

### ***Northern Lights Optics***

( [http://www.minerals.sk.ca/atm\\_design/FUTURE/coatings.html](http://www.minerals.sk.ca/atm_design/FUTURE/coatings.html) ) state:

“Differences in reflectance between the s and p polarizations are small over the spectral range and over the expected angles of incidence”

M. Lampton ( [http://www.ssl.berkeley.edu/~mlampton/TRADE\\_WhySilver.doc](http://www.ssl.berkeley.edu/~mlampton/TRADE_WhySilver.doc) ) quotes the previous site of *Northern Lights*. However, no mention of polarization properties is made, in addition to those in the Northern Light site.

Some information was received from J. Tinbergen through ESO: “... The whole question of OWL polarization is complex: the fast primary plus the partially filled aperture (as M1 is built up and for maintenance), the coating, the oblique M6 are probably the most obvious aspects...”. In conclusion, the polarization aspect of OWL needs careful consideration by the ESO opticians.

### ***Scattered light background***

Excellent baffling of the entire scientific field is of course mandatory.

One might fear that in addition to the usual problems of scattered light (e.g., ghosts and narcissus), the telescope structure and any structure near the focal plane might introduce *time structures* in the photon rate.

To our knowledge, no existing commercial software handles the time distribution of the spurious light. Probably programs like Zeemax or APART can be suitably modified, but this will require a dedicated effort.

### ***Vibrations***

We have to study the effects of possible vibrations in the structure, induced by whatever reason (mechanical, electrical, acoustical, thermal, microseismic, etc.). Although the second moving head should remove most of the first order problem of any fixed-aperture photometer, non negligible differential vibrations might still persist to very high frequency.

### ***Highly efficient algorithms***

It is important to remember that computing high order correlation functions between all the *QuantEYE* SPADs will be a high complexity work. It will be essential to develop a very complete and deep software making the most of the massive computational power given by a cluster of CPUs in order to design a multi-purpose software capable of different tasks depending on the scientific goals or on the specific objectives during *QuantEYE's* life.

## **5.10. Future Design Challenges**

The current *QuantEYE* design is “conservative” in the sense that it is based upon technology that either is already existing or about to become available. That concept thus might be used to, e.g., build a prototype in the rather near future. However, what technologies can one expect to become available at the time of the OWL completion, and how may these affect an optimal instrument design?

Removing the constraint to design the instrument with currently available components, one may speculate what technology might eventually become available in the OWL construction timeframe.

The perhaps main limitation of the present design is that it only permits observations of one point source at a time. Of importance would be the availability of two-dimensional photon-detector arrays of high quantum efficiency, in which each pixel could sustain very high count rates (and ideally even have an energy/wavelength resolution). Such arrays are actively being developed, and if/when their performance reaches satisfactory levels, these should enable an *imaging* system with nanosecond resolution. For example, one could then observe a globular cluster containing an active X-ray source of unknown location, and then search for an optically rapidly variable object somewhere in the field.

The data rates could become quite significant. *If* an imaging system with one megapixel, say, becomes available, and if each pixel is photon-counting at 10 MHz, say, this generates  $10^{12}$  time-tags per second, and petabytes of data already in a short time, stressing the need for efficient real-time data reduction, presumably outputting only the relevant statistical functions from each pixel, with a further on-line selection of the most “interesting” pixels. In some sense, such a data “filtering” is reminiscent of that being designed for high-energy accelerator experiments with analogous very high data flows.

## 5.11. Instrumentation Physics

To eventually obtain high accuracies in astrophysical observations, a number of instrumental and observational issues may need to be understood. Here we exemplify some of them that merit further study:

**\* *Temporal structure of the sky background?*** The night sky is not constant, and has contributions from, e.g., nanosecond-duration flashes of Cherenkov light induced by high-energy gamma rays (otherwise being studied by large light collectors); faint but numerous meteors, or fluctuations in background nightglow from aurorae.

**\* *Atmospheric intensity scintillation?*** Although, to a first approximation, the large OWL aperture averages out scintillation effects, contributions come due to the incompletely filled entrance pupil. The narrow interspaces between the mirror segments will extract the spatially smaller and temporally faster fluctuations (in addition being sensitive not only to scintillation amplitude, but also to the atmospheric wind direction, since the spaces between the hexagonal mirrors have only a few preferred directions); Dravins et al. 1998.

Such scintillation signatures in very large apertures may actually be possible to study already now, by using some of the large flux collectors set up to study Cherenkov radiation from cosmic gamma rays. These have analogous segmented mirrors, and studies of the fluctuations in light from bright stars should reveal such scintillation signatures irrespective of the poor image quality in these flux collectors. The scintillation originates as varying illumination sweeping across the entrance pupil, and is independent of how precisely that light is later focused. Even if these flux collectors would not be in the same geographical areas as being considered for OWL, such future observations might give valuable insights in one of the noise sources to be expected.

**\* *Intensity fluctuations by adaptive optics?*** The accurate photometry of [constant] objects across adaptive-optics corrected fields of view has already been discussed in the literature. Any rapidly moving adaptive mirror will likely modulate the intensity of the source observed (at least changing the intensity fluctuations caused by the atmosphere). Since the adaptive-optics correction varies across the field, perhaps a calibration source elsewhere might not undergo the same modulation; cf. Figure 5.34.

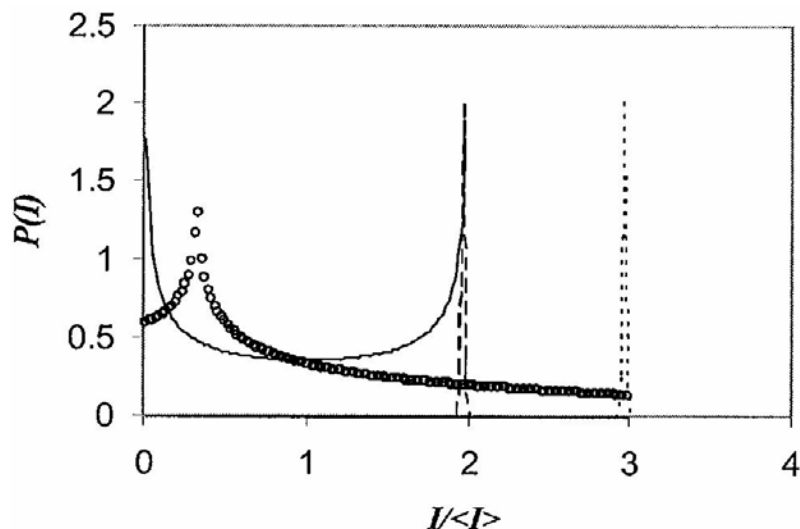


**Fig.5.34.** Probability intensity distribution of light intensity at the PSF core of an adaptive-optics-compensated image for three different  $D/r_0$  values (Canales & Cagigal 2001)

**\* Microphysics of photon detection?** Contrary to common language usage, *photons* as such are never directly detected – rather one studies photo-*electrons* that result from the photon interaction inside the detector. As discussed in Sect.1.13, electrons with their half-integer spin are fermions, obey Fermi-Dirac statistics and the Pauli exclusion principle that prohibits any electron “bunching” in the same quantum state. At least on first sight, this would appear to complicate the study of such properties in photon streams that are prohibited by Fermi-Dirac statistics; in any case it points to the need to understand the physics of the detection process and the various timescales that it may involve.

**\* Quantum statistics changes inside the instrument?** Photon statistics may be affected by many factors, including the re-direction of light, for example through a beamsplitter. While in the classical case, a beamsplitter would split the amplitude of a light wave as 50-50%, say, in the quantum case, the beamsplitter is “cleaving” the photon gas with all its photon correlations into two parts whose statistics, i.e. the amount of photon bunching in time, are changed after passage of the beamsplitter (e.g., Aspect & Grangier 1991; Bachor & Ralph 2004). On one hand, this illustrates how photon statistics are carrying information beyond the classical one, but it also demonstrates the need to understand the quantum behavior of the telescope + instrument system: in the quantum world the observer may not be separable from what is being observed.

## 5.12. Quantum Information and Quantum Computing

Quantum information theory and quantum computing might become of extreme importance in a near future, as already stated in the Introduction. A quantum computer (QC) has, intrinsic in its nature, extraordinary properties. The temporal evolution of the information inside a QC is necessarily unitary, controlled by unitary operators. This characteristic implies in some sense that in a QC each operation has the property of reversibility. Another important consideration is that, remembering that information is coded on “small” quantum systems, the computation itself will be more efficient than the classical one. Furthermore, quantum machines are also extremely parallelized. From the *QuantEYE* scientific point of view, there are some quantum algorithms that can be very useful inside a QC (see Figure 5.35). For instance, the Grover algorithm is very interesting, as it searches elements inside big databases with a lower computational complexity than the classical one.

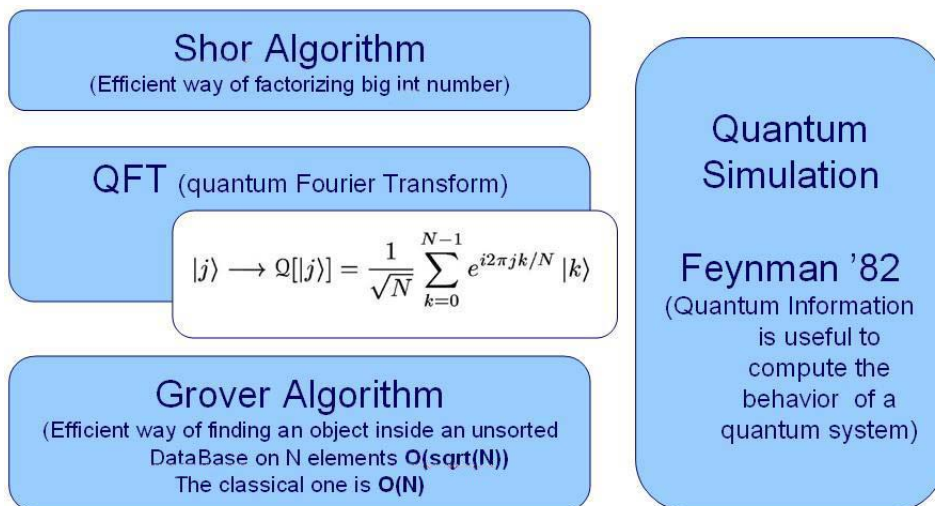


*Fig. 5.35. QuantEYE and quantum computing*



Therefore, quantum logic, quantum algorithms and quantum computers can accelerate the process of data acquisition and data analysis. Even more exciting, one could ask if Feynman's suggestion of quantum simulation could be applied to the description of astrophysical systems.

### 5.13. A Possible Precursor for VLT

One of the 8 Nasmyth foci of the VLT (*Melipal*, UT3) is reserved for Visitor Instruments (VI), i.e. for instruments provided by institutes or consortia which can be temporarily mounted at this focus. The side port of the Nasmyth Adaptive Optics System (NAOS) may also host a VI. VI's should be fully standalone, complete instruments, including their own data acquisition and storage capabilities. VI's should comply with VLT standards, including those for safety, interface to the Nasmyth adapter/rotator, power and coolant supplies, and LAN connection to the VLT. VI's shall be operated exclusively in visitor mode. The use of observation block procedures shall be optional.

Preliminary considerations:

From the VLT optical data ( $f = 108827$  mm,  $f/13.4$ ), 1" corresponds to  $528 \mu\text{m}$  on the focal plane.

Therefore, two non-imaging possibilities can be considered:

1. A scaled-down version of the *QuantEYE* baseline. For instance, using a collimator having a focal length of 400 mm, we have a 30 mm diameter parallel beam which can be intercepted by a  $3 \times 3$  lenslet array. Each lens is a square of  $10 \times 10$  mm. With a 30 mm focal length ( $f/3$ ) we get a 40 micrometer spot, well inside a  $50 \mu\text{m}$  SPAD.
2. A demagnification  $1/11$  will bring this FoV inside a *single*  $50 \mu\text{m}$  SPAD. To achieve this demagnification one can utilize a 82 mm diameter collimator with focal length 1100 mm, followed by another 82 mm telescope with 100 mm focal length ( $f/1.2$ ). If the chromatic aberrations are not too critical, this system could be entirely refractive.

Possible imaging solutions have also been considered. For example, suppose we want a 3 arcsec FoV with resolution  $0''.3$  per SPAD. The SPAD array will remain the same of the baseline solution, namely  $10 \times 10$  SPADs. Two concepts could be:

- a) Tapered fiber bundle on the focal plane,  $150 \mu\text{m}$  on image side,  $50 \mu\text{m}$  on SPAD side (not critical loss at fiber cladding).
- b)  $5 \times$  or  $10 \times$  focal length enlarger, followed by a microlens array to focus on SPADs (through fibers or not). The solution has the same criticalities already pointed out for OWL, namely lenses and detector arrays. Technological breakthroughs must occur before further consideration.



## 6. Observing with *QuantEYE*

This Section gives a selection of potential observing targets as examples of possible future observing programs with *QuantEYE*. The objects mainly represent various aspects of “extreme astrophysics”, i.e. sources with extreme values of their physical parameters such as matter flows in very strong gravitational fields; enormous magnetic flux densities; luminosities close to the Eddington limit; or expected laser emission. Other objects give examples of situations where very high time resolution can add unique knowledge, e.g. stellar occultations by remote solar-system bodies of unknown size and unknown atmosphere. Appendix 3, besides describing high-speed instrumentation efforts worldwide, also gives numerous examples of actual observations made of such types of objects, exemplifying today’s state of the art, i.e. what can be achieved with existing front-line instruments on existing telescopes.

Many objects from these classes are today known only from their X-ray or radio emission, with their optical counterparts either as yet unknown or too faint for meaningful study with today’s telescopes. The light-collecting power of OWL will make very many of these accessible. We recall the advantage of the optical: X-rays often originate from very close to, e.g., compact objects, and thus would at first sight appear to be most relevant to study. However, the effective areas of foreseen X-ray telescopes (even XEUS or Constellation-X) remain too small to produce sufficiently high X-ray photon fluxes from typical sources to enable studies at the highest time resolutions. Large radio telescopes (e.g., SKA), can reach the highest resolutions; however that radio radiation normally originates in lower-density regions some distance from, e.g., compact objects, thus again precluding their direct study. By contrast, *QuantEYE* on OWL will produce megahertz photon-count rates in white light, permitting microsecond studies from sources as faint as  $V=20$ !

Since, to study high-speed variability, a significant count rate is required, *QuantEYE* will primarily be targeting brighter sources, and thus be an instrument to be used mainly during full-Moon periods.

Of course, the present list of objects is selected based on *today’s* knowledge and does reflect *today’s* scientific problems. Even if we cannot predict what all new phenomena will be discovered during the next decades, this sample of objects nevertheless demonstrates the potentially very rich field for exploring extreme astrophysics at its very shortest timescales during the future OWL epoch.

### 6.1. Astronomical Targets

In the listing below, representative visual or infrared magnitude estimates are given, sometimes as an interval (many sources are strongly variable). There are additional classes of objects not listed here, in particular transient sources such as gamma-ray bursts or new [super]novae. Since the geographical location of OWL is not yet decided, objects are selected from all over the sky (and their coordinates are not listed here).

### LOW-MASS X-RAY BINARIES

These systems typically contain neutron stars, and several have optical counterparts that may be targeted with *QuantEYE*. *Example of astrophysical problem:* Magnetohydrodynamic gas-flow instabilities in the accretion flow onto the neutron star surface.

Aql X-1 = V1333 Aql	$m_V \approx 18.2$
Cen X-4 = V822 Cen	$m_V \approx 15.9$
Cir X-1	$m_B \approx 21.4$
Cyg X-2 = V1341 Cyg	$m_V \approx 14.5$
GX 17+2 = NP Ser	$m_V \approx 17.5$
Sco X-1 = V818 Sco	$m_V \approx 12.7$
V4641 Sgr	$m_V \approx 14.7$

... and many more objects in the updated on-line listing by Ritter & Kolb (2005)

### BLACK-HOLE CANDIDATES

These are a subgroup of Low-Mass X-Ray Binaries; some are also microquasars, i.e. sources of relativistic jets. *Example of astrophysical problem:* Behavior of matter and radiation close to the innermost stable orbit (and beyond), close to the black-hole horizon?

Source	Apparent magnitude
A0620-00 = V616 Mon = Mon X-1	$m_V = 11.2 - 18.4$
GX 339-4 = V821 Ara	$m_V \approx 15.5$
J1650-4957	$m_V = 17 - 24$
KV UMa = J1118+4802	$m_V = 12.5 - 19.0$
MM Vel = Nova Vel 1993	$m_V = 13.8 - 21.9$
V381 Nor = J1550-5628	$m_V = 16.0-22.2$
V404 Cyg	$m_B \approx 11.5$
V4641 Sgr	$m_V = 12.4-17$
V518 Per = GRO J0422+32	$m_V = 12.6 - 22.4$
V1033 Sco = GRO J1654-40	$m_V = 14 - 18$
V1727 Cyg = 4U2129+47	$m_V \approx 16.9$
XTE J1650-500	$m_B \approx 18.2$

... and several others: see Ritter & Kolb (2005)

### HIGH-MASS X-RAY BINARIES

These also include systems with black-hole candidates. *Example of astrophysical problem:* Temporal flickering of polarization in line emission from accretion disk.

Cyg X-1	spec.type 09.7Iab	$m_V = 8.9$
LMC X-1	spec.type 08III	$m_V = 14.5$
SMC X-3	spec.type 09 IVe	$m_V = 14.9$
X Per	spec.type 09.5pe	$m_V = 6.1$

... and more than a hundred others: see Liu et al. (2000).

## PULSARS

*Example of astrophysical problem:* Emission physics of nanopulses during some parts of the pulsar period; Alfvén waves in neutron-star magnetospheres.

The table gives also the pulsar periods, and the estimated magnetic flux density at the neutron-star surface, given in units of MT (megatesla =  $10^{10}$  Gauss).

Crab pulsar	P = 33 ms	$B_{\text{surface}} = 400 \text{ MT}$	$m_V = 16.5$
Vela pulsar	P = 89 ms	$B_{\text{surface}} = 300 \text{ MT}$	$m_V = 23.6$
PSR B1509-58	P = 150 s		$m_V = 22.4$
PSR B1951+32	P = 40 ms		$m_V = 25$
PSR J2051-0827	P = 4.5 ms		$m_R = 23$
PSR 0545-69 [in LMC]	P = 50 ms	$B_{\text{surface}} = 500 \text{ MT}$	$m_V = 22.7$
PSR 0656+14	P = 385 ms	$B_{\text{surface}} = 500 \text{ MT}$	$m_B = 25.1$

Not very many pulsars have so far been identified optically. Numerous millisecond and X-ray pulsars have been found in radio or X-rays; very plausibly several of these will become observable also optically with OWL.

## MAGNETARS

*Example of astrophysical problem:* Electrical discharges (“sparks of lightning”) close to the magnetic poles; free-electron laser emission in the extremely strong magnetic fields?

The table also gives estimated magnetic flux density at the neutron-star surface, now in units of GT (gigatesla =  $10^{13}$  Gauss).

SGR 1806-20	P = 7.5 s	$B_{\text{surface}} = 180 \text{ GT}$	$m_K = 21$
XTE J1810-197	P = 5.5 s	$B_{\text{surface}} = 17 \text{ GT}$	$m_K = 21$
1E 1048.1-5937	P = 6.5 s	$B_{\text{surface}} = 42 \text{ GT}$	$m_I = 26.2$
1E 2259+586	P = 7.0 s	$B_{\text{surface}} = 6 \text{ GT}$	$m_K = 21.5$
4U 0142+61	P = 8.7 s	$B_{\text{surface}} = 13 \text{ GT}$	$m_V = 25.6$
1RXS J170849.0-400910	P = 11.0 s	$B_{\text{surface}} = 47 \text{ GT}$	$m_H = 18.7$
1E 1841-045,	P = 11.8 s	$B_{\text{surface}} = 71 \text{ GT}$	$m_K = 19.4$

Catalog data taken from McGill Pulsar Group:

<http://www.physics.mcgill.ca/~pulsar/magnetar/main.html>

## NEUTRON STARS

At present, the only known isolated neutron stars are optically very faint. However, from statistical arguments, they should be numerous in our Galaxy, and quite possibly some nearby and relatively brighter ones will be found from X-ray imaging in the near future, offering more suitable targets for time-resolved studies. *Example of astrophysical problem:* Small localized spots across neutron star surfaces; magnetic-field inhomogeneities, and acoustic spectra of non-radial oscillations.

Geminga	isolated pulsar; tiny (ca 100 meters) hot-spot found in X-rays; P = 0.24 s	$m_V = 25.5$
RX J1856.5-3754	isolated neutron star	$m_V = 25.7$

A few tens of isolated neutron stars have been observed in X-rays or radio, e.g.: PSR J1210-5226 = 1E1207.4-5209; RXJ1856.5-3754, and INS RXJ0720.4-3125. Quite plausibly, the light-collecting power of OWL may suffice to identify their optical fluxes.

### CATAclysmic AND NOVA-LIKE VARIABLES

*Example of astrophysical problem:* Magnetic dynamo in the differentially rotating accretion disk.

CP Com	$m_B \approx 16.4$
DP Leo	$m_V \approx 17.5$
GG Leo	$m_V \approx 16.5$
GK Per = Nova Per 1901	$m_V \approx 12.9$
IW And	$m_B = 14.2 - 17.4$
RZ Leo = Nova Leo 1918	$m_B \approx 11.5$
U Sco = N Sco 1987	$m_V = 17.9-19.5$
WZ Sge	$m_V \approx 15.2$

... and several hundreds more; see: Ritter & Kolb (2005).

### MAGNETIC CATAclysmic VARIABLES

These are also called polars, and AM Her-type objects. *Example of astrophysical problem:* Plasma instabilities inside the accretion column hitting the magnetic poles of the white dwarf?

AN UMa	$m_V \approx 15.5$
AR UMa	$m_B \approx 14.5$
EF Eri	$m_V \approx 13.7$
EU UMa	$m_V \approx 17.0$
HU Aqr	$m_B \approx 15.3$
HY Eri	$m_V \approx 17.5$
VV Pup	$m_V \approx 14.6$
V834 Cen = E1405-451	$m_V \approx 14.2$

### HOT EMISSION-LINE STARS

*Examples of astrophysical problem:* Spectral width of laser emission line components, and their photon statistics; wave propagation in the stellar wind; photon “bubbles” emerging through the gas in extremely luminous stars close to (or even above) the Eddington luminosity.

Cen X-3 = V779 Cen	high-mass X-ray binary with kHz fluctuations	$m_V = 13.3$
LMC X-4	high-mass X-ray binary; spec.type 07 IV	$m_V = 14.0$
MWC 349A	Circumstellar recombination-line lasers	$m_R = 10.1$
RW Hya	symbiotic star; suspected laser emission	$m_V = 8.9$
V4647 Sgr = "Pistol star"	extremely massive variable, reddened	$m_H = 9.1; m_K = 7.5$
$\eta$ Car	circumstellar atomic laser-line emission	$m_V = 6.2$
V1016 Cyg	symbiotic star; Raman-scattered emission lines	$m_V = 10.0$
$\gamma^2$ Vel	Wolf-Rayet + O-type binary; colliding winds	$m_V = 1.8$

### ACTIVE GALACTIC NUCLEI

*Example of astrophysical problem:* Rapid fluctuations in mass flow and radiation emerging from close to the central black-hole engine.

Cen A	$m_V \approx 7.0$
Mrk 421	$m_V \approx 13.5$
Mrk 501	$m_V \approx 13.8$
M87	$m_V \approx 8.7$
PKS 1622-297	$m_V \approx 20.5$
0836+710	$m_V \approx 16.5$
3C273	$m_V \approx 12.9$
3C 279	$m_V \approx 17.8$

### WHITE-DWARF SURFACE STRUCTURE AND DYNAMICS

*Example of astrophysical problem:* Timescales and dynamics of white-dwarf surface convection along the temperature sequence (with expected millisecond scales for the convective features).

Procyon B	$m_V = 10.7$
Sirius B	$m_V = 8.4$
$\sigma^2$ Eri B = 40 Eri B	$m_V = 9.5$
Wolf 28 (Van Maanen's Star)	$m_V = 12.4$

... and thousands more.

## **BROWN DWARFS AND OTHER STARS**

*Example of astrophysical problems:* Electrical discharges (“lightning”) in dusty brown-dwarf atmospheres; modulation of coronal emission due to heating by magnetohydrodynamic waves; flares and flashes on magnetic stars; stellar microvariability due to hydrodynamic instabilities.

## **SOLAR-SYSTEM OBJECTS**

*Example of astrophysical problems:* Determine size and shape of distant small asteroids; dynamics of planetary-ring particles; size and center-to-limb variations of stellar disks and envelopes; atmospheric structure, dynamics and chemistry on solar-system planets and planetary moons.

Observations: Stellar occultations by Kuiper-belt objects; by small planetary satellites; by planetary rings; by planetary atmospheres; by the dark lunar limb.

## **6.2. Connection to Other Astronomy Projects**

OWL and other extremely large optical telescopes of the early 21<sup>st</sup> century will come into existence during the same period as other currently planned great facilities. In this Section, we briefly comment on the potential synergy between the scientific program foreseen with *QuantEYE*, and those possible to realize at these other facilities.

### **Synergy with the Square Kilometer Array**

*SKA*, the *Square Kilometer Array* is the large international radio telescope now being planned for longer radio wavelengths. One of its key science drivers is strong-field tests of gravity using pulsars and black holes. The radio emission normally comes from lower-density regions in the magnetospheres around such objects, and expected studies of strong gravitational fields will focus on studying the orbit evolution of pulsars in orbit around other compact objects. The *SKA*'s sensitivity will likely enable the discovery of more than 10,000 pulsars in our Galaxy, including more than 1,000 millisecond ones. Many of these will likely be optically detectable with *QuantEYE* on OWL, and the *SKA* identifications will offer an excellent list of new targets for optical study.

Hydrogen recombination lasers/masers at the epoch of atomic recombination in the *very* early Universe ( $Z \approx 1000$ ) were discussed in Sect.2.2.6. *SKA* might be able to observe these emission lines, strongly redshifted into the long-wavelength radio. However those detections are likely to be marginal and difficult. *QuantEYE* on OWL, on the other hand, should be able to study the equivalent physical processes of recombination lasers/masers in nearby Galactic sources such as MWC 349A (Sect.2.2.5). This should place the interpretation of the cosmological emissions on a firmer physical basis, and could become an excellent example of the synergy between great telescopes operating in widely different wavelength regions.

Quantum effects are more readily reached at the longer radio wavelengths, where the number of photons per coherence volume can be large. Indeed, the manifestation of the bunching of photons in the optical corresponds to “wave noise” in the radio. Such aspects also more readily produce conditions for maser emission in astronomical sources. The very shortest nanosecond radio bursts seen from a few pulsars imply extremely high brightness temperatures and essentially reach the quantum limit (Figure 6.1).



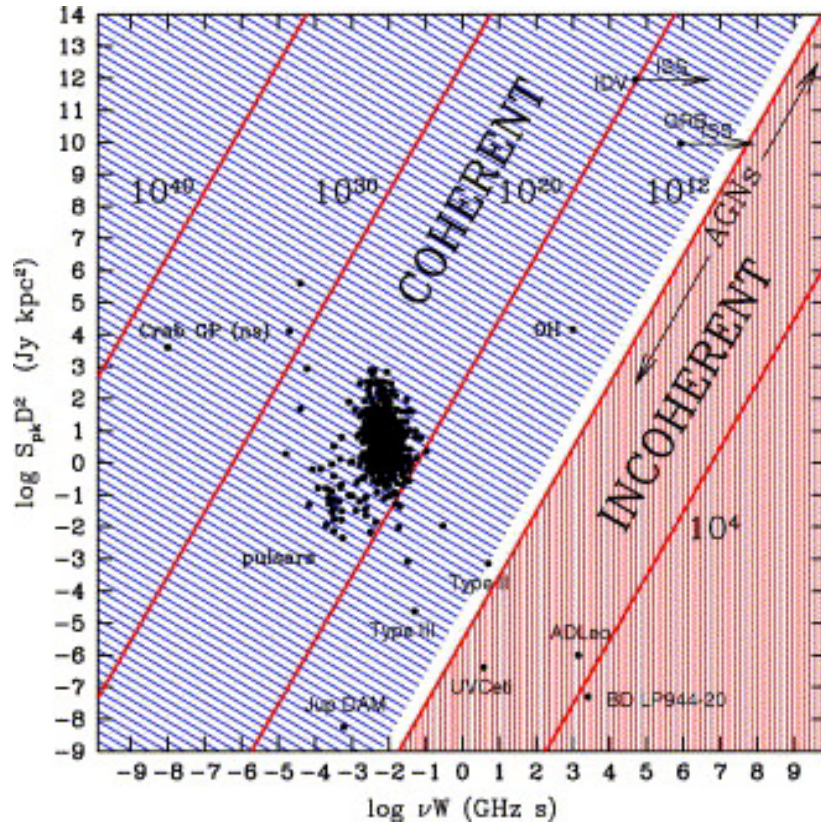


**Fig.6.1.** Phase space for known and anticipated transient radio signals. The horizontal axis is the product of transient duration  $W$  and radio frequency  $\nu$  while the vertical axis is the product of the peak flux density  $S_{pk}$  and the square of the distance  $D$  and is proportional to luminosity. Lines of constant brightness temperature are shown, and the uncertainty principle requires that signals be to the right of  $\nu W = 10^{-9}$ . (Wilkinson et al. 2004)

Thus, radio observations offer powerful tools that offer excellent complimentary to those available in the optical. The optical probes higher-density regions close to stars and compact objects (rather than low-density clouds); optical spectral lines are those of atomic transitions (rather than those of molecules); and the optical permits full studies of quantum phenomena that require the counting of individual photons, not yet practical at longer radio wavelengths.

Radio observations permit various studies related to quantum statistics of radiation (some of which have already been pursued), e.g., the statistics of microwave maser radiation. Among future challenges remains the study of photon statistics of the cosmic microwave background; possibly this could be one task in observational cosmology, once its currently sought polarization has been mapped?

### Synergy with future X-ray observatories

Preparatory work is in progress for future space missions to observe soft X-rays, in particular studies are made for the ESA mission *XEUS* (X-ray Evolving Universe Spectroscopy:), and for the NASA mission *Constellation-X*, both aiming at a launch sometime after 2015. Both these are planned to offer order-of-magnitude improvements in sensitivity over the current generation of space observatories represented by *XMM/Newton*, *Rossi XTE*, and *Chandra*.

To some extent, the scientific aims of *QuantEYE* overlap with some of those for *XEUS* and *Constellation-X*. In all cases, important studies are foreseen of phenomena in the strong gravity fields around neutron stars and black holes. Since X-rays normally are produced quite close to, e.g., the neutron-star surface in an accreting system, X-ray diagnostics may directly probe conditions of strong gravitational fields, such as gravitationally redshifted lines from near neutron-star surfaces. However, the optical and *QuantEYE* enjoy the advantage of much higher typical photon fluxes, thus permitting searches for phenomena on much shorter timescales (albeit perhaps diluted to smaller amplitudes than if such studies had been possible in X-rays). In addition, quantum-optical phenomena can not realistically be detected in X-rays (cf. Figure 1.1): the tiny number of observable X-ray photons within any coherence volume makes them behave like classical particles.

Thus, *QuantEYE* on OWL, and future X-ray missions like *XEUS* and *Constellation-X* will have excellent complementarity: to no small extent they will address related astrophysical problems, but their instrumental specifics will enable such studies within different parameter domains, and with respect to different physical processes.

Other foreseen space telescopes such as the *James Webb Space Telescope* for the optical and infrared, or the proposed *World Space Observatory* for the ultraviolet appear to be of too small apertures to permit significant scientific overlap with the high-speed observing programs foreseen with *QuantEYE*.

## 7. Conclusions

Almost all of astronomy depends on the observation and interpretation of properties of electromagnetic radiation (“light”) from celestial sources. How well we understand our Universe depend upon how well we can observe and interpret subtle properties in the light reaching us from celestial bodies.

Over past centuries, astronomical telescopes have been equipped with auxiliary instruments for either obtaining images or recording spectra. Imaging and spectroscopy implied to studying the spatial and temporal coherence of light, properties which can be ascribed to individual photons, or to groups of individual photons. During recent decades it has been realized both theoretically and in the laboratory that light can carry further quantum-optical information beyond this [first-order] coherence, e.g. encoded in the temporal distribution of photon arrival times or in the amount of photon orbital angular momentum. It is now realized that both individual photons and photon streams are more complex and may carry more information than was generally appreciated in the recent past. **Optical astronomy** is the application of optical physics to astronomical observations. Now, that the frontiers of optics have increasingly moved towards photonics\*, i.e. the study and manipulation of individual photons, the time seems ripe to develop also **photonic astronomy!**

Among the sciences, astronomy is uniquely dependent upon the remote sensing of its objects, and upon the interpretation of subtleties in the light reaching us from them. In the laboratory, many effects of non-linear optics have become accessible thanks to the intense light from lasers. In astronomy, the observability of non-linear effects in the photon stream from astronomical sources may soon become accessible thanks to the intense light from extremely large telescopes. Since statistical functions of arriving photon streams increase with at least the square of the intensity, ELT’s will permit enormously more sensitive searches for high-speed phenomena in astrophysics. Although the observability of more complex photon statistics in astronomical sources is not yet established, quantum optics could ultimately offer a fundamentally novel information channel also for astronomy. *QuantEYE* is designed to be the instrument to boldly go and explore this new parameter domain.

Since the present *QuantEYE* design is conservatively based upon existing technologies, a prototype or test instrument could be constructed already in the very near future. As far as we are aware, no other astronomical instrument has been built on its pupil-slicing and photon-counting principles, why a test instrument on some existing large telescope could, already in the near future, become a productive precursor for exploring astrophysics on its very shortest timescales.

*\* Indeed, just as this report was being finished, news did reach us that the 2005 Nobel prize in physics has been awarded in the field of quantum optics! One half of the prize was awarded to Roy Glauber “for his contribution to the quantum theory of optical coherence”. His pioneering papers in this field were discussed in our Section 1, and are listed among the references. The other half of the prize was shared between John L. Hall and Theodor W. Hänsch “for their contributions to the development of laser-based precision spectroscopy, including the optical frequency comb technique”. This concerns the development of optical clocks and accurate timing, discussed in Section 5.*



## APPENDICES

### A1. Coherence Properties of Light

This Appendix gives more details about the arguments expounded in Section 1.9.

Almost all physical optics experiment (interference, diffraction, image formation) can be explained by *classical* electromagnetic field theory (electromagnetic waves). Even non-linear optics (e.g. frequency doubling), and many properties of lasers can be described by classical means.

*However, experiments with very low light intensities (e.g. individual photon counting) lead to a new vision.*

For instance, the experiment by Taylor (1909) of the Young double slit with less than a photon at a time. The classical explanation and the quantum interpretation (interference of probability amplitude) can be made to coincide assuming that the probability of counting a photon is proportional to the intensity of the classical field. The experiment cannot distinguish between the two explanations.

The search for uniquely quantum effects continued with intensity interferometry, through the measurement of fluctuations and correlations between the arrival times of photons. Hanbury Brown and Twiss (HBT, 1957, 1974) measured the fluctuations of the currents from two different photomultipliers illuminated by the same *thermal* light source, finding an enhancement in the two-time intensity correlation function for short time delays (photon bunching). However, even the HBT experiment can be explained by the classical theory that includes the large intensity fluctuations of the electrical field from thermal light.

The development of lasers in the 60's allowed the distinction between *incoherent* (*thermal*, e.g. incandescent matter, gas discharges) and *coherent* (e.g. *laser*) light, on the basis of photon statistics. Arecchi and coworkers (1966) demonstrated that photon counting statistics goes from super-Poissonian at threshold to Poissonian far above threshold: *a strong laser beam well above threshold shows no photon bunching*, instead the light has a Poissonian counting statistics. One consequence is that lasers cannot be perfectly quiet, they show *shot noise* in intensity. This result can be derived both from quantum and from classical models.

Glauber (1963), from his quantum formulation of quantum coherence showed the possibility of uniquely quantum phenomena. One such prediction is *photon anti-bunching*, corresponding to a greater than average separation between photon arrival times of photons. The statistics can become sub-Poissonian and the fluctuations of the photocurrents would be smaller than shot noise. These findings cannot be reconciled with classical electrodynamics, they are entirely of quantum nature. *Light emitted by resonance fluorescence from a two level atom would exhibit anti-bunching*. Today, using e.g. individual trapped ions, one can observe both photon anti-bunching and sub-Poissonian statistics in the same system.

*Quantum noise* (a 'white' noise) is an intrinsic property of the light and it appears for both laser and thermal light. It can be regarded i) as a consequence of the Heisenberg uncertainty principle, or ii) as consequence of the statistical properties of a stream of photons: the photons do not interact with each other, so that the natural state of this system is represented by a Poissonian distribution. As a consequence the photocurrent will display fluctuations dictated by the Poisson statistics. This second point of view is very useful for the interpretation of

*intensity fluctuations.* The first point of view can also handle phase and interference, and therefore it is very useful for instance in the quantum description of beamsplitters and interferometers. Beamsplitters in particular can be interpreted as random selector of photons.

Recently, the role of photon generation processes started to be explored. For instance, it has been shown that the noise of the light might be below the standard quantum limit if the pumping process exhibits sub-Poissonian statistics (e.g. with LEDs).

Another quantum effect is the suppression, or *squeezing*, of quantum fluctuations. This squeezing is not inside the detector but the noise suppression is achieved by means of non linear optical devices (e.g. *a non-linear optical medium*) in the laser light path. For a coherent state the uncertainties in the quadratures are equal and minimize the product in Heisenberg's uncertainty principle. In a squeezed state one quadrature might have reduced fluctuations at the expense of increased fluctuations in the other.

### **A1.1. Deviation from the Average, and Correlation Functions**

In many cases we are concerned with fluctuations of the electromagnetic field, both in time and in space, often too rapid to be measured directly; however, we can derive information about correlations between the fluctuations at two or more space-time points.

In the following we shall consider the fluctuation of the intensity  $I(t)$  of the light. In many practical situations we can put  $I(t) = \langle I \rangle + \delta I(t)$ , where  $\delta I$  (noise) is a quantity with zero mean, and uncorrelated with  $I$ .

In *classical* theory it is possible to make *any noise arbitrarily small* (at least in principle) in the amplitude and phase, such that the amount of information that can be carried by a beam of light is limited only by technical considerations. *This is not true in the quantum theory of light*, strict bound apply to the amount of information that can be encoded in a beam of a particular power.

The *deviation*  $\delta x$  of a quantity  $x$  from its average  $\langle x \rangle$  is defined as:

$$\delta x = x - \langle x \rangle.$$

The *mean square deviation*  $\text{MSD} = \langle (\delta x)^2 \rangle$  is a first measure of the fluctuation:

$$\langle (\delta x)^2 \rangle = \langle (x - \langle x \rangle)^2 \rangle = \langle x^2 \rangle - \langle 2x\langle x \rangle \rangle + \langle x \rangle^2 = \langle x^2 \rangle - \langle x \rangle^2$$

(Sometimes it will be necessary to consider also higher-order deviations).

Consider the distribution  $g(x)dx$  which gives the number of systems in  $dx$  at  $x$ , and its Fourier Transform (namely the *characteristic function* of the distribution):

$$u(t) = \frac{1}{\sqrt{2\pi}} \int_{-\infty}^{+\infty} g(x)e^{ixt} dx$$

On differentiating  $u(t)$ :

$$\langle x^n \rangle = i^{-n} \sqrt{2\pi} \left[ \frac{d^n}{dt^n} u(t) \right]_{t=0}, \quad \langle x^2 \rangle = -\sqrt{2\pi} \left[ \frac{d^2}{dt^2} u(t) \right]_{t=0}$$

In the following we shall be concerned with the fluctuation of the intensity  $I(t)$  of the light. We wish to evaluate the *variance* for a certain detection time  $t_d$ . The variance  $Var(I(t))$  for a classical quantity such  $I$ , is defined as:

$$\Delta I^2(t) = Var(I(t)) = \langle (I(t) - \langle I \rangle)^2 \rangle = \langle I(t) - \langle I \rangle \rangle^2 = \langle (\delta I)^2 \rangle = \langle (\delta I) \rangle^2$$

where  $\langle I \rangle$  is the average intensity and the brackets  $\langle \dots \rangle$  denote averaging over a time interval of length  $t_d$ . The square root of the variance is called the Root-Mean-Square (RMS) of the intensity.

The variance, however, carries no information on the spectral distribution of the noise, therefore it is convenient to introduce another statistical quantity, namely the spectral variance, or noise spectrum:

$$V(\Omega) = \frac{1}{2\pi} \int_{-\infty}^{+\infty} e^{i2\pi\Omega\tau} \langle I(t)I(t+\tau) \rangle d\tau$$

namely the Fourier transform (FT) of the autocorrelation function of the intensity.

In many practical situations we can put  $I(t) = \langle I \rangle + \delta I(t)$ , where  $\delta I$  is a small quantity with zero mean ( $\langle \delta I \rangle = 0$ ) and uncorrelated with  $I$ . Under this condition, the noise spectrum is:

$$V(\Omega) = \langle |\delta FTI(\Omega)|^2 \rangle$$

where  $FTI(\Omega)$  is the component at frequency  $\Omega$  of the Fourier transform of the intensity.

For example, suppose that the fluctuations  $\delta I$  are composed of two parts, namely a deterministic cosine function  $\delta I_{sign} = G \cos(2\pi\Omega t)$  plus a randomly varying noise represented by the stochastic function  $\delta I_{noise} = F\zeta(t)$ , with  $G$  and  $F$  two positive constants. The FT of the signal is a pair of delta functions at  $\pm\Omega$ ; squaring and averaging over a small interval of frequencies around  $\pm\Omega$ , we end up with two signals of strength  $G^2$ . The noise is random over all time scales, thus it will contribute  $F^2\delta\Omega$  at all frequencies. The signal-to-noise (SNR) ratio in this case can be defined as:

$$SNR = -1 + \frac{G^2}{F^2\delta\Omega}$$

The Relative Intensity Noise (RIN) is the ratio of the variance to the average intensity; for a bandwidth  $\delta\Omega = 1$  Hz it is:

$$RIN(\Omega) = \frac{Var(I(\Omega))}{\langle I \rangle^2}$$

As we have already stated, in classical theory it is possible to make any noise arbitrarily small (at least in principle) in the amplitude and phase such that the amount of information that can be carried by a beam of light is limited only by technical considerations. *This is not true in*

the quantum theory of light, strict bound apply to the amount of information that can be encoded in a beam of a particular power.

## A1.2. Correlation Functions

Two important statistical descriptions of the light are provided by the *first and second order correlation functions*,  $G^{(1)}(t)$  and  $G^{(2)}(t)$ .

Suppose we have a light source oscillating at frequency  $\nu$  with amplitude  $\alpha(t) = \alpha_0 e^{i2\pi\nu t}$ ; we split the beam and then superimpose again the two beams, by means of a 50/50 beamsplitter with a delay  $\tau$  in one of the two. The action of the beamsplitter is to produce an output amplitude:

$$\alpha_{out}(t) = \frac{1}{\sqrt{2}} \alpha_0 \left( e^{i2\pi t} + e^{i2\pi(t+\tau)} \right)$$

The detector will produce an output current proportional to the intensity of the output amplitude, averaged over a suitable integration time  $t_d$ :

$$\langle |\alpha_{out}|^2 \rangle = \frac{1}{t_d} \int |\alpha_{out}|^2 dt = \alpha_0^2 + \cos(2\pi\nu\tau + \phi) \langle \alpha^*(t) \alpha(t+\tau) \rangle$$

The photocurrent is thus modulated according to the time delay, and the basic effect is a set of oscillations (fringes). The temporal coherence of light is quantified by the *first order correlation function*:

$$G^{(1)}(\tau) = \frac{\langle \alpha^*(t) \alpha(t+\tau) \rangle}{\alpha_0^2}$$

whose modulus is also equal to the fringe visibility:

$$|G^{(1)}(\tau)| = V(\tau) = \frac{I_{max} - I_{min}}{I_{max} + I_{min}}$$

in the Michelson interferometer.

In the simple example of a perfectly sinusoidal wave of constant amplitude, the visibility function would be always = 1, and the first order correlation function totally independent of  $\tau$  (*infinite coherence time*). More realistically, the signal will have some (even small) spread  $\Delta\nu$  around the central frequency  $\nu$ , which we can approximate with a Gaussian function in the frequency domain:

$$FT(\alpha(\Omega)) = \alpha_0 e^{-2\pi(\nu-\Omega)^2 / \Delta\nu^2}$$

and in the time domain:

$$\alpha(t) = \alpha_0 \frac{\Delta\nu}{\sqrt{2}} e^{-\pi\Delta\nu^2 t^2}, \quad G^{(1)}(\tau) = e^{-\pi\Delta\nu^2 \tau^2 / 2}, \quad G^{(1)}(0) = 1 > G^{(1)}(\tau > 0)$$



In other words, the first-order correlation function is a Gaussian function of  $\tau$  whose width is *inversely proportional to the frequency spread*: for a broad spectrum the correlation time becomes very short.

*Any realization of a Michelson type interferometer measures this first order correlation function.*

Let us now consider the **intensity interferometer**. The two beams (originating from the same source) are **not** optically mixed together, but a time delay  $\tau$  is imposed on one of the two. The outputs of the two photomultipliers (namely the intensities) are then multiplied together in a correlator, whose output is proportional to the *second order correlation function* defined by:

$$G^{(2)}(\tau) = \frac{\langle I(t)I(t+\tau) \rangle}{\langle I(t) \rangle^2}$$

From the symmetry of the definition, it follows that  $G^{(2)}(-\tau) = G^{(2)}(\tau)$ , so that measurements need to be taken only for positive (or negative) time delays.

Notice also that the second order correlation function is not bounded between 0 and 1.

At  $\tau = 0$  it is easy to show that:

$$G^{(2)}(0) = \frac{\langle I(t)I(t) \rangle}{\langle I(t) \rangle^2} = \frac{\Delta I^2}{\langle I \rangle^2} + 1 \geq 1$$

Using the Schwarz inequality:

$$\frac{\langle I(t)I(t+\tau) \rangle^2}{\langle I(t) \rangle^2 \langle I(t+\tau) \rangle^2} \leq 1$$

For ergodic or time-stationary systems the two terms at the denominator are equal, consequently we must have  $G^{(2)}(\tau) \leq G^{(2)}(0)$ . For a perfectly stable wave, the sign = applies, so that  $G^{(2)}(\tau) = G^{(2)}(0) = 1$  for all time delays.

For any classical wave, the degree of coherence should also be less than  $G^{(2)}(0)$ .  
*This result is contradicted for quantum states of light.*

### A1.3. Temporal Coherence and the Coherence Time

Consider a beam of quasi-monochromatic light ( $\Delta\nu/\nu_c \ll 1$ ) of central frequency  $\nu_c$  from a (macroscopically) steady source  $\sigma$ . Suppose the beam is divided into two beams as in the Michelson interferometer, and then reunited after a (sufficiently small) path difference  $\Delta l = c\Delta t$ . In the observing plane **B** a system of fringes is observed, which is a manifestation of the *temporal coherence* of the two beams (see Figure A1.1).

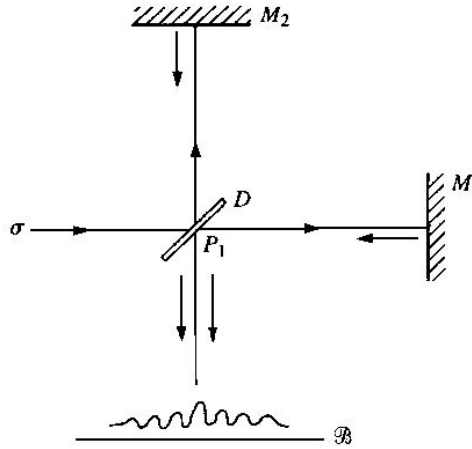


**Fig.A1.1.** Michelson interferometer schematics.

It is a well know experimental fact that the fringes are observed only if:

$$\Delta t \cdot \Delta \nu \leq 1.$$

The time delay:  $\Delta t \approx \frac{1}{\Delta \nu}$  is called the *coherence time*, and the corresponding path difference

$\Delta l = c\Delta t \approx \frac{c}{\Delta \nu}$  is called the *longitudinal coherence length* of the light. We easily obtain:

$$\Delta l = c\Delta t \approx \frac{c}{\Delta \nu} = \left( \frac{\lambda_c}{\Delta \lambda} \right) \lambda_c$$

The formation of the fringes can be understood in different ways, in particular for our purposes by considering the concept of *correlations*. In the observing plane **B** there will be a strong correlation between the fluctuations in the two beams if the time delay is short compared to the correlation time  $1/\Delta \nu$ , no correlation if the time delay is long with respect to the coherence time. The coherence time is thus a measure of the time interval in which appreciable amplitude correlations and phase correlations of the light vibrations at a particular point will persist.

Thus, phenomena with long coherence times will be sharply peaking with respect to their spectrum, i.e., they will be composed of fewer frequencies. The limit of this is an infinite coherence time, which would mean the signal is composed of a singular frequency.

For non-thermal light there is in general no single time that characterizes the range of all correlation functions. There may exist a whole hierarchy of correlation times, characterizing correlations of different orders.

A more precise analysis leads to the following *reciprocity inequality*:  $\Delta t \cdot \Delta \nu \geq 1/4\pi$ , but here we are concerned with order-of-magnitude estimates.

*Example:*

For thermal light, typically  $\Delta\nu \approx 10^8 - 10^9$  Hz,  $\Delta t \approx 10^{-9} - 10^{-8}$  s. Therefore, the longitudinal coherence length  $\Delta l = c\Delta t$  varies from 30 cm to 3 m. If  $\nu_c = 6 \times 10^{14}$  Hz, then  $\Delta\nu/\nu_c = \Delta\lambda/\lambda_c$  varies from  $1.67 \times 10^{-7}$  to  $1.67 \times 10^{-6}$ , and if  $\lambda_c = 500$  nm then  $\Delta\lambda$  varies from  $8.35 \times 10^{-4}$  Å to  $8.35 \times 10^{-3}$  Å.

For a well stabilized laser  $\Delta\nu \approx 10^5$  Hz,  $\Delta l \approx 3$  km. For a green laser (532 nm,  $5.6 \times 10^{14}$  Hz),  $\Delta\nu/\nu_c = \Delta\lambda/\lambda_c = 1.77 \times 10^{-10}$ ,  $\Delta\lambda \approx 9.5 \times 10^{-7}$  Å.

### A1.4. Spatial Coherence and the Coherence Area

Consider now the double slit (Young) experiment with a quasi-monochromatic *thermal light source*  $\sigma$  of extension  $\Delta s$  (such as a square, see Figure A1.2).

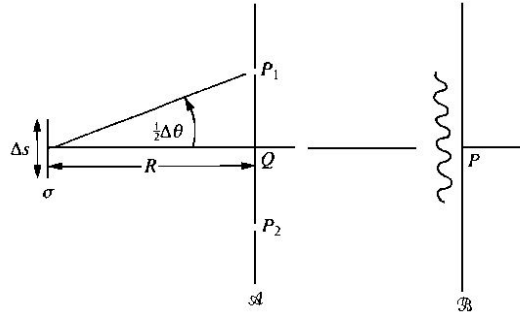


**Fig.A1.2.** Double-slit (Young) experiment schematics. The light is assumed to come from a thermal source.

The pinholes  $P_1$  and  $P_2$  are sufficiently close to the axis of symmetry. Interference fringes are observed in the neighborhood of  $P$ , which are a manifestation of the *spatial coherence* between the two beams. If the distance  $R$  is sufficiently large, fringes will form only if  $\Delta\theta\Delta s \leq \lambda_c$ , or else, if  $\Delta A$  is the area containing the two pinholes, if:

$$\Delta A \approx (R\Delta\theta)^2 \approx R^2 \frac{\lambda_c^2}{(\Delta s)^2}$$

Let us introduce the invariant quantity  $(\Delta s)^2/R^2$ , that is the solid angle  $\Delta\Omega'$  subtended by the source at  $Q$ . Therefore:

$$\Delta A \approx \frac{\lambda_c^2}{\Delta\Omega'}$$

is the lateral coherence area, and the lateral coherence length will be  $\Delta a \approx (\Delta A)^{1/2}$ . Notice the similarity with Airy's radius,  $a_A = 1.22 \lambda/fD$ , where  $f$  is the focal length and  $D$  the diameter of the telescope. For instance, the coherence area of Betelgeuse ( $\theta \approx 0''.047$ ) in the visible is  $\Delta A \approx 6$  m<sup>2</sup>,  $\Delta a \approx 2.5$  m.

These results can again be understood in terms of the correlations: even if each point in the source is statistically independent, they will give rise to correlations in the field, and these correlations are generated in the process of propagation and superposition.

*An example for OWL:* Calculate the apparent diameter  $\Delta\theta$  producing  $\Delta a \approx 100\text{m}$  at four typical wavelengths.

Since

$$\Delta\Omega' \approx \frac{\lambda_c^2}{\Delta A},$$

then:

$$\Delta\theta'' \approx 206265 \times \sqrt{\frac{\Delta\Omega'}{\pi}} \approx 206265 \times \sqrt{\frac{\lambda_c^2}{\Delta A}} \approx 0''.002\lambda_c \quad (\lambda_c \text{ in } \mu\text{m})$$

See the results in Table A1.1. The last three columns translate the angle in astronomically meaningful dimension and distance combinations.

$\lambda_c$	$\Delta\theta''$	1 $R_\odot$ at	1 AU at	1 pc at
350 nm	$7 \times 10^{-4}$	6.6 pc	215 pc	44 Mpc
500 nm	0.001	4.8 pc	158 pc	32 Mpc
1.5 $\mu\text{m}$	0.003	1.5 pc	49.4 pc	10 Mpc
10 $\mu\text{m}$	0.021	0.2 pc	7.5 pc	1.5 Mpc

**Table A1.1.** *The angle of an astronomical thermal source producing  $\Delta a \approx 100\text{m}$*

This example shows why stellar images observed e.g. with the HST have the appearance of a diffraction pattern from a strictly coherent source. The secondary wavelets entering the aperture of the telescope and propagating to the image plane will superpose in the same way as wavelets from a totally coherent beam. The same would be true for a ground telescope if not for the atmospheric seeing.

### A1.5. Coherence Volume and the Degeneracy Parameter

We can call *coherence volume* the cylinder of length  $\Delta l$  and base  $\Delta A$ . For a quasi-monochromatic plane wave the coherence volume is independent of the particular location of this volume.

For the *thermal* source we have:

$$\Delta V \approx \frac{1}{\Delta\Omega'} \frac{\lambda_c}{\Delta\lambda} \lambda_c^3$$

For instance, for the Sun in the visible, and for a very narrow wavelength interval (say  $\Delta\lambda/\lambda_c = 10^{-7}$ ,  $\Delta\lambda = 5 \times 10^{-4} \text{ \AA}$ ),  $\Delta l \approx 5\text{m}$ ,  $\Delta A \approx 1 \text{ mm}^2$ ,  $\Delta V \approx 5 \text{ cm}^3$ . For Betelgeuse, with the same filter,  $\Delta V \approx 30 \text{ m}^3$ .

The concept of coherence volume *applies also to non-thermal sources*, e.g. to lasers. Furthermore, the coherence volume can be interpreted in the context of the description of light as composed by photons. Consider the elementary volume of the phase space  $\Delta\mathbf{x}\Delta\mathbf{p} = h^3$ ; photons having the same polarization and belonging to a region of the phase space not larger than  $h^3$  are *intrinsically indistinguishable* from each other. It can be shown (by using de Broglie's relation between momentum and wavelength of the photon,  $\mathbf{p} = (h/\lambda)\mathbf{n}$ , where  $\mathbf{n}$  is the unit vector in the direction of  $\mathbf{p}$ ) that this is also the meaning of the *coherence volume*,

namely that region of the Cartesian space throughout which the photons are intrinsically indistinguishable.

Let us apply these consideration to a large thermally insulated cavity filled of black-body radiation. Photons in a region of volume  $V$  inside the cavity, having energies in the range  $\Delta E$  around  $E = h\nu_c$ , belong to the same volume of the phase space (and therefore are completely indistinguishable) if:

$$\frac{8\pi}{c^3} V \nu_c^2 \Delta \nu \leq 1, \quad V_{\max} = \frac{1}{8\pi} \left( \frac{\lambda_c}{\Delta \lambda} \right) \lambda_c^3$$

We understand the factor  $4\pi$  because the radiation comes inside  $V$  from all directions, and the extra-factor 2 because the radiation is an equal mixture of two polarization states. We now recall that mean photon density is:

$$\langle \rho \rangle = \frac{(kT)^3}{\pi^2 c^3 \hbar^3}$$

but it can also be shown that the coherence volume is of the order of

$$V \approx \frac{c^3 \hbar^3}{(kT)^3}$$

with the interesting result that the average number of photons within a coherence volume of blackbody radiation is always of the order unity.

*Influence of seeing on the coherence volume:* If we use as typical cell dimension the Fried radius  $r_0$ , the coherence volume becomes  $r_0 \times r_0 \times c\tau$ . Assume  $r_0 \approx 10$  cm,  $c\tau \approx 10$  ms, then in order to find at least 10 photons inside the volume, over a bandwidth of 100 nm at 550 nm, a  $V = 12$  star is necessary. This explains the low sensitivity of any type of interferometer. Notice that the coherence volume increases very rapidly with the wavelength, as  $\lambda^{18/5}$ .

## A1.6. Bose-Einstein Statistics

Particles of symmetrical spins (*bosons*) must have symmetrical wave functions. There is no limit to the number of particles in a state, but states of the whole system differing only by the interchange of two particles are identical and must not be counted as distinct. Let:  $k$  be the Boltzmann constant,  $T$  the absolute temperature,  $\varepsilon$  the energy and  $\mu$  an appropriate parameter (sometimes called Fermi level, but not to be confused with the Fermi energy of the fermions; in particular, for photons  $\mu = 0$ , as explained later in this paragraph).

The Bose-Einstein distribution applies:

$$n(\varepsilon) = \frac{1}{e^{(\varepsilon-\mu)/kT} - 1}, \quad x_i = e^{(\mu-\varepsilon_i)/kT},$$

$$\bar{n}_j = \frac{\sum n_j x_j^{n_j}}{\sum x_j^{n_j}} = x_j \frac{\partial}{\partial x_j} \sum n_j x_j^{n_j} = x_j \frac{\partial}{\partial x_j} \frac{1}{1-x_j}$$

or else, for a single level:

$$\bar{n}_j = \frac{1}{e^{(\varepsilon_j - \mu)/kT} - 1}$$

with  $\bar{n}_j \geq 0$  as the number of particles in a state cannot be negative. Therefore:

$$\langle (\delta n_i)^2 \rangle = \bar{n}_i(1 + \bar{n}_i) \quad , \quad \frac{\langle (\delta n_i)^2 \rangle}{\bar{n}_i^2} = 1 + \frac{1}{\bar{n}_i}$$

*It is a remarkable feature of the Bose gas that the relative fluctuations are of the order of unity for large  $\bar{n}_i$ . Fluctuations are not smoothed as  $\bar{n}$  increases.*

*Einstein (1924, 1925) and Heisenberg (1930) pointed out that the first term on the right corresponds to fluctuations arising from the wave character of light, and the second term to fluctuations in a gas consisting of distinguishable particles.*

Photons in particular are zero rest mass bosons with spin = 1, and we may excite as many photons into a given state as we like (the electric and magnetic field intensities may be made as large as we like). The Fermi level  $\mu$  is equal to zero, and the energy of each photon is  $\varepsilon = h\nu$ .

It is worth at this stage to recall the differences between Maxwell-Boltzmann, Bose-Einstein, and Fermi-Dirac distributions:

- 1) Maxwell-Boltzmann: it applies to *distinguishable non-exclusive* particles (atoms, molecules):

$$n_i = g_i \left[ \frac{N}{(2\pi mkT)^{3/2} CV} \right] e^{-\varepsilon_i/kT} = g_i e^{-\alpha(kT) - \varepsilon_i/kT}$$

The parameter  $\alpha$  depends on temperature, the number of molecules and the distribution of possible energy levels, but the ratio  $f(\varepsilon_1) / f(\varepsilon_2)$  depends only on the difference of energy in units of  $kT$ :  $\frac{f(\varepsilon_1)}{f(\varepsilon_2)} = e^{-(\varepsilon_1 - \varepsilon_2)/kT}$

- 2) Bose-Einstein distribution: it applies to *undistinguishable non exclusive* particles (*bosons*: photons, pions, alpha-particles, in general by all particles with zero or integer spins):

$$n_i = g_i (e^{\alpha + \varepsilon_i/kT} - 1)^{-1}$$

where for photons  $\alpha = 0$ .

- 3) Fermi-Dirac: it applies to *indistinguishable exclusive* particles (*fermions* : electrons, muons, protons, neutrons, in general all particles of half-integer spins)

$$n_i = g_i (e^{(-\varepsilon_F + \varepsilon_i)/kT} + 1)^{-1}$$

Let us call *occupation index* of the energy level  $\varepsilon_i$  the ratio  $f(\varepsilon_i) = n_i/g_i$ .

For the FD distribution the meaning of  $f(\varepsilon)$  is simple: it represents the probability that the state is occupied. No such simple interpretation is possible for MB and BE distributions, because many non-exclusive particles can occupy the same state.

Comparing the BE distribution with MB, it is found that for small energies the occupancy index is larger for the BE distribution than for the MB distribution, while at energies large compared with  $kT$ , the BE distribution approaches the MB form.

Let us examine the FD distribution: the Fermi energy  $\varepsilon_F$  is that for which the occupation index is  $\frac{1}{2}$ . At  $T = 0$  K, the occupancy index is  $= 1$  for all states with  $\varepsilon < \varepsilon_F$ , and is  $= 0$  for all higher states. As  $T$  is raised, a number of particles are excited to energy states a little above the Fermi level from states a little below this level. As  $T$  is raised to very high values, the FD distribution becomes more and more like the MB distribution.

Therefore, when  $e^{\alpha+\varepsilon/kT} \gg 1$ , it is more and more true that  $\frac{f(\varepsilon_1)}{f(\varepsilon_2)} = e^{-(\varepsilon_1-\varepsilon_2)/kT}$  for all three distributions.

*Clearly, the introduction of exclusiveness prevents particles from bunching together in a common energy state. Thus BE statistics leads to more bunching and FD statistics to less bunching than that given by MB statistics.*

## A1.7. Photon Antibunching and Sub-Poissonian Statistics

Photon antibunching and sub-Poissonian photon-counting statistics are manifestations of certain *non-classical states* of light having no description in terms of electromagnetic waves. Both these effects were first observed in the process of resonant fluorescence from atoms. Often confused because usually happening together, the two effects are really different, and need not occur together (Zou & Mandel 1990).

We have already demonstrated that photons tend to distribute themselves in bunches, *so that a photodetector will detect more photon pairs close together (in time) than further apart.*

For stationary light fields, the joint probability density  $P_2(t, t+\Delta t)$  for detecting one photon at a time  $t$  and another photon at a time  $t+\Delta t$  can be written as:

$$P_2(t, t + \Delta t) = K \langle I(t) \rangle^2 [1 + \Lambda(\Delta t)]$$

where  $K$  is an instrumental constant,  $I$  is the light intensity operator ( $\langle I \rangle$  being time-independent) and  $\Lambda(\Delta t)$  a suitable *correlation function* depending only on the time difference  $\Delta t$ . Therefore:

- photon bunching implies that  $P_2$  decreases with increasing  $\Delta t$ , namely  $\Lambda(0) > \Lambda(\Delta t)$
- photon antibunching implies that  $P_2$  increases with increasing  $\Delta t$ , namely  $\Lambda(0) < \Lambda(\Delta t)$ .

This latter condition violates the Schwarz inequality for a field obeying classical statistics, and therefore can occur only in a quantum field.

By contrast some authors have regarded negative values of  $\Lambda(0)$  as signature of antibunching, irrespective of the question whether  $\Lambda(\Delta t)$  increases with  $\Delta t$  from  $t = 0$  or not.

On the other hand, from the probability  $P_N(t, t+T)$  that the detector registers  $N$  photodetections in the time interval  $(t, t+T)$ , for a stationary field we have also:

$$\langle (\Delta N)^2 \rangle - \langle N \rangle = \langle N \rangle^2 \frac{1}{T^2} \int_{-T}^T \Lambda(\tau)(T - |\tau|) d\tau$$

It follows that the sign of  $\Lambda(\Delta t)$  is crucial in determining the sign of the above condition, i.e. whether the photon counting statistics are super- or sub-Poissonian. A negative correlation function for all  $\Delta t$  always implies sub-Poissonian statistics, and this is also a signature of non-classical states.

In the process of *resonance fluorescence from atoms* the photons always exhibit anti-bunching, but the photon counting statistics can be either super- or sub-Poissonian. The opposite can also occur, the photons can exhibit bunching in time and still have sub-Poissonian statistics.

It can be shown then:

$$\langle (\Delta n)^2 \rangle = \langle n \rangle \left[ 1 + \langle n \rangle \frac{\theta(T)}{T} \right]$$

where  $R = \langle n \rangle / T$  is the average counting rate,  $\theta(T)$  is :

$$\theta(T) = \int_{-T}^T \left( 1 - \frac{|\tau|}{T} \right) \Lambda(\tau) d\tau$$

and  $\Lambda$  is the (normalized) intensity correlation function. Therefore the parameter  $Q$  expresses the fractional deviation of the variance from the Poisson variance:

$$Q = \frac{\langle (\Delta n)^2 \rangle - \langle n \rangle}{\langle n \rangle} = \langle n \rangle \frac{\theta(T)}{T} = R\theta(T)$$

Hence, the variance is greater or less than the Poisson variance according to the sign of  $\theta(T)$ . For instance, the counts from a fluorescent light radiated by a two-level atom in the presence of a coherent exciting field in resonance, fluctuate in a sub-Poissonian matter.

Notice also that, by calling  $G(T)$  the function:

$$G(T) = \langle (\Delta n)^2 \rangle - \langle n \rangle = R^2 T \theta(T)$$

then (given that  $\Lambda(-\tau) = \Lambda(\tau)$ ):

$$\frac{dG}{dT} = 2R^2 \int_0^T \Lambda(\tau) d\tau \quad , \quad \frac{d^2G}{dT^2} = 2R^2 \Lambda(T)$$

Double derivation of the counts produces then  $\Lambda(\tau)$ , but of course in any process of double derivation noise is a crucial parameter.



## A1.8. Photons from a Black Body

The duality wave-particles emerges very clearly in the present paragraph, where we need a different concept for photons. In any detection process we can think of photons as localized non-interacting particles with energy  $h\nu$ , zero rest mass, momentum  $\hbar k$ , spin  $\hbar$ .

*Alternatively, we can think of the photon number of a radiation field mode. Each mode has energy states like a harmonic oscillator; the excitation of the mode is said to be the number of photons in the mode. In this view the photons are distributed, they are a property of the entire mode. A laser beam can be described as a single mode propagating from the laser; the photon number of the mode is linked to the flux of photons in the external beam, which can be detected and measured. This number of photons in a laser is very high.*

*In contrast, in the visible, for thermal light the possible number of modes can greatly exceed the number of photons, unless the temperature becomes higher than 1000 K (see Table A1-2).*

According to Planck's law, the mode density is:

$$\rho_\nu d\nu = \frac{8\pi\nu^2}{c^3} d\nu$$

thermally excited according to a Boltzmann distribution:

$$P(E_n) = \frac{1 - e^{-E_n/kT}}{\sum e^{-E_n/kT}}$$

Assuming  $E_n = (n + \frac{1}{2})h\nu$  for the energy of a mode (in other words, for a box in the phase space with  $n$  photons; notice the factor  $\frac{1}{2}$ , unobservable ground energy), we derive the probability distribution for  $n$  photons in one mode:

$$P_n(\nu, T) = \frac{1 - e^{-h\nu/kT}}{e^{nh\nu/kT}}$$

Therefore the average number of photons (or *degeneracy*) in a mode is:

$$\delta = \langle n(\nu, T) \rangle = \sum_0^\infty n P_n(\nu, T) = \frac{1}{e^{h\nu/kT} - 1}$$

Some values are given in Table A1.2 over the wavelength regime of OWL and for several temperatures of astrophysical interest. Notice that at high temperatures  $\delta \approx \delta_0 T$ . (Numerical values:  $h = 6.62 \times 10^{-27}$ ,  $k = 1.38 \times 10^{-16}$ )

$\nu$	$T = 10^3$ K	$T = 10^4$ K	$T = 10^5$ K	$T = 10^6$ K	$T = 10^7$ K
$8.6 \times 10^{14}$ Hz ( $\lambda$ 350 nm)	$1.42 \times 10^{-18}$	0.02	2.00	23.04	242.87
$6 \times 10^{14}$ Hz ( $\lambda$ 500 nm)	$3.16 \times 10^{-13}$	0.06	3.00	34.27	347.17
$3.75 \times 10^{14}$ Hz ( $\lambda$ 800 nm)	$1.56 \times 10^{-8}$	0.20	5.08	55.13	555.78
$3 \times 10^{14}$ Hz ( $\lambda$ 1.0 $\mu$ m)	$5.68 \times 10^{-7}$	0.31	6.46	69.04	694.84
$1 \times 10^{14}$ Hz ( $\lambda$ 3.0 $\mu$ m)	0.0084	1.62	20.36	208.10	$2.08 \times 10^3$
$6 \times 10^{13}$ Hz ( $\lambda$ 5 $\mu$ m)	0.0597	3,01	34.27	347.17	$3.48 \times 10^3$
$3 \times 10^{13}$ Hz ( $\lambda$ 10 $\mu$ m)	0.3110	6.46	69.04	694.84	$6.95 \times 10^3$

**Table A1.2.** Average number of photons in a mode

Since the different modes are independent, the optical photons produced by thermal sources are also independent, *but only to a first approximation*, so that it is only approximately true that  $\langle (\Delta n)^2 \rangle \approx \langle n \rangle$ , which is characteristic of Poisson statistics. Nevertheless, the small departures from strict Poisson distribution can lead to important observable effects, as discussed later.

### A1.9. Fluctuations of Black-Body and Thermal Radiation

Regarding the instantaneous fluctuating intensity of blackbody radiation, it can be shown that the probability and moments are:

$$\Pi(I) = \frac{3}{2} \frac{(3I)^2}{\langle I \rangle^3} e^{-3I/\langle I \rangle}, \quad \langle I \rangle \cdot \Pi(I) = \frac{27}{2} \left( \frac{I}{\langle I \rangle} \right)^3 e^{-3I/\langle I \rangle},$$

$$\langle I^n \rangle = \frac{(n+2)!}{2} \left( \frac{\langle I \rangle}{3} \right)^n$$

so that the most probable value of  $I$  is  $2\langle I \rangle/3$ .

For the variance:

$$\langle (\Delta I)^2 \rangle = \langle I^2 \rangle - \langle I \rangle^2 = \frac{1}{3} \langle I \rangle^2$$

These results must be modified for the so-called *thermal* light (or also *chaotic* light), coming from sources that are only approximately in thermal equilibrium. For instance, the light exiting from a small opening in black body cavity and *imaged through a filter*. In particular, suppose that the total intensity  $I$  is the sum of two orthogonal components  $I_1$  and  $I_2$ ,  $I = I_1 + I_2$ ,  $\langle I \rangle = \langle I_1 \rangle + \langle I_2 \rangle$ , with degree of polarization  $P$ .

$$P = \frac{\langle I_1 \rangle - \langle I_2 \rangle}{\langle I_1 \rangle + \langle I_2 \rangle} ,$$

The probability and the moments become:

$$\langle I \rangle \cdot \Pi(I) = \frac{1}{P} \left[ e^{-2I/(\langle I \rangle (1+P))} - e^{-2I/(\langle I \rangle (1-P))} \right] , \quad \langle I^n \rangle = \frac{n! \langle I \rangle^n}{2^{n+1} P} \left[ (1+P)^{n+1} - (1-P)^{n+1} \right]$$

so that the variance becomes:

$$\langle (\Delta I)^2 \rangle = \langle I^2 \rangle - \langle I \rangle^2 = \frac{1}{2} \langle I \rangle^2 (1+P)^2$$

which ranges from  $1 \langle I \rangle^2$  for a totally polarized beam to  $\langle I \rangle^2 / 2$  for a totally unpolarized beam.

## A1.10. Statistical Analysis when Photon Counting

The multiple photoelectric detection probability is related to the probability of detection at a certain place and time; this is an important quantity that characterizes the optical field we want to analyze. There are different classes of sophisticated measurements that can involve correlations between photodetections in different points of the whole detector. The simplest scheme is a situation represented by two photodetectors of area  $S$  and located in different points  $r_1$  and  $r_2$  of our large detector. In the plane wave approximation, the joint probability that two events are detected by the first device at time  $t_1$  within  $\Delta t_1$  and by the second in  $t_2$  and  $\Delta t_2$ , is:

$$P(r_1, t_1, \Delta t_1; r_2, t_2, \Delta t_2)$$

for a field in a coherent state  $|\nu\rangle$ . The probability of the first photodetection is

$$P_1 \sim QE \cdot I(r_1, t_1) \cdot S_1 \cdot \Delta t_1,$$

where  $QE$  is the quantum efficiency of the detector,  $I(r_1, t_1)$  the light intensity,  $S_1$  the detector's area. For two or more detectors the probabilities must be multiplied together. In our case we obtain

$$P = \prod_1^N QE_i \cdot I(r_i, t_i) \cdot S_i \cdot \Delta t_i$$

where  $N$  is the number of independent detectors (in our case  $N \approx 100$ ).

The multiple detection of events in states for which photon counting correlations exist evidently will not occur at random, and the study of their correlation in space and time could give important information about the nature of the source. An example is the already cited Hanbury Brown–Twiss experiment. In some sources the correlation is shown by measuring the joint detection probability of the detector in two different times  $P(r_1, t_1, \Delta t_1; r_1, t_2, \Delta t_2)$ , as a function of the separation  $|t_2 - t_1| = \tau$  in time, obtained via photon counting. If the field is stationary, its normalized correlation function between two joint detections  $C(r_1, t_1; r_1, t_2)$  is a function only of the time difference  $\tau$ . In the case where  $C(0) > C(\tau)$  we have **bunching**: two

events are more likely to occur close together in time. The opposite case is *antibunching*, where  $C(0) < C(\tau)$ .

In the chaotic dynamics jargon, those behaviors are known as Joseph and Noah effects; the semi-classical counterparts of our phenomena are described by black and pink noises, related to fractional Brownian motion. An interesting tool in this classical view is Hurst analysis (Feder 1988).

The more conventional problem of detecting *fast variability* in a peculiar object using photon counting, has been treated in several places, and many statistical tools have been developed in the past literature. Previous experiments in the astronomical context (e.g. MANIA, see Appendix 3) derived the correlation functions from the counting statistics, either with custom developed statistical techniques or from second moment of the photoelectron counts, which contains information about the correlation function of the measured events.

The data were accumulated as a sequence of photon time arrivals chopped from the object and from a comparison star, and then analyzed by the  $y_2$  and  $d_2$  functions technique by Shvartsman (1977), Beskin et al. (1994). The  $y_2$  function method, which is based on the statistical analysis of the time intervals between successive photon detections, has been developed for the search of variability having timescale  $\tau \sim 10^{-7} - 10^{-2}$  sec. It is based on the statistical analysis of the time intervals between each successive photodetection:

$$y_{2i}(\tau_i, \tau_{i+1}) = \frac{p_{\text{object}}(\tau_i, \tau_{i+1}) - p_{\text{star}}(\tau_i, \tau_{i+1})}{p_{\text{star}}(\tau_i, \tau_{i+1})}$$

where  $p_{\text{object}}$  and  $p_{\text{star}}$  are the fraction of intervals of duration from  $\tau_i$  to  $\tau_{i+1}$  for the object and the reference star respectively.

The  $d_2$  function, instead, was developed in the case when the variability is searched on much longer timescales. This is achieved by dividing the observing time  $T$  in  $m_i$  sub-intervals of size  $\tau_i$ . The number of photons detected in the  $j$ -th interval are  $n_{\text{object}}^j(\tau_i)$  and  $n_{\text{star}}^j(\tau_i)$ . The  $d_2$  function is defined as:

$$d_2(\tau_i) = \frac{\Delta[n_{\text{object}}(\tau_i)]}{\langle n_{\text{object}}^2(\tau_i) \rangle} - \frac{\Delta[n_{\text{star}}(\tau_i)]}{\langle n_{\text{star}}^2(\tau_i) \rangle}$$

where  $\Delta[n_{\text{object}}(\tau_i)]$  and  $\Delta[n_{\text{star}}(\tau_i)]$  are the dispersion in the photon numbers  $n_{\text{object}}^j(\tau_i)$  and  $n_{\text{star}}^j(\tau_i)$ . The quantities  $\langle n_{\text{object}}^2(\tau_i) \rangle$  and  $\langle n_{\text{star}}^2(\tau_i) \rangle$  are the mean quadratic values. If there is no variability in the object both the functions are null. Beskin et al. (1994) analyzed with this method the fast time variations of two flares having 0.25 s of total time duration and characteristic rising time of 50-60 ms from the LMXRB MXB 1735-44X ( $m_v = 17.5$ ), with the 2.15 meter CASLEO telescope in Argentina.

### **A1.11. Experimental Evidence of Correlated Photon Fluctuations from Thermal Sources**

Experiments bearing on large photon fluctuations were reported by Hanbury Brown and Twiss in 1956; they found positive correlations between photons in two coherent beams of light originating from a *thermal* source: when a photon is registered in one channel, the probability

of detecting a photon in the second channel in the same time interval is higher than if the events were uncorrelated.

The correlation depends on the *square of the number of quanta* per unit time in the beam.

According to Bose-Einstein statistics, this correlation can be explained by *bunching of photons* in the same phase-space cell. For very short intervals, the probability of finding a second photon is twice than for two independent particles. If the two detectors are effectively in the same cell of the phase space, for example they are separated parallel to the incoming wavefront, then the arrival of photons will appear to be correlated in time; they will tend to arrive in pairs.

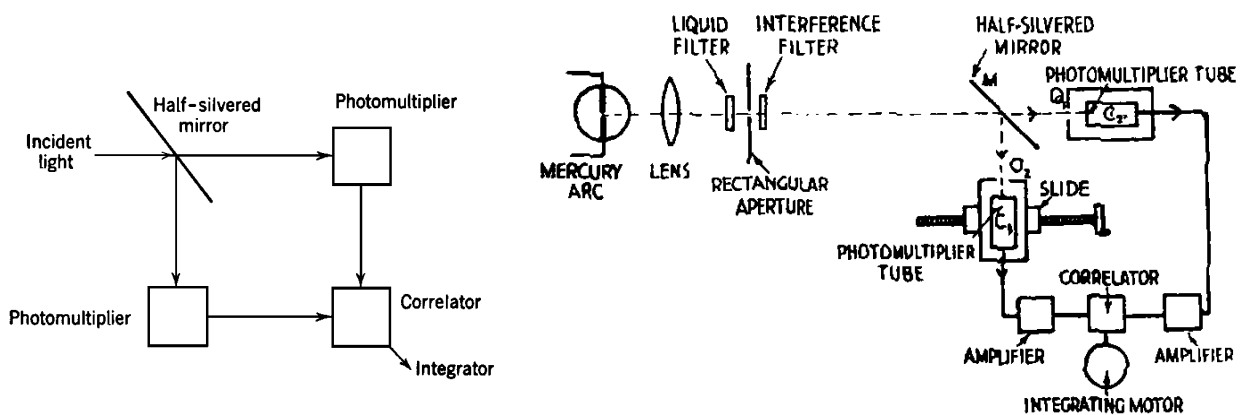


**Fig.A1.3.** Hanbury Brown and Twiss original experiment (1956). The left side shows the principle. The right side shows a simplified diagram of the real experiment. Notice that the lower PM tube could be moved on the slide in order to increase the separation of the two tubes as seen from the source, from zero to a maximum distance of three times the width of the cathode. In this way the coherence between the two sources could be varied at will.

Purcell (1956) explained the phenomenon in terms of *wave packet*: think of a stream of wave packets, each about  $c/\Delta\nu$  long, in a random sequence. Each packet contains one photon. There is a certain probability that two such wave trains accidentally overlap. When the packet overlap they interfere, and the result is a packet with something in between 0 and 4 photons. Thus the *photon density fluctuations are large* (if we do the same experiment with electrons we find a fluctuations suppression, not an enhancement, because of the Pauli exclusion principle).

We can express the same concept in a different semi-classical way: the two currents fluctuate, and the fluctuations are partially correlated. The principal component of the fluctuations is the uncorrelated shot noise in the electronics. In addition, there is a smaller component called *wave noise* which corresponds to the fluctuations in intensity of the light wave. *Those two wave noises are at least partially correlated, provided there is some degree of coherence between the light at the two detectors.*

As already stated, the fringe visibility in the Michelson interferometer is given by:

$$V_d = \frac{I_{\max} - I_{\min}}{I_{\max} + I_{\min}}$$

In the intensity interferometer, the correlation of the wave noise component is proportional to the square of the degree of coherence of light at the two detectors, and thus to the square of the of the fringe visibility that would be observed in a Michelson interferometer under the same conditions:

$$c(d) = c_0(d) \langle \Delta i_1 \Delta i_2 \rangle / (\langle i_1 \rangle \langle i_2 \rangle) = |\gamma_d|^2 = V_d^2, \quad V_d = |\gamma_d|$$

The degree of coherence  $\gamma_d$  of the light at the two apertures depends upon the angular diameter  $\theta$  of the star, the wavelength  $\lambda$  of the light and the separation  $d$  of the two mirrors. For a uniform disc of size  $\theta$ , the first zero of the visibility function is reached at  $d = 1.22\lambda / \theta$ .

## A2. Intensity Interferometry

Here we provide some additional information on the Hanbury Brown – Twiss (HBT) interferometer at Narrabri (New South Wales, Australia), and give some examples of what has been expounded in Section 1.10 (*The intensity interferometer*).

### A2.1. The Original Interferometer at Narrabri

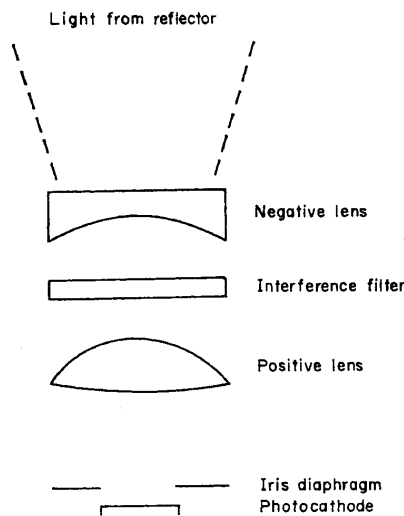


*Fig.A2.1. The focal stations*

The converging beam was collimated by a negative lens with a diameter of 9 cm and passed through an interference filter which was approximately 10 nm wide. It was then focused by a positive lens, through an iris diaphragm, on the photocathode having a minimum useful diameter of 42 mm. The photomultipliers (PMTs) had a  $q_e$  of about 0.2 at 440 nm and were adjusted in gain to give a photocurrent of about 100  $\mu$ A. The fluctuations in the anode current were carried by high-frequency coaxial cables to the central station, where they were amplified by wide-band amplifiers (10-110 MHz) and combined in the linear multiplier. Actually, a phase switch was inserted in one of the cables so that the sign of the integrated correlation was changed every 10 seconds.

To see how the HBT interferometer works, consider two point sources  $P_1$  and  $P_2$  on the surface of the star. The two points will act as perfectly uncorrelated light sources, having a spectrum represented by the superposition of Fourier components of every frequency  $\omega$ . Detector A sees the superposition of all these components from  $P_1$  and  $P_2$ , say for two components of a plane-polarized wave:

$$i_A = K_A [E_1 \sin(\omega_1 t + \phi_1) + E_2 \sin(\omega_2 t + \phi_2)]^2$$

where  $K_A$  is an instrumental constant. The same for detector B, but with a different phase:

$$i_B = K_B [E_1 \sin(\omega_1(t + d_1/c) + \phi_1) + E_2 \sin(\omega_2(t + d_2/c) + \phi_2)]^2$$

Let us assume that the bandwidth of the detector is limited by an interference filter (which was approximately 10 nm wide in the Narrabri interferometer, but it could be made narrower) so that the two frequencies will be very nearly equal. Expanding the squares of the two currents, we easily find a constant term (the total intensity, which is filtered out by the filters, and can be measured separately), plus terms in  $2\omega_1$ ,  $2\omega_2$ ,  $(\omega_1 + \omega_2)$ , which again are rejected by the electric filter, plus finally a term in  $(\omega_1 - \omega_2)$  which is the one that concerns us:

$$i_A = K_A E_1 E_2 [\cos(\omega_1 - \omega_2)t + (\phi_1 - \phi_2)]$$

$$i_B = K_B E_1 E_2 [\cos(\omega_1 - \omega_2)t + (\phi_1 - \phi_2) + \omega_1 d_1/c - \omega_2 d_2/c]$$

These two components have therefore the same frequency  $(\omega_1 - \omega_2)$  but they differ in phase. Let us calculate now their product (*correlation*), with the assumption  $\omega_1 \approx \omega_2$ :

$$c_d = \frac{1}{2} K_A K_B E_1^2 E_2^2 \cos\left[\frac{\omega}{c}(d_1 - d_2)\right] = \frac{1}{2} K_A K_B E_1^2 E_2^2 \cos\left(\frac{2\pi d}{\lambda}\theta\right)$$

By integrating over all possible pairs of points, over all wavelengths through the interference filter, and over all electrical frequencies, we conclude that *the correlation is proportional to the square of the modulus of the complex degree of coherence of the light at the two detectors, and therefore also proportional to the square of the fringe visibility in a Michelson interferometer having the same baseline.*

## A2.2. Examples of Intensity Fluctuations When Photon Counting

We provide some numeric examples of the basic equations:

$$\begin{aligned} N_{tot}(T_0) &= N_r(T_0) + N_c(T_0) = N_r(T_0) \left[1 + \frac{q_e^2 N_0^2 \tau_0 T_0}{4q_e^2 N_0^2 \tau_c T_0}\right] = N_r(T_0) \left[1 + \frac{\tau_0}{4\tau_c}\right] = \\ &= N_r(T_0) \left[1 + \frac{1}{4(\Delta\nu/\nu_0)\nu_0\tau_c}\right] \end{aligned}$$

$$\frac{S}{N} = \frac{N_c(T_0)}{f_r(T_0)} = \frac{1}{2} q_e N_0 \tau_0 \sqrt{\frac{T_0}{2\tau_c}} = \frac{1}{2} q_e \frac{N_0}{\Delta\nu} \sqrt{\frac{T_0}{2\tau_c}} = \frac{1}{2} q_e A n_0 \sqrt{\frac{T_0}{2\tau_c}}$$

Visible light,  $\nu_0 = 6 \times 10^{14}$  Hz (in wavelength:  $\lambda_0 = 500$  nm), bandpass  $\Delta\lambda = 0.1$  nm =  $1\text{\AA}$ , then  $\Delta\lambda/\lambda_0 = \Delta\nu/\nu_0 = 2 \times 10^{-4}$ ,  $\Delta\nu = 1.2 \times 10^{11}$  Hz,  $\tau_0 = 8.33 \times 10^{-12}$  s.

With a time tagging capability  $\tau_c = 1 \times 10^{-10}$  s = 0.1 ns, then the term  $\tau_0/4\tau_c = 2.1 \times 10^{-2}$

*Example with the (conservative) assumption  $\tau_c = 1 \times 10^{-9}$  s :*

From the calibration of Vega, and an average atmospheric extinction of 0.2 mag ( $\approx 20\%$ ) at the zenith, we receive

$N_{ph, A}(V=0) = 860$  ph $\cdot$ cm $^{-2}$  $\cdot$ s $^{-1}$  $\text{\AA}^{-1}$  at 500 nm, corresponding to:



$n_{\text{ph,Hz}} (V=0) = 7.1 \times 10^{-9} \text{ ph} \cdot \text{s}^{-1} \cdot \text{cm}^{-2} \cdot \text{Hz}^{-1}$  at  $\nu = 6 \times 10^{14} \text{ Hz}$ .

Over the OWL aperture ( $\approx 7.3 \times 10^7 \text{ cm}^2$ , including obscuration), with an assumed overall reflectivity of 0.6, and  $q_e = 0.4$  (with SPADs), Vega would produce a count rate of:

$$q_e A n_0 = q_e \cdot A \cdot R^6 \cdot n_{\text{ph, Hz}} = 0.4 \times 7.3 \times 10^7 \times 0.6 \times 7.1 \times 10^{-9} = 2.66 \times 10^{10} \text{ c} \cdot \text{s}^{-1} \cdot \text{\AA}^{-1} = 1.24 \times 10^{-1} \text{ c} \cdot \text{s}^{-1} \cdot \text{Hz}^{-1}$$

By letting:  $T_0 = 3600 \text{ s} = 1 \text{ h}$ ,  $\tau_c = 1 \times 10^{-10} \text{ s}$ , we derive:  $\sqrt{\frac{3600}{2 \times 10^{-10}}} = 4.24 \times 10^6$

so that in 1 hour integration time:  $S/N (V=0)_{1\text{h}} \approx 5.3 \times 10^5$ ,  $S/N (V=5)_{1\text{h}} \approx 5.3 \times 10^3$ ,  $S/N (V=10)_{1\text{h}} \approx 53$ ,  $S/N (V=12.5)_{1\text{h}} \approx 5.3$ .

Or else, at the limit  $S/N = 3$ :

$$\boxed{S/N(D=100\text{m}, T_0=1\text{h}, q_e = 0.4, \tau_c = 1 \times 10^{-10} \text{ s}) = 3 \quad \text{at } V \approx 13.5 (\lambda = 500 \text{ nm})}$$

a result that clearly confirms the intrinsically low sensitivity of the technique.

For the near-IR: assume to obtain SPADs having in the H band ( $\lambda \sim 1.6 \mu\text{m}$ ), the same  $q_e$  and timing characteristics  $\tau_c$  as in the visible. Using the same calibration adopted for V:

$n_{\text{ph,Hz}} (H=0) = 1.60 \times 10^{-8} \text{ ph} \cdot \text{s}^{-1} \cdot \text{cm}^{-2} \cdot \text{Hz}^{-1}$  at  $\nu = 0.92 \times 10^{14} \text{ Hz}$ ,

$$q_e A n_0 = q_e \cdot A \cdot R^6 \cdot n_{\text{ph, Hz}} = 0.4 \times 7.3 \times 10^7 \times 0.6 \times 1.6 \times 10^{-8} = 2.7 \times 10^{-1} \text{ c} \cdot \text{s}^{-1} \cdot \text{Hz}^{-1}$$

so that in 1 hour integration time:  $S/N (J=0)_{1\text{h}} \approx 10^6$ ,  $S/N (J=5)_{1\text{h}} \approx 10^4$ ,  $S/N (J=10)_{1\text{h}} \approx 10^2$ ,  $S/N (J=12.5)_{1\text{h}} \approx 10$ .

Or else, in the  $J$  band:

$$\boxed{S/N(D=100\text{m}, T_0=1\text{h}, q_e = 0.4, \tau_c = 1 \times 10^{-10} \text{ s}) = 3 \quad \text{at } H \approx 14.0 (\lambda = 1.3 \mu\text{m})}$$

The previous analysis must be refined by inserting the following factors:

- the *partial coherence factor*  $\Delta(D, \nu_0)$ , which is function of the parameter  $\pi a D \nu_0 / c R_0$ , where:  
 $a$  = linear dimension of the light source  
 $D$  = linear dimension of the photocathode  
 $R_0$  = distance of the light source  
 $\nu_0$  = mid-band frequency
- the *normalized correlation factor*  $\Gamma^2(d, \nu_0)$  which is function of the parameters  $\pi a D \nu_0 / c R_0$ ,  $\pi a d \nu_0 / c R_0$ , where  $d$  is the linear separation between the two photocathodes.
- the factors  $\gamma_1, \gamma_2$  introduced to allow for any loss of correlation in the optical and electronic systems, and for the effect of dark current and background light (see later a detailed discussion).

The ratio  $\rho_c$  of the number of correlated to random coincidences is then given by:

$$\rho_c = \frac{N_c(T_0)}{N_r(T_0)} = \frac{1}{4} \frac{\tau_0}{\tau_c} \Delta(D, \nu_0) \Gamma^2(d, \nu_0) \gamma_1 \gamma_2$$

Therefore, the S/N becomes:

$$\frac{S}{N} = \frac{N_c(T_0)}{f_r(T_0)} = \frac{1}{2} q_e N_0 \tau_0 \sqrt{\frac{T_0}{2\tau_c}} \Delta(D, \nu_0) \Gamma^2(d, \nu_0) \gamma_1 \gamma_2$$

Regarding the S/N, in Paper III (1958) HBT provide the following expression (for totally unpolarized light, and for their realization with a linear multiplier):

$$\frac{S}{N} = \varepsilon q_e \sqrt{A_1 A_2} \gamma \frac{\mu-1}{\mu} \frac{1}{1+\delta} \sqrt{\frac{b_v}{2\eta}} N_0 \tau_0 \Delta(D, \nu_0) \Gamma^2(d, \nu_0) \frac{\sum_1^m T_r \rho_r^{2\sec\zeta_r} \sigma_r}{\sqrt{\sum_1^m T_r \rho_r^{2\sec\zeta_r} (1+a_r)^2}}$$

where:

$N_0 \tau_0 = n_0 =$  nr. of photons ( $m^{-2}s^{-1}Hz^{-1}$ ) on the top of the atmosphere;

$\gamma =$  the product of the mirror reflectivity and filter transmission,

$\rho =$  the average atmospheric transmission at the Zenith,  $\zeta$  is the Zenith distance,

$(1+a_r) =$  the ratio between the total flux on each photocathode (sky plus star) to the star only flux,

$\varepsilon$  is the combined loss of correlation in the optical and electronic equipment,

$(1+\delta) =$  the excess noise produced in the electronics,

$\mu/(\mu-1) =$  the excess noise in the photomultiplier;

$b_v =$  the cross-correlation bandwidth of the two channels of complex frequency characteristics  $F$ :

$$b_v = \frac{1}{2F_{\max}^2} \int_0^{\infty} [F_1(f)F_2^*(f) + F_1^*(f)F_2(f)] df$$

$\eta =$  the normalized spectral density of the fluctuations at the output of the two amplifiers defined by:

$$\eta = \frac{1}{b_v F_{\max}^4} \int_0^{\infty} |F_1^2(f)F_2^2(f)| df$$

$\sigma_r =$  the normalized spectral density of the light incident on the photocathodes defined by:

$$\sigma_r = \frac{1}{\alpha \gamma \rho_r^{\sec\zeta_r} n_0} \frac{\int \alpha(\nu)^2 \gamma(\nu)^2 \rho_r^{2\sec\zeta_r} n_0(\nu)^2 d\nu}{\int \alpha(\nu) \gamma(\nu) \rho_r^{\sec\zeta_r} n_0(\nu) d\nu}$$

In the original Narrabri realization, HBT achieved the following approximate values:

$$b_v/\eta = 7 \times 10^7 \text{ Hz} ; \quad \varepsilon = 1 ; \quad \mu/(\mu-1) = 0.8 ; \quad \sigma = 0.8 ; \quad \gamma = 0.7 ; \quad (1+\delta) = 1.0$$

The flux of photons from a star of apparent magnitude  $B$  outside the atmosphere was assumed  $n_0(4300A) = 6.67 \times 10^{(-9.0-0.4B)}$ . The cathode efficiency was  $q_e = 0.2$  at 430 nm.

The optical quality of the telescope was very poor, with a sky of radius 6 arcmin. The sky brightness was equivalent to a 4<sup>th</sup> mag star per sq degree (i.e. a star of 7.5<sup>th</sup> mag through the aperture; in a darker site, the value could be 5<sup>th</sup> mag star per sq degree).

In order to examine the influence of the several parameters, the S/N ratio from an unresolved star can be rewritten in the following way:

$$\frac{S}{N} = K_{instr} \cdot q_e \cdot A \cdot n_0(m) \cdot \sqrt{T \cdot ElectricalBandwidth} \cdot g(sky)$$

The quantum efficiency  $q_e$ , the area  $A$  and the photon flux per unit frequency bandwidth  $n_0$  enter with the first power, the exposure time and the electric bandwidth with the  $\frac{1}{2}$  power. Therefore we can use a better detector and a wider electric bandwidth ( $\tau_c$  as short as possible), in conjunction with a larger telescope and excellent optical quality to minimize the influence of the sky background.

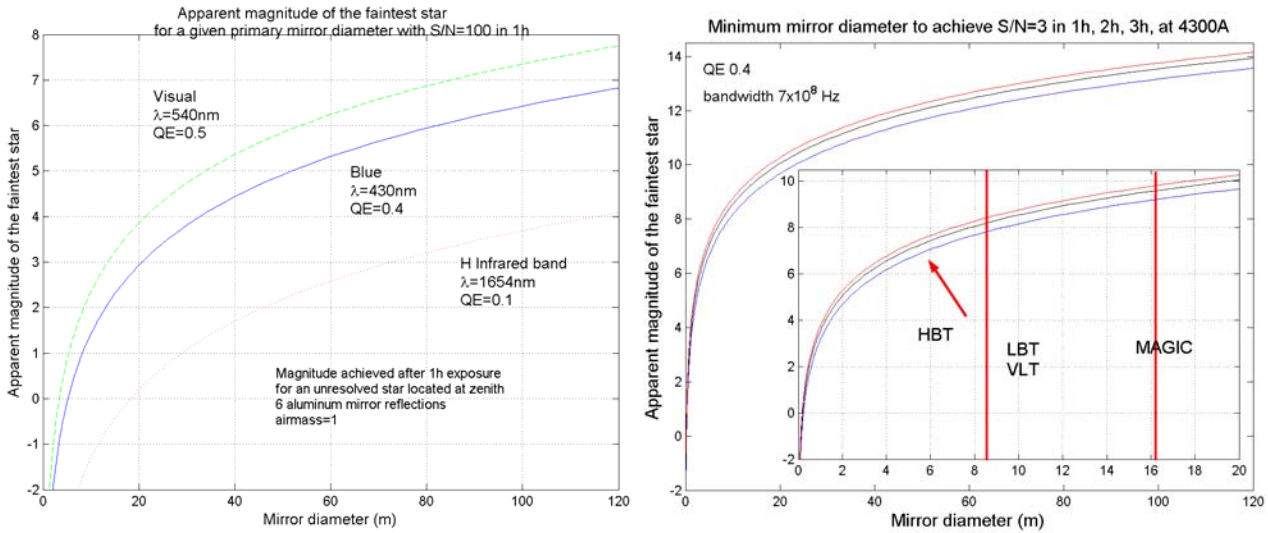


**Fig.A2.2.** Left: the magnitude of a star producing  $S/N = 100$  in 1h observing time as function of the mirror diameter, in three bands (B, V, H). The star is at the zenith, 6-mirrors Al coated optical train. The detector insures  $\tau_c = 10^{-9}$  s. Right: the mirror diameter needed to achieve  $S/N = 3$  in 1<sup>h</sup>, 2<sup>h</sup>, 3<sup>h</sup> at a given B magnitude, assuming a QE of 0.4 and an electrical bandwidth of only  $7 \times 10^8$  Hz. The inset expands the curve to show the capabilities of VLT and LBT, and of MAGIC. The arrow HBT indicates the limiting magnitude achieved by the original Narrabri interferometer, often with week-long integrations.

A general program has been written to calculate the performance of an intensity interferometer at any wavelength from the blue to the near IR, with different detector characteristics (quantum efficiency, time tagging capability), at different elevations, with different sky contributions and transparency models. As examples of the output, the left panel of Figure A2.2 gives the magnitude of a star at the zenith producing  $S/N = 100$  (namely, a  $S/N$  value adequate to provide data about the limb darkening) in 1<sup>h</sup> exposure time, as function of the telescope diameter, for three bands (B, V, H). The magnitude on the ordinate refers to the magnitude in each particular band. The optical quality of the telescope was assumed 1", so that the sky contribution is negligible, the reflectivity is insured by 6 aluminized mirrors. The bandwidth was assumed  $1 \times 10^9$  Hz. The right panel gives instead the

minimum mirror diameter needed to achieve  $S/N = 3$  in 1<sup>h</sup>, 2<sup>h</sup>, 3<sup>h</sup> at a given B magnitude, assuming a QE of 0.4 and an electrical bandwidth of only  $7 \times 10^8$  Hz. The inset expands the curve to show the capabilities of VLT and LBT, and of MAGIC. The arrow HBT indicates the limiting magnitude achieved by the original Narrabri interferometer, often with *week-long* integrations.

### A2.3. Resolution vs. Stellar Surface Temperature

For main-sequence stars, we can use the relation:

$$2 \log T_{\text{eff}} = 8.44 - 0.2C_V - 0.2V - \log \theta_0 \quad (\text{with } \theta_0 \text{ in mas})$$

where  $C_V$  is the bolometric correction:  $C_V = M_{\text{bol}} / M_V$ . For stars hotter than 3500 K the approximate relationships hold:

$$0.2C_V = -8.5 + 2 \log T_{\text{eff}} + 5800 / T_{\text{eff}}, \quad \log \theta_0 = +16.95 - 4 \log T_{\text{eff}} - \frac{5800}{T_{\text{eff}}} - 0.2V$$

Table A2.1. contains a few results:

$T_{\text{eff}}$	$\theta_0$ (V=0) (mas)	$\theta_0$ (V=5) (mas)	$\theta_0$ (V=10) (mas)
50000	0.011	0.0011	0.00011
29000	0.074	0.0074	0.00074
20000	0.30	0.030	0.0030
10000	2.5	0.25	0.025
8000	4.3	0.43	0.043
5800	8.2	0.82	0.082
4000	12.9	1.29	0.129
3500	13.7	1.37	0.137

**Table A2.1.** The apparent diameter of main-sequence stars as function of the effective temperature  $T_{\text{eff}}$ .

It can be shown that the factor  $D^2 \cdot \Delta \cdot \Gamma^2$  has a maximum value when:

$$\pi \theta_0 D \nu_0 \approx 2c \quad \pi \theta_0 D \approx 2\lambda_0 \quad \theta_0 \approx 0.64\lambda_0 / D$$

Examples at  $\nu_0 = 6 \times 10^{14}$  Hz are given in Table A2.2:

Telescope diameter (m)	Angular diameter $\theta_0$ (mas)	$T_{\text{eff}}$ (V=0)	$T_{\text{eff}}$ (V=5)	$T_{\text{eff}}$ (V=10)
6.5	10.0	5000	-	-
8	8.3	5800	-	-
36	1.8	9000	-	-
100	0.66	15000	6000	-

**Table A2.2.** Telescope optimal diameter vs. the angular diameter of main-sequence stars at 500 nm

Let us take for example the diameter of the original Narrabri realization (6.5m). From the point of view of the single mirror, the resolution of 10 mas is reached for a V = 0 Main Sequence star at  $T = 5,000$  K. *All hotter MS stars would remain unresolved, all cooler stars would be resolved*, with a rapid decrease of  $\Delta$ , and therefore of the S/N, with decreasing  $T_{\text{eff}}$ . From the interferometer point of view, the minimum possible separation (13m) corresponds to 5 mas, namely to a V = 0 MS star hotter than 7,500 K. All cooler stars of same magnitude would cause a decrease in  $\Gamma^2$ .

The full aperture of OWL will resolve *all* V = 0 main-sequence stars cooler than 15,000 K (therefore even Sirius and Vega), and *all* V = 5 stars cooler than 6,000 K.

For giants and supergiants, the following values of radii in terms of the solar radius, and of ratio with the values along the main sequence (in parenthesis), apply (see Table A2.3).

Sp Type	$T_{\text{eff}}$	I	(I/V)	III	(III/V)	V
O5	50000	-		-		18
B0	29000	20	(3)	16	(2.5)	7
B2	20000	30	(8)	10	(2.5)	4
A0	10000	40	(16)	6	(2.5)	2.5
A5	8000	50	(30)	-		1.7
G2	5800	100	(100)	10	(10)	1
K0	5000	150	(180)	16	(19)	0.85
K5	4000	400	(600)	25	(33)	0.75
M0	3500	500	(800)	-		0.65

**Table A2.3.** *Radii of supergiant, giant, and main-sequence stars in units of solar radius (in parenthesis, relative to main-sequence stars)*



### A3. High-Speed Instrumentation Worldwide

High time-resolution in astronomy has been a topic of interest for many applications also in the past, although the meaning of “rapid” variability has meant quite different absolute timescales to different authors, or when applied to different classes of phenomena. A broad introduction to astronomical issues and observational aspects is given by the book “High speed astronomical photometry” by Brian Warner (1988). That textbook introduces atmospheric issues (scintillation, atmospheric transparency changes); lunar and planetary occultations; flare stars; cataclysmic variables; X-ray binaries; gamma-ray bursts; optical pulsars; white-dwarf pulsations; peculiar A-type stars; and active galactic nuclei.

For the study of such and other high-speed phenomena, a number of instruments for ground- and space-based observations have been developed over the years. In this chapter, a selection of these is described, together with some of their science highlights, as a background to our present evaluation of optimum instrumentation.

#### A3.1. HSP on Hubble Space Telescope

The High Speed Photometer (HSP) was one of the four original axial instruments on the Hubble Space Telescope (HST). The HSP on HST was designed to make very rapid photometric observations of astrophysical sources in a variety of filters and passbands from the near ultraviolet to the visible. The simplest of the original scientific instruments on HST, the High Speed Photometer had no moving parts. Its five detectors measured the brightness of celestial objects in several different spectral bands in the ultraviolet, as well as in visible. The High Speed Photometer (HSP) was designed and built at the University of Wisconsin by a group led by principal investigator Robert C. Bless. Pre- and post-launch overviews are given by Bless (1982, 1997).

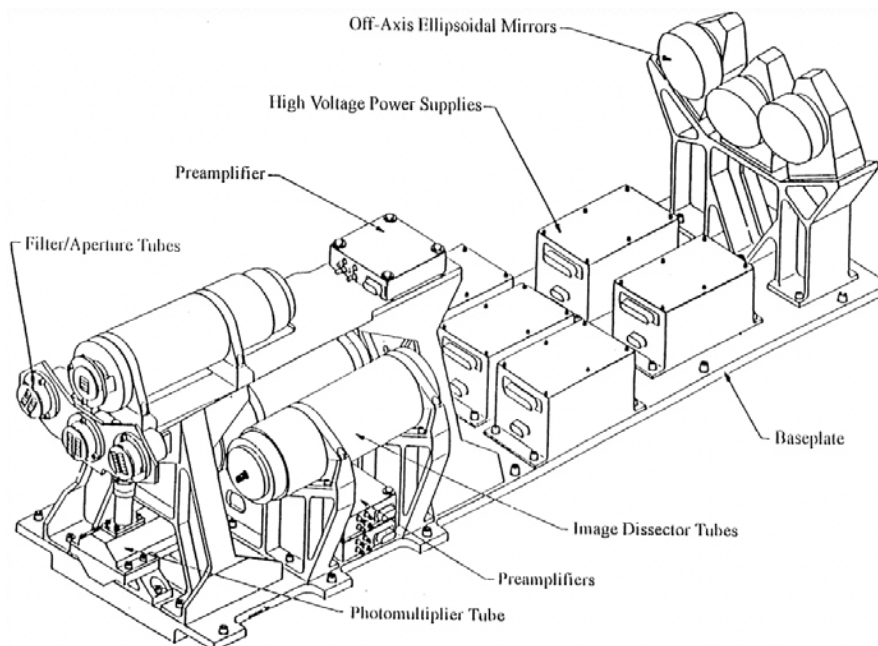


*Fig.A3.1. Layout of detectors and optical components of HSP (Bless et al. 1999)*

The HSP was to take advantage of the lack of atmospheric scintillation for a telescope in orbit, as well as to provide good ultraviolet performance. Integrations as short as 10  $\mu$ s were possible, over a broad wavelength range (120 to 800 nm), and polarimetry was also possible. Observations were carried out through aperture diameters of 1.0" with the visual and ultraviolet detectors, and 0.65" with the polarimetry detector. The detectors were four image dissectors: two sensitive in the UV and solar blind, the others sensitive in the visible and near-infrared.

### HSP actual performance

In actual flight, the HSP performance was not very good because of the disaster with the HST primary mirror. About 50% of the light was lost at the 1 arcsec HSP photometry apertures and 75% at the 0.65 arcsec polarimetry apertures. Because of the significant amounts of light beyond the edges of these apertures, any pointing error, drift, or jitter resulted directly in photometric errors for data collected by the instrument (see below). The smallest (0.4 arcsec) apertures were unusable.

HSP was used for only a relatively small fraction (5%) of HST observing in Cycles 1-3, since the HSP science program was among the more severely compromised by spherical aberration. Only limited instrument expertise is available at STScI in support of HSP Archival Research. However, the extremely high speed with which some HSP data was acquired make these data still unique for either past, current or planned HST capabilities. (Text from STScI website)

The HSP was removed from HST during the First Servicing Mission in December 1993, to make room for the COSTAR, the optical device for correcting the catastrophic error in the primary mirror. When the HSP was removed, it was the only instrument on board not to have suffered a failure of a major subsystem. In terms of economic effort, this must have been the most ambitious instrumentation project in high-speed astronomy.

### Astronomy with HSP

Examples of observations carried out with HSP on HST:

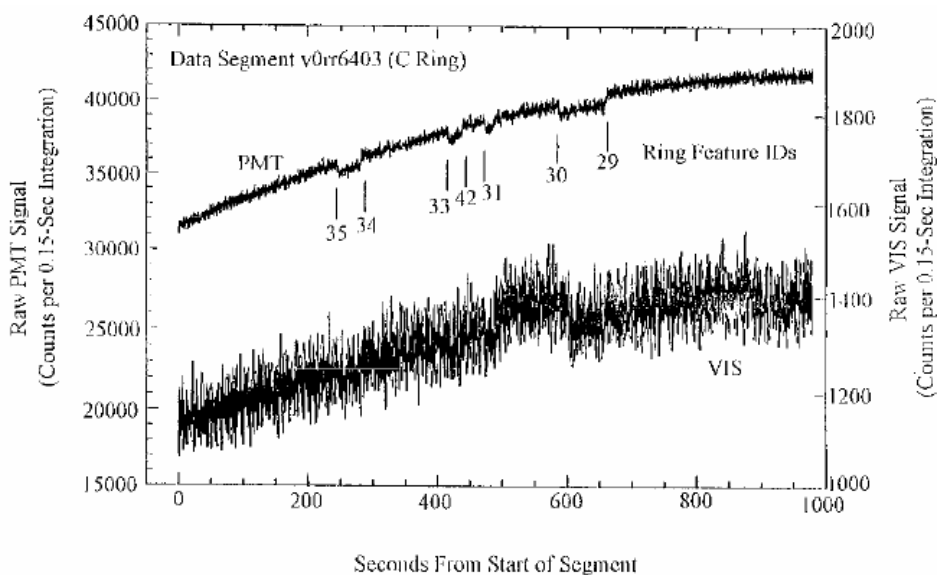


**Fig.A3.2.** One segment of a stellar occultation by Saturn's rings, showing several ring features (Bless et al. 1999)



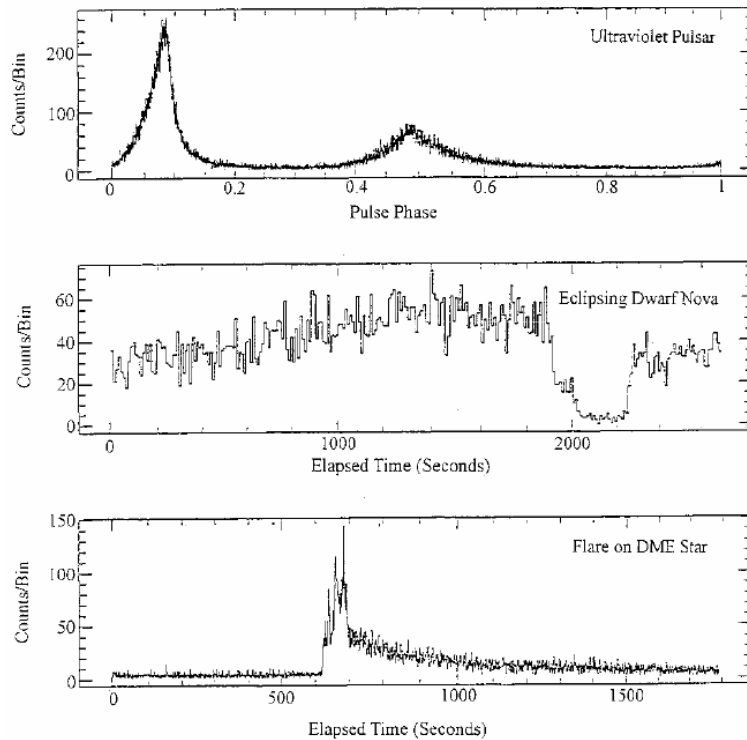


**Fig.A3.3.** Top: Broadband ultraviolet observations of the Crab pulsar at  $20\mu\text{s}$  resolution. Middle: 45 minutes of photometry of the cataclysmic variable Z Cha at 155 nm, during quiescence. Bottom: 240 nm photometry of a flare on CN Leo. (Bless et al. 1999)

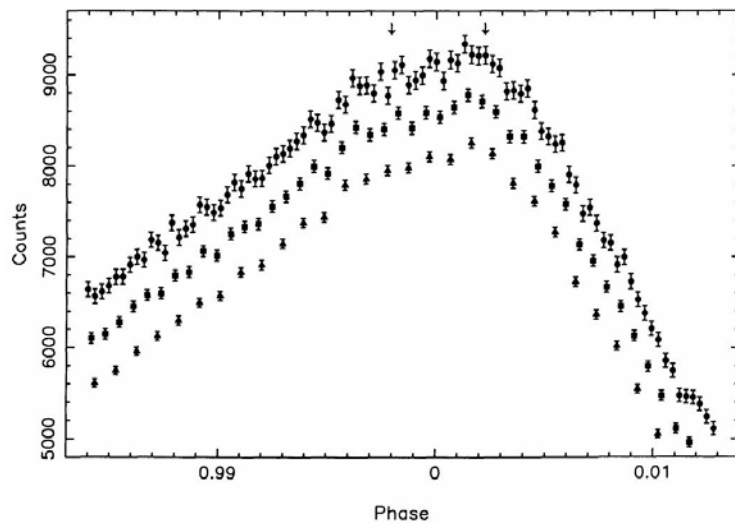


**Fig.A3.4.** Close-up of the peak of the Crab pulsar main pulse in the visible (400-700 nm). The observed count rates with  $22.8\mu\text{s}$  effective time resolution are represented by filled circles. Offset below are pulse profiles formed by summing two and three consecutive samples. (Percival et al. 1993)

**HSP Documentation:**

A limited collection of HSP-related documents, including the final *HSP Instrument Handbook*, the IDT SV report, and some of the references listed at the end of Chapter 42 may be found among the STScI web resources (<http://www.stsci.edu> )

The HSP resources can currently be found by looking under "Observing with HST" then "Instruments and Calibration." Additionally, notices concerning any updates to HSP documentation will be posted here, though none are presently planned.

### **HSP Instrument Handbook**

The final version of the *HSP Instrument Handbook* (version 3.0, April 1992) is a useful description of the technical capabilities of the instrument and practical information for its use:

Bless, R.C., Percival, J.W., Walter, L.E., White, R.L.: *High Speed Photometer Instrument Handbook*, v.3.0 (1992): <http://www.stsci.edu/hst/hsp/documents/HSPIHv30.pdf>

### **High Speed Photometer Pulsar Timing and Light Curve Reduction (5/92)**

Percival, J.W., "High Speed Photometer Pulsar Timing and Light Curve Reduction", *HSP Instrument Science Report #12*, 1992  
<http://www.stsci.edu/hst/hsp/documents/hspisr12.pdf>

### **HSP Orbital Verification Report (November, 1991)**

<http://www.stsci.edu/hst/hsp/documents/HSPOV.pdf>

### **HSP Data Handbook**

<http://www.stsci.edu/hst/hsp/documents/HSP.pdf>

### **HSP Science Verification Test Report (July, 1992)**

<http://www.stsci.edu/hst/hsp/documents/HSPSV.pdf>

### **HSP Final Report (DRAFT) (October, 1995)**

<http://www.stsci.edu/hst/hsp/documents/HSPRPT.pdf>

## ***HSP2***

After it became clear that the High Speed Photometer was to be replaced by COSTAR, the HST project asked the P.I. group at Wisconsin what sort of instrument might be made with the returned hardware and a modest amount of new hardware. A proposal for HSP2 was prepared involving instruments mounted in the old HSP axial enclosure including a simplified High Speed Photometer, HSP2 which, had it been realized, would have extended the science domain of the HST to fast UV/optical photometry.

The proposed detectors were image dissector tubes, with filters covering 125-700 nm, aperture sizes down to 0.3 arcsec, and sample times down to 10.7  $\mu$ s. The time resolution was set such to be able to sample all objects that vary as rapidly as millisecond pulsars. A summary of this proposal is in Bless et al. (1996).

## **A3.2. HIPO on the SOFIA Airborne Telescope**

An airborne telescope minimizes scintillation, both because it flies above most of the atmospheric turbulence, and because intensity scintillation (in contrast to seeing) originates far away from the observer; the remaining atmospheric contributions are only very slight ones coming from maybe 20 km altitude. The flight speed does however change the scintillation characteristics in that their temporal power spectrum is shifted towards higher frequencies (the atmospheric disturbances are passing faster; Dravins et al. 1998).

The SOFIA airborne 2.5 m telescope is currently being readied for flight (<http://www.sofia.usra.edu>), with operations currently foreseen to begin in 2006. SOFIA is a joint project between NASA and the German DLR, designed for a 20-year lifetime. One among the instruments being developed for SOFIA, is HIPO, the High-speed Imaging Photometer for Occultations (0.3 – 1.1  $\mu\text{m}$ ). The principal investigator is E. Dunham at Lowell Observatory, and the HIPO website is at [http://www.sofia.usra.edu/Science/instruments/instruments\\_hipo.html](http://www.sofia.usra.edu/Science/instruments/instruments_hipo.html).

There, its expected performance is summarized as:

“HIPO ... is designed to provide simultaneous high-speed time resolved imaging photometry at two optical wavelengths. It will be possible to ... allow data acquisition at two optical wavelengths and one near-IR wavelength.

The main scientific interest is in the use of HIPO for observing stellar occultations. In a stellar occultation, a star serves as a small probe of the atmospheric structure of a solar system object or the surface density structure of a planetary ring or comet. Such observations provide information at high spatial resolution that would otherwise require a space mission to obtain. This work makes use of SOFIA's mobility, freedom from clouds, and near-absence of scintillation noise to provide the best possible occultation data.

The low atmospheric scintillation in airborne photometry gives HIPO the potential to detect P-mode stellar oscillations in sunlike stars and will provide excellent photometry of stellar transits by extrasolar planets.

### ***Optical Layout***

The basic HIPO optical system incorporates two dichroic beamsplitters, one to divert the infrared beam to a side camera, and one to split the red and blue sides of the HIPO optical paths.

The HIPO instrumental performance [requirements] include:

Detectors: CCD's (1024  $\times$  1024 pixels) in two wavelength channels (blue: from UV cutoff at 300 nm to 650 nm; red channel: 400-1100 nm). Each channel has an 8-position filter wheel. Photometry-related performance requirements (Dunham et al. 2004):

Readout noise @ 1 Mpx/s: 6 electrons rms

Readout noise @ 20 Kpx/s: 3 electrons rms

Full frame read rate:  $\geq 2$  Hz

Three 80  $\times$  80 subframes  $\geq 50$  Hz (3  $\times$  3 binned)

One optimal 80  $\times$  80  $\geq 100$  Hz (3  $\times$  3 binned)

(Pixels are normally binned to match the seeing blur size.)

Time accuracy is set by GPS, 50  $\mu\text{s}$  is required, actually achieved is around 200 ns.

Mechanical stiffness (HIPO alone): lowest resonance frequency required is  $\geq 100$  Hz. Actually measured:

Mirror mounts – 96, 99, 170 Hz

Detector mounts – 130 Hz

Optics box – 110 Hz

The cost for HIPO is stated as USD 2.0 M, the same amount as for FLITECAM (Casey et al. 2004).

HIPO is a successor to the instrument, SNAPSHOT on KAO, the Kuiper Airborne Observatory. This earlier instrument was described in Dunham et al. (1985).

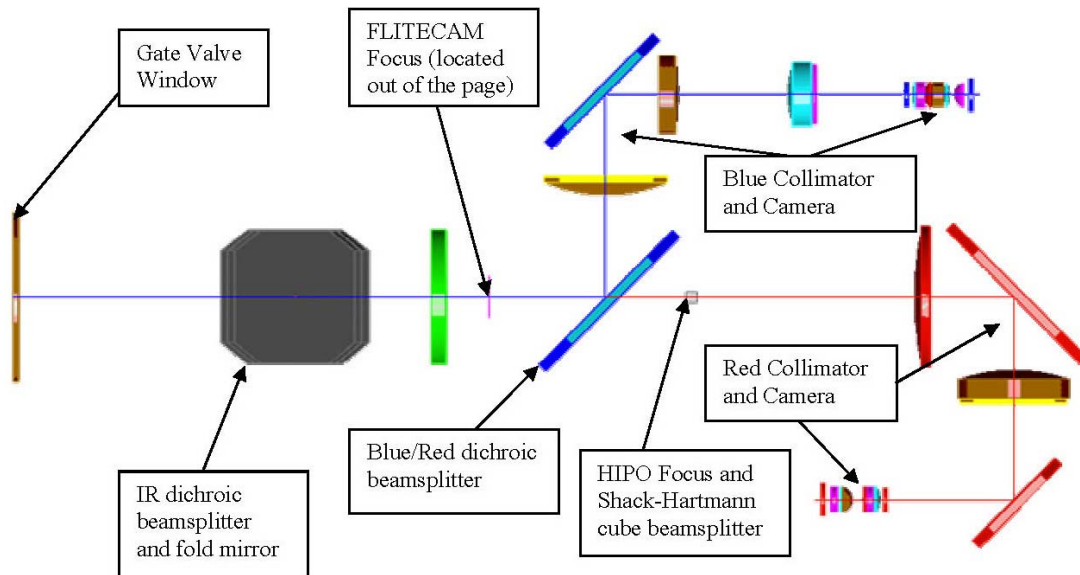


**Fig.A3.5.** Layout of the HIPO instrument in the case where the side-camera FLITECAM is co-mounted. The IR dichroic and fold mirror form a periscope bringing the beam up with the axis of the FLITECAM optics. If FLITECAM is not mounted the IR dichroic beamsplitter will be removed. (Dunham 2003)

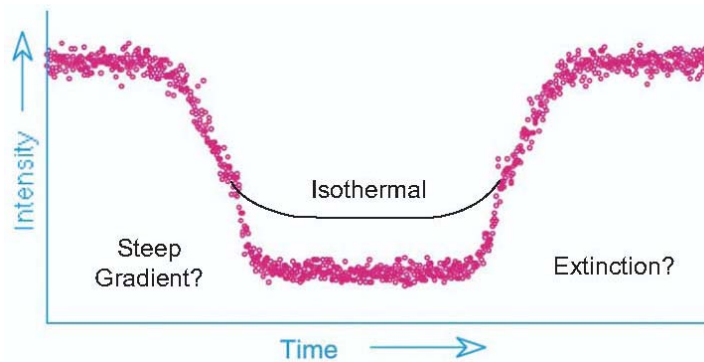


**Fig.A3.6.** In an occultation by an object with an atmosphere, differential refraction is normally the only significant factor causing the star's brightness to decrease. This lightcurve (Elliot et al., Icarus 77, 148, 1989) can be explained either in terms of a strong thermal gradient in Pluto's atmosphere or by extinction due to aerosols. Such competing models can be tested with an occultation by Pluto simultaneously in optical and infrared bands. (HIPO Instrument Informational Flyer, 2004)

### A3.3. ULTRACAM

ULTRACAM is a fast, triple-beam CCD camera, designed to provide imaging photometry at high temporal resolution in three different colors simultaneously. The instrument, funded by PPARC (300 k£), had first light on the 4.2m William Herschel Telescope (WHT) on La Palma

in May 2002; in May 2005, it was commissioned at the VLT visitor focus on *Melipal*. The principal investigators are Vik Dhillon (University of Sheffield) and Tom Marsh (previously University of Southampton; now University of Warwick); it also involves the U.K. Astronomy Technology Centre in Edinburgh.

At the Nasmyth (Visitor) focus of the VLT (UT3, *Melipal*), ULTRACAM provides a 2.6 arcmin field on its three 1024x1024 CCDs (i.e. 0.15 arcsec/pixel). Incident light is first collimated and then split into three different beams, using a pair of dichroic beamsplitters. Each beam is dedicated to one specific color filter. Because ULTRACAM employs frame-transfer chips, the dead-time between exposures is negligible. In full-frame mode, it is possible to read out the unbinned chips in 2 seconds with only 24 milliseconds dead time; in drift-mode, it is possible to read out two small, binned windows at up to 360 frames per second with only 0.5 milliseconds dead time. Each image taken by ULTRACAM is time-stamped using a dedicated GPS system to an accuracy of better than 50 microseconds and a pipeline data reduction system is provided to enable real-time assessment and full reduction of the light curves.

Total weight of ULTRACAM and its ancillary equipment, including the 7 packing crates: 1000 kg. Approximate value of equipment: 600 k€. Weight at the focus (including ancillary equipment) is approx. 300 kg on the Nasmyth rotator and a further 300 kg on the Nasmyth platform.

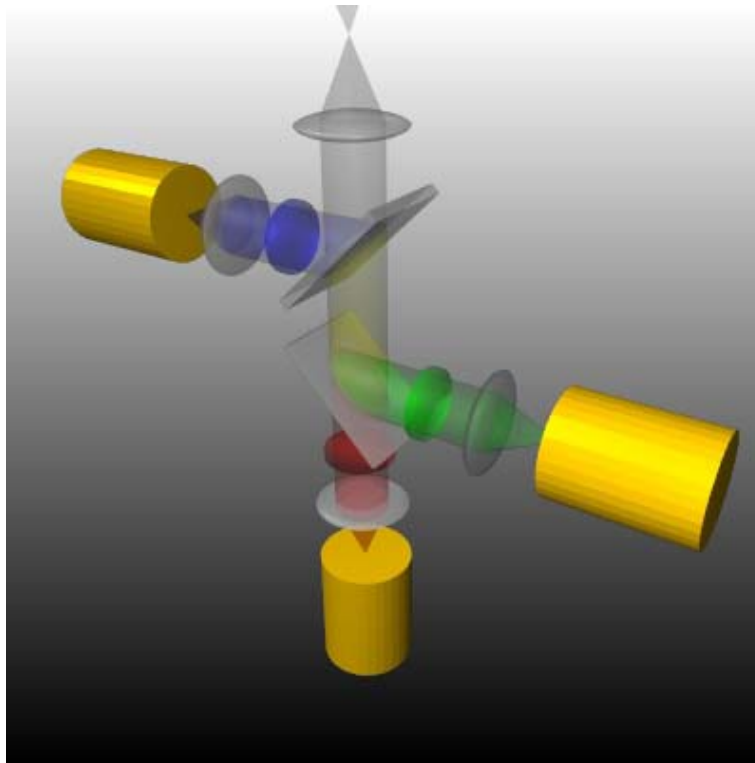


**Fig.A3.7.** *ULTRACAM* - there are four optical units - the collimating fore-optics, the dichroic beamsplitters, the filters and the re-imaging lenses. The collimating fore-optics collimate the light from the telescope. This is an interchangeable lens unit which enables *ULTRACAM* to work on telescopes of different focal ratio whilst retaining the same pixel scale (0.3 arcseconds/pixel). The light is split into blue, green and red wavelengths by two dichroic beamsplitters and then passes through a filter. On passing through the filters, the light is re-focused onto the CCD chip using re-imaging optics positioned in front of the detectors.

The scientific aims for ULTRACAM are to explore photometry of faint objects on timescales of seconds to milliseconds. Foreseen applications include: optical emission from pulsars, and optical analogs of the kilohertz quasi-periodic oscillations (QPO's) and related small-scale accretion phenomena found in X-ray binary stars.

A design requirement was the simultaneous recording of at least one comparison star in order to provide differential photometry and hence increase the accuracy of the variability studies and to allow measurements to be taken in non-photometric conditions.

**OPTICS:** The optical layout of ULTRACAM is shown in Figure A3.7.

(<http://www.shef.ac.uk/physics/people/vdhillon/ultracam/>):

**MECHANICS:** There are no moving parts in ULTRACAM, which simplifies the design (and reduces the cost) considerably. A single opto-mechanical chassis houses all of the optics and provides mounting points for the 3 CCD heads. An interchangeable flange at the collimator enables attachment to a variety of Cassegrain turntables. Note that mechanical flexure is not of great concern as ULTRACAM is primarily an imaging photometer.

**DETECTOR SYSTEM:** ULTRACAM uses three back-illuminated, thinned, Marconi 47-20 frame-transfer CCD chips as the detectors, as shown in the figure. The chips are cooled using a three-stage Peltier device and water chiller, resulting in dark current of only 0.1 e-/pixel/s. This is insignificant compared to the sky counts, which in the worst case (the U-band La Palma dark sky on a 2-m telescope) gives 0.3 e-/pixel/s. The chips will be coated by Marconi with their broad-band coating, resulting in quantum efficiencies of between 35-84% in the filter band-passes.

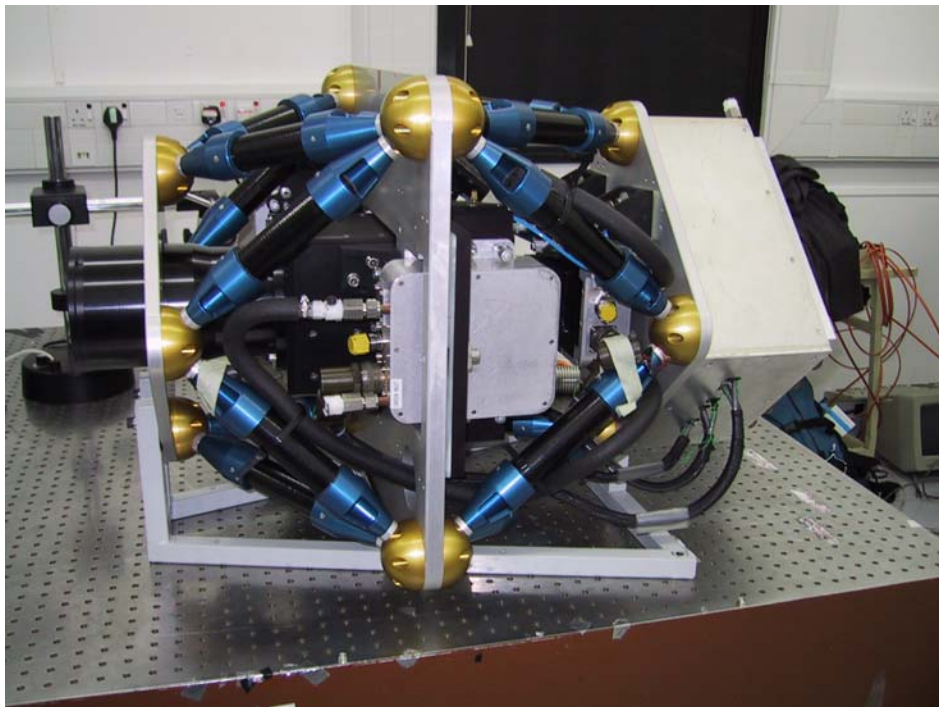


*Fig.A3.8. ULTRACAM on the WHT test bench. It is approximately 0.5 m wide, deep and high. (Beard et al. 2002)*

The use of frame transfer chips is essential, as it provides a means of taking data in the imaging area whilst data in the masked area is being read out. As long as the exposure time is longer than the time it takes to read the data, the dead-time is essentially zero. Hence, for

small windows it is possible to take 0.001 s exposures with negligible (0.0001 s) dead-time, thereby meeting the scientific requirements outlined above. Even full-frame images can be read out with millisecond dead-times as long as the exposure times are no shorter than approximately 1 s. ULTRACAM can be programmed to repeat an exposure any number of times in quick succession or to repeat exposures continuously until commanded to stop. The current ULTRACAM system uses  $1024 \times 1024$  pixel frame transfer CCDs, with  $13 \mu\text{m}$  pixels, and supports a variety of different readout modes. The maximum data-flow rate from the CCD chips is 3.6 Mb/s. Given this rate, one could accumulate up to 130 Gb during a 10-hour night.

The ULTRACAM readout options are:

1. **Full frame mode.** This mode provides a slower readout but gives a wider field of view (e.g. 5 arcminutes at 0.3 arcseconds per pixel on the WHT). At maximum readout speed a full frame can be read out in about 2 seconds.
2. **Windowed readout.** ULTRACAM achieves high speeds in windowed readout mode. Frame rates of up to 100 Hz can be achieved. Only the pixels from up to three variable-sized pairs of windows are read out.
3. **Drift scan mode.** In this mode ULTRACAM achieves its fastest speed by repeatedly making an exposure and rapidly shifting the charge into the frame storage area. This mode significantly reduces any dead time between exposures, allowing frame rates up to 500 Hz to be realized.

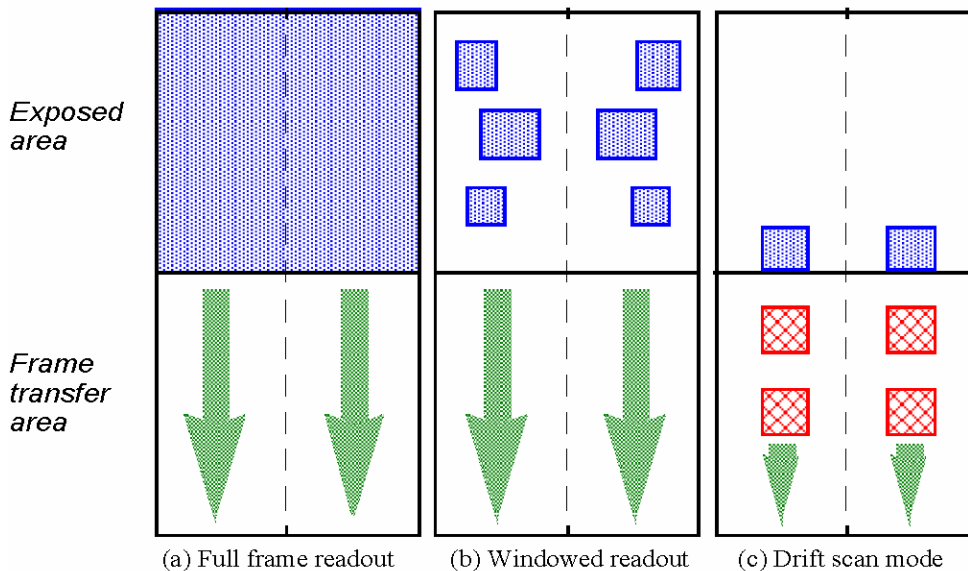


**Fig.A3.9.** ULTRACAM CCD readout options (Beard et al. 2002). The lower sections of the frames in the above figure represent the masked-off frame transfer area. The CCDs have two readout channels which can, in parallel, read out pixels from the left and right sides of the chip as separated by the dotted lines in the diagrams.

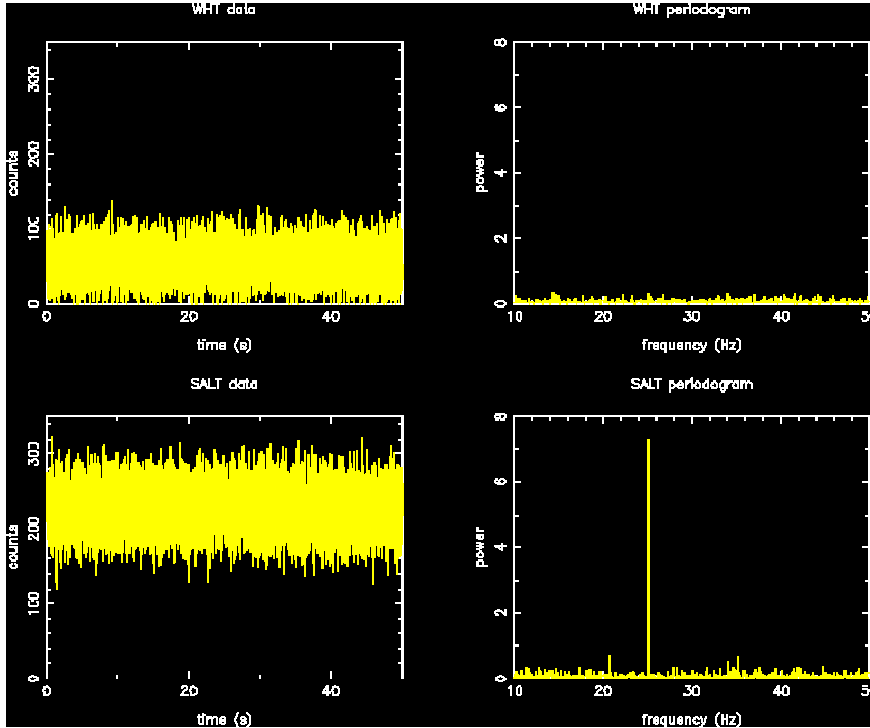


**Fig.A3.10.** Simulated light-curves and periodograms with ULTRACAM on the 4.2-m WHT and 9.1-m SALT. The source is an  $R = 16$  variable star observed at the zenith during bright time in 1 arcsec seeing using 5 ms exposures. The source is varying with an amplitude of 2.5% and a period of 40 ms. It can be seen that light-curves are of only limited use when acquiring data at the highest rates and, in fact, it is periodograms which prove to be the most useful tools (in this case, finding that the data exhibits a 25 Hz modulation). The advantages of using large-aperture telescopes are also apparent, in which the 25 Hz (i.e. 40 ms) peak is non-existent in the WHT data but very prominent in the SALT data.

**Sample observations:**

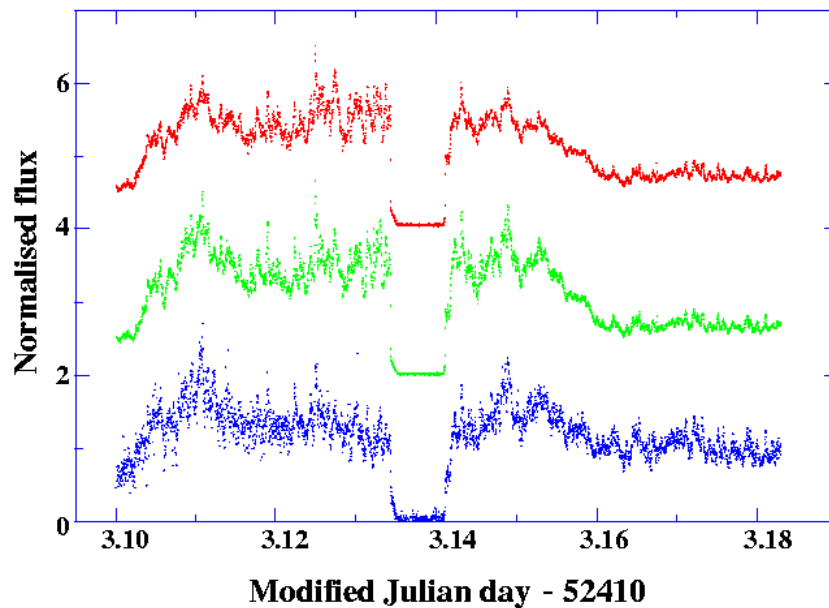


**Fig.A3.11.** ULTRACAM observations of the light curve of the cataclysmic variable HU Aqr in red (upper), green (middle) and blue (lower) channels. The green and red plots have been shifted upwards respectively by 2 and 4 units of flux. (Beard et al. 2002)



## ULTRACAM links:

ULTRACAM: <http://www.shef.ac.uk/physics/people/vdhillon/ultracam/>

Vic Dhillon (University of Sheffield):

<http://www.shef.ac.uk/physics/people/vdhillon/>

Tom Marsh (University of Warwick):

<http://www2.warwick.ac.uk/fac/sci/physics/research/astro/people/marsh/>

### A3.4. STJ & TES: Superconducting Energy-Resolving Detectors

Some types of detectors offer intrinsic wavelength resolution, thus in principle combining an imaging camera with a spectrometer. If such detectors, in addition, have a good time resolution, they are potentially very interesting. A few classes of superconducting devices have been developed with such capabilities, originally applied for X-rays, but now also developed for the visual. These are the STJ's (Superconducting Tunnel Junctions) and the TES's (Transition Edge Sensors). For optical astronomy, cameras using STJ detectors have been developed by ESA/ESTEC, and TES cameras by Stanford University. An overview of such sensors is by Mather (1999).

#### STJ, Superconducting Tunnel Junctions

[Text from ESA website <http://sci.esa.int/>] A Superconducting Tunnel Junction (STJ - or Josephson junction) consists of two thin films of a superconducting metal such as niobium, tantalum or hafnium separated by a thin insulating layer.

When operated at temperatures well below the superconductor's critical temperature (typically below 1 K), the equilibrium state of the junction is easily perturbed by any photon striking it. By applying a small bias voltage across the junction and a suitable parallel magnetic field to suppress the Josephson current, an electrical charge proportional to the energy of the perturbing photon can be extracted from the device.

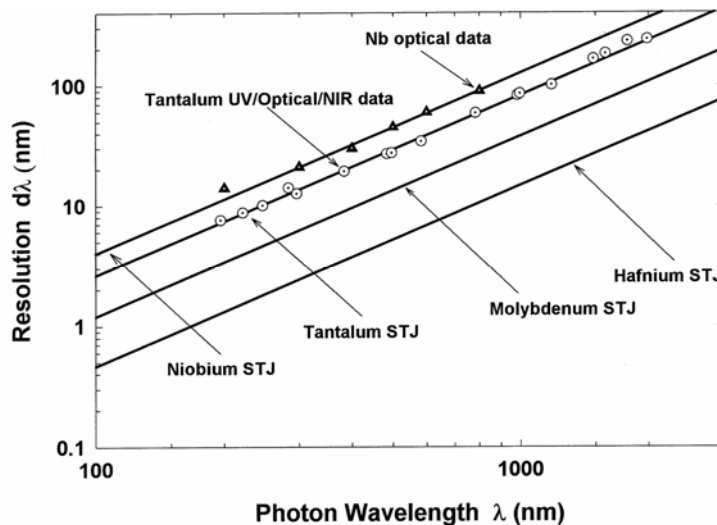


**Fig.A3.12.** Tunnel-effect limited spectral resolution (full width at half-maximum) for STJ detectors based on different superconducting elements. (Rando et al. 2000)

Since the energy gap of superconducting niobium is some three orders of magnitude lower than the energy of optical photons, on the order of one thousand electrons are released per detected optical photon. The functioning of STJ detectors involves release of charge through the breaking of "Cooper pairs", and the amount of charge carriers generated by an absorbed photon is proportional to the energy  $E$  of the absorbed photon, which permits the wavelength resolution. Since different elemental superconductors have different energy gaps, also their [theoretically] achievable spectral resolutions differ. These are of order one part in ten to one part in a hundred in the near-UV, varying as the square root of the photon energy.

By arranging a number of STJ devices into a two dimensional array, a "three dimensional" astronomical detector can be constructed, whose output is not just the number of photons registered in each pixel of the image, but their distribution in energy throughout the UV, visible and near-IR. In order to be able to distinguish the relatively feeble charges generated by the STJ detector above the thermal background noise, it is necessary that such devices operate at extremely low temperatures, typically below one degree above absolute zero.

### STJ's for Hubble Space Telescope?

As part of discussions aimed at extending ESA's participation in HST beyond the year 2001, an ESA-provided STJ camera was studied as a potential Hubble Space Telescope instrument. A key scientific driver for considering this concept was the goal of measuring the redshifts and spectral energy distributions of the extremely faint remote galaxies that HST is uncovering through very deep imaging. In fact, the dramatic gain in sensitivity promised by the STJ Camera's 'dispersionless' approach to spectroscopy may well represent the only hope of following up on this important discovery with the present HST. For examples of spectroscopy with STJ's, see de Bruijne et al. (2002), and Reynolds et al. (2003).

### S-Cam's by ESA/ESTEC

The STJ cameras by ESA/ESTEC are designated "S-Cam", and their first astronomical light was at the WHT on La Palma in February 1999, followed by several other campaigns. The first S-Cam's had an array of  $6 \times 6$  array of small Ta-Al STJ's. These Ta-Al STJ's have high detection efficiencies ( $\sim 70\%$  in the visible), reasonable spectral resolution ( $\sim 10$  at 300 nm) and fast response times (on the order of 10 microseconds). The maximum photon count rate was 5 kHz/pixel. The next version, S-Cam 3, has increased field-of-view; extending the 'red' response towards  $\sim 1\mu\text{m}$ ; increased energy resolution; increased readout speed and the system's photon-rate capability, etc. A resolution  $R = 13$  at 500 nm has been measured. S-Cam 3 saw first light at the 4.2 m WHT on La Palma in July 2004.

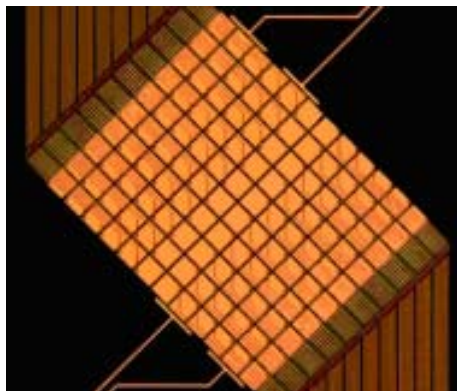


**Fig.A3.13.** The detector array in S-Cam 3 array;  $10 \times 12$  pixels, each  $33 \times 33 \mu\text{m}^2$ , with  $4 \mu\text{m}$  gaps

Detector	12x10 Ta/Al STJs
Pixel size	33 x 33 $\mu\text{m}^2$
Fill factor	76%
Plate scale	0.8"/pixel
FOV	11"x9"
Pass band	330-745 nm
Maximum detection efficiency (@500nm)	30%
$\lambda/\Delta\lambda$ @ $\lambda=500\text{nm}$	8-11
Event time resolution	$\sim 5 \mu\text{s}$
Max. event rate/pixel	>8000 cts/s
Max. overall event rate	$\sim 106$ cts/s
Max. observation time	24 h
Operating temperature	285 mK

**Table A3.1.** Summary of S-Cam 3 Characteristics:

### S-Cam's 4, -5 & -6

In the previous STJ detectors, each pixel had its own wiring and readout electronics, a concept limiting the size of future arrays. For future cameras, the "Distributed Read Out Imaging Detector (DROID)" is foreseen. Photons are not absorbed directly in the STJ but in a superconducting absorber strip. The resultant charge carriers diffuse along the strip until they reach each end where they are trapped by a lower energy gap material and enter the STJs. The sum of the two STJ signals provides the energy of the photon while their ratio is a measure of the position in one-dimension, the second dimension being simply the width of the strip. Such systems have been tested successfully at optical wavelengths. Packaging such individual DROIDS into arrays will allow large field coverage.

The programs for S-Cam 5 and S-Cam 6 aim at making the systems easier to use, further increasing the field of view (larger detector arrays), and improving the spectral resolution. For ease of cryogenic operation at, e.g., remote sites, a closed-cycle helium cooling is foreseen, while the development of detectors based not on tantalum (which has a tunnel-effect limiting resolving power of  $\approx 25$  at 500 nm), but on elements with lower bandgaps such as molybdenum and aluminum. (Wentzel 2003).

### TES, Transition-Edge Sensors

There exist other classes of wavelength-resolving detectors, such as superconducting Transition-Edge Sensors. These are microcalorimeters biased at a constant voltage to set up a negative electrothermal feedback mechanism that keeps the pixel in its superconducting-to-normal transition region. When a photon's energy is absorbed in the TES, it is warmed, causing it to move up in the transition region. Increased resistance at a constant voltage means that the current passing through the TES is lowered. The TES is coupled, through an inductor in series, to a low noise SQUID amplifier. Although TES quickly returns to its

equilibrium condition, one can measure the current pulse and reconstruct the energy of the incident photon.

TES is basically a fast bolometer, offering good broadband quantum efficiency from mid-infrared, through the optical, and into the far ultraviolet. They offer a modest spectral resolution ( $\lambda/\Delta\lambda \approx 20$ ), and a photon arrival-time resolution  $\approx 300$  ns.

### Imaging TES Array

A group at Stanford University has built a portable imaging array of TES pixels for use in astronomical observations. This optical TES program uses small tungsten pixels to directly absorb photon energy. The sensors are squares about  $20 \mu\text{m}$  on a side and detect single photon events above a threshold of  $0.3$  eV ( $4 \mu\text{m}$  wavelength), with an energy resolution of  $0.15$  eV full width at half maximum at  $3$  eV, and with a risetime (falltime) of  $0.5 \mu\text{s}$  ( $60 \mu\text{s}$ ). Cabrera et al. (1998); Romani et al. (2001).

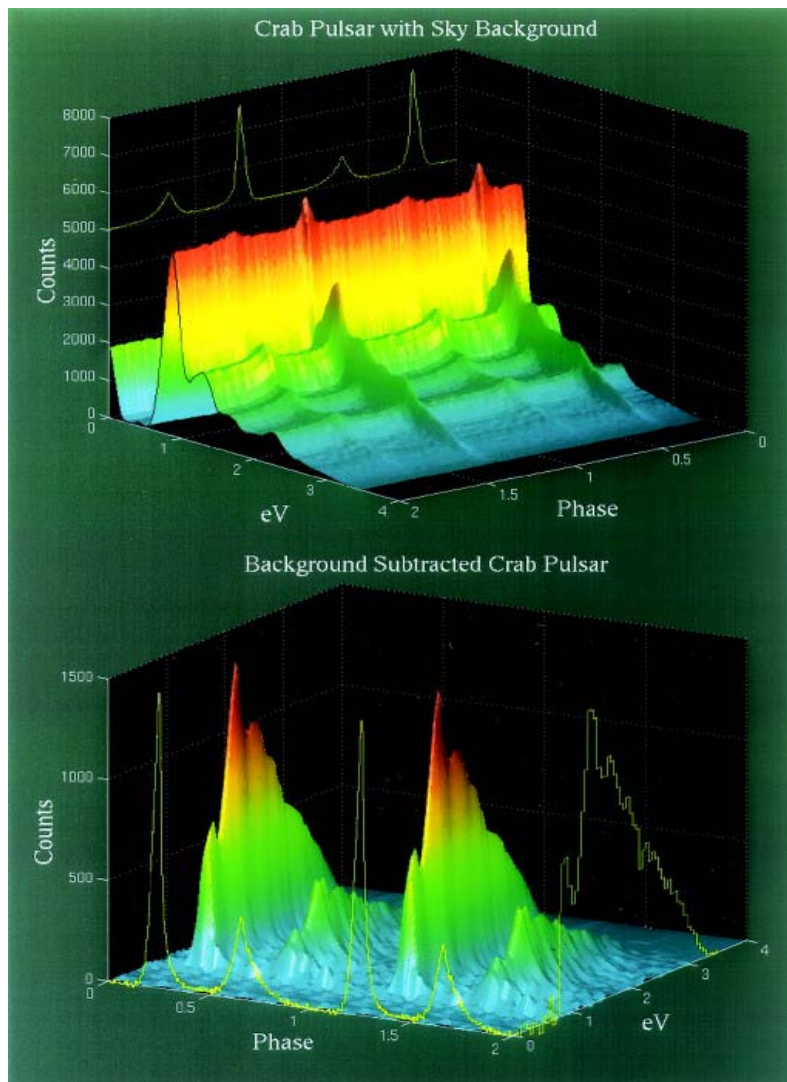


**Fig.A3.14.** Phase-resolved spectra of the Crab pulsar optical/IR emission, measured with a TES detector on a 60 cm-telescope. Top: spectra folded into 200 phase bins. Bottom: After off-pulse sky subtraction. (Romani et al. 1999)

A 32 pixel array of such tungsten TES's is coupled to a 50 mK substrate that is cooled using an adiabatic demagnetization refrigerator. The individual detectors are small (20  $\mu\text{m}$  on a side) thin film tungsten pixels deposited on a silicon substrate with aluminum wiring.

Similar to the STJ case, an apparent TES main limitation is the finite photon count rate that can be sustained. Single-pixel count rates up to  $\approx 30$  kHz are achieved (Romani et al. 2001).

First astronomical applications have been (as usual!) observations of the Crab pulsar. This was first done as a demonstration with a small (60-cm) telescope (Romani et al. 1999), later extended into a more detailed study with the 2.7 m telescope at McDonald (Romani et al. 2001).

### **STJ Links:**

*ESA Research and Scientific Support Department:* <http://www.rssd.esa.int/>

*S-Cam 2:*

<http://www.sci.esa.int/science-e/www/object/index.cfm?fobjectid=33541>

*S-Cam 3:*

<http://sci.esa.int/science-e/www/object/index.cfm?fobjectid=36685>

*S-Cam 4:*

<http://sci.esa.int/science-e/www/object/index.cfm?fobjectid=36686>

**Transition-Edge Sensors:** <http://hep.stanford.edu/~cabrera/>

## **A3.5. OPTIMA**

*OPTIMA* (Optical Pulsar TIMing Analyzer) of the Max-Planck-Institute for Extraterrestrial Physics in Garching is a high-speed photon-counting instrument used to measure the optical counterparts of (primarily) gamma-ray sources, especially pulsars with high time resolution (microseconds) and high sensitivity.

The detector contains eight fiber fed avalanche photodiode single photon counters (SPADs), a GPS timing receiver, a CCD camera for target acquisition and a computerized control unit. The central fibers are configured as a hexagonal bundle around the target fiber, while one fiber is located at a distance of  $\approx 1$  arcmin as a monitor for the night sky background.

### **OPTIMA layout**

Combining tapered optical fibers feeding several SPADs, *OPTIMA* is that among existing high-speed instruments most closely resembles *QuantEYE* in its optical layout.

*OPTIMA* was primarily designed for studying the optical light curves of faint pulsars ( $m_v \sim 25$ ) where the flux from the astronomical target lies considerably below the brightness of the night sky. The pulsar signal can then be recovered by phase-coherent folding of sufficiently long observations at the pulsar's rotational frequency. To minimize the dilution of the source's

signal by the underlying atmospheric background, the flux of the target is isolated in the focal plane of the telescope by the use of an optical fiber-bundle pick-up which acts as a diaphragm. Target and sky background photons are then transferred through the fibers to photon detectors. There is a hexagonal packed array of seven fibers. Each single fiber leads to a separate channel of the detector system i.e. seven avalanche photodiode detectors (SPADs). A full description of the detector system is given in Kanbach and Straubmeier (2002).

### OPTIMA photometer

Most previous systems for recording single optical photons with time resolutions of a few microseconds used photomultiplier tubes or similar detector types. Their photo cathodes have a peak quantum efficiency of typically 20% and a narrow wavelength range of sensitivity. Much better quantum efficiencies can be reached with solid state detectors. OPTIMA uses avalanche photodiodes (APDs). These silicon devices have been produced with peak quantum efficiencies of up to 80% and a wide band of sensitivity ranging from 250 to 1100 nm. OPTIMA uses APD single photon counting modules of type SPCM-AQR-15-FC produced by PerkinElmer. The diodes have a diameter of 200  $\mu\text{m}$  and are electrically cooled with Peltier elements. The selected units offer low dark count rates of typically less than 50 Hz. They could record photons up to rates of several MHz before noticeable dead-time losses occur, although the present OPTIMA data acquisition can not keep up with such rates. Bandwidth and quantum efficiency gains of APDs results in about a factor of 6 improvement in sensitivity compared to PMT based systems.

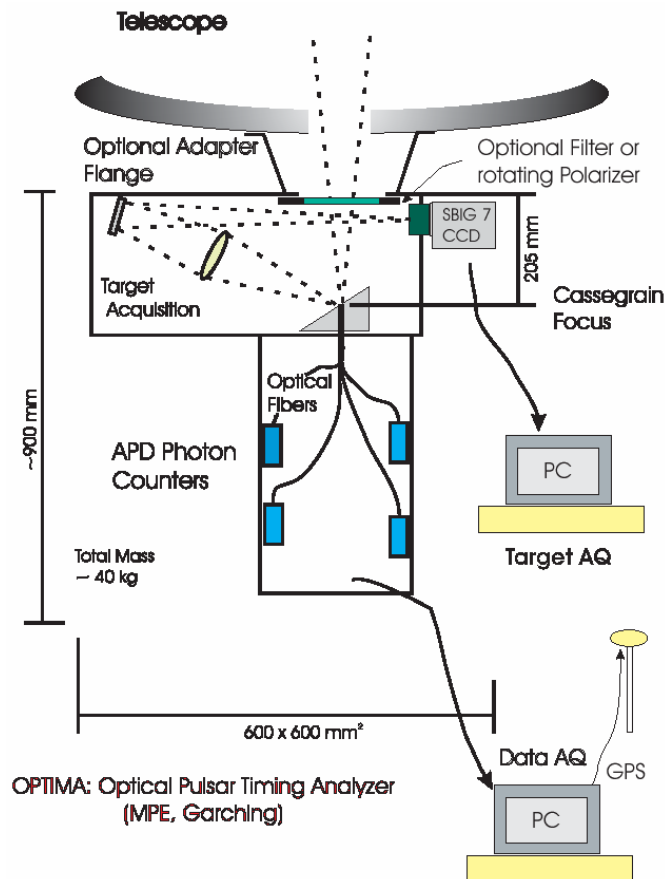
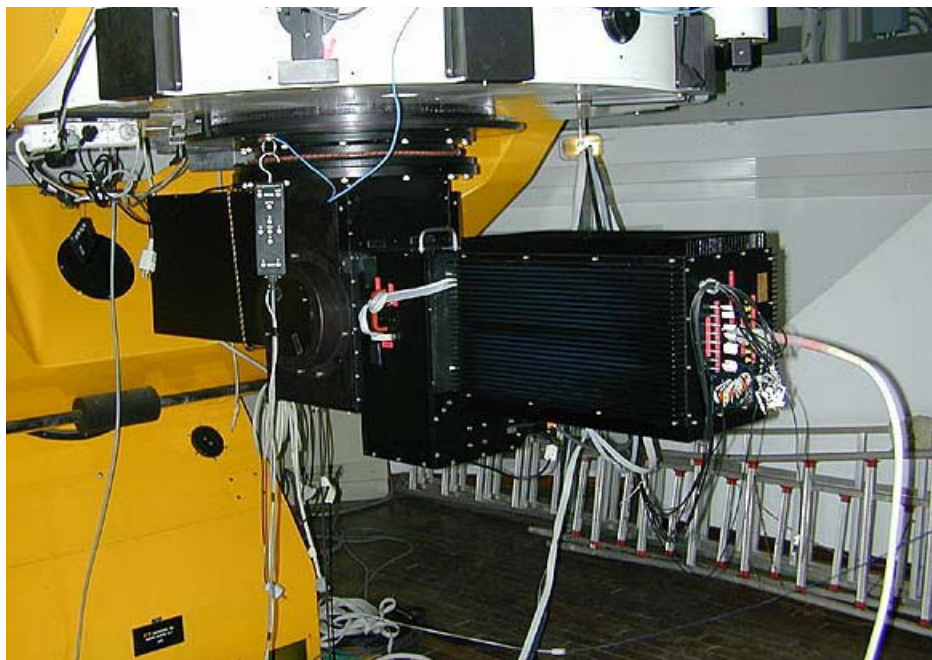


Fig.A3.15. Schematic layout of the OPTIMA instrument (Kanbach et al. 2003)

### **OPTIMA timing and data acquisition**

OPTIMA obtains its absolute time base from the GPS global positioning satellite system. A receiver processes clock pulses of up to six GPS satellites simultaneously and reaches an absolute time accuracy of better than  $2\mu\text{s}$  on the "pulse per second (PPS)" GPS signal. This signal disciplines a local high frequency oscillator with the same precision which provides a continuous UTC time signal to the system bus of the PC used for data acquisition (DAQ). (Kanbach et al. 2003]

New developments include the possibility to measure with high time resolution also the polarization of objects (OPTIMA photo-polarimeter (Kellner (2002), Kanbach et al. (2002)) and spectral colors in several bands simultaneously.



**Fig.A3.16** *OPTIMA is a portable instrument and has been used with several telescopes such as the 3.5 m at Calar Alto, the Nordic Optical Telescope on La Palma; the 2.2 m on La Silla, and elsewhere. Here it is mounted at the Cassegrain focus of the 1.3 m telescope at Skinakas Observatory on Crete.*



**Fig.A3.17.** The OPTIMA instrument with its side opened, showing locations of its photon-counting avalanche photodiodes (3). The target acquisition optics (filters, target imaging, and fiber pick-up) is located in (1), and the CCD camera is mounted externally (2). (Kanbach et al. 2003).

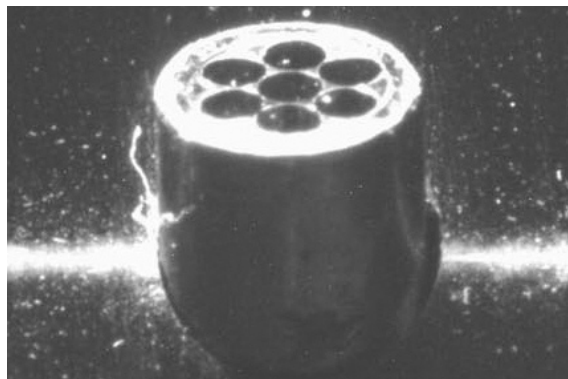


**Fig.A3.18.** OPTIMA focal-plane layout with hexagonal bundle of seven optical fibers fed through a hole in the slanted mirror at the focal plane of the telescope. For handling reasons the fibers are packed into a protective steel tube. Each fiber has an entrance diameter of 0.3 mm, being tapered down to 0.1 mm at the detector end. The horizontal bright line is formed by an auxiliary mark on the mirror to ease focusing of the CCD optics. (Straubmeier et al. 2001)

OPTIMA has also been equipped with a rotating polarization filter, allowing one to determine linear polarization in rapidly varying sources (and has recently been further redesigned for improved polarization measurements) The Crab nebula pulsar was observed at the 3.5 m telescope at Calar Alto. The wavelength range for these measurements extends from 450 to 950 nm. The analysis of about 3 hours of exposure (Kellner, 2002) resulted in the preliminary polarization characteristics:



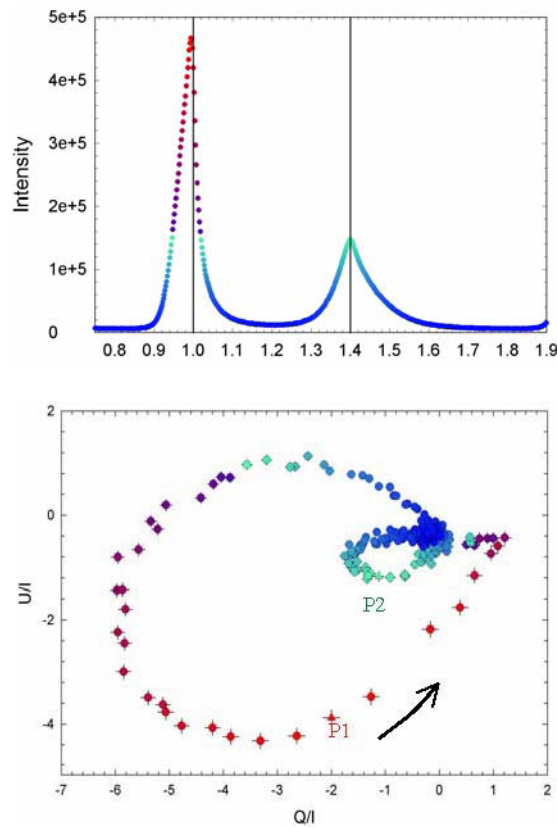


**Fig.A3.19.** The normalized Stokes parameters  $Q$  and  $U$  for linear polarization of optical light from the Crab pulsar, observed with OPTIMA at the 3.5 m telescope on Calar Alto. The color coding corresponds to that of the adjacent light curve. The pulsar rotational phase increases counter-clockwise, as marked by the arrow. (Kanbach et al. 2002)

### Black holes: Casting light on X-ray emissions

One opportunity to observe a black hole at both X-ray and optical wavelengths was exploited between January and August 2000, the unusually long duration of the X-ray transient XTE J1118+480. This is a candidate black hole in the Milky Way's halo. Simultaneous high-time-resolution X-ray and optical observations of this transient source show a strong but puzzling correlation between the emissions.

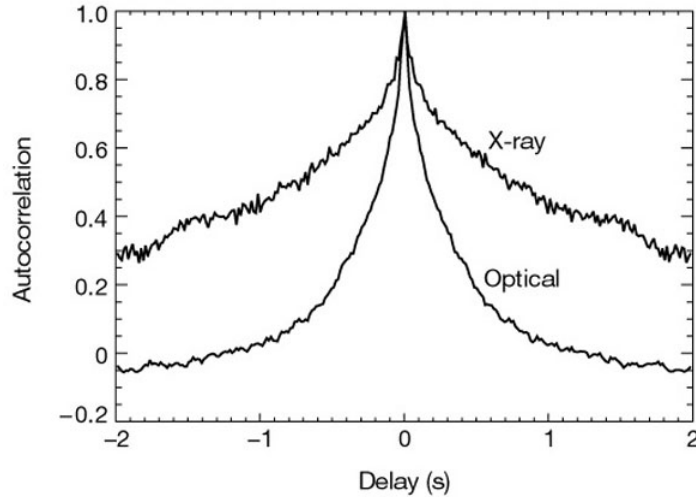


**Fig.A3.20.** Autocorrelations of the X-ray and optical time series for the black-hole candidate XTE J1118+480, showing that the optical variability is not due to reprocessing of the X-rays. Timescales shorter than 70 ms are present in both the X-ray and optical light curves, but the **optical autocorrelation is significantly narrower than the X-ray one**, which appears to **exclude any reprocessing model for the optical emission**. The optical observations were made with OPTIMA at the 1.3 m telescope on Skinakas, simultaneously with the Rossi X-ray Timing Explorer, RXTE. (Kanbach et al. 2001)

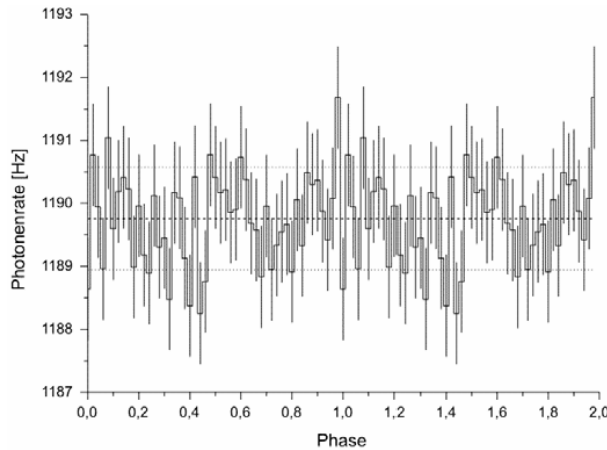


**Fig.A3.21.** Light curve of the optically faint ( $m_v = 25.5$ ) pulsar Geminga (but one of the brightest high-energy gamma-ray sources in the sky), observed with OPTIMA at the 3.5 m telescope on Calar Alto. Total exposure time from four nights equals about 24 h. The dashed lines indicate single phase bin deviations at the  $1\sigma$  level. The data were folded with the known rotational ephemeris known from gamma-ray observations; however no optical modulation can be identified here (Kanbach et al. SPIE 2003). Geminga is a prime example of sources whose optical studies will greatly benefit from future ELT's.

**OPTIMA link:**

<http://www.mpe.mpg.de/gamma/instruments/optima/www/optima.html>

### A3.6. MANIA

*MANIA* is a project at the Special Astrophysical Observatory (SAO) in Northern Caucasus involving hard- and software for the study of optical emission variations of astrophysical objects on time scales from 0.1  $\mu$ s to 100 s. Among all previous high-speed astrophysics projects this is, arguably, the one with the most visionary astrophysical outlook towards new types of phenomena that eventually might be identified.

The acronym *MANIA* stands for “*Multichannel Analysis of Nanosecond Intensity Alterations*”; its analogous name in Russian is *МАНИЯ* – “*Многоканальный Анализ Наносекундных Изменений Яркости*”.

The *MANIA* project was started at the 6-m telescope in Northern Caucasus in 1972, initially led by the late Viktorij Shvartsman. An overview of the project and its astrophysical aims is by Shvartsman (1977; in Russian); some technical details are in Shvartsman & Tsarevskij (1977), Demchuk et al. (1977), and Zhuravkov et al. (1994); for shorter descriptions in English see, e.g., Shvartsman et al. (1996) and Beskin et al. (1997). An overview of *MANIA* astronomical observations is given by Beskin et al. (1998).

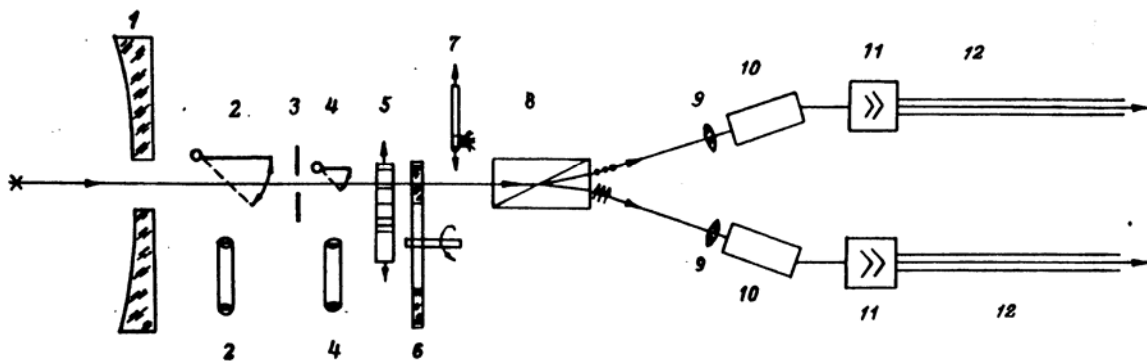


Рис.2. Оптическая схема фотометра.

1 – телескоп, 2-2 – подсмотр поля, 3 – диафрагма, 4-4 – подсмотр диафрагмы, 5 – оптический клин, 6 – блок светофильтров, 7 – эталонный источник света, 8 – двухлучевая поляризационная призма, 9-9 – линзы поля, 10-10 – фотоумножители первого и второго каналов, 11-11 – широкополосные усилители, 12-12 – широкополосные линии передачи импульсного сигнала на измеритель-регистратор (преобразователь время-код-аналог, ЭВМ М-222, анализатор импульсов АИ-256, магнитофон).

*Fig.A3.22. Layout of the original MANIA instrument. A two-channel photometer-polarimeter design is used to avoid effects of detector afterpulsing. (Shvartsman & Tsarevskij 1977)*

Shvartsman had earlier (1971) shown that due to interstellar gas accretion, isolated stellar-mass black holes must be surrounded by luminous halos, and the main radiation mechanism will be the synchrotron one. The crucial test to find stellar-mass relativistic objects is the detection of superfast brightness fluctuations with characteristic times up to  $r^*/c \approx 10^{-5}$

-  $10^{-3}$  seconds. Although several other astrophysical objectives (including study of X-ray sources, optical pulsars, laser emission from stars, and optical SETI) are listed in Shvartsman's early presentation (1977), the search for black holes was a main scientific driver. The observational signature would be intensity fluctuations on timescales  $10^{-6}$  -  $10^{-2}$  seconds, caused by instabilities in the magnetized plasma, but without any periodicity expected. Later work at SAO has also pointed out some potentials of quantum optics in polarization measurements (Efremov & Najdenov 1992).

After some developments at smaller telescopes, the first observations with MANIA on the 6-meter BTA in Northern Caucasus were made in 1977; in 1991 the instrumentation complex was for a while also used at a 2.15 m telescope at the Observatory El Leoncito (CASLEO) in Argentina. The SAO group has also developed other instruments and methods for high-time resolution astronomy and carried out joint observational projects, especially with the group in Galway, Ireland. For examples of this, in particular utilizing observations with the TRIFFID detector on the 6-m telescope, see Golden et al. (2000); O'Sullivan et al. (1998); and Shearer et al. (1998). Recently, the MANIA group at SAO has been led by Gregory Beskin, while a contact astronomer is Vladimor Plokhotnichenko.

Recent characteristics of the system (data from MANIA webpage):

- accuracy of recording the photon arrival times is 20 ns;
- apparatus dead-time is 100 ns;
- limiting intensity of the flux recorded is 370,000 counts/s.

Information on the moments of photon detection times is recorded. The accumulated data are processed with software developed at the SAO and primarily searched for stochastic variability and investigation of periodical intensity variations. Intensity variations of an 18 - 19 magnitude object on time scales of 10 - 100 $\mu$ s can be recognized, provided the power of the variable component is about 40%.

The system can be used for data acquisition from any detector producing standard output TTL pulses when detecting each photon. In particular, a coordinate-sensitive photon counter can serve as the detector. Such a "Multicolor Panoramic Photometer-Polarimeter" with a resolution of 1  $\mu$ s, has been developed, built upon a position-sensitive microchannel detector (Plokhotnichenko et al. 2003).

**Fresh supernovae:** A search was conducted with MANIA on the 6-m telescope for optical variability in supernovae that appeared in 1979 in the galaxies NGC 4647 and NGC 4321. Throughout the time-scale range investigated, 1  $\mu$ s to 100 s, variability was found to be absent.

**The X-ray source Cyg X-2** has been observed with the 6-m telescope in violet and ultraviolet filters. Sporadic variability has been detected on time scales of 10-100 sec, but on scales of  $10^{-6}$  s to 1 s variability was absent from all the observations. (Beskin et al. 1979).

**Crab pulsar:**

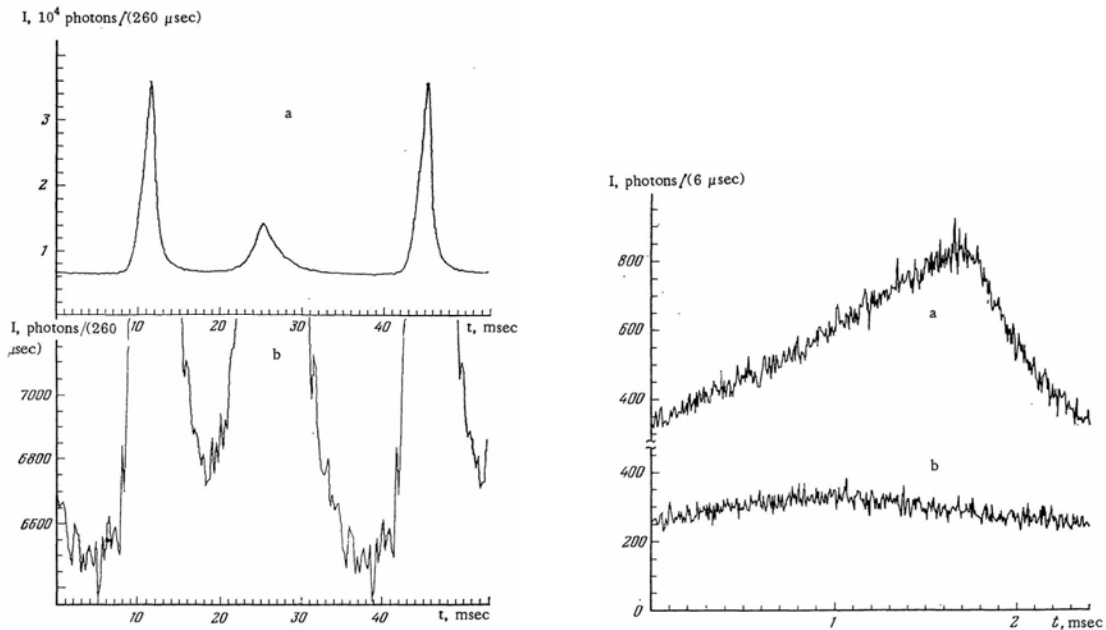


**Fig.A3.23.** Crab pulsar in R-band, observed with the 6-m telescope at 6  $\mu$ s resolution, showing an averaged light curve in which temporal fine structure is absent. For time scales of order 10  $\mu$ s, upper limits on the modulation depth are 10 percent for the main pulse and 15 percent for the interpulse. Both peaks are flattened, with characteristic widths (at 0.97 maximum intensity) of roughly 100 and 400  $\mu$ s, respectively. (Beskin et al. 1983)

**SS433:** Also for the relativistic object SS433, limits of the variable component of the optical flux from SS433 on timescales between 0.3  $\mu$ s and 10 s were obtained from 6-m telescope observations. (Beskin et al. 1985).

However, the limits set on the variability of Cyg X-2, SS433, and other sources are very coarse, especially for the shortest timescales; e.g. on sub-microsecond scales for SS433, only a statement could be made that less than 50% of the light is modulated; even on a 0.1 second level, the limits were around 5%. The reason was the limited photon-count rate (during standard observations through a V-filter around 8 kHz), and the short observing periods (in total on the order of a few hours on the 6-m telescope). At the time, the early version of the MANIA complex could not handle higher count rates; while observations in white light yielded photomultiplier rates around 50 kHz, the data handling system could only register every n:th photon count with n=10 or more. This should not be read as any criticism of the pioneering MANIA project, but it does illustrate the need for high photon rates in order to reach more subtle astrophysical phenomena.

**A0620-00 - A Search for Ultrafast Optical Variability:** MANIA observations of the A0620-00 system, whose compact element is probably a black hole, were carried out on a 6-m telescope, detecting double ultrashort flares with a duration of 0.5-5 ms and a leading front duration of 0.1-1 ms. Low estimates of the brightness temperature in the flare generation zones amount to  $10^9$  to  $10^{11}$  K, suggesting highly nonthermal processes in the A0620-00 system in the course of accretion onto a black hole. (Figure A3.24; Shvartsman et al. 1989):

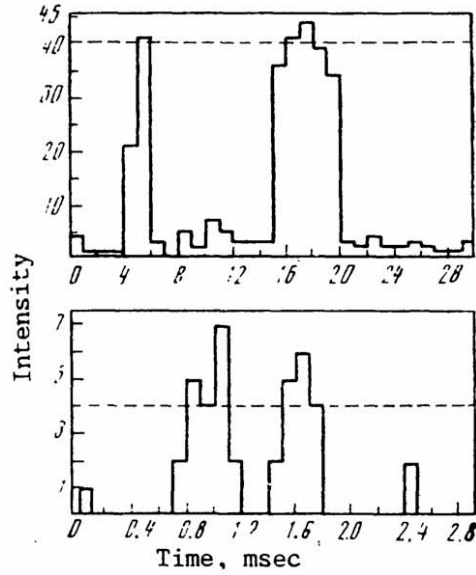


**Fig.A3.24.** Ultrashort flashes observed in A0620-00. Diaphragm 4.3 arcsec, star images 1.5 arcsec. Unit of intensity; photons per 1 ms bin (upper); per 0.1 ms bin (lower). Dashed lines show highest intensity level that can be handled by the instrument computer (Shvartsman et al. 1989)

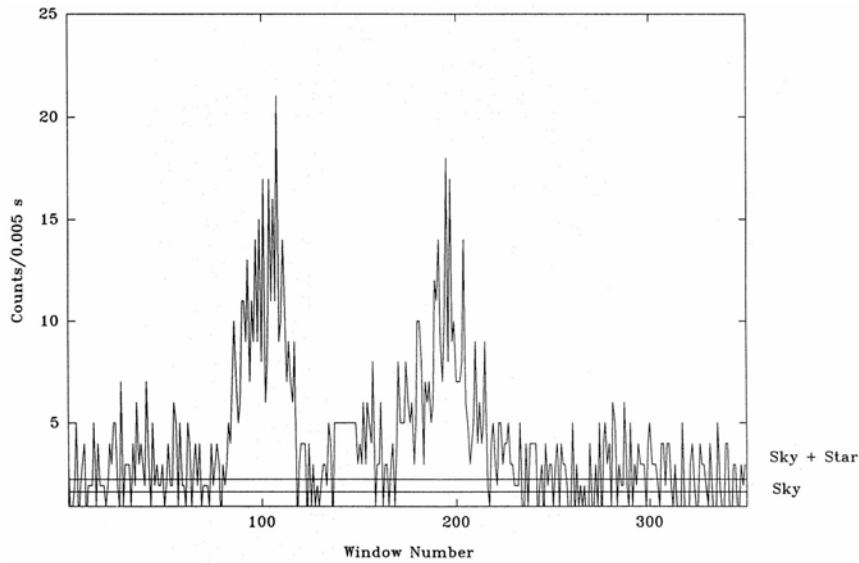


**Fig.A3.25.** Light curves of flares in the Low-Mass X-ray burster MXB 1735-44: observed using the MANIA instrument attached to the 2.15 m telescope of CASLEO, Argentina. Window size is 5 ms. (Beskin et al. 1994)

**Optical study of LMXBs with high temporal resolution:** Evidence for non-thermal flares from MXB 1735-44 was found from MANIA observations with a 2.15 m telescope in Argentina. Two flares of approximately = 0.25 sec in duration were recorded from the MXB 1735-44 X-ray burster. Brightness of the object increased approximately 15-30 times during these flares with very steep forward fronts (characteristic rising time being approximately = 50-60 ms), displaying a fine structure on timescales of approximately = 5-6 ms). Brightness temperatures

for different phases of the flares ranged from  $5 \cdot 10^7$  K to  $10^{10}$  K; this can only be explained by non-thermal processes, or by a highly improbable coherent thermal mechanism. (Figure A3.25; Beskin et al. 1994):

### **MANIA Links:**

SAO Laboratory of Relativistic Astrophysics - <http://www.sao.ru/hq/ra/>

MANIA experiment: <http://www.sao.ru/hq/ra/manija.html>

## **A3.7. Optical SETI**

Searches for extraterrestrial intelligence (SETI) have historically been oriented at finding traces of signals which somehow correspond to an advanced version of human activities. Recently, the development of terrestrial lasers has illustrated that current technology (picosecond pulses of more than a petawatt,  $10^{15}$  W) permits to generate a directed laser pulse that [for a very short moment] outshines the broadband visible light of the Sun by some four orders of magnitude: optical interstellar communication is thus technically plausible. Even at ranges of several hundred parsecs, a single nanosecond laser pulse would deliver a thousand photons to a 10-meter receiving telescope. However, unlike its radio counterpart (where the listening assumes one is finding stray signals), optical SETI requires that any extraterrestrial civilization be deliberately signaling in the direction of our solar system. A number of institutes are now running optical SETI programs, typically surveying nearby stars in the search for possible very short pulses (nanosecond, say) in the dark cores of spectral lines. Although we do not really foresee using OWL for SETI applications, the experience gained with the detectors and observational techniques within these projects may be relevant for our instrument study.

### **Harvard program:**

At Harvard, a detector system for optical SETI saw first light in 1998; a second system began synchronized observations at Princeton in 2001. A summary article is Howard et al. (2004), while earlier reports appeared in Horowitz et al. (2001). Various [potential] sources of noise or false "alarms" are discussed in Howard & Horowitz (2001), and also Deffenbaugh (2002).

The Harvard system rides piggyback on a spectrometer (the CfA Digital Speedometer), mounted on a 1.5 m reflector. Roughly half the light reflected off the entrance slit of the echelle spectrometer is deflected into the SETI photometer. Incoming light passes through a beamsplitter onto two hybrid avalanche photodiodes (Hamamatsu R7110U-07), whose outputs feed a pair of multilevel discriminators with levels corresponding to roughly 3, 6, 12, and 24 photoelectrons. By time stamping level crossings, approximate "waveforms" of incoming pulses are obtained to a precision of 0.6 ns. Arrival times are recorded twice - by a GPS clock (0.1  $\mu$ s precision and accuracy) and by a computer's internal clock (1 ms precision, but only  $\approx$ 50 ms accuracy). A "hot event" veto filters out a class of large-amplitude bipolarity signals that appear to be produced by breakdown events in the photodetectors.

A pair of systems is used to detect nanosecond pulsed optical signals from a target list of Sun-like stars; some 16,000 observations totaling nearly 2400 hr have been made during five years of operation. A beamsplitter-fed pair of hybrid avalanche photodetectors at a 1.5 m telescope at the

Harvard/Smithsonian Oak Ridge Observatory (Agassiz Station) triggers on a coincident pulse pair, initiating measurement of pulse width and intensity at subnanosecond resolution. An identical system at the 0.9 m Cassegrain at Princeton's Fitz-Randolph Observatory performs synchronized observations with 0.1  $\mu$ s event timing, permitting unambiguous identification of even a solitary pulse. Among the 11,600 artifact-free observations at Harvard, the distribution of 274 observed events shows no pattern of repetition, and is consistent with a model with uniform event rate, independent of target. The search and candidate events are described by Howard et al. (2004).

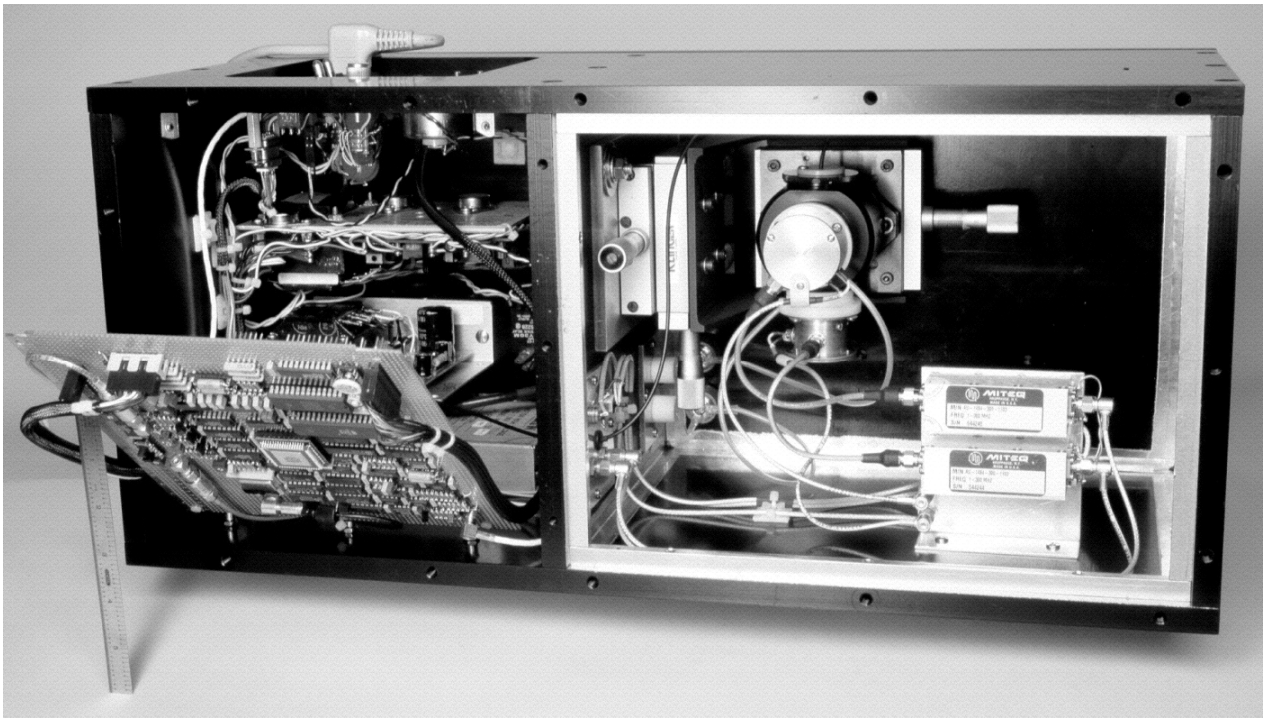


**Fig.A3.26.** Harvard SETI photometer. Light enters from the rear of the right-hand compartment, focused onto a 30 arcsec aperture, then passes through a beam splitter onto the pair of HAPDs on their 3-axis stage. The detectors run at a gain of  $\approx 4 \times 10^4$ , producing  $\approx 50 \mu$ V negative pulses into  $50\Omega$ , which are amplified and sent to the electronics in the left-hand compartment. The latter perform coincidence, 4-level ADC, timing, logging, hot-event veto, and communication with the host computer. The photometer measures 25 $\times$ 25 $\times$ 60 cm, and weighs 30 kg. (Howard et al. 2004)

In the five years of observations, 4746 "triggers" were recorded (i.e., instances when the lowest thresholds are simultaneously exceeded in both channels). Although all triggers are recorded, the reported waveforms are passed through a filter that enforces certain validity checks: the signals seen in each channel must be roughly the same amplitude (within one level of each other), and they must overlap in time. The subset of triggers that pass this test are labeled "events"; to date, 1117 events have been registered. Since the 1117 events are distributed impartially among 6176 objects, there is confidence that the majority of the events arise from natural causes. Furthermore, in attempts to identify their source, events were logged even during tests with the observatory dome closed. Clearly, instrumental effects contribute background events. In the analysis an attempt was made to remove the instrumental backgrounds from the Harvard data to look for residual events, possibly of extraterrestrial



origin. Also the Harvard observations were examined during which Princeton provided verification through simultaneous observations; with one possible exception, we found no events synchronously occurring at the two observatories. A histogram of the event rate by month figure below reveals the largest source of background events, evidenced by a marked systematic seasonal trend in the event rate, apparently due to ambient humidity: the event rates are 30–40 times higher during the warmer and more humid summer months (May–September), as shown.

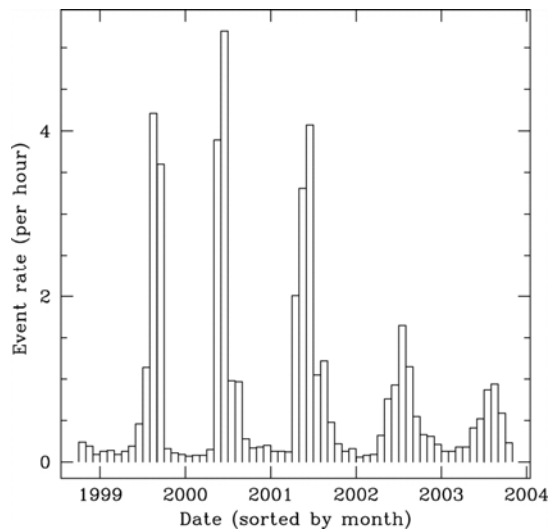


**Fig.A3.27.** *Seasonal variation in the event rate of Harvard SETI photometer. Corona breakdown substantially elevates the rate during the humid summer months. This plot includes all observations, regardless of quality. (Howard et al. 2004)*

Neither the Harvard search (Howard et al. 2004) nor previous searches with the MANIA experiment in Russia (Shvartsman et al. 1994) have found any evidence for artificial extraterrestrial signals.

### **What natural phenomena may trigger false readings?**

There appear to be few astrophysical, atmospheric, or terrestrial mechanisms able to produce events like the nanosecond photon pileup expected from an intentional and powerful pulsed laser beacon. Potential sources we considered include lightning (too extended in time), cosmic-ray induced atmospheric Cherenkov flashes (fast enough, but fluence less than  $10^{-3}$  photon per pulse owing to its extended source sky region and large terrestrial footprint), and local effects of the background muon flux (the rate of scintillation events in the optics upstream of the beam splitter plus that of estimated direct ionization events in the detectors themselves produce event rates  $\lesssim 10^{-5} \text{ s}^{-1}$ ). Effects being considered include:

\* Cherenkov flashes can produce no more than one photon during a nanosecond, not enough to render a significant reading in the detector.

\* Lightning from distant storms is also insignificant, since it is unlikely to deliver pulses under a microsecond in duration.

\* Atmospheric glow produces a steady stream of photons, but only about 100 per pixel per second in a 1 square meter telescope, which in a 10,000 pixel detector would only result in .001 photons per nanosecond; not nearly enough to render false readings. OSETI can theoretically be conducted during the day, if the sky is clear.

\* The high voltages used within our detectors cause electrical arcing within the detectors, which in turn trigger the detectors. We therefore use two detectors, and ignore all "detections" that do not occur in both detectors simultaneously. Only coincident detections in both detectors are considered as possible OSETI events.

\* Cosmic rays striking the atmosphere cause cascades of high energy particles and photons, which can in turn trigger our detectors if the photons enter our telescope. Photons generated by one such cosmic ray could not enter both our telescope and Harvard's telescope, so we and Harvard compare the timing of our possible OSETI events to eliminate such atmospheric sources. We detect about one possible OSETI event per hour of observation.

[text above from Princeton OSETI website]

Howard & Horowitz (2001) discuss various instrumental and terrestrial background sources that might produce spurious nanosecond signals (including cosmic ray particles; Cherenkov radiation, photodetector problems, lightning, blinking lights on airplanes, and others). Further observational issues are discussed by Deffenbaugh (2002)

### Lick Observatory program

An overview of the optical SETI program at Lick is given by Wright et al. (2004). In particular, a three-detector system is used to increase the rejection of nearly all "false-positive" signals.

Wright et al. (SPIE 2001) noted that two-detector optical SETI systems have experienced a surprising incidence of false positive signals. They describe a three-detector system designed to alleviate this difficulty, as now used at Lick Observatory:

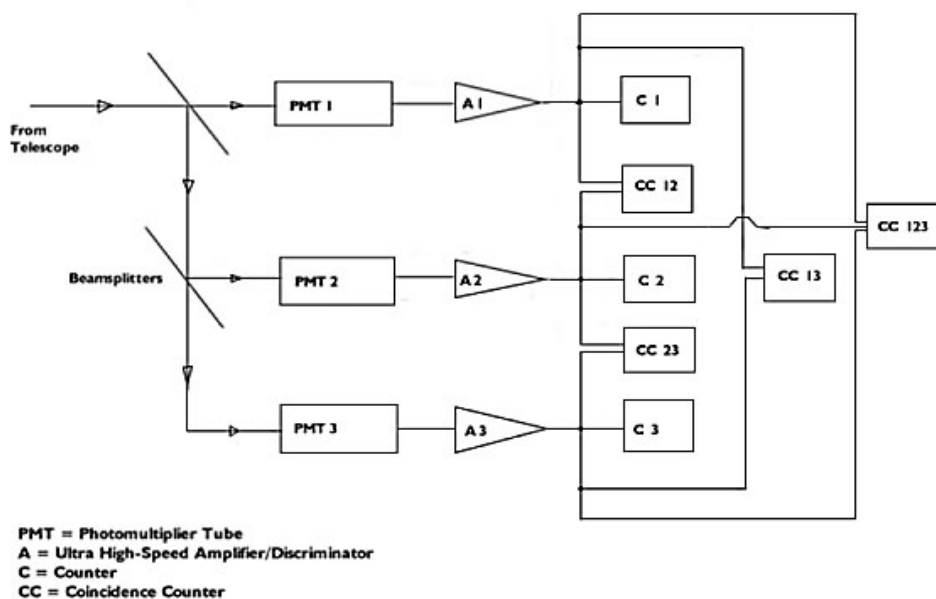


Fig.A3.28. Lick Observatory three-detector logic diagram for optical SETI (Wright et al. 2001)

### Optical SETI web links:

Berkeley optical SETI: <http://seti.ssl.berkeley.edu/opticalseti>

Optical SETI at Harvard: <http://seti.harvard.edu/OSETI>

Lick Observatory optical SETI: <http://seti.ucolick.org/optical>

Princeton optical SETI: <http://observatory.princeton.edu/oseti>

## A3.8. Lunar- & Satellite Laser Ranging

Very high time resolution is required and realized in experiments with optical laser ranging to satellites in Earth orbit, and to retro-reflectors placed on the Moon. Normally, a high-power pulsed laser beam is sent into space through a collimating telescope, and its echo (of often only very few photons) is received by either the same, or some adjacent telescope. The desired precision is on the level of picoseconds (corresponding to millimeters in the measured distance to the object). Lunar laser ranging provides a test of the constancy of Newton's gravitational constant,  $G$  (currently limited to a variation of less than a part in  $10^{12}$  per year). Relativistic geodetic precession is also now verified at a high level of precision; further applications include tests of the motional influence on gravitational attraction (gravitomagnetism) at the 0.1% level, further permitting to set limits on deviations from the expected  $1/r^2$  law of gravity.

Since the detectors used in such systems often are photon-counting avalanche photodiodes or similar, the techniques and experiences from these projects are quite relevant also for our instrument study. The very high temporal precision requirements (picosecond) have led to systematic studies of phenomena affecting photon detection on such levels, e.g. propagation effects in the Earth's atmosphere (typically causing a scatter on the order of 10 ps); differential delays inside detectors (e.g., the dependence on exactly where in the detector volume a particular photon is absorbed); and methods for accurate time keeping and time transfer between different observing stations.

Various front-line detectors are being developed and applied for these projects, such as infrared-sensitive APD's and APD arrays. Laser ranging, however, has somewhat different detector requirements and sensitivities to their imperfections. For example, in the case of infrared photon-counting detectors dark-signal rates of even MHz may be acceptable since one is measuring the return signal during only a very short interval when its return is expected. If integrated during 1  $\mu$ s, say, even a dark signal of 1 MHz is expected to produce only one single count, normally not the limiting parameter.

Among the most ambitious laser ranging projects is *APOLLO* (Apache Point Observatory Lunar Laser-ranging Operation), which uses the 3.5 meter telescope at Apache Point in southern New Mexico. The large aperture in combination with good atmospheric seeing permits to record multiple returned photons per pulse, in contrast to the typically 0.01 photon-per-pulse experienced by previous Lunar ranging facilities. The aim is to measure the round-trip travel time of laser pulses bounced off lunar retro-reflectors to a precision of a few picoseconds, corresponding to about one millimeter of precision in range to the Moon.

**Detector considerations for high-accuracy timing** (Murphy et al. 2004): One of the elements in the error budget for laser ranging is the avalanche spreading phenomenon inside the detector. A full avalanche current is established once the entire active area of the detector element is participating in the avalanche. This state is attained most expediently if the avalanche begins in the center of the element and propagates outward from there. On the other extreme, if an avalanche begins at one edge, it could take roughly twice as long to establish full current. The rest of the random error budget includes things such as the effects of the finite laser pulse width, other temporal uncertainties in the APD detectors, timing electronics jitter, and timebase jitter.

One further precision-limiting aspect is that the detector only responds to the first photon to trigger an avalanche. In order to avoid biasing the range measurement to shorter values, multiple detector elements must be available to collect photons. Because of this, the APOLLO setup uses an APD array detector:

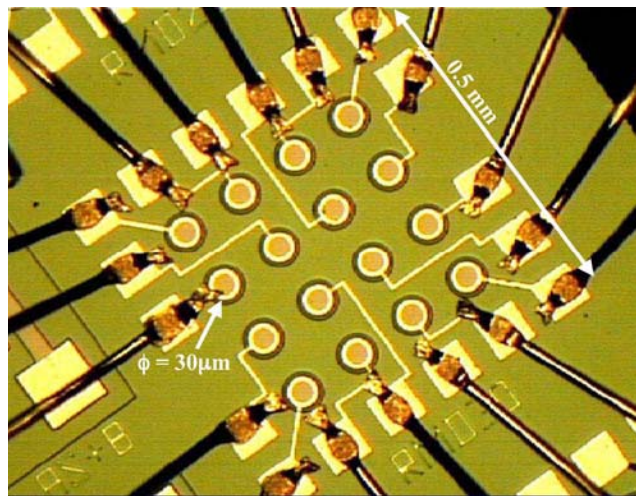


**Fig.A3.29.**  $4 \times 4$  APD array made by Lincoln Labs, used in APOLLO, the Apache Point Lunar Laser-Ranging Operations. The  $30 \mu\text{m}$  diameter active detectors are on  $100 \mu\text{m}$  centers. The array provides multiple detectors to accommodate a multi-photon return, and also allows closed-loop signal tracking. Lincoln Labs have fabricated also larger arrays ( $32 \times 32$  reported), and in the future, the APOLLO project plans to use much larger arrays than this  $4 \times 4$  one. (Murphy et al. 2004)

Lincoln Labs APD array characteristics	
Element Spacing	$100 \mu\text{m}$
Active Diameters	$20, 30, 40 \mu\text{m}$
Device Thickness	$\sim 20 \mu\text{m}$
Formats Produced	$4 \times 4$ and $32 \times 32$
Breakdown Voltage	$\sim 25 \text{ V}$
Photon Detection Efficiency	$30\%$ ( $> 50\%$ with AR coating)
Dark Count Rate	$\sim 2400e^{0.106T} \text{ s}^{-1}$ , $T$ in $^{\circ}\text{C}$
Effective Resistance	$25 \text{ k}\Omega$
Effective Capacitance	$< 2 \text{ pF}$

**Table A3.2.** Characteristics of the avalanche diode array used in the APOLLO lunar ranging experiment (Strasburg et al. 2003)

The spacing between detector elements in the array results in a low fill-factor, why a microlens array is used in front of the detector to recover nearly 100% fill-factor. The lenslet array is itself located at a re-imaged telescope focus. In this way, each lens, or “pixel” represents a spatial position on the sky - in this case about 0.35 arcseconds on a side. The detector array is then located roughly one focal-length away from the lenslets, so that a pupil image is formed within the confines of the 30  $\mu\text{m}$  detector element:

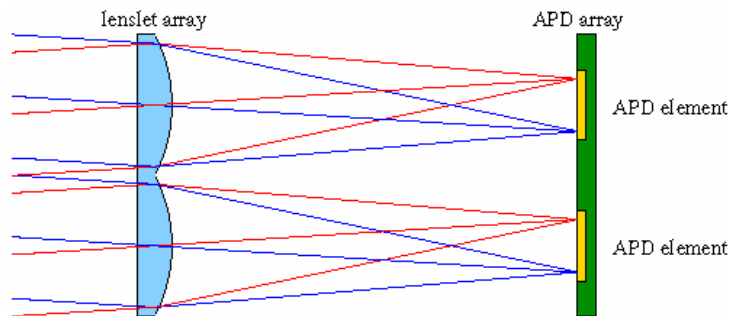


**Fig.A3.30.** The microlens array concentrates incoming light onto the individual APD elements. The lenslet itself is located at a telescope focus. The rays in the figure are color-coded to indicate origin of location on the primary mirror. An image of the primary is formed on each APD element. (Murphy et al. 2004)

### Avalanche initiation location

The spread in location of the incident photon within the APD element translates to a timing uncertainty. When a photon impinges on an avalanche photodiode, it penetrates some distance before creating an electron-hole pair in the semiconductor. For silicon, the characteristic penetration depth at a wavelength of 532 nm is about 1.0  $\mu\text{m}$ . The penetration depth varies from photon to photon, leading to a spread in the initial depth of the electron-hole pair. An electric field drives the electron toward the p-n junction and multiplication region. At a saturation velocity of about  $10^5$  m/s, (0.1  $\mu\text{m}/\text{ps}$ ), the variable penetration depth translates to roughly 10 ps of variability in when an electron reaches the multiplication region. At this point, a microplasma of avalanching electron-hole pairs spreads across the disk-shaped multiplication region. It may be assumed that the front of this plasma propagates across the silicon at a uniform speed – presumably not much slower than the thermal speed of an electron in silicon ( $1.2 \times 10^5$  m/s). In this model, an avalanche initiated in the center of the detector element reaches saturation current (the whole disk in avalanche) sooner than an avalanche initiated at the edge of the element. Variation may be expected to be  $>150$  ps for a 30  $\mu\text{m}$  element. This effect has been studied in the APD elements, by illuminating the detector with a pulsed laser spot a few microns across, and measuring report time while scanning this spot across the spatial extent of the array:

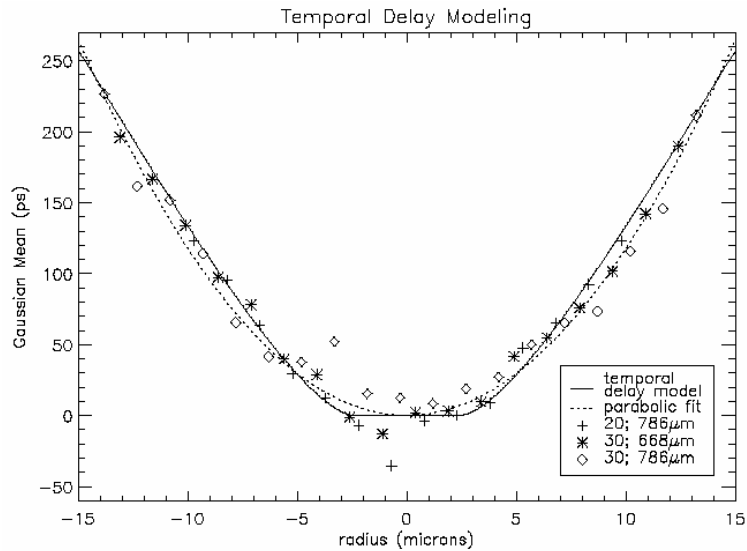


**Fig.A3.31.** Spatial scans of avalanche initiation delay for two different devices at two different wavelengths. A crude parabolic fit is plotted, as well as a model based on linear spread of the avalanche front. (Murphy et al. 2004)

### Satellite & lunar ranging links:

APOLLO (Apache Point Observatory Lunar Laser-ranging Operation):

<http://physics.ucsd.edu/~tmurphy/apollo/apollo.html>

McDonald Laser Ranging Station, University of Texas:

<http://www.csr.utexas.edu/mlrs/>

International Laser Ranging Service: <http://ilrs.gsfc.nasa.gov/>

Proc. 12th International Workshop on Laser Ranging, Matera, Italy, 2000:

<http://geodaf.mt.asi.it/GDHTL/news/iwlr/index.htm>

Proc. 13<sup>th</sup> International Workshop on Laser Ranging, Washington, DC:

[http://cddis.gsfc.nasa.gov/lw13/lw\\_proceedings.html](http://cddis.gsfc.nasa.gov/lw13/lw_proceedings.html)

Proc. 14<sup>th</sup> International Workshop on Laser Ranging, San Fernando, Spain, 2004:

<http://cddis.gsfc.nasa.gov/lw14/>

The 15<sup>th</sup> workshop in this series is to be held in 2006 in Canberra, Australia.

### A3.9. QVANTOS

*QVANTOS* (“*Quantum-Optical Spectrometer*”) is an instrument developed at Lund Observatory for the study of very rapid astrophysical phenomena. Basically, it is a very fast stellar photometer equipped with digital signal processors that are capable of handling large volumes of data in real time.

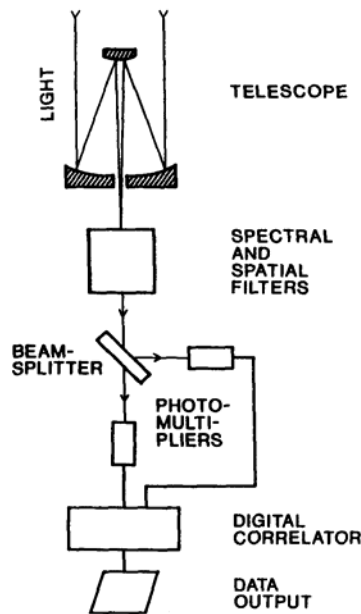


**Fig.A3.32.** Layout of *QVANTOS Mark I*, used for studying stellar scintillation on La Palma. When required, effects of correlated detector noise can be minimized through the use of two detectors, whose output pulse trains are cross correlated. (Dravins et al. 1997a)

The nanosecond time resolution and other specifications were chosen to ultimately enable also the detection of quantum-optical effects. Its first Mark I version used photomultipliers while current work is on the Mark II version, equipped with SPAD's. *QVANTOS Mark I* was used on La Palma for comprehensive observations of atmospheric intensity scintillation of stars, while Mark II electronics have been used for observations at Skinakas on Crete, together with SPAD detectors in the *OPTIMA* instrument from MPE Garching. In Lund, various laboratory studies of detector properties have been made to better understand how APD's can be used for accurate photometry.

#### Atmospheric intensity scintillation

The Earth's turbulent atmosphere causes stars to "twinkle", i.e. to undergo rapid fluctuations in their intensity. Already simple optical effects lead to image distortions (seeing), while only [differential] effects of higher order also cause the intensity to be modulated (scintillation). Stellar intensity scintillation in the optical was extensively studied at Roque de los Muchachos on La Palma, with measurements throughout some 25 full nights, during different seasons of year. Besides studies of scintillation as such, an aim was to understand how to design observing programs for astrophysical milli- and microsecond phenomena that have to be segregated from the fluctuations superposed by the terrestrial atmosphere.

**Temporal statistics of scintillation:**

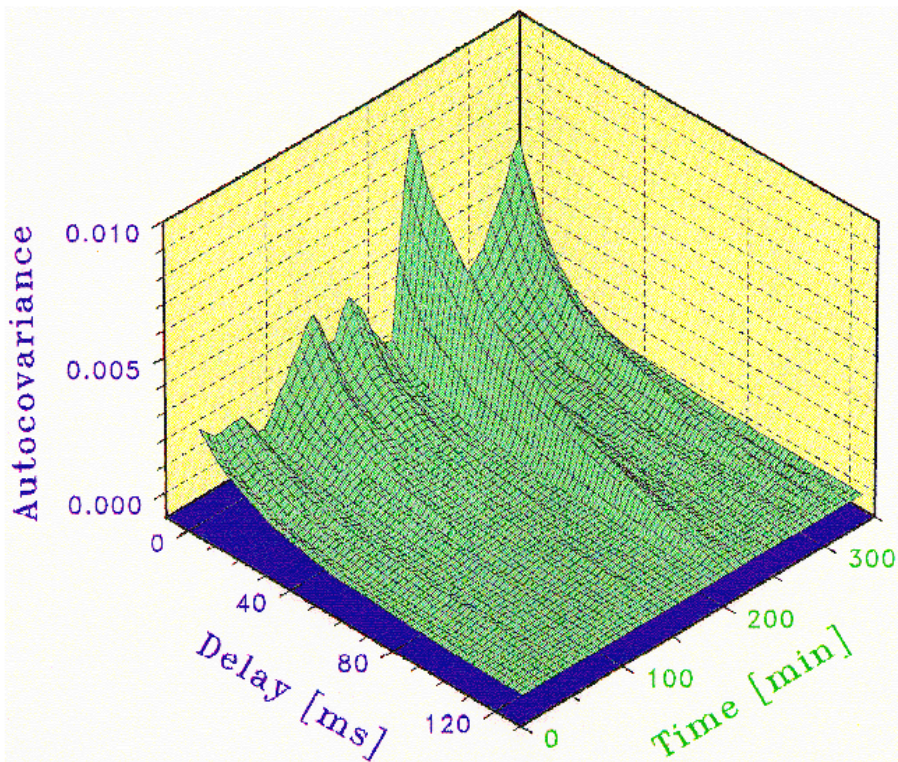


**Fig.A3.33:** Evolution of the autocovariance of stellar intensity during a night, observed through a 60 cm telescope. The star was Polaris, assuring a constant position in the sky. The amplitude at the origin equals the intensity variance  $\sigma^2$ . Each curve represents a 120-second integration. The amplitude and temporal structure of scintillation changes on typically tens of minutes. (Dravins et al. 1997a)

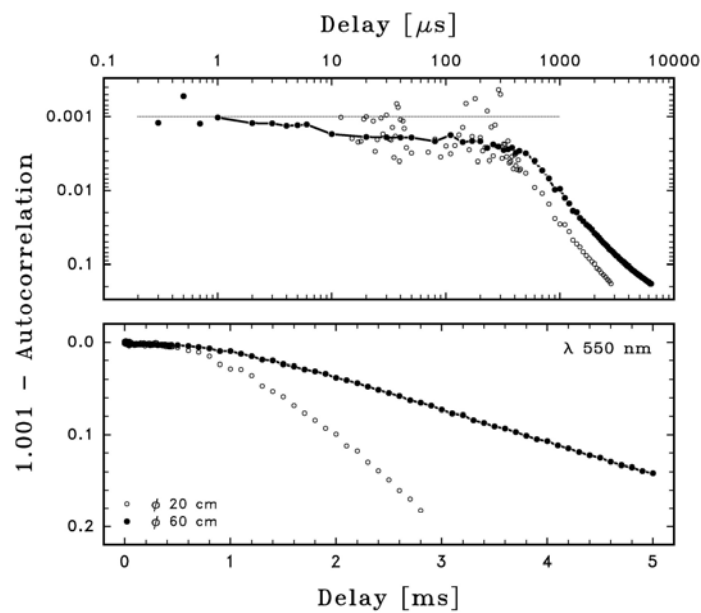


**Fig.A3.34.** Although the main scintillation power is around 10 ms, with sufficient measuring precision, stellar scintillation can be followed also to very short timescales. The apparent break in the curve near 300  $\mu$ s may be connected to atmospheric inner scale (linear size 3 mm at windspeeds of 10 m/s) Dravins et al. (1997a)



## Color dependence

Scintillation depends on wavelength. For small apertures, the "flying shadows" on the Earth's surface are resolved. Here the fluctuations are more rapid (and have a greater amplitude) in the blue than in the red. In large telescopes, these color differences nearly vanish.

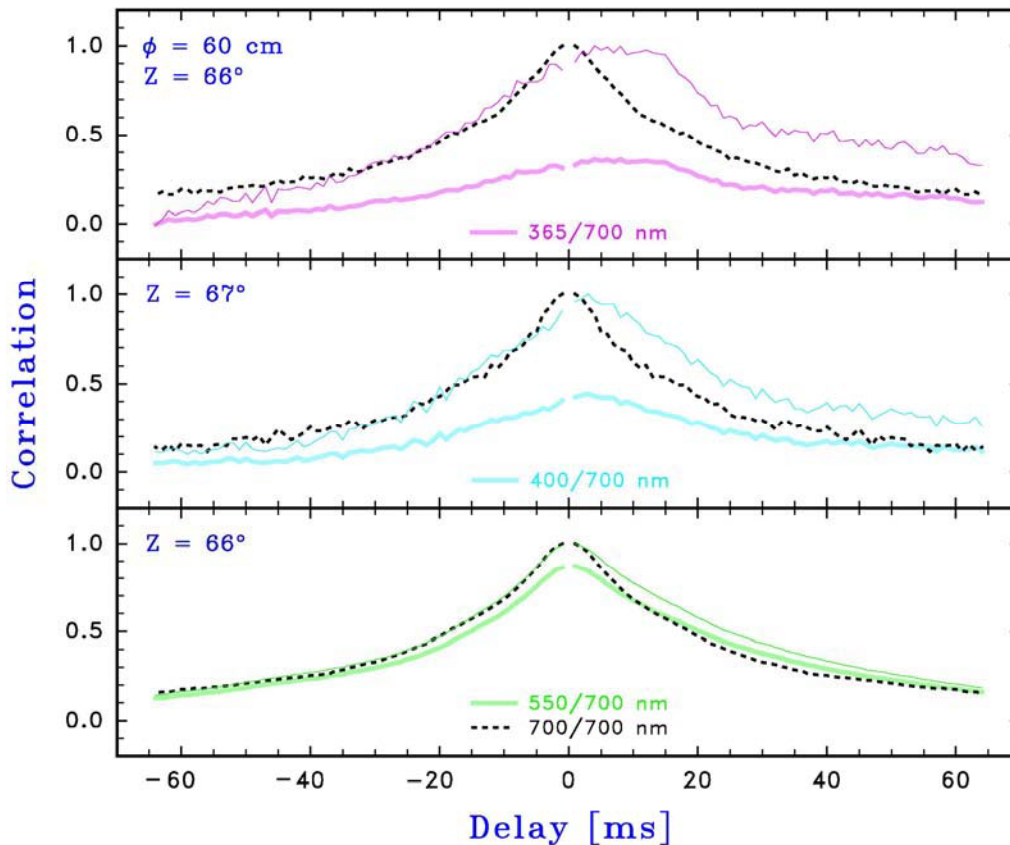


**Fig.A3.35.** Cross correlations of atmospheric intensity scintillation between different pairs of colors. Scintillation at 700 nm was successively cross correlated with that simultaneously measured at 550, 400, and 365 nm. With increasing wavelength difference, (a) the "agreement" (i.e. degree of correlation) between scintillation in different colors decreases, and (b) the time delay increases, visible as a shift of the correlation maximum. In the violet, the dispersion of air changes rapidly with wavelength, which explains the significant differences between the nearby wavelengths of 365 and 400 nm. This timelag between scintillation in different colors is a signature that **does not decrease in large telescopes.** (Dravins et al. 1997b)

At zenith, the fluctuations in different colors are simultaneous, but shift out of phase with increasing zenith distance, due to atmospheric chromatic dispersion. This timelag is independent of telescope size, and is one scintillation property that remains unchanged also in very large telescopes, and may be relevant in, e.g., searches for cross correlations between astrophysical emission variability between spectral lines at different wavelengths:

### Dependence on the shape of the telescope aperture

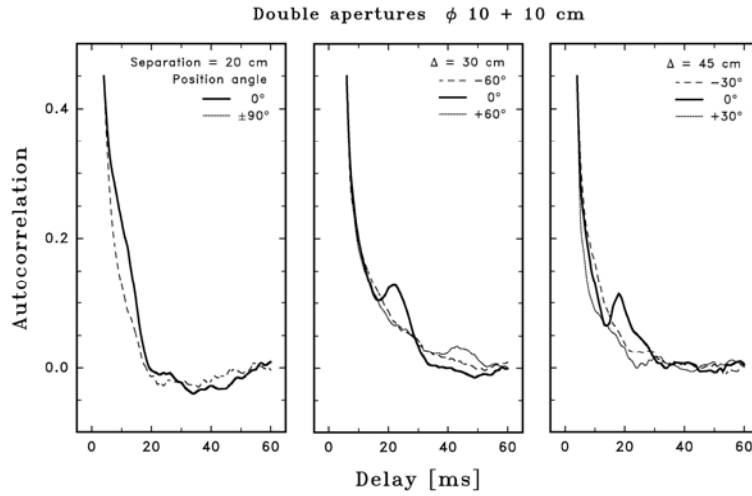


**Fig.A3.36.** Scintillation measured through masks with two apertures, at different separations and position angles. If the same flying-shadow pattern crosses both apertures, a secondary peak appears in the autocorrelation, revealing the flying-shadow speed and direction. The autocorrelation changes significantly with position angle: the secondary peak is reproducible only within a rather narrow range (about 30 degrees). For apertures separated by 30 cm, typical delays of 20 ms indicate a flying-shadow speed of about 15 m/s. Signatures related to these might be expected in ELT's, whose segmented primaries have cm-scale gaps between them. (Dravins et al. 1998)

### Measuring rapid optical variability

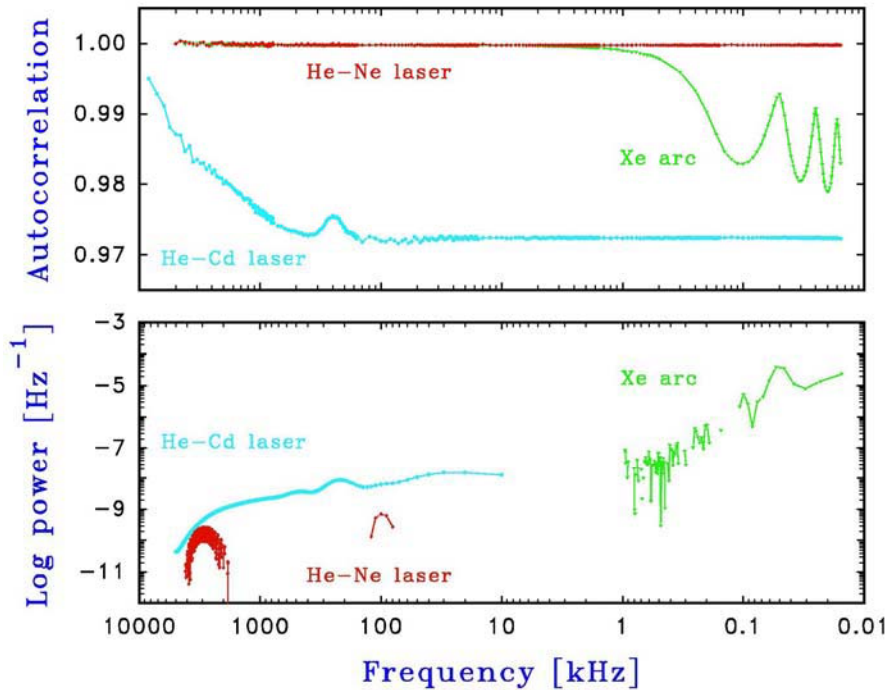


**Fig.A3.37.** Rapid optical variability in different laboratory sources, measured with the QVANTOS Mark I instrument. Autocorrelation functions and power spectra are shown for: [a] Stabilized He-Ne laser; [b] Xenon arc lamp, stable on very short timescales, but variable over tens of milliseconds and longer; [c] He-Cd laser, stable on longer timescales, but variable over microseconds and shorter. The peak around 4 microseconds is a signature of plasma oscillations at 250 kHz in this low-pressure source. Further, there is apparent flickering down to the measurement limit of 100 nanoseconds. (Dravins et al. 1994)

Laboratory experiments are pursued to identify optimum strategies for detecting optical variability on microsecond and shorter timescales. Figure A3.37 shows how extremely rapid optical fluctuations in some laboratory sources are seen by the QVANTOS Mark I instrument. The search for unknown variability is made on many different timescales: Autocorrelation functions and power spectra are shown over six decades in time resolution. Optical fluctuations this rapid have not yet been detected in any astronomical object.

### Instrumentation studies:

The use of APD's as *scientific* detectors (i.e. not merely technical ones) requires that their photometric properties are well understood. While there is a whole literature on photomultiplier properties, APD's have not yet been as thoroughly examined. Laboratory studies are therefore being made of different types of single-photon-counting units. (Dravins et al. 2000).

**Light emission ("diode afterglow"):** Immediately following the detection of a photon, a shower of others may be emitted out from the APD, as it recovers after the avalanche. For high-speed applications in large telescopes, such secondary light could find its way back onto the detector, causing optical "ringing".

**Dark-count instabilities:** The dark signal from an avalanche diode may exhibit bistability, with the count rate jumping between discrete levels.

**Dead-time & afterpulsing:** Similar to photocathode detectors, detector dead-times limit the maximum count rates possible, while afterpulsing may influence time-correlated measurements.

**Very small detectors at very large telescopes:** Photon-counting APD's are commercially available only in very small sizes (fraction of one mm), becoming challenging to optically interface to large telescopes, if the entrance pupil is to be imaged onto the detector.

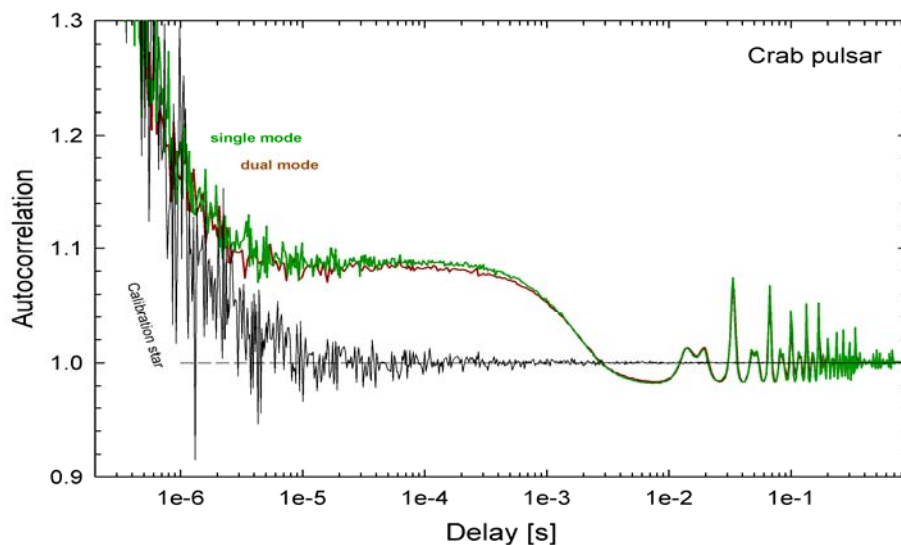


**Fig.A3.38.** Autocorrelation functions recorded of the Crab pulsar (period = 33 ms). Skinakas Observatory 1.3 m telescope, Oct.2004; OPTIMA (MPE) + QVANTOS Mark II (Lund).

**Recent observational work:** During 2004, the compatibility of the OPTIMA instrument, and its APD detectors, and the QVANTOS Mark II signal processing system was verified, and a joint observing campaign was carried out during two weeks at Skinakas Observatory during October 2004 (Figure A3.38).

As this is being written, laboratory work is in progress in Lund with a simulated digital stellar intensity interferometer using the QVANTOS Mark II detectors and electronics (1.6 ns time resolution), while feasibility studies are being made with a view of possibly using the signal processors together with photomultiplier detectors on large optical flux collectors, as steps towards optical observing with extremely large telescopes.

**QVANTOS link:** <http://www.astro.lu.se/~dainis/HTML/HISPEED.html>

### **A3.10. TRIFFID, MEKASPEK & MCCP, SUBARU, SALT, ESO-VLT, OPTICON, and Other**

There are being planned, currently exist, or have recently existed, several other instruments specifically designed or useful for high-time-resolution astrophysics. We mention here a few further projects:

#### **TRIFFID**

TRIFFID (*TRansputer Instrument For Fast Image Deconvolution*) is a high-speed image-sharpening camera from Ireland (National University of Ireland, Galway & Dublin Institute for Advanced Studies). It uses as multianode multichannel array MAMA two-dimensional detector with fast readout. By rapid recording of images it is possible to overcome some effects of atmospheric seeing, and to achieve a post-exposure image enhancement by a suitable shift-and-add of time-resolved subimages to compensate for atmospheric tip-tilt distortions. TRIFFID has been used with, WHT and Kapteyn telescopes on La Palma, and with the NTT on La Silla to achieve image sharpness improvements of about a factor of two in crowded fields such as globular clusters. (Butler et al. 1998). Also pulsars have been observed with the TRIFFID camera,

#### **MEKASPEK & MCCP**

*MEKASPEK (MEhr-KAnal-SPEKtralphotometer*, Universitäts-Sternwarte München) is a fiber-optical multichannel photometer (Barwig et al. 1998). Four fiber ends form the entrance slit of a prism spectrograph which projects the individual spectra onto a two-dimensional photon-counting micro-channel plate detector (*Mepsicron*). MEKASPEK has been used on several telescopes, both at “its home” on Wendelstein in Bavaria, and at Calar Alto and on La Silla. The scientific programs have mainly concerned flare stars, cataclysmic variables, and other rapidly variable stars, with time resolutions of some 10 milliseconds. A previous instrument version was MCCP (*Multi-Channel multi-Color Photometer*); Barwig & Schoembs (1987); Barwig et al. (1987); Mantel & Barwig (1993). Here, three sources (object, calibration, sky) are picked up by fibers that go through prism spectrographs for 5 colors each, ultimately detected by 15 photomultipliers with a time resolution of 1 ms.

MCCP: <http://www.wendelstein-observatorium.de:8002/mccp/mccp.html>

**MEKASPEK:**

[http://www.wendelstein-observatorium.de:8002/meka/index\\_german.html](http://www.wendelstein-observatorium.de:8002/meka/index_german.html)

**SUBARU**

For the Japanese 8.2 m SUBARU telescope on Mauna Kea, some work towards high-speed instrumentation has been made:

FOCAS, the *Faint Object Camera and Spectrograph* is an imaging and spectroscopy unit which can be installed at the SUBARU Cassegrain focus. FOCAS uses refracting optics for both the collimator and camera and has gratings to achieve high throughput optimized for the wavelength range of 365-900 nm. It has four operating modes: imaging, spectroscopy (long slit and multi-slit), polarimetry, and spectropolarimetry, and covers a circular 6' field of view.

For FOCAS, a high-speed option is being developed with an aim to achieve down to  $\approx 0.1$  s time resolution. This is to be achieved by a high-speed CCD camera that can replace the regular one (Sekihuchi et al. 2004).

A design study of a high-speed spectro-photo-polarimeter for SUBARU has been made, evaluating STJ and TES detectors as well as hybrid photodiode arrays. The time-resolution goals were stated as 1 ms for photometry and 100 ms for polarimetry (Sekiguchi et al. 2000).

FOCAS instrument: <http://www.naoj.org/Observing/Instruments/FOCAS/>

**SALT**

SALTICAM: an imaging and acquisition camera, is part of the first-light instrument complement on SALT, the 11-meter *Southern African Large Telescope* to be inaugurated in late 2005.

It has been built at SAAO, with D. O'Donoghue as the PI. This instrument has been conceived as a multi-purpose device, capable of performing roles of both an acquisition camera and an imager/photometer, capable of conducting science. Like PFIS, it is situated at the prime focus, but fed by a 45-degree mirror. Fore-optics provide focal reduction (to  $f/2$ ) to produce a suitable plate scale and allow the entire science and guidance fields to be imaged (i.e. to 5 arcmin radius). Frame transfer, science grade, CCDs, with fast readout times, allow for science imaging and high-time resolution photometry. Continuous photometry of  $\sim 20$  ms integrations might be feasible with windowing, charge shuffling and a suitably fast bus. The "normal" readout times, however, range over several seconds:

**Readout times:**

Mode	Prebin	Observer Specifies	Readout Speed ( $\mu\text{s}/\text{pix}$ )	Readout Noise ( $e^-/\text{pix}$ )	Readout Time (sec)
Full Frame	2x2	Slow	10.0	3.3	11.2
Full Frame	2x2	Fast	4.0	5	4.6
Frame Transfer	2x2	Slow	10.0	3.3	5.7
Frame Transfer	2x2	Fast	4.0	5	2.4

SALT: <http://www.salt.ac.za/>

Salticam: <http://www.salt.ac.za/content/science/salticam.htm>

## ESO VLT

In the planning of instrumentation for the VLT, also various concepts for a high time-resolution instrument were considered, though never realized. A working group was set up, and some of its considerations are in the proposal for FRISPI (*Fast Recording Imager and Spectro-Photometric Instrument*). Building upon the experience of MEKASPEK, this was envisioned as a fiber-fed spectrometer, capable of observing four sources simultaneously with selectable spectral resolution  $R \geq 1000$ . Various filter passbands would then be synthesized in software from the spectrum. As a detector, a multinode multichannel array (MAMA) was foreseen. The time resolutions would range from 4 seconds for the full image, though 1 ms in a binning mode, to 0.1  $\mu$ s in a photon-count time-tagged mode: Barwig & Mantel (1995); Barwig et al. (1994).

## OPTICON

The OPTICON collaboration (*Optical Infrared Coordination Network for Astronomy*), funded by the EU Sixth Framework Programme (FP6) for a 5-year program 2004-2008. Their programs include “*Joint Research Activities in Research and Technology*”, one of which is JRA3: “*Fast Readout High Performance Optical Detectors*”, chaired by S.Wagner (Heidelberg). One of the work packages identified within this JRA3 is “APD Arrays” with A.Shearer (Galway) as the coordinator. The stated goal is 100 ns resolution (Wagner: presentation of JRA3 to the OPTICON board in April 2004:

[http://www.astro-opticon.org/presentations/jra3\\_opticon\\_ghent\\_04.pdf](http://www.astro-opticon.org/presentations/jra3_opticon_ghent_04.pdf) ).

OPTICON: <http://www.astro-opticon.org/>

JRA3: <http://www.lsw.uni-heidelberg.de/projects/htra/>

## General instrumentation issues

There are various other instrumentation issues being addressed that are not specific to any particular instrument design. For example, high-speed data acquisition systems for multichannel photometry are being developed, including facilities for precise GPS timing (Moon et al. 2001; Moon 2004).

## Acknowledgements

The work in Lund was supported by the Swedish Research Council, the Royal Physiographic Society in Lund, and European Southern Observatory. At Lund Observatory we acknowledge valuable discussions with, in particular, Hans-Günter Ludwig, Sveneric Johansson, Vladilen Letokhov (visiting from Troitsk/Moscow), Eva Mezey, Bo Nilsson, and Torbjörn Wiesel. Various observational and instrumental concepts were tested during observations at Skinakas observatory on Crete of compact astrophysical objects, made jointly with the OPTIMA group of the Max-Planck Institute for Extraterrestrial Physics in Garching (in particular Gottfried Kanbach, Alexander Stefanescu and Fritz Schrey); while evaluations of instrumentation have been enhanced by contacts with Michael Perryman (ESTEC) and Jixiang Zhu (Correlator.com).

The work in Padova was supported by the University of Padova, INAF and the European Southern Observatory. We are greatly indebted to several persons who provided advice and material: G. Bianco (ASI Matera), R. Biasi and A. Giudice (MPD), G. Biscotti (Becker & Hickel), S. Centro and M. Mariotti (University of Padova), S. Cova (Politecnico Milano), S. Leschiutta (University of Torino), G. Longo (University of Naples), C. Mackay (University of Cambridge), M. Perryman (ESTEC), I. Prochazka (Czech Technical University in Prague). AleniaSpazio and Carlo Gavazzi Space provided material on space facilities for time distribution. S. Cocuzza (CISAS) helped with the rendering of *QuantEYE*.





## References and bibliography

### 1. The Road to Quantum Astronomy

Alexander, G.

"Bose-Einstein and Fermi-Dirac interferometry in particle physics"  
Rep. Progr. Phys. **66**, 481-522 (2003)

Aleksandrov, E.B.; Golubev, Yu.M.; Lomakin, A.V.; Noskin, V.A.

"Intensity-fluctuation spectroscopy of optical fields with non-Gaussian statistics"  
Sov. Phys. Usp. **26**, 643-663 (1983) = Usp. Fiz. Nauk **140**, 547-582 (1983)

Aoki, T.

"Multidetector photon statistics"  
Phys. Rev. A **16**, 2432-2436 (1977)

Arecchi, F.T.

"Measurement of the statistical distribution of Gaussian and laser sources"  
Phys. Rev. Lett. **15**, 912-916 (1965)

Arndt, M.; Nairz, O.; Vos-Andreae, J.; Keller, C.; der Zouw, G.V.; Zeilinger, A.

"Wave-particle duality of  $C_{60}$  molecules"  
Nature **401**, 680-682 (1999)

Aspect, A.; Grangier, P.; Roger, G.

"Experimental realization of the Einstein-Podolsky-Rosen-Bohm Gedankenexperiment: A new violation of Bell's inequalities"  
Phys. Rev. Lett. **49**, 91-94 (1982)

Bachor, H.-A.; Ralph, T.C.

"A Guide to Experiments in Quantum Optics"  
Wiley-VCH (2004)

Barakat, R.; Blake, J.

"Theory of photoelectron counting statistics: An essay"  
Phys. Rep. **60**, 225-340 (1980)

Basini, G.; Cappozziello, S.; Longo, V.

"Black holes as parts of entangled systems"  
Astron. Nachr. **324**, 275-279 (2003)

Becker, W.; Zubairy, M.S.

"Photon statistics of a free-electron laser"  
Phys. Rev. A **25**, 2200-2207 (1982)

Bell, J.S.

"On the Einstein-Podolsky-Rosen paradox"  
Physics **1**, 195 (1964)

Blake, G.D.; Scarl, D.

"Two-photon correlations in amplified laser light"  
Phys. Rev. A **19**, 1948-1953 (1979)

Boal, D.H.; Gelbke, C.-K.; Jennings, B.K.

"Intensity Interferometry in Subatomic Physics"  
Rev. Mod. Phys. **62**, 553-602 (1990)

Bohr, N.

"*Can quantum-mechanical description of physical reality be considered complete?*"  
Phys.Rev. **48**, 696-702 (1935)

Born, M.; Wolf, E.

"*Principles of Optics: Electromagnetic theory of propagation, interference and diffraction of light*"  
Cambridge Univ.Press (1999) [BF]

Bowler, M.G.

...

Particle World 2, No.1, 1-..., (1991)

Degiorgio, V.; Lastovka, J.B.

"*Intensity-correlation spectroscopy*"  
Phys.Rev.A **4**, 2033-2050 (1971)

Dirac, P.A.M.

"*The Principles of Quantum Mechanics*"  
Oxford Univ.Press (1958)

Dravins, D.

"*Astrophysics on its shortest timescales*"  
ESO Messenger No. **78**, 9-19 (1994)

Einstein, A.

...

Berlin.Ber., 3-... (1924)

Einstein, A.

...

Berlin.Ber., 261-... (1925)

Einstein, A.; Podolsky, B.; Rosen, N.

"*Can quantum-mechanical description of physical reality be considered complete?*"  
Phys.Rev., **47**, 777-780 (1935)

Feder, ...

"*Fractals*"  
Springer 1988

Gil, J.

"*Fluctuations of pulsar emission with sub-microsecond time-scales*"  
ApSS **110**, 293-296 (1985)

Glauber, R.J.

"*The quantum theory of optical coherence*"  
Phys.Rev. **130**, 2529-2539 (1963a)

Glauber, R.J.

"*Coherent and incoherent states of the radiation field*"  
Phys.Rev. **131**, 2766-2788 (1963b)

Glauber, R.J.

"*Optical coherence and photon statistics*"  
in C.DeWitt, A.Blandin, C.Cohen-Tannoudji, eds. *Quantum Optics and Electronics*,  
Gordon and Breach, pp.65-185 (1965)

Glauber, R.J.

"*Quantum Theory of Coherence*"  
in S.M.Kay, A.Maitland, eds. *Quantum Optics*, Academic Press, pp.53-125 (1970)

- Hanbury Brown, R.  
"The Intensity Interferometer"  
Taylor & Francis (1974)
- Hanbury Brown, R.  
"Photons, Galaxies and Stars" (selected papers)  
Indian Academy of Sciences, Bangalore (1985)
- Hanbury Brown, R.; Davis, J.; Allen, R.L.  
"The stellar interferometer at Narrabri, I. A. description of the instrument and the observational procedure"  
MNRAS **137**, 375-392 (1967)
- Hanbury Brown, R.; Davis, J.; Allen, L.R.; Rome, J.M.  
"The stellar interferometer at Narrabri Observatory-II. The angular diameters of 15 stars"  
MNRAS **137**, 393-417 (1967)
- Hanbury Brown, R.; Twiss, R.Q.  
"Correlation between photons in two coherent beams of light"  
Nature **177**, 27-29 (1956)
- Hanbury Brown, R.; Twiss, R.Q.  
"A test of a new type of stellar interferometer on Sirius"  
Nature **178**, 1046-1048 (1956)
- Hanbury Brown, R., Twiss, R.Q.  
"Interferometry of the intensity fluctuations in light III"  
Proc. Roy. Soc. London, Ser. A, **248**, 199-221 (1958)
- Hankins, T.H.; Kern, J.S.; Weatherall, J.C.; Eilek, J.A.  
"Nanosecond radio bursts from strong plasma turbulence in the Crab pulsar"  
Nature, **422**, 141-143 (2003)
- Heisenberg, W.  
"Physical Principles of Quantum Theory",  
Dover, pp.95-101 (1930)
- Heitler, W.  
"The Quantum Theory of Radiation"  
Dover, pp.401-404 (1954)
- Hughes, A.J.; Jakeman, E.; Oliver, C.J.; Pike, E.R.  
"Photon-correlation spectroscopy: Dependence of linewidth error on normalization, clip level, detector area, sample time and count rate"  
J. Phys. A: Math., Nucl. Gen, **6**, 1327-1336 (1973)
- Jakeman, E.  
"Statistical accuracy in the digital autocorrelation of photon counting fluctuations"  
J. Phys. A: Gen. Phys. **3**, L55-L59 (1970)
- Jakeman, E.  
"The effect of heterodyne detection on the statistical accuracy of optical linewidth measurements"  
J. Phys. A: Gen. Phys. **5**, L49-L52 (1972); Corrigendum *ibid.* **5**, 1738 (1972)
- Johansson, S.; Letokhov, V.S.  
"Possibility of measuring the width of narrow Fe II astrophysical laser lines in the vicinity of Eta Carinae by means of Brown-Twiss-Townes heterodyne correlation interferometry"  
New Astron. **10**, 361-369 (2005) = astro-ph/0501246

Kiesel, H.; Renz, A.; Hasselbach, F.

"*Observation of Hanbury Brown-Twiss anticorrelations for free electrons*"  
Nature **418**, 392-394 (2002)

Kikkawa, A.; Ohkubo, K.; Suzuki, N.

"*Spectral linewidth and time interval distribution of photoelectric pulses*"  
Japan J. Appl. Phys. **14**, Suppl.14-1, 97-98 (1975)

Kimble, K.; Dagenais, M.; Mandel, L.

"*Photon bunching in resonance fluorescence*"  
Phys. Rev. Lett. **39**, 691 (1977)

Klein, R. I.; Arons, J.; Jernigan, G.; Hsu, J. J.-L.

"*Photon bubble oscillations in accretion-powered pulsars*"  
ApJ **457**, L85-L89 (1996)

Koppel, D. E.

"*Statistical accuracy in fluorescence correlation spectroscopy*"  
Phys. Rev. A **10**, 1938-1945 (1974)

Krichevsky, O.; Bonnet, G.

"*Fluorescence correlation spectroscopy: the technique and its applications*"  
Rep. Prog. Phys. **65**, 251-297 (2002)

Lavrinovich, N. N.; Letokhov, V. S.

"*The possibility of the laser effect in stellar atmospheres*"  
Sov. Phys. - JETP **40**, 800-805 (1975) = Zh. Eksp. Teor. Fiz. **67**, 1609-1620 (1974)

Lavrinovich, N. N.; Letokhov, V. S.

"*Detection of narrow "laser" lines masked by spatially inhomogeneous broadening in radiation emitted from stellar atmospheres*"  
Sov. J. Quantum Electron. **6**, 1061-1064 (1976) = Kvantovaya Elektron. **3**, 1948-1954 (1976)

Lim, T.-S.; Chern, J.-L.; Otsuka, K.

"*Higher-order photon statistics of single-mode laser diodes and microchip solid-state lasers*"  
Opt. Lett. **27**, 2197-2199 (2002).

Lorusso, G. F.; Capozzi, V.; Minafra, A.

"*Experimental photon statistics of multiscattered light*"  
Phys. Rev. E **49**, 3531-3534 (1994)

Loudon, R.

"*Non-classical effects in the statistical properties of light*"  
Rep. Prog. Phys. **43**, 913-949 (1980)

Loudon, R.

"*The Quantum Theory of Light*"  
3<sup>rd</sup> ed., Oxford Univ. Press (2000)

Mandel, L.

"*Photoelectric correlations and fourth order coherence properties of optical fields*"

In M. A. Machado, L. M. Narducci, eds.: *Optics in Four Dimensions*,  
American Inst. Phys., pp. 178-194 (1981)

Mandel, L.; Wolf, E.

"*Coherence properties of optical fields*"  
Rev. Mod. Phys. **37**, 231-287 (1965)

- Mandel, L.; Wolf, E.  
"Optical Coherence and Quantum Optics"  
Cambridge Univ. Press (1995)
- McDermott, P.N.; van Horn, H.M.; Hansen, C.J.  
"Nonradial oscillations of neutron stars"  
ApJ **325**, 725-748 (1988)
- Meystre, P.; Sargent, M.  
"Elements of Quantum Optics"  
Springer (1990)
- Meystre, P.; Walls, D.F., eds.  
"Nonclassical Effects in Quantum Optics"  
American Inst. Phys. (1991)
- Nash, P.J.; King, T.A.  
"A heterodyne photon correlation spectrometer of advanced design"  
J. Phys. E: Sci. Instrum. **18**, 319-327 (1985)
- Oliver, C.J.  
"The extraction of spectral parameters in photon-correlation spectroscopy"  
Adv. Phys. **27**, 387-435 (1978)
- Peřina, J., ed.  
"Selected Papers on Photon Statistics and Coherence in Nonlinear Optics"  
SPIE MS **39** (1991)
- Phillips, D.T.; Kleiman, H.; Davis, S.P.  
"Intensity-correlation linewidth measurement"  
Phys. Rev. **153**, 113-115 (1967)
- Pike, E.R.  
"Optical spectroscopy in the frequency range  $1-10^8$  Hz"  
Rev. Phys. Techn. **1**, 180-194 (1970)
- Pike, E.R.  
"Photon correlation spectroscopy"  
in R.A. Smith, ed. "Very High Resolution Spectroscopy", Chap. 3, pp. 51-73,  
Academic Press (1976)
- Purcell, E.M.:  
[On the paper "Correlation between photons in two coherent beams of light" by  
R. Hanbury Brown and R.Q. Twiss]  
Nature **178**, 1447-1449 (1956)
- Rebolledo, M.A.; Lopez, R.J.  
"Espectroscopia de alto poder resultativo mediante estadística de fotones"  
Opt. Pura y Aplicada **10**, 223-230 (1977)
- Saleh, B.A.  
"Statistical accuracy in estimating parameters of the spatial coherence function  
by photon counting techniques"  
J. Phys. A: Math. Nucl. Gen. **6**, 980-986 (1973)
- Saleh, B.A.  
"Photoelectron Statistics"  
Springer (1978)
- Saleh, B.E.A.; Cardoso, M.F.  
"The effect of channel correlation on the accuracy of photon counting digital  
autocorrelators"  
J. Phys. A: Math. Nucl. Gen. **6**, 1897-1909 (1973)

Singh, M.

"Higher-order photon counting statistics of Gaussian-Lorentzian light"  
Optica Acta **31**, 1293-1305 (1984)

Soglasnov, V.A.; Popov, M.V.; Bartel, N.; Cannon, W.; Novikov, A.Yu.;  
Kondratiev, V.I.; Altunin, V.I.

"Giant pulses from PSR B1937+21 with widths  $\leq 15$  Nanoseconds and  $T_b \geq 5 \times 10^{39}$  K,  
the highest brightness temperature observed in the Universe"  
ApJ **616**, 439-451 (2004)

Srinivasan, S.K.; Sukavanam, S.

"Photocount statistics of Gaussian light of arbitrary spectral profile"  
J.Phys.A **5**, 682-694 (1972)

Twiss, R.Q.; Little, A.G.

"The detection of time-correlated photons by a coincidence counter"  
Austral.J.Phys. **12**, 77 (1959)

Vannucci, G.; Teich, M.C.

"Computer simulation of superposed coherent and chaotic radiation"  
Appl.Opt. **19**, 548-553 (1980)

Van Rijswijk, F.C.; Smith, U.L.

"Fluctuations in doubly scattered laser light"  
Physica **83A**, 121-142 (1976)

Vogel, W.; Welsch, D.-G.

"Lectures in Quantum Optics"  
Akademie-Verlag (1994)

Walls, D.F.; Milburn, G.J.

"Quantum Optics"  
Springer (1994)

Weihs, G.; Jennewein, T.; Simon, C.; Weinfurter, H.; Zeilinger, A.

"Violation of Bell's inequality under strict Einstein locality conditions"  
Phys.Rev.Lett. **81**, 5039-5043 (1998)

Wheeler, J.A.: "Mathematical Foundations of Quantum Mechanics", Academic Press,  
pp.9-48 (1978)

Zeilinger, A.

"Fundamentals of quantum information"  
Physics World, ...-... (1998)

Zou, X.T.; Mandel, L.

"Photon antibunching and sub-Poissonian photon statistics"  
Phys.Rev.A **41**, 475-476 (1990)

## 2. Quantum Phenomena in Astronomy

Abraham, N.B.; Huang, J.C.; Kranz, D.A.; Rockower, E.B.

"Amplified-spontaneous-emission intensity fluctuations"  
Phys.Rev.A **24**, 2556-2566 (1981)

Allen, L.; Peters, G.I.

"Amplified spontaneous emission and external signal amplification in an inverted  
medium"  
Phys.Rev.A, **8**, 2031-2047 (1973)

- Basini,G.; Capozziello,S.; Longo,G.  
"Black holes as parts of entangled systems"  
Astr.Nachr. **324**, 275-279 (2003)
- Basini,G.; Capozziello,S.; Longo,G.  
"Gamma ray bursts as a signature for entangled gravitational systems"  
Astropart.Phys. **20**, 457-466 (2003)
- Battersby,S.  
"Twisting the light away"  
New Scientist **182**, No.2451 pp.36-40 (12 June 2004)
- Bautista,M.A.; Gull,T.R.; Ishibashi,K.; Hartman,H.; Davidson,K.:  
"Excitation of SrII lines in Eta Carinae"  
MNRAS **331**, 875-879 (2002)
- Benford,G.; Tzach,D.  
"Coherent synchrotron emission observed: Implications for radio astronomy"  
MNRAS **317**, 497-500 (2000)
- Beth,R.A.  
"Mechanical detection and measurement of the angular momentum of light"  
Phys.Rev. **50**, 115-125 (1936)
- Bingham,R.; Kellett,B.J.; Cairns,R.A.; Tonge,J.; Mendonça,J.T.  
"Cyclotron maser radiation from astrophysical shocks"  
ApJ **595**, 279-284 (2003)
- Bowen,I.S.  
"The origin of the chief nebular lines"  
PASP **39**, 295-297 (1927)
- Bowen,I.S.  
"The spectrum and composition of the gaseous nebulae"  
ApJ **81**, 1-16 (1935)
- Bowen,I.S.  
"Excitation by line coincidence"  
PASP **59**, 196-198 (1947)
- Burdyuzha,V.V.; Shelepin,L.A.  
"The possibility of an X-ray recombination laser in hydrogen-like ions for the conditions of accreting neutron stars"  
AdSpR **10**, 163-165 (1990)
- Castor,J.I.; Nussbaumer,H.  
"On the excitation of C III in Wolf-Rayet envelopes"  
MNRAS **155**, 293-304 (1972)
- Chesneau,O.; Min,M.; Herbst,T.; Waters,L.B.F.M.; Hillier,D.J.; Leinert,Ch.; de Koter,A.; Pascucci,I.; Jaffe,W.; Köhler,R.; Alvarez,C.; van Boekel,R.; Brandner,W.; Graser,U.; Lagrange,A.M.; Lenzen,R.; Morel,S.; Schöller,M.  
"The sub-arcsecond dusty environment of Eta Carinae"  
A&A **435**, 1043-1061 (2005)
- Cohen,M.; Biegging,J.H.; Welch,W.J.; Dreher,J.W.  
"The binary system MWC 349"  
ApJ **292**, 249-256 (1985)
- Cooper,J.; Ballagh,R.J.; Burnett,K.; Hummer,D.G.  
"On redistribution and the equations for radiative transfer"  
ApJ **260**, 299-316 (1982)

- Cordes, J.M.; Bhat, N.D.R.; Hankins, T.H.; McLaughlin, M.A.; Kern, J.  
"The Brightest Pulses in the Universe: Multifrequency observations of the Crab pulsar's giant pulses"  
ApJ **612**, 375-388 (2004)
- Cox, P.; Martin-Pintado, J.; Bachiller, R.; Bronfman, L.; Cernicharo, J.; Nyman, L.-Å.; Roelfsema, P.R.  
"Millimeter recombination lines towards  $\eta$  Carinae"  
A&A **295**, L39-L42 (1995)
- Danchi, W.C.; Tuthill, P.G.; Monnier, J.D.  
"Near-infrared interferometric images of the hot inner disk surrounding the massive young star MWC 349A"  
ApJ **562**, 440-445 (2001)
- Das, B.; Giammichele, S.  
"Multivariate statistics of the intensity fluctuations of a heavily saturated amplified spontaneous emission and coupled-mode optical systems"  
J.Opt.A **4**, 57-65 (2002)
- Das Gupta, S.; Das Gupta, S.R.  
"Laser radiation in active amplifying media treated as a transport problem - Transfer equation derived and exactly solved"  
Ap&SS **184**, 77-142 (1991)
- Davidson, K.; Ebbets, D.; Johansson, S.; Morse, J.A.; Hamann, F.W.  
"HST/GHRS observations of the compact slow ejecta of Eta Carinae"  
AJ **113**, 335-345 (1997)
- Deming, D.; Espenak, F.; Jennings, D.; Kostiuik, T.; Mumma, M.; Zipoy, D.  
"Observations of the 10-micron natural laser emission from the mesospheres of Mars and Venus"  
Icarus **55**, 347-355 (1983)
- Deming, D.; Mumma, M.J.  
"Modeling of the 10-micron natural laser emission from the mesospheres of Mars and Venus"  
Icarus **55**, 356-368 (1983)
- DeNoyer, L.K.; Dodd, J.G.  
"Detecting saturation in astrophysical masers"  
Bull.AAS **14**, 638 (1982)
- Dravins, D.  
"Quantum-optical signatures of stimulated emission"  
in T.Gull et al. eds. *Eta Carinae & Other Mysterious Stars*, ASPC **242**, 339-345 (2001)
- Eichler, D.; Gedalin, M.; Lyubarsky, Y.  
"Coherent emission from magnetars"  
ApJ **578**, L121-L124 (2002)
- Elitzur, M.  
"Masers in the sky"  
Scient.Am. **272**, No.2, 52-58 (Feb.1995)
- Eriksson, M.; Veenhuizen, H.; Wahlgren, G.M.; Johansson, S.  
"Fe II fluorescence in symbiotic stars"  
Rev.Mex.Astron.Astrof.(Ser.Conf.) **21**, 132-136 (2004)
- Evans, N.J.; Hills, R.E., Rydbeck, O.E.H., Kollberg, E.  
"Statistics of the radiation from astronomical masers"  
Phys.Rev.A **6**, 1643-1647 (1972)



Falcke, H.; Melia, F.; Agol, E.

"Viewing the shadow of the black hole at the Galactic center"  
ApJ **528**, L13-L16 (2000)

Fang, L.Z.

"Stimulated recombination emission from rapidly cooling regions in an accretion disc and its application to SS 433"  
MNRAS **194**, 177-185 (1981)

Ferland, G.J.

"A masing [Fe XI] line"  
ApJS **88**, 49-52 (1993)

Fleishman, G.D.

"Effect of random inhomogeneities on electron cyclotron maser emission"  
ApJ **601**, 559-564 (2004)

Gahm, G.F., Lindgren, B., Lindroos, K.P.

"A compilation of fluorescent molecular lines originating in or around stellar objects with strong atomic emission lines"  
A&AS **27**, 277-283 (1977)

Ghosh, T.K., Das, A.K., Mukherjee, T.K., Mukherjee, P.K.

"The  $2p^53l$  configurations of highly stripped Ne-like ions: Possibility of X-ray laser emission"  
ApJ **452**, 949-953 (1995)

Gordon, M.A.; Holder, B.P.; Jisonna, L.J., Jr.; Jorgenson, R.A.; Strel'nitski, V.S.

"3 year monitoring of millimeter-wave radio recombination lines from MWC 349"  
ApJ **559**, 402-418 (2001)

Gray, M.D.; Bewley, S.L.

"Broad-band maser radiation and phase transport in the quantum and semi-classical treatment"  
MNRAS **344**, 439-447 (2003)

Greenhouse, M.A.; Feldman, U.; Smith, H.A.; Klapisch, M.; Bhatia, A.K.; Bar-Shalom, A.

"Infrared coronal emission lines and the possibility of their laser emission in Seyfert nuclei"  
ApJS **88**, 23-48 (1993); Erratum *ibid.* **99**, 743 (1995)

Hanbury Brown, R.

"The Intensity Interferometer", Taylor & Francis (1974)

Hankins, T.H.; Kern, J.S.; Weatherall, J.C.; Eilek, J.A.

"Nanosecond radio bursts from strong plasma turbulence in the Crab pulsar"  
Nature, **422**, 141-143 (2003)

Hartman, H.; Johansson, S.

"Ultraviolet fluorescence lines of Fe II observed in satellite spectra of the symbiotic star RR Telescopii"  
A&A **359**, 627-634 (2000)

Harwit, M.

"Photon orbital angular momentum in astrophysics"  
ApJ **597**, 1266-1270 (2003)

Heitler, W.

"The Quantum Theory of Radiation", 3<sup>rd</sup> ed.  
Clarendon Press (1954)

Hengel,C.; Kegel,W.H.

"Radiative transfer effects in hydrogen recombination masers"  
A&A **361**, 1169-1177 (2000)

Hofmann,K.H.; Weigelt,G.

"Speckle masking observations of  $\eta$  Carinae"  
A&A **203**, L21-L22 (1988)

Hofmann,K.H., Balega,Y., Ikhsanov,N.R., Miroshnichenko,A.S., Weigelt,G.

"Bispectrum speckle interferometry of the B[e] star MWC 349A"  
A&A **395**, 891-898 (2002)

Jacobson,T.; Liberati,S.; Mattingly,D.

"Astrophysical Bounds on Planck Suppressed Lorentz Violation"  
Lect.Notes Phys.,in press, 30 pp.; hep-ph/0407370 (2004)

Jefferies,J.T.

"Population inversion in the outer layers of a radiating gas"  
A&A **12**, 351-362 (1971)

Jenet,F.A.; Anderson,S.B.; Prince,T.A.

"The first detection of coherent emission from radio pulsars"  
ApJ **558**, 302-308 (2001)

Johansson,S.; Davidson,K.; Ebbets,D.; Weigelt,G.; Balick,B.; Frank,A.;

Hamann,F.; Humphreys,R.M.; Morse,J.; White,R.L.

"Is there a dichromatic UV laser in Eta Carinae?"

in P.Benvenuti, F.D.Macchetto & E.J.Schreier, eds. *Science with the Hubble Space Telescope-II*, 361-365 (1996)

Johansson,S.; Letokhov,V.S.

"Laser action in a gas condensation in the vicinity of a hot star"  
JETP Lett. **75**, 495-498 (2002) = Pis'ma Zh.Éksp.Teor.Fiz. **75**, 591-594 (2002)

Johansson,S.; Letokhov,V.S.: "Radiative cycle with stimulated emission from atoms and ions in an astrophysical plasma", Phys.Rev.Lett. **90**, 011101-1 - 011101-4 (2003a)

Johansson,S.; Letokhov,V.S.

"Astrophysical lasers with radiation pumping by accidental resonance"  
PASP **115**, 1375-1382 (2003b)

Johansson,S.; Letokhov,V.S.

"Anomalous Fe II spectral effects and high H I Ly-alpha temperature in gas blobs near Eta Carinae"

Astron.Lett. **30**, 58-63 (2004) = Pis'ma Astron.Zh. **30**, 67-73 (2004a)

Johansson,S.; Letokhov,V.S.

"Astrophysical lasers operating in optical Fe II lines in stellar ejecta of Eta Carinae"

A&A **428**, 497-509 (2004b)

Johansson,S.; Letokhov,V.S.

"Possibility of measuring the width of narrow Fe II astrophysical laser lines in the vicinity of Eta Carinae by means of Brown-Twiss-Townes heterodyne correlation interferometry"

New Astron. **10**, 361-369 (2005)

Johnson,M.A.; Betz,A.L.; McLaren,R.A.; Townes,C.H.; Sutton,E.C.

"Nonthermal 10 micron CO<sub>2</sub> emission lines in the atmospheres of Mars and Venus"  
ApJ **208**, L145-L148 (1976)

Johnson, M.A.; Betz, A.L.; Townes, C.H.

"10-micron heterodyne stellar interferometer"

Phys.Rev.Lett. **33**, 1617-1620 (1974)

Klimov, V.; Johansson, S.; Letokhov, V.S.

"The origin of the anomalous intensity ratio between very bright UV FeII lines and their satellites in gaseous condensations close to the star Eta Carinae"

A&A **385**, 313-327 (2002)

Kostiuk, T.; Mumma, M.J.

"Remote sensing by IR heterodyne spectroscopy"

Appl.Opt. **22**, 2644-2654 (1983)

Lavrinovich, N.N.; Letokhov, V.S.

"The possibility of the laser effect in stellar atmospheres"

Sov.Phys. - JETP **40**, 800-805 (1975) = Zh.Eksp.Teor.Fiz. **67**, 1609-1620 (1974)

Lavrinovich, N.N.; Letokhov, V.S.

"Detection of narrow "laser" lines masked by spatially inhomogeneous broadening in radiation emitted from stellar atmospheres"

Sov.J.Quantum Electron. **6**, 1061-1064 (1976) = Kvantovaya Elektron. **3**, 1948-1954 (1976)

Leach, J.; Padgett, M.J.; Barnett, S.M.; Franke-Arnold, S.; Courtial, V.

"Measuring the orbital angular momentum of a single photon"

Phys.Rev.Lett. **88**, 257901-1 (2002)

Lee, L.C.; Jokipii, J.R.

"Strong scintillations in astrophysics. III - The fluctuations in intensity"

ApJ **202**, 439-453 (1975)

Lekht, E.E.; Rudnitskii, G.M.; Franquelin, O.; Drouhin, J.-P.

"Statistical properties of the emission of OH maser sources"

Pis'ma Astron.Zh. **1**, 29-32. (1975) = Sov.Astron.Lett. **1**, 37-38 (1975)

Lerche, I.

"Scintillations in astrophysics. I - An analytic solution of the second-order moment equation"

ApJ **234**, 262-274 (1979a)

Lerche, I.

"Scintillations in astrophysics. II - An analytic solution of the fourth-order moment equation"

ApJ **234**, 653-668 (1979b)

Letokhov, V.S.

"Astrophysical lasers"

Quant.Electr. **32**, 1065-1079 (2002) = Kvant.Elektron. **32**, 1065-1079 (2002)

Lu, Y.; Zhang, S.N.

"Maser mechanism of optical pulsations from anomalous X-ray pulsar 4U 0142+61"

MNRAS **354**, 1201-1207 (2004)

Macháček, M.

"A quantum mechanical description of the transfer of radiation. I - The radiation processes"

Bull.Astron.Inst.Czechosl. **29**, 268-277 (1978)

Macháček, M.

"The quantum mechanical description of the transfer of radiation. II - The equation of transfer"

Bull.Astron.Inst.Czechosl. **30**, 23-28 (1979)

- Mair,A.; Vaziri,A.; Weihs,G.; Zeilinger,A.  
"Entanglement of the orbital angular momentum states of photons"  
Nature **412**, 313-316, 2001
- Martin-Pintado,J.; Bachiller,R.; Thum,C.; Walmsley,M.  
"A radio recombination line maser in MWC349"  
A&A **215**, L13-L16 (1989)
- Mashoon,B.  
"Scattering of electromagnetic radiation from a black hole"  
Phys.Rev.D **7**, 2807-2814 (1973)
- Melrose,D.B.  
"Coherent emission in AGN: A critique"  
Publ.Astron.Soc.Australia **19**, 24-38 (2002)
- Menegozzi,L.N.; Lamb,W.E.  
"Laser amplification of incoherent radiation"  
Phys.Rev.A **17**, 701-732 (1978)
- Menzel,D.H.  
"Physical processes in gaseous nebulae. I."  
ApJ **85**, 330-339 (1937)
- Menzel,D.H.  
"Laser Action in Non-LTE Atmospheres"  
in H.G.Groth, P.Wellmann, eds. *Spectrum formation in stars with steady-state extended atmospheres*, Nat.Bur.Stds.Spec.Publ. **332**, 134-137 (1970)
- Mumma,M.J.; Buhl,D.; Chin,G.; Deming,D.; Espenak,F.; Kostiuik,T.  
"Discovery of natural gain amplification in the 10-micrometer carbon dioxide laser bands on Mars - A natural laser"  
Science, **212**, 45-49 (1981)
- Ojaste,J.; Sapar,A.  
"Statistics of photons and its recording"  
Publ.Tartu Astrof.Obs. **47**, 93-102 (1979),
- Padgett,M.; Courtial,J.; Allen,L.  
"Light's orbital angular momentum"  
Phys.Today, **57**, May 2004; 35-40 (2004)
- Paschenko,M.; Rudnitskij,G.M., Slysh,V.I., Fillit,R.  
"A measurement of the one-dimensional distribution function of the signal from some Galactic OH radio sources"  
Astr.Tsirk. No.626 [3 pp.] (1971)
- Peng,J.; Pradhan,A.K.  
"Laser action in far-infrared astrophysical sources"  
ApJ **432**, L123-L126 (1994)
- Quirrenbach,A.; Frink,S.; Thum,C.  
"Spectroscopy of the peculiare emission line star MWC349"  
in T.R.Gull, S.Johannson, & K.Davidson, eds. *Eta Carinae and other mysterious stars: The hidden opportunities of emission spectroscopy*", ASPC **242**, 183-186 (2001)
- Saha,S.K.  
"Modern optical astronomy: technology and impact of interferometry"  
Rev.Mod.Phys. **74**, 551-600 (2002)

Sakhibullin, N.A.; Shimansky, V.V.

"Non-LTE effects for NaI lines in X-ray illuminated stellar atmospheres"  
Astron.Lett. **26**, 309-318 (2000) = Pis'ma Astr.Zh. **26**, 369-379 (2000)

Sapar, A.

"Transfer equation for the density matrix of phase space cell occupation number states"  
Publ.Tartu Astrof.Obs. **46**, 17-32 (1978)

Scappaticci, G.A.; Watson, W.D.

"Radiative instabilities in three-dimensional astrophysical masers"  
ApJ **448**, 862-864 (1995)

Schilke, P.; Mehringer, D.M.; Menten, K.M.

"A submillimeter HCN laser in IRC +10216"  
ApJ **528**, L37-L40 (2000)

Schmid, H.M.

"Identification of the emission bands at  $\lambda\lambda$  6830, 7088"  
A&A **211**, L31-L34 (1989)

Shang, H.; Glassgold, A.E.; Shu, F.H.; Lizano, S.

"Heating and ionization of X-winds"  
ApJ **564**, 853-876 (2002)

Shearer, A.; Stappers, B.; O'Connor, P.; Golden, A.; Strom, R.; Redfern, M.; Ryan, O.

"Enhanced optical emission during Crab giant radio pulses"  
Science, **301**, 493-495 (2003)

Shved, G.M.; Ogibalov, V.P.

"Natural population inversion for the CO<sub>2</sub> vibrational states in Earth's atmosphere"  
J.Atmos.Solar-Terr.Phys. **62**, 993-997 (2000)

Smith, H.A.

"Population inversions in ions of astrophysical interest"  
ApJ **158**, 371-383 (1969)

Smith, H.A.; Larson, H.P.; Fink, U.

"The spectrum of the Becklin-Neugebauer source in Orion from 3.3 to 5.5 microns"  
ApJ **233**, 132-139 (1979)

Smith, H.A.; Strel'nitski, V.; Miles, J.W.; Kelly, D.M.; Lacy, J.H.

"Mid-infrared hydrogen recombination line emission from the maser star MWC 349A"  
**AJ** **114**, 2658-2663 (1997)

Smits, J.M.; Stappers, B.W.; Macquart, J.-P.; Ramachandran, R.; Kuijpers, J.

"On the search for coherent radiation from radio pulsars"  
A&A **405**, 795-801 (2003)

Soglasnov, V.A.; Popov, M.V.; Bartel, N.; Cannon, W.; Novikov, A.Yu.;

Kondratiev, V.I.; Altunin, V.I.

"Giant pulses from PSR B1937+21 with widths  $\leq 15$  nanoseconds and  $T_b \geq 5 \times 10^{39}$  K, the highest brightness temperature observed in the Universe"  
ApJ **616**, 439-451 (2004)

Sorokin, P.P.; Glow'nia, J.H.

"Lasers without inversion (LWI) in Space: A possible explanation for intense, narrow-band, emissions that dominate the visible and/or far-UV (FUV) spectra of certain astronomical objects"  
A&A **384**, 350-363 (2002)

Spaans, M.; Norman, C.A.

"Hydrogen recombination line masers at the epochs of recombination and reionization"

ApJ **488**, 27-34 (1997)

Stepanova, G.I.; Shved, G.M.

"The natural 10- $\mu$  CO<sub>2</sub> laser in the atmospheres of Mars and Venus"

Sov.Astron.Lett. **11**, 162-163 (1985) = Pis'ma Astron.Zh. **11**, 390-394 (1985)

Streater, A.; Cooper, J.; Rees, D.E.

"Transfer and redistribution of polarized light in resonance lines. I - Quantum formulation with collisions"

ApJ **335**, 503-515 (1988)

Strel'nitski, V.

"Masers, lasers and the interstellar medium"

Ap&SS **252**, 279-287 (1997)

Strel'nitski, V.; Haas, M.R.; Smith, H.A.; Erickson, E.F.; Colgan, S.W.J.; Hollenbach, D.J.

"Far-Infrared Hydrogen Lasers in the Peculiar Star MWC 349A"

Science, **272**, 1459-1461 (1996)

Strel'nitski, V.S.; Ponomarev, V.O.; Smith, H.A.

"Hydrogen masers. I. Theory and prospects"

ApJ **470**, 1118-1133 (1996a)

Strel'nitski, V.S.; Smith, H.A.; Ponomarev, V. O.

"Hydrogen masers. II. MWC349A"

ApJ **470**, 1134-1143 (1996b)

Stupp, A.

"Electron-cyclotron maser observable modes"

MNRAS **311**, 251-268 (2000)

Swartzlander, G.A.

"Peering into darkness with a vortex spatial filter"

Opt.Lett. **26**, 497-499 (2001)

Talbot, V.

"Laser action in recombining plasmas"

MSc thesis, University of Ottawa (1995)

Tamburini, F.; Umbriaco, G.; Anzolin, G.; Barbieri, C.; Bianchini, A.

"FrogEye, the quantum coronagraphic mask. The photon orbital angular momentum and its applications to astronomy"

proc. XLIX<sup>th</sup> meeting Italian Astron.Soc. (2005); astro-ph/0505564

Teukolsky, S.A.

"Rotating black holes: Separable wave equations for gravitational and electromagnetic perturbations"

Phys.Rev.Lett. **29**, 1114-1118 (1972)

Thackeray, A.D.

"The emission line  $\lambda$  4511 in late-type variables"

ApJ **81**, 467-473 (1935)

Thum, C.; Martín-Pintado, J.; Quirrenbach, A.; Matthews, H.E.

"Infrared lasers in the circumstellar disk of MWC 349"

A&A **333**, L63-L66 (1998)

Thum, C.; Morris, D.

"A strong magnetic field in the disk of MWC 349"  
A&A **344**, 923-929 (1999)

Thum, C.; Strel'nitski, V.S.; Mart n-Pintado, J.; Matthews, H.E.; Smith, H.A.

"Hydrogen recombination beta-lines in MWC 349"  
A&A **300**, 843-850 (1995)

Townes, C.H.; Sutton, E.C.; Storey, J.W.V.

"Infrared heterodyne interferometry"  
in F.Pacini, W.Richter, R.N.Wilson, eds. *ESO Conference, Optical Telescopes of the Future*, pp.409-426 (1978)

Trigilio, C.; Leto, P.; Leone, F.; Umana, G.; Buemi, C.

"Coherent radio emission from the magnetic chemically peculiar star CU Virginis"  
A&A **362**, 281-288 (2000)

Trigilio, C.; Leto, P.; Umana, G.; Leone, F.; Buemi, C.S.

"A three-dimensional model for the radio emission of magnetic chemically peculiar stars"  
A&A **418**, p.593-605 (2004)

Uscinski, B.J.

"The Elements of Wave Propagation in Random Media"  
McGraw-Hill (1977)

Varshni, Y.P.; Lam, C.S.

"Laser action in stellar envelopes"  
Ap&SS **45**, 87-97 (1976)

Varshni, Y.P.; Nasser, R.M.

"Laser action in stellar envelopes. II - He I"  
Ap&SS **125**, 341-360 (1986)

Vaziri, A.; Weihs, G.; Zeilinger, A.

"Superpositions of the orbital angular momentum for applications in quantum experiments"  
J.Opt.B **4**, S47-S51 (2002)

Verga, A.D.

"Irreversible thermodynamics in a radiating fluid"  
ApJ **260**, 286-298 (1982)

Weatherall, J.C.

"A relativistic-plasma Compton maser"  
ApJ **559**, 196-200 (2001)

Weenen, J.

"On physical processes in Wolf-Rayet stars. Paper 2: Wolf-Rayet stars and the hypothesis of thermal ionization"  
Bull.Astron.Inst.Netherlands, **11**, 176-179 (1950)

West, D.K.

[Conference discussion on possible laser action in C III  $\lambda$  1909 Å line of  $\gamma$  Vel]  
in K.B.Gebbie, R.N.Thomas, eds. *Wolf-Rayet Stars*, Nat.Bur.Stds.Spec.Publ. **307**, 221-227 (1968)

Wiersma, D.

"Laser physics: The smallest random laser"  
Nature **406**, 132-133 (2000)

Wilkinson, P.N.; Kellermann, K.I.; Ekers, R.D.; Cordes, J.M.; Lazio, T.J.W.  
"The exploration of the unknown"  
New Astron.Rev. **48**, 1551-1563 (2004)

Wu, Y.C.  
"Nonlinear optics in celestial natural maser-laser environment"  
ApSS **209**, 113-121 (1993)

### 3. Observational High-Speed Astrophysics

Abramowicz, M.A.; Kluźniak, W.  
"A precise determination of black hole spin in GRO J1655-40"  
A&A **374**, L19-L20 (2001)

Beskin, G.M.; Neizvestnyi, S.I.; Pimonov, A.A.; Plakhotnichenko, V.L.;  
Shvartsman, V.F.  
"The minimum optical variability time scale of V1341 Cygni (Cygnus X-2) measured  
with the 6-meter telescope"  
Sov.Astron.Lett. **5**, 271-274 = Pis'ma Astron.Zh. **5**, 508-513 (1979)

Boccaletti, A., Labeyrie, A., Ragazzoni, R.  
"Preliminary results of dark-speckle stellar coronagraphy"  
A&A **338**, 106-110 (1998)

Chakrabarty, D.  
"High-speed optical photometry of the ultracompact X-ray binary 4U 1626-67"  
ApJ **492**, 342-351 (1998)

Chakrabarty, D.; Morgan, E.H.; Muno, M.P.; Galloway, D.K.; Wijnands, R.; van der  
Klis, M.; Markwardt, C.B.  
"Nuclear-powered millisecond pulsars and the maximum spin frequency of neutron  
stars"  
Nature **424**, 42-44 (2003)

Cooray, A.  
"Kuiper belt object sizes and distances from occultation observations"  
ApJ **589**, L97-L100 (2003)

Covault, C.E.  
"Large area solar power heliostat arrays for OSETI"  
in S.A.Kingsley, R.Bhatal, eds. *The Search for Extraterrestrial Intelligence  
(SETI) in the Optical Spectrum III*, SPIE Proc. **4273**, 161-172 (2001)

Dravins, D.; Lindegren, L.; Mezey, W.; Young, A.T.  
"Atmospheric intensity scintillation of stars. I. Statistical distributions and  
temporal properties"  
PASP **109**, 173-207 (1997a)

Dravins, D.; Lindegren, L.; Mezey, W.; Young, A.T.  
"Atmospheric intensity scintillation of stars. II. Dependence on optical  
wavelength"  
PASP **109**, 725-737 (1997b)

Dravins, D.; Lindegren, L.; Mezey, W.; Young, A.T.  
"Atmospheric intensity scintillation of stars. III. Effects for different  
telescope apertures"  
PASP **110**, 610-633 (1998); erratum *ibid.* **110**, 1118 (1998)



- Ford, E.C.; van der Klis, M.  
"Strong correlation between noise features at low frequency and the kilohertz quasi-Periodic oscillations in the X-ray binary 4U 1728-34"  
ApJ **506**, L39-L42 (1998)
- Frank, J.; King, A.; Raine, D.J.  
"Accretion Power in Astrophysics", 3<sup>rd</sup> ed.  
Cambridge Univ. Press (2002)
- Franzen, A.; Gillessen, S.; Hermann, G.; Hinton, J.  
"Optical observations of the Crab pulsar using the first H.E.S.S. Cherenkov telescope"  
in *The 28<sup>th</sup> International Cosmic Ray Conference*, Universal Academy Press (2003)
- Gies, D.R.; McKibben, W.P.; Kelton, P.W.; Opal, C.B.; Sawyer, S.  
"Time-resolved H-alpha spectroscopy of the Be star Pleione during a lunar occultation"  
AJ **100**, 1601-1609 (1990)
- Grebenev, S.A.; Syunyaev, R.A.; Pavlinskii, M.N.; Dekhanov, I.A.  
"Detection of quasiperiodic oscillations of X-rays from the black-hole candidate GX:339-4"  
Sov. Astron. Lett. **17**, 413-415 (1991) = Pis'ma Astron. Zh. **17**, 985-990 (1991)
- Horne, K.; Peterson, B.M.; Collier, S.J.; Netzer, H.  
"Observational Requirements for High-Fidelity Reverberation Mapping"  
PASP **116**, 465-476 (2004)
- Imamura, J.N.; Kristian, J.; Middleditch, J.; Steiman-Cameron, T.Y.  
"The 8 second optical quasi-periodic oscillations in GX 339-4"  
ApJ **365**, 312-316 (1990)
- Imamura, J.N.; Steiman-Cameron, T.Y.; Middleditch, J.  
"A possible 1.13 millisecond periodicity in GX 339-4"  
ApJ **314**, L11-L13 (1987)
- Kato, S.; Fukue, J.; Mineshige, S. (eds.)  
"Black-Hole Accretion Disks"  
Kyoto University Press (1998)
- Labeyrie, A.  
"Images of exo-planets obtainable from dark speckles in adaptive optics"  
A&A **298**, 544-548 (1995)
- Lewin, W.H.G.; van Paradjis, J.; Taam, R.E.  
"X-ray bursts"  
Space Sci. Rev. **62**, 223-389 (1993)
- Malzac, J.; Dumont, A.M.; Mouchet, M.  
"Full radiative coupling in two-phase models for accreting black holes"  
A&A **430**, 761-769 (2005)
- Mauche, C.W.; Liedahl, D.A.; Mathiesen, B.F.; Jimenez-Garate, M.A.; Raymond, J.C.  
"Reprocessing of soft X-ray emission lines in black hole accretion disks"  
ApJ **606**, 168-172 (2004)
- Marković, D.  
"Bound near-equatorial orbits around neutron stars"  
astro-ph/0009450 (2000)

Miller, M.C.; Lamb, F.K.; Psaltis, D.

"Sonic-point model of kilohertz quasi-periodic brightness oscillations in low-mass X-ray binaries"  
ApJ **508**, 791-830 (1998)

Morsink, S.M.; Stella, L.

"Relativistic precession around rotating neutron stars: Effects due to frame dragging and stellar oblateness"  
ApJ **513**, 827-844 (1999)

Motch, C.; Ricketts, M.J.; Page, C.G.; Ilovaisky, S.A.; Chevalier, C.

"Simultaneous X-ray/optical observations of GX339-4 during the May 1981 optically bright state"  
A&A **119**, 171-176 (1983)

O'Brien, K.; Horne, K.; Hynes, R.I.; Chen, W.; Haswell, C.A.; Still, M.D.

"Echoes in X-ray binaries"  
MNRAS **334**, 426-434 (2002)

Oña-Wilhelmi, E.; Cortina, J.; de Jager, O.C.; Fonseca, V.

"Determination of the night sky background around the Crab pulsar using its optical pulsation"  
Astropart.Phys. **22**, 95-102 (2004)

Pedersen, H.; Lub, J.; Inoue, H.; Koyama, K.; Makishima, K.; Matsuoka, M.; Mitsuda, K.; Murakami, T.; Oda, M.; Ogawara, Y.; Ohashi, T.; Shibazaki, N.; Tanaka, Y.; Hayakawa, S.; Kunieda, H.; Makino, F.; Masai, K.; Nagase, F.; Tawara, Y.; Miyamoto, S.; Tsunemi, H.; Yamashita, K.; Kondo, I.; Jernigan, J.G.; van Paradijs, J.; Beardsley, A.; Cominsky, L.; Doty, J.; Lewin, W.H.G.

"Simultaneous optical and X-ray bursts from 4U/MXB 1636-53"  
ApJ **263**, 325-339 (1982)

Radick, R.R.; Africano, J.L.

"The angular diameter of Aldebaran at 8540 Å"  
AJ **86**, 906-908 (1981)

Remillard, R.A.; Morgan, E.H.; McClintock, J.E.; Bailyn, C.D.; Orosz, J.A.

"RXTE observations of 0.1-300 HZ quasi-periodic oscillations in the microquasar GRO J1655-40"  
ApJ **522**, 397-412 (1999)

Ribak, E.N.; Laor, A.; Faiman, D.; Biryukov, S.; Brosch, N.

"Converting PETAL, the 25 m solar collector, into an astronomical research facility"  
in W.A. Traub, ed. *Interferometry for Optical Astronomy II*, SPIE Proc. **4838**, 1031-1036 (2003)

Richichi, A.

"Lunar occultations of stars with exo-planets"  
A&A **397**, 1123-1127 (2003)

Richichi, A.

"Combining optical interferometry with Lunar occultations"  
in R.W. Hidlitch, H. Hensberge, K. Pavlovsk, eds. *Spectroscopically and Spatially Resolving the Components of the Close Binary Stars*, ASPC **318**, 148-156 (2004a)

Richichi, A.

"Interferometry and Lunar occultations: Status and prospects of ground-based milliarcsecond resolution observations"  
in C. Allen, C. Scarfe, eds. "The Environment and Evolution of Double and Multiple Stars", IAU Coll. 191. Rev. Mex. Astron. Astrof. (Ser. Conf.) **21**, 247-250 (2004b)

Roques, F.; Moncuquet, M.

"A detection method for small Kuiper belt objects: The search for stellar occultations"

Icarus **147**, 530-544 (2000)

Schmidtke, P.C.; Africano, J.L.; Quigley, R.

"KPNO Lunar occultation summary. II"

AJ **97**, 909-916 (1989)

Shvartsman, V.F.; Beskin, G.M.; Mitronova, S.N.; Neizvestnyi, I.S.;

Plakhotnichenko, V.L.

"A0620-00 - A search for ultrafast optical variability and UBVR photometry"

Sov.Astron.Lett. **15**, 252-255 = Pis'ma Astron.Zh **15**, 590-596 (1989a)

Shvartsman, V.F.; Beskin, G.M.; Pustil'nik, L.A.

"High time resolution photoelectric observations of low mass close X-ray binaries"

Sov.Astron.Lett. **15**, 352-355 = Pis'ma Astron.Zh **15**, 816-823 (1989b)

Stella, L.; Vietri, M.

"Lense-Thirring precession and quasi-periodic oscillations in low-mass X-ray binaries"

ApJ **492**, L59-L62 (1998)

Stella, L.; Vietri, M.; Morsink, S.M.

"Correlations in the quasi-periodic oscillation frequencies of low-mass X-ray binaries and the relativistic precession model"

ApJ **524**, L63-L66 (1999)

Strohmayer, T.E.

"Discovery of a 450 Hz quasi-periodic oscillation from the microquasar GRO J1655-40 with the Rossi X-ray Timing Explorer"

ApJ **552**, L49-L53 (2001)

Strohmayer, T.E.; Zhang, W.; Swank, J.H.; Smale, A.; Titarchuk, L.; Day, C.; Lee, U.:

"Millisecond X-ray variability from an accreting neutron star system"

ApJ **469**, L9-L12 (1996)

Takato, N.

"Pupil-segmented photometry for Lunar occultation observation"

in M. Iye, A.F.M. Moorwood, eds. *Instrument Design and Performance for*

*Optical/Infrared Ground-based Telescopes*, SPIE proc. **4841**, 622-626 (2003)

Titarchuk, L.; Osherovich, V.; Kuznetsov, S.

"Timing spectroscopy of quasi-periodic oscillations in the low-mass X-ray neutron star binaries"

ApJ **525**, L129-L132 (1999)

van der Klis, M.

"Rapid X-ray variability"

in W. Lewin, M. van der Klis, eds. *Compact Stellar X-ray Sources*, Cambridge Univ. Press, 75 pp., in press (2006); astro-ph/0410551

van der Klis, M.; Swank, J.H.; Zhang, W.; Jahoda, K.; Morgan, E.H.; Lewin, W.H.G.; Vaughan, B., van Paradijs, J.

"Discovery of submillisecond quasi-periodic oscillations in the X-ray flux of *Scorpius X-1*"

ApJ **469**, L1-L4 (1996)

van der Klis, M.; Wijnands, R.A.D.; Horne, K.; Chen, W.

"Kilohertz quasi-periodic oscillation peak separation is not constant in *Scorpius X-1*"

ApJ **481**, L97-L100 (1997)

van Paradjis, J.; McClintock, J.E.  
"Optical and ultraviolet observations of X-ray binaries"  
in W.H.G.Lewin, J.van Paradjis, E.P.J.van den Heuvel, eds. *X-ray Binaries*,  
pp.58-125, Cambridge Univ.Press (1995)

Young, A.T.  
"Photometric error analysis. VI. Confirmation of Reiger's theory of  
scintillation"  
AJ **72**, 747-753 (1967)

Warner, B.  
"High Speed Astronomical Photometry"  
Cambridge Univ.Press (1988)

Wijnands, R.; van der Klis, M.  
"A millisecond pulsar in an X-ray binary system"  
Nature **394**, 344-346 (1998)

Wijnands, R.; van der Klis, M.; Homan, J.; Chakrabarty, D.; Markwardt, C.B.;  
Morgan, E.H.  
"Quasi-periodic X-ray brightness fluctuations in an accreting millisecond  
pulsar"  
Nature **424**, 44-47 (2003)

Zhang, W.; Smale, A.P.; Strohmayer, T.E.; Swank, J.H.  
"Correlation between energy spectral states and fast time variability and  
further evidence for the marginally stable orbit in 4U 1820-30"  
ApJ **500**, L171-L174 (1998)

#### 4. Instrumental Requirements

Asplemeyer, M.; et al.  
"QSpace"  
ESA Contract (2003)

Aull, B.F.; Loomis, A.H.; Young, D.J.; Heinrichs, R.M.; Felton, B.J.; Daniels, P.J.;  
Landers, D.J.  
"Geiger-mode avalanche photodiodes for three-dimensional imaging"  
Lincoln Lab.J. **13**, 335-350 (2002)

Belluso, M.; Mazzillo Cataldo, M.; Bonanno, G.; Billotta, S.; Scuderi, S.; Cali, A.;  
Timpanaro, M.C.; Sanfilippo, D.; Fallica, P.G.; Sciacca, E.; Lombardo, S.;  
Morabito, A.  
"SPAD array detectors for astrophysical applications"  
Italian Astron.Soc. (2005)

Chuang, I.L.  
"Quantum algorithm for distributed clock synchronization"  
Phys.Rev.Lett. **85**, 2006-2009 (2000)

Cova, A.; Ghioni, M.; Lotito, A.; Rech, I.; Zappa, F.  
"Evolution and prospects for single-photon avalanche diodes and quenching  
circuits"  
J.Mod.Opt. **51**, 1267-1288 (2004)

Fumin, Y.; Zhongping, Z.; Wanzhen, C.; Xin, L.; Juping, C.; Bin, W.  
Presentation at 14th International Laser Ranging Workshop:  
<http://www.roa.es/14workshop-laser/#Presentations> (2004)

Giunta, D.; Busca, G.; Della Torre, A.; Vitta, V.; De Perini, V.; Grimoldi, R.; Stehlin, X.; Rochat, P.  
"Recent Developments in Time & Frequency Dissemination Systems"  
ESA Patent (2004)

Graff, W.; Rosselet, A.C.; Wild, U.P.; Gschwind, R.; Keller, C.U.  
"Handling of huge multispectral image data volumes from a spectral hole burning device (SHBD)"  
in M.R.Descour et al. eds. *Imaging Spectrometry*, Proc. SPIE **2480**, 445-452 (1995)

Heinrichs, R.M.; Aull, B.F.; Fouche, D.G.; Hatch, R.E.; McIntosh, K.A.; Marino, R.M.; O'Brien, M.E.; Rowe, G.S.; Zayhowski, J.J.  
"3-D laser radar development with arrays of photon-counting detectors and Avalanche photodiodes"  
in Conf. Lasers and Electro-optics, CLEO/QELS (June 2003)

Keller, C.U.  
"5,000 by 5,000 spatial by 15,000 spectral resolution elements: First astronomical observations with a novel 3-D detector"  
in W.van Breugel, J.Bland-Hawthorn, eds. *Imaging the Universe in Three Dimensions*, ASPC **195**, 495-500 (2000)

Keller, C.U.; Gschwind, R.; Renn, A.; Rosselet, A.; Wild, U.P.  
"The spectral hole-burning device: a 3-dimensional photon detector"  
A&AS **109**, 383-387 (1995)

Nogies, G.; Rauschenbeutel, A.; Osnaghi, S.; Brune, M.; Raimond, J.M.; Haroche, S.  
"Seeing a single photon without destroying it"  
Nature **400**, 239-242 (1999)

Prochazka, I.; Hamal, K.; Sopko, B.  
"Recent achievements in single photon detectors and their applications"  
J.Mod.Opt. **51**, 1289-1313 (2004)

Rarity, J.G.; et al.  
"Quantum Communication in Space"  
ESA Report (2003)

Ravet, M.; Samain, E.; Dalla, R.; Aubry, P.; Torre, J.M.; Paris, J.; Mangin, J.F.; Martinot Lagarde, G.  
"T2L2", Presentation at 14th International Laser Ranging Workshop:  
<http://www.roa.es/14workshop-laser/#Presentations> (2004)

Rosselet, A.C.; Graff, W.W.; Urs, P.; Keller, C.U.; Gschwind, R.  
"Persistent spectral hole burning used for spectrally high-resolved imaging of the Sun"  
in M.R.Descour et al. eds. *Imaging Spectrometry*, Proc. SPIE **2480**, 205-212 (1995)

Sobolevsky, R.  
"Ultrafast superconducting single-photon optical detectors and their applications"  
E Review Nr.93 (2004)

Valencia, A.; Scarcelli, G.; Shih, Y.  
"Distant clock synchronization using entangled photon pairs"  
Appl.Phys.Lett. **85**, 2655-2657 (2004)

Wang, Y.; Kempa, K.; Kimball, B.; Carlson, J.B.; Benham, G.; Li, W.Z.; Kempa, T.; Rybczynski, J.; Herczynski, A.; Ren, Z.F.  
"Receiving and transmitting light-like radio waves; Antenna effect in arrays of aligned carbon nanotubes"  
Appl.Phys.Lett. **85**, id. 2607 (2004)

Weinfurter, H.; Zeilinger, A.; Rarity, J.; Barbieri, C.  
"Tesat"

Qinetic, Contraves Space, Carlo Gavazzi Space, QIPS: Quantum Information and Quantum Physics in Space, a proposal to ESA (2005)

Zeilinger, A.; et al.

"Space-QUEST: Quantum Entanglement In Space Experiments"  
proposal to ESA (2005)

## 5. **QuantEYE** Conceptual Instrument Design

Brown, R.G.W.; Grant, R.S.

"Photon statistical properties of visible laser diodes"  
Rev.Sci.Instr. **58**, 928-931 (1987)

Canales, V.F.; Cagigal, M.P.

"Non-Gaussian speckle statistics in adaptive-optics partial compensation"  
Opt.Lett. **26**, 737-739 (2001)

Cox, A.N.

"Allen's Astrophysical Quantities", 4<sup>th</sup> ed.  
Springer (2000)

de Oliveira, M.C.; Sun, H.B

"Modeling of optical detection of spin-polarized carrier injection into light-emitting devices"  
Phys.Rev.B, **69**, 085322 (2004)

Fujisaki, H.; Shimizu, A.

"Quantum Langevin equations for semiconductor light-emitting devices and the photon statistics at a low-injection level"  
Phys.Rev. A **57**, 3074-3083 (1998)

Schmid, K.F.

"Experimental investigation of the light intensity statistics of semiconductor lasers"  
PhD thesis, ETH Zurich, 248 pp. (1982)

Sumitomo, H.; Kadoya, Y.; Yamanishi, M.

"Wideband deep penetration of photon-number  $f$  fluctuations into the quantum regime in series-coupled light-emitting diodes"  
Opt.Lett. **24**, 40-42 (1999)

Yin, J.; Wang, Y.; Xiao, M.; Wang, Y.

"A new semiclassical model to analyze sub-Poissonian light in high-impedance-driven semiconductor light emitters"  
Phys.Lett.A, **283**, 44-52 (2001)

## 6. Observing with **QuantEYE**

Liu, Q.Z.; van Paradijs, J.; van den Heuvel, E.P.J.

"A catalogue of high-mass X-ray binaries"  
A&AS **147**, 25-49 (2000)

Ritter, H.; Kolb, U.

"Catalogue of cataclysmic binaries, low-mass X-ray binaries and related objects (7<sup>th</sup> ed.)"

A&A **404**, 301-303 (2003). Revised version: <http://www.mpa-garching.mpg.de/RKcat/>

Wilkinson, P.N.; Kellermann, K.I.; Ekers, R.D.; Cordes, J.M.; Lazio, T.J.W.  
"The exploration of the unknown"  
New Astron. Rev. **48**, 1551-1563 (2004)

## Appendices

### A1. Coherence Properties of Light

### A2. Intensity Interferometry

See references for Section 1. The Road to Quantum Astronomy

### A3. High-Speed Instrumentation Worldwide

#### A3.1. HSP on Hubble Space Telescope

Bless, R.C.

"The High Speed Photometer for the Space Telescope"  
in D.N.B.Hall, ed. "The Space Telescope Observatory", NASA CP-2244, 106-113  
(1982)

Bless, R.C., Percival, J.W.; Gallagher, J.S.; Hoessel, J.G.; Shroeder, D.J.  
"Wisconsin study of a possible HST instrument"  
in P.Benvenuti, F.D.Macchetto, A.J.Schreier, eds. *Science with the Hubble Space Telescope - II*, .616-619 (1996)

Bless, R.C.; Richards, E.E.; Bosh, A.; Dolan, J.F.; Elliot, J.L.; Nelson, M.;  
Percival, J.W.; Robinson, E.L.; Taylor, M.; van Citters, G.W.; White, R.L.  
"The Hubble Space Telescope's High-Speed Photometer"  
PASP **111**, 364-375 (1999)

Bless, R.C.; Richards, E.E.; Dolan, J.F.; Elliott, J.L.; Nelson, M.J.; Percival, J.W.;  
Robinson, E.L.; Taylor, M.J.; van Citters, G.W.; White, R.L.  
"The Hubble Space Telescope High Speed Photometer"  
Univ. Wisconsin Astrophysics No.659 (1997)

Elliot, J.L.; Bosh, A.S.; Cooke, M.L.; Bless, R.C., Nelson, M.J., Percival, J.W.,  
Taylor, M.J.; Dolan, J.F.; Robinson, E.L.; van Citters, G.W.  
"An occultation by Saturn's rings on 1991 October 2-3 observed with the Hubble  
Space Telescope"  
AJ **106**, 2544-2572 (1993)

Percival, J.W.; Biggs, J.D.; Dolan, J.F.; Robinson, E.L.; Taylor, M.J.; Bless, R.C.;  
Elliot, J.L.; Nelson, M.J.; Ramseyer, T.F.; van Citters, G.W.; Zhang, E.  
"The Crab pulsar in the visible and ultraviolet with 20 microsecond effective  
time resolution"  
ApJ **407**, 276-283 (1993)

Richards, E.E.; Percival, J.W.; Nelson, M.J.; Townsley, L.C.; Hatter, E.  
"Operations experiences of the Space Telescope high speed photometer"  
in P.Y.Bély, J.B.Breckinridge, eds. *Space Astronomical Telescopes and  
Instruments II*, SPIE proc. **1945**, 301-307 (1993)

Taylor, M.J.; Nelson, M.J.; Bless, R.C.; Dolan, J.F.; Elliot, J.L.; Percival, J.W.;  
Robinson, E.L.; van Citters, G.W.  
"High speed ultraviolet photometry of HD 60435"  
ApJ **413**, L125-L128 (1993)

White, R.L.  
"High Speed Photometer Instrument Handbook"  
Space Telescope Science Institute, 47 pp. (1985)

### **A3.2. HIPO on the SOFIA Airborne Telescope**

Casey, S.C.; Savage, M.L.; Becklin, E.E.  
"The SOFIA science instrument program: lessons learned"  
in G. Hasinger, M.J. Turner, eds. *UV and Gamma-Ray Space Telescope Systems*,  
Proc. SPIE **5492**, 1053-1063 (2004)

Dunham, E.W.  
"The optical design of HIPO: a high-speed imaging photometer for occultations"  
in R.K. Melugin, H.-P. Roeser, eds. *Airborne Telescope Systems II*, Proc. SPIE  
**4857**, 62-72 (2003)

Dunham, E.W.; Baron, R.L.; Elliot, J.L.; Vallergera, J.V.; Doty, J.P., Ricker, G.R.  
"A high-speed, dual-CCD imaging photometer"  
PASP **97**, 1196-1204 (1985)

Dunham, E.W.; Elliot, J.L.; Bida, T.A.; Taylor, B.W.  
"HIPO: a high-speed imaging photometer for occultations"  
in A.F. Moorwood, M. Iye, eds. *Ground-based Instrumentation for Astronomy*, Proc.  
SPIE **5492**, 592-603 (2004)

Dunham, E.W.; Elliot, J.L.; Taylor, B.W.  
"HOPI: a high-speed occultation photometer and imager for SOFIA" [sic.]  
in R.K. Melugin, H.-P. Roeser, eds. *Airborne Telescope Systems*, Proc. SPIE **4014**,  
77-85 (2000)

### **A3.3. ULTRACAM**

Beard, S.M.; Vick, A.J.A.; Atkinson, D.; Dhillon, V.S.; Marsh, T.; McLay, S.;  
Stevenson, M.; Tierney, C.  
"ULTRACAM camera control and data acquisition system"  
in H. Lewis, ed. *Advanced Telescope and Instrumentation Control Software II*,  
proc. SPIE **4848**, 218-229 (2002)

Brinkworth, C.S.; Marsh, T.R.; Dhillon, V.S.; Feline, W.J.  
"ULTRACAM Observations of the braking rate of the pre-CV NN Ser"  
in J.M. Hameury, J.P. Lasota, eds. *The Astrophysics of Cataclysmic Variables and  
Related Objects*, ASPC **330**, 329-... (2005)

Dhillon, V.; Marsh, T.  
"ULTRACAM - studying astrophysics on the fastest timescales"  
New Astron. Rev. **45**, 91-95 (2001)

Feline, W.J.; Dhillon, V.S.; Marsh, T.R.; Brinkworth, C.S.  
"ULTRACAM photometry of the eclipsing cataclysmic variables XZ Eri and DV UMa"  
MNRAS **355**, 1-10 (2004)

Feline, W.J.; Dhillon, V.S.; Marsh, T.R.; Stevenson, M.J.; Watson, C.A.;  
Brinkworth, C.S.  
"ULTRACAM photometry of the eclipsing cataclysmic variable OU Vir"  
MNRAS **347**, 1173-1179 (2004). Erratum: *ibid.* **354**, 1279 (2004)



#### A3.4. STJ & TES: Superconducting Energy-Resolving Detectors

Bay, T.J.; Burney, J.A.; Brink, P.L.; Cabrera, B.; Castle, J.P.; Romani, R.W.; Tomada, A.; Young, B.A.; Nam, S.W.; Miller, A.J.; Martinis, J.M.; Kenny, T.W.; Wang, E. "Development of superconducting transition edge sensors for time- and energy-resolved single-photon counters with application to imaging astronomy" in R.E.Longshore, S.Sivananthan, eds. *Materials for Infrared Detectors III*, proc.SPIE **5209**, 192-200 (2003)

Bridge, C.M.; Cropper, M.; Ramsay, G.; Perryman, M.A.C.; de Bruijne, J.H.J.; Favata, F.; Peacock, A.; Rando, N.; Reynolds, A.P. "STJ observations of the eclipsing polar HU Aqr" MNRAS **336**, 1129-1138 (2002)

Cabrera, B.; Clarke, R.M.; Colling, P.; Miller, A.J.; Nam, S.; Romani, R.W. "Detection of single infrared, optical, and ultraviolet photons using superconducting transition edge sensors" Appl.Phys.Lett. **73**, 735-737 (1998)

Cropper, M.; Barlow, M.; Perryman, M.A.C.; Horne, K.; Bingham, R.; Page, M.; Guttridge, P.; Smith, A.; Peacock, A.; Walker, D.; Charles, P. "A concept for a superconducting tunnelling junction based spectrograph" MNRAS **344**, 33-44 (2003)

de Bruijne, J.H.J.; Reynolds, A.P.; Perryman, M.A.C.; Peacock, A.; Favata, F.; Rando, N.; Martin, D.; Verhoeve, P.; Christlieb, N. "Direct determination of quasar redshifts" A&A **381**, L57-L60 (2002)

Gimenez, A., ed. "Report on the activities of the Research and Scientific Support Department 2003-2004" ESA SP-1288, p.45-47 (2005)

Mather, J.C. "Super photon counters" Nature **401**, 654-655 (1999)

Perryman, M.A.C.; Cropper, M.; Ramsay, G.; Favata, F.; Peacock, A.; Rando, N.; Reynolds, A. "High-speed energy-resolved STJ photometry of the eclipsing binary UZ For", MNRAS **324**, 899-909 (2001)

Perryman, M.A.C.; Foden, C.L.; Peacock, A. "Optical photon counting using superconducting tunnel junctions" Nucl.Instr.Meth.Phys.Res. **A325**, 319-325 (1993)

Rando, N.; Peacock, A.; Favata, F.; Perryman, M. "S-Cam: An imaging spectro-photometer based on superconducting tunnel junctions" Exp.Astron. **10**, 499-517 (2000)

Reynolds, A.P.; de Bruijne, J.H.J.; Perryman, M.A.C.; Peacock, A.; Bridge, C.M. "Temperature determination via STJ optical spectroscopy" A&A **400**, 1209-1217 (2003)

Reynolds, A.P.; Ramsay, G.; de Bruijne, J.H.J.; Perryman, M.A.C.; Cropper, M.; Bridge, C.M.; Peacock, A. "High-speed, energy-resolved STJ observations of the AM Her system V2301 Oph" A&A **435**, 225-230 (2005)

Romani, R.W.; Miller, A.J.; Cabrera, B.; Figueroa-Feliciano, E.; Nam, S.W.  
"First astronomical application of a cryogenic transition edge sensor spectrophotometer"  
ApJ **521**, L153-L156 (1999)

Romani, R.W.; Miller, A.J.; Cabrera, B.; Nam, S.W.; Martinis, J.M.  
"Phase-resolved Crab Studies with a Cryogenic Transition-Edge Sensor Spectrophotometer"  
ApJ **563**, 221-228 (2001)

Steeghs, D.; Perryman, M.A.C.; Reynolds, A.; de Bruijne, J.H.J.; Marsh, T.; Dhillon, V.S.; Peacock, A.  
"High-speed energy-resolved STJ photometry of the eclipsing dwarf nova IY UMa"  
MNRAS **339**, 810-816 (2003)

Wenzel, K.-P., ed.  
"Report on the activities of the Research and Scientific Support Department 2001-2002"  
ESA SP-1268, p.54-59 (2003)

### **A3.5. OPTIMA**

Kanbach, G.; Kellner, S.; Schrey, F.; Steinle, H.; Straubmeier, C.; Spruit, H.C.  
"Design and results of the fast timing photo-polarimeter OPTIMA"  
in M.Iye, A.F.M. Moorwood, eds. *Instrument Design and Performance for Optical/Infrared Ground-based Telescopes*, SPIE proc. **4841**, 82-93 (2003)

Kanbach, G.; Steinle, H.; Kellner, S.  
"Optical polarimetry of the Crab pulsar"  
Poster at MPE meeting (2002)

Kanbach, G.; Straubmeier, C.; Spruit, H.C.; Belloni, T.  
"Correlated fast X-ray and optical variability in the black-hole candidate XTE J1118+480"  
Nature **414**, 180-182 (2001)

Malzac, J.; Belloni, T.; Spruit, H.C.; Kanbach, G.  
"The Optical and X-ray flickering of XTE J1118+480"  
A&A **407**, 335-345 (2003)

Schwobe, A.D.; Hambaryan, V.; Schwarz, R.; Kanbach, G.; Gänsicke, B.T.  
"A multiwavelength timing analysis of the eclipsing polar DP Leo"  
A&A **392**, 541-551 (2002)

Spruit H.C.; Kanbach G.  
"Correlated X-ray and optical variability in KV UMa"  
A&A **391**, 225-233 (2002)

Straubmeier, C.; Kanbach, G.; Schrey, F.  
"OPTIMA: A photon counting high-speed photometer"  
Exp.Astron. **11**, 157-170 (2001)

### **A3.6. MANIA**

Beskin, G.M.; Komarova, V.N.; Mitronova, S.N.; Neizvestny, S.I.; Plokhotnichenko, V.L.; Popova, M.Yu.  
"Investigation of relativistic and fast variable objects with high time resolution"  
Bull.Spec.Astrophys.Obs. **44**, 43-49 (1998)

- Beskin, G.; Komarova, V.; Neizvestny, S.; Plohotnichenko, V.; Popova, M.; Zhuravkov, A.  
"The investigations of optical variability on time scales of  $10^{-7}$  -  $10^2$  s: hardware, software, results", *Exper. Astron.* **7**, 413-420 (1997)
- Beskin, G.M.; Lebedev, V.S.; Neizvestnyi, S.I.; Plakhotnichenko, V.L.; Shvartsman, V.F.  
"A search for young optical pulsars in the galaxies NGC4647 and NGC4321"  
*Sov. Astr. Lett.* **7**, 300-303 (1981) = *Pis'ma Astron. Zh.* **7**, 537-542 (1981)
- Beskin, G.M.; Neizvestnyj, S.I.; Pimonov, A.A.; Plakhotnichenko, V.L.; Fabrika, S.I.; Shvartsman, V.F.  
"Absence of optical variability of relativistic object SS 433 on timescales of  $10^{-6}$  to  $10$  s"  
*Astrofiz. Issled.* **20**, 72-77 (1985)
- Beskin, G.M.; Neizvestnyi, S.I.; Pimonov, A.A.; Plakhotnichenko, V.L.; Shvartsman, V.F.  
"A fine resolution optical lightcurve of the Crab nebula pulsar"  
*Sov. Astr. Lett.* **9**, 148-151 (1983) = *Pis'ma Astron. Zh.* **9**, 280-285 (1983)
- Beskin, G.M.; Neizvestnyi, S.I.; Pimonov, A.A.; Plakhotnichenko, V.L.; Shvartsman, V.F.  
"The minimum optical variability time scale of V1341 Cygni (Cygnus X-2) measured with the 6-meter telescope"  
*Sov. Astr. Lett.* **5**, 271-274 (1979) = *Pis'ma Astron. Zh.* **5**, 508-513 (1979)
- Beskin, G.; Neizvestny, S.; Plohotnichenko, V.; Popova, M.; Zhuravkov, A.; Benvenuto, O.G.; Feinstein, C.; Mendez, M.  
"Optical study of LMXBs with high temporal resolution: Evidence for non-thermal flares from MXB 1735-44"  
*A&A* **289**, 141-147 (1994)
- Demchuk, M.I.; Evseyev, O.A.; Shvartsman, V.F.; Tsarevskij, G.S.; Yakushev, A.K.  
"Instrumentation complex of MANIA experiment" [in Russian]  
*Soob. Spec. Astrophys. Obs.* **20**, 15-17 (1977)
- Efremov, V.G.; Najdenov, I.D.  
"On the possibility of polarimetric measurements of astronomical objects using quantum optics"  
*Soob. Spec. Astrophys. Obs.* **69**, 137-147 (1992)
- Golden, A.; Shearer, A.; Redfern, R.M.; Beskin, G.M.; Neizvestny, S.I.; Neustroev, V.V.; Plohotnichenko, V.L.; Cullum, M.  
"High speed phase-resolved 2-d UVB photometry of the Crab pulsar"  
*A&A* **363**, 617-628 (2000)
- Karpov, S.; Bad'in, D.; Beskin, G.; Biryukov, A.; Bondar, S.; Chuntunov, G.; Debur, V.; Ivanov, E.; Katkova, E.; Plohotnichenko, V.; Pozanenko, A.; Zolotukhin, I.; Hurley, K.; Palazzi, E.; Masetti, N.; Pian, E.; Nicastro, L.; Bartolini, C.; Guarnieri, A.; Nanny, D.; Piccioni, A.; Brosch, N.; Eichler, D.; Shearer, A.; Golden, A.; Redfern, M.; Atteia, J.-L.; Boer, M.  
"FAVOR (FAst Variability Optical Registration) - two-telescope complex for detection and investigation of short optical transients"  
*Astron. Nach.* **325**, 677-677 (2004)
- Mansurov, V.N.; Shvartsman, V.F.  
"Program-algorithmic complex of MANIA experiment (First stage)" [in Russian]  
*Soob. Spec. Astrophys. Obs.* **19**, 52-71 (1977)

O'Sullivan,C.; Shearer,A.; Colhoun,M.; Golden,A.; Redfern,M.; Butler,R.; Beskin,G.M.; Neizvestny,S.I.; Neustroev,V.V.; Plokhotnichenko,V.L.; Danks,A.  
"A search for the optical counterpart of PSR B1951+32 in the supernova remnant CTB 80"  
A&A **335**, 991-994 (1998)

Plokhotnichenko,V.L.  
"Program-algorithmic complex of "MANIA" experiment. The second stage. Search for variability program" [in Russian]  
Soob.Spec.Astrophys.Obs. **38**, 29-80 (1983)

Plokhotnichenko,V.; Beskin,G.; Debur,V.; Panferov,A.; Panferova,A.  
"The multicolor panoramic photometer-polarimeter with high time resolution based on the PSD"  
Nucl.Instrum.Meth. **A513**, 167-171 (2003)

Shearer,A.; Golden,A.; Harfst,S.; Butler,R.; Redfern,R.M.; O'Sullivan,C.M.M.; Beskin,G.M.; Neizvestny,S.I.; Neustroev,V.V.; Plokhotnichenko,V.L.; Cullum,M.; Danks,A.  
"Possible pulsed optical emission from Geminga"  
A&A **335**, L21-L24 (1998)

Shvartsman,V.F.  
"Halos around 'Black holes'"  
Sov.Astron. **15**, 377-384 (1971) = Astron.Zh. **48**, 479-488 (1971)

Shvartsman,V.F.  
"The MANIA experiment. Astrophysical problems, mathematical methods, instrumentation complex, results of the first observations" [in Russian]  
Soob.Spec.Astrophys.Obs. **19**, 5-38 (1977)

Shvartsman,V.F.; Bernstein,I.N.; Beskin,G.M.; Komarova,V.N.; Neizvestny,S.I.; Plokhotnichenko,V.L.; Popova,M.Yu.; Zhuravkov,A.V.  
"Superfast photometry with MANIA complex"  
in G.H.Jacoby, J.Barnes, eds. *Astronomical Data Analysis Software and Systems V*, ASPC **101**, 428-431 (1996)

Shvartsman,V.F.; Beskin,G.M.; Mitronova,S.N.; Neizvestnyi,I.S.; Plakhotnichenko,V.L.  
"A:0620-00 - A search for ultrafast optical variability and UBVR photometry"  
Sov.Astr.Lett. **15**, 252-255 (1989) = Pis'ma Astron.Zh. **15**, 590-596 (1989)

Shvartsman,V.; Beskin,G.; Mitronova,S.; Neizvestny,S.; Plakhotnichenko,V.; Pustil'nik,L.  
"Results of the MANIA experiment: An optical search for extraterrestrial intelligence"  
in G.S.Shostak, ed. *Third Decennial US-USSR Conference on SETI*, ASPC **47**, 381-390 (1993)

Shvartsman,V.F.; Beskin,G.M.; Mitronova,S.N.; Pustil'nik,S.A.  
"The results of search for isolated black holes in MANIA experiment"  
Soob.Spec.Astrophys.Obs. **64**, 36-39 (1990)

Shvartsman,V.F.; Tsarevskij,G.S.  
"Arrangement and technique of MANIA experiment" [in Russian]  
Soob.SAO **19**, 39-51 (1977)

Zhuravkov,A.V.; Pimonov,A.A.; Plokhotnichenko,V.L.  
"'Quantochron' - A Multichannel Time-to-Code Converter"  
Bull.Spec.Astrophys.Obs. **37**, 159-172 (1994)

### A3.7. Optical SETI

Bhathal, R.

"Optical SETI in Australia"

in S.A.Kingsley, R.Bhathal, eds. *The Search for Extraterrestrial Intelligence (SETI) in the Optical Spectrum III*, proc. SPIE **4273**, 144-152 (2001)

Deffenbaugh, N.

"Optical SETI at Princeton: November 2001 - April 2002"

Bachelor's thesis, Princeton University;

<http://observatory.princeton.edu/aseti/thesis.pdf>

Horowitz, P.; Coldwell, C.; Howard, A.; Latham, D.; Stefanik, R.; Wolff, J.; Zajac, J.

"Targeted and all-sky search for nanosecond optical pulses at Harvard-Smithsonian"

in S.A.Kingsley, R.Bhathal, eds. *The Search for Extraterrestrial Intelligence (SETI) in the Optical Spectrum III*, proc. SPIE **4273**, 119-127 (2001)

Howard, A.B.; Horowitz, P.

"Is there RFI in pulsed optical SETI?"

in S.A.Kingsley, R.Bhathal, eds. *The Search for Extraterrestrial Intelligence (SETI) in the Optical Spectrum III*, proc. SPIE **4273**, 153-160 (2001)

Howard, A.W.; Horowitz, P.; Wilkinson, D.T.; Coldwell, C.M.; Groth, E.J.; Jarosik, N.; Latham, D.W.; Stefanik, R.P.; Willman, A.J., Wolff, J.; Zajac, J.M.

"Search for nanosecond optical pulses from nearby solar-type stars"

ApJ **613**, 1270-1284 (2004)

Lampton, M.

"Optical SETI: The next search frontier"

in G.A.Lemarchand, K.J.Meech, eds. *Bioastronomy '99. A New Era in Bioastronomy*, ASPC **213**, 565-570 (2000)

Shvartsman, V.F.; Beskin, G.M.; Mitronova, S.N.; Neizvestny, S.I.;

Plokhotnichenko, V.L.; Pustil'nik, L.A.

"The search for optical signals of cosmic civilizations"

Bull.Spec.Astrophys.Obs. **37**, 178-186 (1994)

Wright, S.A.; Drake, F.; Stone, R.P., Treffers, R.; Werthimer, D.

"An improved optical SETI detector"

in S.A.Kingsley, R.Bhathal, eds. *The Search for Extraterrestrial Intelligence (SETI) in the Optical Spectrum III*, proc. SPIE **4273**, 173-177 (2001)

Wright, S.A.; Stone, R.P.S.; Drake, F.; Muñoz, M.; Treffers, R.; Werthimer, D.;

Evans, R.A.; Isotalo, T.; Vance, S.

"Optical SETI at Lick Observatory: A status report"

in R.Norris, F.Stootman, eds. *Bioastronomy 2002: Life Among the Stars*, IAU Symp. **213**, 415-418 (2004)

### A3.8. Lunar- & Satellite Laser Ranging

Kral, L.; Prochazka, I.; Hamal, K.

"Optical signal path delay fluctuations caused by optical turbulence"

Opt.Lett. **30**, 1767-1769 (2005)

#### **12th International Workshop on Laser Ranging:**

Electronic proceedings: <http://geodaf.mt.asi.it/GDHTL/news/iwlr/> (2000)

Murphy, T.W.; Strasburg, J.D.; Stubbs, C.W.; Adelberger, E.G.; Angle, J.;

Nordtvedt, K.; Williams, J.G.; Dickey, J.O.; Gillespie, B.

"The Apache Point Observatory Lunar Laser-ranging Operation (APOLLO)"

**13th International Workshop on Laser Ranging:**

Proceedings on CD-ROM: R.Noomen et al. eds.: NASA/CP-2003-212248 (2003);  
<http://cddis.gsfc.nasa.gov/lw13/>

Martin, J.; Hink, P.

*"Characterization of a microchannel plate photomultiplier tube with high sensitivity GaAs photocathode"*

Murphy, T.W.; Adelberger, E.G.; Strasburg, J.D.; Stubbs, C.W.

*"APOLLO: Multiplexed Lunar laser ranging"*

Samain, E.; Dalla, R.; Prochazka, I.

*"Time walk compensation of an avalanche photo-diode with a linear photo-detection"*

Strasburg, J.D.; Murphy, T.W.; Adelberger, E.G.; Stubbs, C.W.; Miller, D.W.; Angle, J.I.

*"The advantages of avalanche photodiode (APD) arrays in laser ranging applications"*

**14th International Workshop on Laser Ranging:**

Electronic proceedings: <http://cddis.gsfc.nasa.gov/lw14/> (2004)

Kral, L.; Prochazka, I.; Kirchner, G.; Koidl, F.

*"Atmospheric contribution to the laser ranging jitter"*

Mulacova, J.; Hamal, K.; Kirchner, G.; Koidl, F.

*"Effects of the atmosphere on the SLR precision"*

Murphy, T.W.; Strasburg, J.D.; Stubbs, C.W.; Adelberger, E.G.; Tom, L.; Orin, A.E.; Michelsen, E.L.; Battat, J.; Hoyle, C.D.; Swanson, E.; Williams, E.

*"APOLLO: Meeting the millimeter goal"*

**A3.9. QVANTOS**

Dravins, D.

*"Astrophysics on its shortest timescales"*

ESO Messenger No.78, 9-19 (1994)

Dravins, D.

*"Beyond imaging, spectroscopy and interferometry: Quantum optics at the largest telescopes"*

in T.Andersen, A.Ardeberg, R.Gilmozzi, eds. *Bäckaskog Workshop on Extremely Large Telescopes*, ESO Conf.Workshop proc. **57**, 36-42 (2000)

Dravins, D.

*"Quantum-optical signatures of stimulated emission"*

in T.R.Gull, S.Johannson, K.Davidson, eds. *Eta Carinae and Other Mysterious Stars: The Hidden Opportunities of Emission Line Spectroscopy*, ASPC **242**, 339-345 (2001)

Dravins, D.; Faria, D.; Nilsson, B.

*"Avalanche diodes as photon-counting detectors in astronomical photometry"*

in M.Iye, A.F.Moorwood, eds. *Optical and IR Telescope Instrumentation and Detectors*, SPIE proc. **4008**, 298-307 (2000)

Dravins, D.; Hagerbo, H.O.; Lindegren, L.; Mezey, E.; Nilsson, B.

*"Optical astronomy on milli-, micro-, and nanosecond timescales"*

in D.L.Crawford, E.R.Craigne, eds. *Instrumentation in Astronomy VIII*, SPIE proc. **2198**, 289-301 (1994)

Dravins, D.; Lindegren, L.; Mezey, W.; Young, A.T.  
"Atmospheric intensity scintillation of stars. I. Statistical distributions and temporal properties"  
PASP **109**, 173-207 (1997)

Dravins, D.; Lindegren, L.; Mezey, W.; Young, A.T.  
"Atmospheric intensity scintillation of stars. II. Dependence on optical wavelength"  
PASP **109**, 725-737 (1997)

Dravins, D.; Lindegren, L.; Mezey, W.; Young, A.T.  
"Atmospheric intensity scintillation of stars. III. Effects for different telescope apertures"  
PASP **110**, 610-633 (1998); erratum *ibid.* **110**, 1118 (1998)

### **A3.10. TRIFFID, MEKASPEK & MSCP, SUBARU, SALT, ESO-VLT, Opticon, and Other**

Barwig, H.; Mantel, K.-H.  
"VLT high-speed spectro-photometry: A powerful tool for exploring compact stellar objects and related phenomena"  
in J.R.Walsh, I.J.Danziger, eds. *Science with the VLT*, 134-138 (1995)

Barwig, H.; Mantel, K.H.; Kieseewetter, S.  
"FRISPI - A Fast Recording Imager and Spectro-photometric Instrument for the VLT"  
in S.D'Odorico, ed. *Future VLT Instruments: Scientific Drivers and Concept Definitions*, ESO Scient.Rep. No.**15**, 2-11 (1994)

Barwig, H.; Mantel, K.H.; Kieseewetter, S.  
"The impact of fiber optics on photometry - Design of two high-speed multichannel instruments"  
in S.Arribas, E.Mediavilla, F.Watson, eds. *Fiber Optics in Astronomy III*, ASPC **152**, 320-328 (1998)

Barwig, H.; Schoembs, R.  
"MSCP: Photometry through clouds?"  
ESO Messenger No.48, 29-31 (1987)

Barwig, H.; Schoembs, R.; Buckenmayer, C.  
"A multichannel multicolour photometer for high time resolution"  
A&A **175**, 327-344 (1987)

Butler, R.F.; Shearer, A.; Redfern, R.M.; Colhoun, M.; O'Kane, P.; Penny, A.J.; Morris, P.W.; Griffiths, W.K.; Cullum, M.  
"TRIFFID photometry of globular cluster cores - I. Photometric techniques and variable stars in M15"  
MNRAS **296**, 379-391 (1998)

Mantel, K.H., Barwig, H.  
"Multichannel-multicolour photometry - experiences from a long term observing campaign"  
in C.Sterken, J.de Groot, eds. *The Impact of Long-Term Monitoring on Variable Star Research*, NATO ASI **C436**, 329-344 (1993)

Moon, D.-S.  
"Instrument development for high-speed infrared and optical photometry and observational studies of pulsars"  
PhD thesis, Cornell Univ., 164 pp. (2004)

Moon, D.-S.; Pirger, B.E.; Eikenberry, S.S.

"A next-generation high-speed data acquisition system for multichannel infrared and optical photometry"

PASP **113**, 646-651 (2001)

Sekiguchi, K.; Charles, P.; van Zyl, L.; Woodhouse, G.F.

"High-speed imaging and spectro-polarimetry with the Subaru telescope"

in S.Vrielmann, M.Cropper, eds. *Magnetic Cataclysmic Variables*, ASPC **315**, 182-183 (2004)

Sekiguchi, K.; Cropper, M.S.; Bingham, R.G.; Guttridge, P.R.; Oliver, W.T.; Hepburn, I.D.

"High-speed spectro-photo-polarimeter for the Subaru Telescope"

in M.Iye; A.F.Moorwood, eds. *Optical and IR Telescope Instrumentation and Detectors*, proc. SPIE **4008**, 405-416 (2000)

